Institute of Chemistry

Plasmonic Chemistry

Plasmon-driven photocatalytic reactions monitored by surface-enhanced Raman spectroscopy

---

Doctoral thesis (cumulative)

In fulfillment of the requirements for the degree

“Doctor rerum naturalium“

(Dr. rer. nat.)

In the scientific discipline “Plasmonic Chemistry”

Submitted to the

Faculty of Science

University of Potsdam

by

Radwan Mohamed Sarhan Radwan

Potsdam, 2019

Author:

Radwan Mohamed Sarhan Radwan

Doctoral committee:

Prof. Dr. Matias Bargheer

Prof. Dr. Sebastian Schlücker

Prof. Dr. Ilko Bald

Published online at the
Institutional Repository of the University of Potsdam:
https://doi.org/10.25932/publishup-43330
https://nbn-resolving.org/urn:nbn:de:kobv:517-opus4-433304

Acknowledgments

I would like to thank and acknowledge so many people for helping and assisting me to complete my PhD and to finish my dissertation. First among them is my supervisor, Prof. Matias Bargheer, who believed in me and gave me the chance to join his research group (UDKM, University of Potsdam). His ideas and guidance have assisted the project from the very beginning. I would also like to express my gratitude to Dr. Wouter Koopman for his direct invaluable support and guidance during my research. I would also like to thank every member of the group for helping me during the general group seminars and the special discussions regarding my data and for providing a good atmosphere in the group.

Special thanks also must go to Prof. Joachim Koetz, Dr. Ferenc Liebig and Dr. Ahed Abouserie for the successful collaborations and for the nice general discussion over several subjects.

I would also like to acknowledge the graduate School of Analytical Sciences Adlershof (SALSA) for their financial and scientific support during my stay.

Outside the group and the university, special thanks go to Prof. Ahmed Elwahy, who always shows up when I need a help.

My deepest gratitude goes to my wife, son and my family in Egypt for being supportive in every way. Thank you all for everything you have done to me.

Contents

List of publications

Related publications

- **Radwan M. Sarhan**, Wouter Koopman, Jan Pudell, Felix Stete, Marc Herzog, Ferenc Liebig, Joachim Koetz, and Matias Bargheer. Scaling-Up Nano-Plasmon Catalysis: the Role of Heat Dissipation, J. Phys. Chem. C 2019, 123, 9352−9357.

- **Radwan M. Sarhan**, Wouter Koopman, Roman Schuetz, Thomas Schmid, Joachim Koetz, and Matias Bargheer. The importance of plasmonic heating for the plasmon-driven photodimerization of 4-nitrothiophenol, Sci. Rep., 2019, 9, 3060.

- Ferenc Liebig, **Radwan M. Sarhan**, Claudia Prietzel, Clemens N.Z. Schmitt, Matias Bargheer, Joachim Koetza. Tuned SERS Performances of undulated Au@Ag Triangles, ACS Appl. Nano Mater., 2018, 1, 1995–2003.

- Ferenc Liebig, **Radwan M. Sarhan**, Claudia Prietzel, Matias Bargheer, Joachim Koetz. Undulated gold nanoplatelets. In situ growth of hemispherical gold nanoparticles onto the surface of gold nanotriangles, Langmuir, 2018, 34, 4584–4594.

- Ferenc Liebig, **Radwan M. Sarhan**, Mathias Sander, Wouter Koopman, Roman Schuetz, Matias Bargheer, and Joachim Koetz. Deposition of Gold Nanotriangles in Large Scale Close-Packed Monolayers for X-ray-Based Temperature Calibration and SERS Monitoring of Plasmon-Driven Catalytic Reactions, ACS Appl. Mater. Interfaces, 2017.

- Ferenc Liebig, Ricky Henning, **Radwan M. Sarhan**, Claudia Prietzel, Matias Bargheer and Joachim Koetz: A new route to gold nanoflowers, Nanotechnology, 2018, 29, 185603.

- Alexander. Von Reppert, **Radwan M. Sarhan**, Felix Stete, Jan Pudell, Natalia Del Fatti, Aurelien Crut, Joachim Koetz, Ferenc Liebig, Claudia Prietzel, Matias Bargheer: Watching the Vibration and Cooling of Ultrathin Gold Nanotriangles by Ultrafast X-ray Diffraction, J. Phys. Chem. C., 2016, 120, 28894.

- Ferenc Liebig, **Radwan M. Sarhan**, Claudia Prietzel, Antjie Reinecke, Joachim Koetz: "Green" Gold Nanotriangles: Synthesis, Purification by Polyelectrolyte/Micelle Depletion Flocculation and Performance in Surface-Enhanced Raman Scattering, RSC adv., 2016, 6, 33561.

Non-related publications

- **Radwan M. Sarhan**, Gumaa A. El-Nagar, Ahed Shawky Mohammed Abouserie, and Christina Roth: Silver-Iron hierarchical microflowers for highly efficient H2O2 non-enzymatic amperometric detection, ACS Sustainable Chem. Eng., accepted 2019.

- Gumaa A. El-Nagar, Iver Lauermann, **Radwan M. Sarhan**, and Christina Roth: Hierarchically Structured Iron-Doped Silver (Ag-Fe) Lotus Flowers for Efficient Oxygen Reduction Reaction, Nanoscale, 2018,10, 7304-7310.

- Gumaa A. El-Nagar, **Radwan M. Sarhan** , Ahed Abouserie , Matias Bargheer, Christina Roth: Efficient 3D-Silver Flower-like Microstructures for Non-Enzymatic Hydrogen Peroxide (H2O2) Amperometric Detection, Sci. Rep. 2017, 7, 12181.

Poster presentations

- **Radwan M. Sarhan**, Wouter Koopman, Ferenc Liebig, Mathias Sander, Roman Schuetz, Joachim Koetz, Matias Bargheer " Heat-enhanced plasmon driven coupling reactions" The 28th International Conference on Photochemistry (ICP 2017), Strasbourg, France, 2017.

- **Radwan M. Sarhan**, Wouter Koopman, Ferenc Liebig, Mathias Sander, Roman Schuetz, Joachim Koetz, Matias Bargheer "SERS monitoring of plasmon-driven coupling reaction on large scale monolayer of gold nanotriangles and the temperature effects" The 14th Confocal Raman Imaging Symposium, Ulm, Germany, 2017.

- **Radwan M. Sarhan**, Wouter Koopman, Matias Bargheer "Ultrafast surface enhanced Raman scattering: A mechanistic study of photocatalytic reactions" SALSA 2nd poster session, Berlin, Germany, 2015.

List of abbreviations

Abbreviation	Meaning
1D	One dimensional
2D	Two dimensional
3D	Three dimensional
4-ATP	4-aminothiophenol
4-MBT	4-methylbenzenethiol
4-NTP	4-nitrothiophenol
AA	Ascorbic acid
AOT	dioctyl sodium sulfosuccinate
AgNO3	silver nitrate
APTES	3-Aminopropyl)triethoxysilane
AuNFs	Gold nanoflowers
AnNTs	Gold nanotriangles
BBO	Barium borate
BDAC	Benzyldimethylammonium chloride
CARS	Coherent anti-stokes Raman scattering
CID	Chemical inetrface damping
CM	Chemical mechanism
CTAB	Cetyltrimethylammoniumm bromide
CTAC	Cetyltrimethylammonium chloride
DDA	Discrete dipole approximation
DLS	Dynamic light scattering
DMAB	Dimercaptoazobenzene
E	Electric field
E_f	Fermi energy
EF	Enhancement factor
EM	Electromagnetic mechanism

et al.	Et alii (masculine), et aliae (feminine)
HEPES	4-(2-hydroxyethyl)-1-piperazineethanesulfonic acid
HOMO	Highest occupied molecule orbital
HRTEM	High resolution transmission electron microscopy
LSPR	Localized surface plasmon resonance
LUMO	lowest unoccupied molecule orbital
MPTMS	(Mercaptopropyl)trimethoxysilane
NIL	Nanoimprint lithography
NPs	Nanoparticles
NTs	Nanotriangles
PalPhBisCarb	poly(N,N′-diallyl-N,N′-dimethylammonium-alt-3,5-bis-carboxyphenyl-maleamic carboxylate)
PEI	poly(ethylenimine)
PES	Potential energy surface
PDMS	Polydimethylsiloxane
RR	Resonance Raman
R6G	Rhodamine 6G
RS	Raman scattering
SAXS	Small angle X-ray scattering
SEM	Scanning electron microscopy
SERS	Surface-enhanced Raman spectroscopy
Si	Silicon
STEM	Scanning transmission electron microscope
TEM	Transmission electron microscopy
TERS	Tip-enhanced Raman scattering
UV	Ultraviolet
UV-vis-NIR	Ultraviolet-visible-near-infrared

Abstract

Plasmonic metal nanostructures can be tuned to efficiently interact with light, converting the photons into energetic charge carriers and heat. Therefore, the plasmonic nanoparticles such as gold and silver nanoparticles act as nano-reactors, where the molecules attached to their surfaces benefit from the enhanced electromagnetic field along with the generated energetic charge carriers and heat for possible chemical transformations. Hence, plasmonic chemistry presents metal nanoparticles as a unique playground for chemical reactions on the nanoscale remotely controlled by light. However, defining the elementary concepts behind these reactions represents the main challenge for understanding their mechanism in the context of the plasmonically assisted chemistry.

Surface-enhanced Raman scattering (SERS) is a powerful technique employing the plasmon-enhanced electromagnetic field, which can be used for probing the vibrational modes of molecules adsorbed on plasmonic nanoparticles. In this cumulative dissertation, I use SERS to probe the dimerization reaction of 4-nitrothiophenol (4-NTP) as a model example of plasmonic chemistry. I first demonstrate that plasmonic nanostructures such as gold nanotriangles and nanoflowers have a high SERS efficiency, as evidenced by probing the vibrations of the rhodamine dye R6G and the 4-nitrothiophenol 4-NTP. The high signal enhancement enabled the measurements of SERS spectra with a short acquisition time, which allows monitoring the kinetics of chemical reactions in real time.

To get insight into the reaction mechanism, several time-dependent SERS measurements of the 4-NTP have been performed under different laser and temperature conditions. Analysis of the results within a mechanistic framework has shown that the plasmonic heating significantly enhances the reaction rate, while the reaction is probably initiated by the energetic electrons. The reaction was shown to be intensity-dependent, where a certain light intensity is required to drive the reaction. Finally, first attempts to scale up the plasmonic catalysis have been performed showing the necessity to achieve the reaction threshold intensity. Meanwhile, the induced heat needs to quickly dissipate from the reaction substrate, since otherwise the reactants and the reaction platform melt. This study might open the way for further work seeking the possibilities to quickly dissipate the

plasmonic heat generated during the reaction and therefore, scaling up the plasmonic catalysis.

Chapter 1. Introduction

Enabled by light absorption, photocatalysis plays a pivotal role in the harvesting of the solar energy, development of clean materials, and spreading of environmentally friendly technologies.[1–3] Photocatalytic processes, moreover, replace the needs of high thermal energy input required during the conventional heat-driven catalysis. However, traditional photocatalysis has remained elusive, relying on materials such as titanium dioxide and zinc oxide that respond only to 5 % of the solar irradiance (UV range of the solar spectrum).[4,5] Recent years have seen the development of plasmonic catalysis, operating the metal platforms efficiently across the ultraviolet, visible, and the infrared regions of the solar spectrum.[6,7] In metals, the high mobility of the free electron gas enables such materials to strongly harvest and interact with light, particularly when the dimension of these materials falls into the nanoscopic range (individual nanoparticles and their assemblies). The collective oscillations of their electron density driven by the incident light are known as the surface plasmons,[8,9] which have been involved in several important applications ranging from single molecule sensing and cancer therapy to the plasmon-driven chemistry all under a heading named “Plasmonics”.[10–12]

Metal nanoparticles act as efficient antennas for electromagnetic radiation from near infrared to UV frequencies. The captured energy can either be reradiated or internally converted into energetic charge carriers (hot electron/hole pair) and subsequently heat.[13,14] Localization of light around these small nanoobjects leads to a very high local electromagnetic field-strength in the near-field close to the particle surface. This strong electric fields can significantly amplify a variety of optical signals.[15] The enhancement is particularly strong in areas called “hot spots”, e.g in nano-sized gaps between the plasmonic particles or at nano-tips with high aspect ratios. The amplification of Raman scattering by this method is known as surface-enhanced Raman scattering (SERS) and enables the detection of traces of a material down to the single-molecule level.[16,17] On the other hand, incorporation of the energetic charge carriers and/or heat into the catalytic processes might, as one advantage, enhance already known chemical reactions and as another advantage, induce novel chemical reactions that are otherwise hindered.[18–20] In this way, the solar energy is transformed into chemical energy in a green and efficient way.

Moreover, unlike the traditional thermal heating, the photon energy can be transformed into energetic electrons that are able to initiate a specific reaction, which increases the selectivity of the reaction and favors the formation of the desired product. However, the mechanistic explanation of plasmon-induced chemistry is still a point of intensive research, where the exact role of the surface plasmon and its decay products is the main topic. Figure 1.1 reflects not only the growing and ongoing interest in plasmonics but also the challenges remaining under investigations.

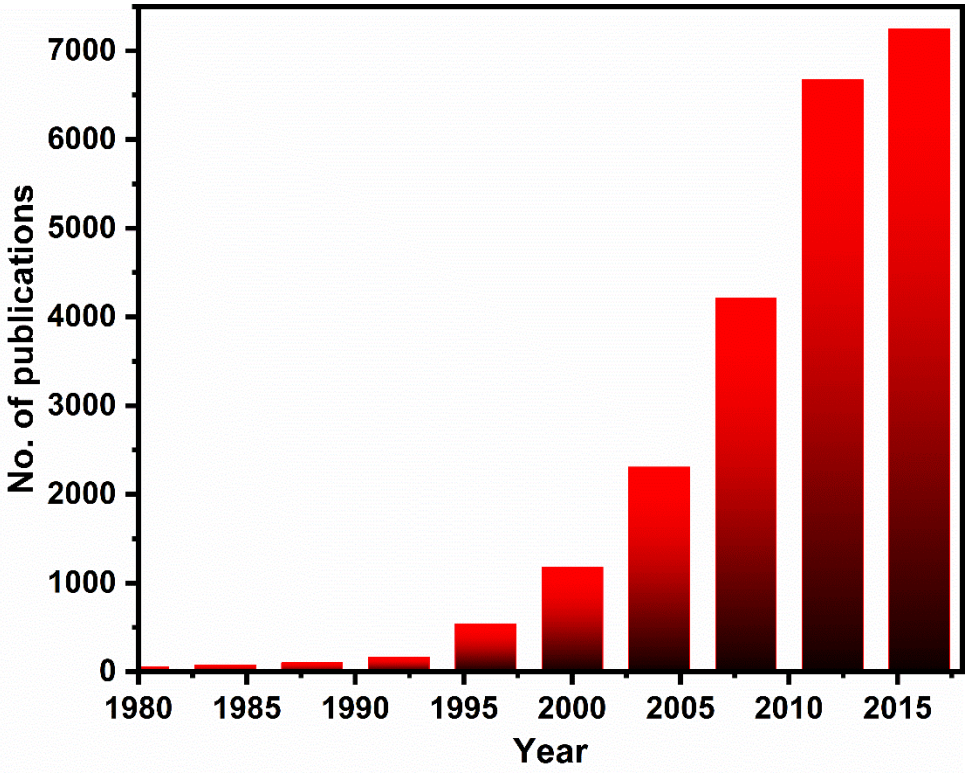

Figure 1.1. The number of annual publications obtained from SCI FINDER with the keyword "Surface plasmons".

The goal of this thesis is to advance the mechanistic understanding of plasmon-driven chemistry, in particular with regard to the role of temperature. In detail, I investigated the dimerization reaction of the 4-NTP to DMAB on the surface of gold nanoparticles, as a model case for plasmonic reactions. DMAB has a distinct Raman signature different from 4-NTP, that conveniently allows monitoring the reaction by SERS microscopy. In these experiments, the Raman laser serves as both, the driver for the plasmonic reactions and the

reaction probe. I further used the X-ray diffraction and Raman thermometry to study the temperature rise of the particles during the reaction. Briefly, I showed the high sensitivity of SERS in observing and monitoring chemical reactions in real time. The temperature rise during the reaction was measured and observed to enhance the reaction rate, whereas, attempts to drive the reaction with only external heating have failed, confirming the photo-driven nature of the reaction. Moreover, the intensity dependence of the reaction showed that the reaction requires a certain threshold of light intensity. Experiments to scale-up the plasmonic catalysis have shown the important role of the efficient heat dissipation from the reaction substrate, otherwise, the plasmonic platform of the reaction may melt.

Hence, I divide my cumulative thesis into 7 chapters focusing on the fundamental aspects of SERS and the plasmonic catalysis along with the results and their discussion.

- Chapter 1 provides a general introduction to the main topic of the thesis.
- Chapter 2 provides a solid background and a literature overview of the plasmonic particles/light interactions together with a literature discussion of the 4-NTP dimerization reaction. Moreover, SERS concepts and substrates are presented.
- Chapter 3 contains details about the preparation methods together with the used analytical tools.
- Chapter 4 contains the manuscripts with comments on my contributions.
- Chapter 5 provides a general discussion of the results presented in the publications.
- Chapter 6 provides a conclusion and summary of the main findings of my thesis and the future prospects of the presented results.
- Chapter 7 presents the publications of the thesis.

Chapter 2. Theoretical background

2.1. Plasmonic nanoparticles

Metal nanoparticles in general, plasmonic nanoparticles (e.g gold, silver, and copper NPs) in particular, have been implemented in tremendous applications such as catalysis, nanomedicine, and photonics, owing to their optical properties that can be finely tuned.[21] Unlike bulk materials, the nanoparticles show unique physical and chemical properties that depend on their size and morphology, owing to their high surface area to volume ratio and the confinement of their electrons (quantum effect). In ancient ages, plasmonic nanoparticles such as silver and gold NPs have been used as coloring agents.[22,23] The Lycurgus cup remained as a witness example of this, which is a Roman cage cup from the 4th century made of a glass colored with a colloidal dispersion of gold and silver nanoparticles.[24] The cup shows different colors based on whether the light is transmitted or scattered as shown in figure (2.1).

In 1850, the modern scientific studies of colloidal gold started when Michael Faraday prepared the first pure colloidal gold sample under the name of "activated gold". In 1857, he further investigated the optical properties of the colloidal gold samples and attributed their colors to the light scattering by the suspended gold particles.[25,26] In 1908, Gustav Mie wrote his famous paper on the light scattering by spherical particles, explaining theoretically the color effects of the colloidal gold with different diameters.[27–29] Recently, metal nanoparticles such as gold and silver nanoparticles have been prepared with different morphologies and size exhibiting different colors, which are now understood based on the Localized Surface Plasmon Resonance (LSPR).[30–33] For example, gold nanospheres exhibit a red color, whereas other anisotropic particles such as nanorods and nanostars display dramatically different colors (e.g blue, brown, purple) owing to the efficient absorption and scattering of certain colors in the visible range of the electromagnetic spectrum.

Figure 2.1. Images of the Lycurgus cup showing different colors upon light illumination (green color for the reflected light and red for the transmitted light). Adapted from ref [24].

The LSPR is the collective coherent oscillations of the electrons in the conduction band of the metal nanoparticles as a result of an external incident electromagnetic field.[34,35] When an oscillating electromagnetic field (i.e photons) excites the nanoparticle, the electron cloud is displaced away from the positively charged nuclei. However, this displaced electron cloud is pulled back by a restoring force toward the electron-deficient core as illustrated in figure (2.2 A). When the frequency of the incident electromagnetic field matches the frequency of the restoring force of the oscillating electrons, the LSPR is established resulting in coherent oscillations of those electrons. However, these coherent oscillations decay within a few tens of femtoseconds.

As shown in figure (2.2 B), the plasmon decay occurs through three different pathways:[36,37] (1) In the radiative pathway, a photon with the same energy as the incident photon is emitted. (2) The non-radiative pathway results in the formation of electron/hole pairs with energies between E_f and $E_f \pm h\upsilon$. This pathway is commonly known as Landau damping. (3) The plasmon decay might also occur by the direct interaction of the plasmon and the unpopulated orbitals of the adsorbate in a mechanism called chemical interface damping (CID).

The plasmon decay might induce chemical transformation of a nearby molecule by several ways. In the CID mechanism, the decay occurs mainly by driving chemical reaction via direct injection of the electrons into the adsorbed molecules. In contrast, in Landau damping, the energetic electrons scatter to populate unpopulated orbitals of the adsorbed molecules initiating chemical transformation known as electron–driven chemical reactions. The reaction can be also initiated by electrons being transferred from the adsorbate to the metal nanoparticle. Furthermore, these energetic electrons undergo a cascading electron-electron scattering to spread their energy to many electrons creating non-equilibrium Fermi-Dirac electron distribution. Afterwards, the electron-phonon coupling would heat the crystal lattice of the nanoparticles. This heat can be transferred to the adsorbed molecules and chemical transformation can be then initiated, which is known as phonon or plasmon heating-driven chemical reactions. It is worth noting that the first two mechanisms occur regardless of the environmental conditions, while the CID mechanism requires the existence of the adsorbate and it was considered as the fastest plasmon dephasing pathway (lifetime is around 5 fs).

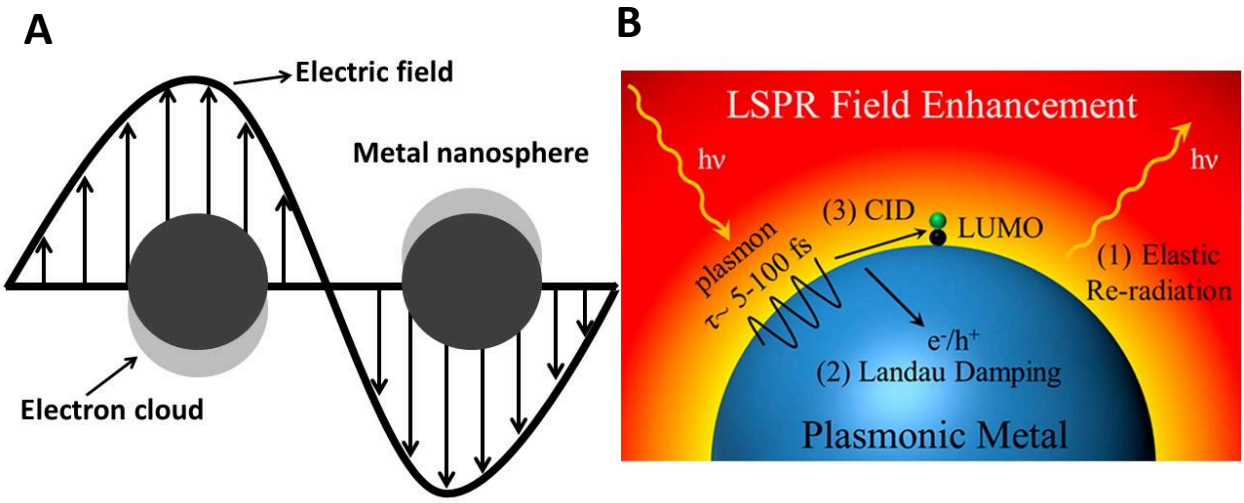

Figure 2.2. Schematics show the Localized Surface Plasmon of the spherical particle (A) and its decay mechanisms (B) adapted from ref [15].

Furthermore, the LSPR is recognized by a strong plasmon band in the extinction spectrum of the nanoparticles solution, while the location (the frequency) of this band depends on the particle's geometry and morphology as well as the dielectric constant of the metal

particles and their surroundings. Therefore, by controlling the particle's size, shape, and coatings, the nanostructures can be tuned to respond strongly to a certain excitation wavelength (e.g the visible light). For instance, the spherical gold nanoparticles display a single LSPR band located around 520 nm,[38,39] while upon changing the shape to nanorods, another band related to the longitudinal LSPR band will be observed. The gold nanorods display a transverse LSPR band around 520 nm and a longitudinal LSPR band located between 550-1300 nm depending on their aspect ratios.[40,41] In another example, the plasmon resonance of the gold nanospheres has been tuned by the deposition of the polyelectrolytes on their surfaces, thereby changing the surrounding dielectric medium (ε_{med}) and therefore, the gold polarizability (α) as seen in equation (2.1).[42] Overall, owing to the photon confinement to a small-sized particle, the LSPR is established offering multiple pathways for biological and chemical applications.

$$\alpha \propto \frac{\varepsilon_{Au} - \varepsilon_{med}}{\varepsilon_{Au} + f\varepsilon_{med}} \qquad (2.1)$$

2.2. Plasmon-induced chemistry

Sunlight is the most abundant source of energy on earth, however, in order to use this energy, we have to capture the light photons first. Noble metals with nanoscopic dimensions (nanostructures) can strongly harvest and interact with the incident light, thanks to their surface plasmon properties. As a result, energetic charge carriers and an increase of the local temperature are generated offering new perspectives of light-driven chemistry through different mechanisms. Indeed, plasmonics and chemistry have been linked a long time ago even before Faraday has performed his first experiments on the controlled synthesis of gold colloids. Figure 2.3 summarizes the light's interaction with the plasmonic particles and their possible reactive channels.[43] Briefly, upon resonant plasmon excitation, generation of energetic electrons, photon re-emission, and an increase of the local temperature will be observed as previously shown and can be used as vehicles to transfer the energy to the adsorbed molecules, initiating their chemical transformation; commonly known as plasmon-induced chemical reactions.

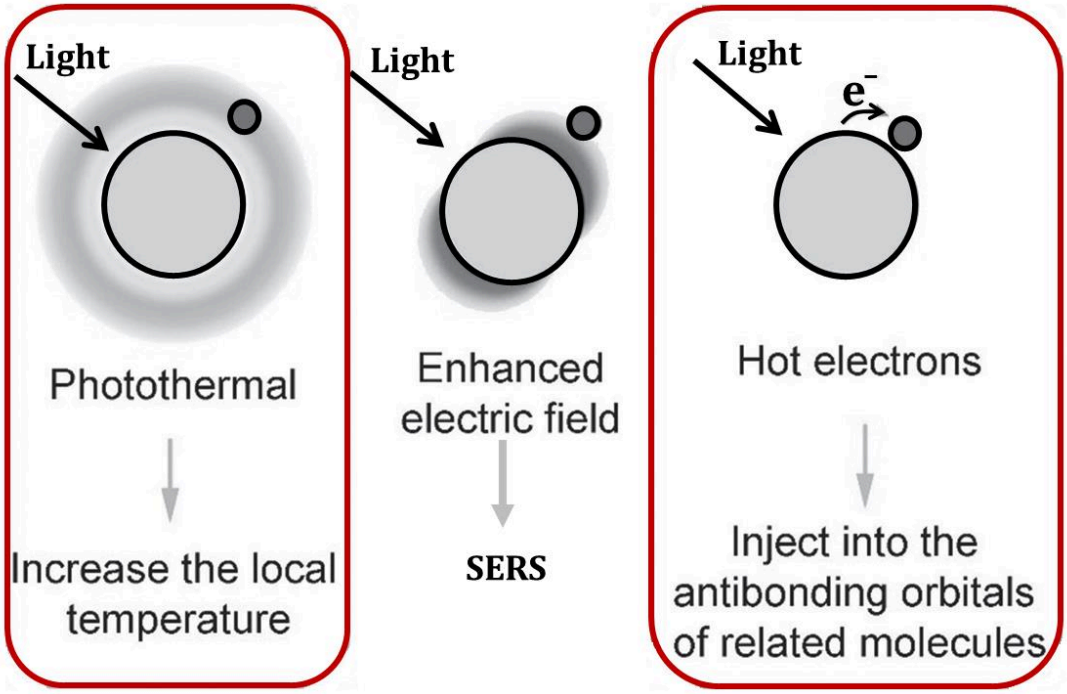

Figure 2.3. Schematic shows the outcomes of the light-nanoparticle interactions adapted from ref [22].

On the other hand, the adsorbed molecules can only absorb the scattered photons if they have an allowable electronic transition with energy similar to the reradiated photons. Therefore, this mechanism would require UV photons to excite the electronic transition of the adsorbate. Thus, absorption of the scattered photons by the adsorbed molecules can be neglected, since most of the organic molecules only absorb light in the UV range. However, chemical reactions of the adsorbates can be driven by charge transfer between the metal nanoparticles and the adsorbed molecules as shown in figure 2.4. In Landau damping, the the energetic electrons generated are scattered to populate an empty orbital of the adsorbates, initiating their chemical transformation.[44] The primary energetic electrons could decay into a large concentration of low energetic electrons by electron-electron colloisions. These low energetic electrons might also induce chemical transformations of the adsorbed molecules owing to their high concentrations and their longer lifetime compared to those of high energies. Furthermore, the CID decay mechanism of the surface plasmon is mainly built on the direct interaction of the plasmons with the accessible electronic states of the adsorbate.[44,45] This interaction results in the direct injection of the

electrons into the empty orbitals of the adsorbates, which might initiate their chemical transformations. The charge-transfer mechanisms driven by Landau damping and CID are often known as the indirect and direct charge transfer, respectively. On the other hand, the heat generated by plasmon excitation can be used to initiate chemical changes of the adsorbed molecules.[44] Therefore, we explain the plasmon-driven reactions as an electron-driven reaction or phonon/ heat-driven reaction and they typically depend on the plasmon resonance as well as the excitation intensity.

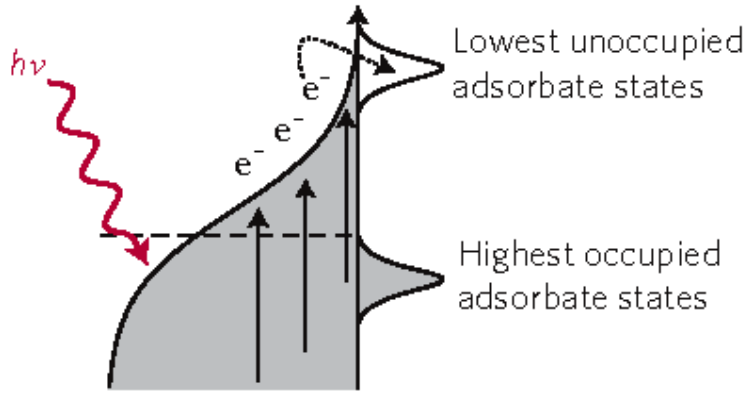

Figure 2.4. Schematic shows the charge-transfer mechanism in the metal-adsorbate system after the formation of the hot electrons. Adapted from ref [43].

2.3. Electron –driven chemical reactions

In 1952, Fukui and co-workers have generally proposed the frontier orbitals (the highest occupied molecular orbital (HOMO) and the lowest unoccupied orbital (LUMO)) to play the decisive role in the chemical activation and therefore the chemical reactions.[46] This concept has enabled a major advancement in understanding and predicting the chemical reactions, predicting that only HOMO and LUMO bands which lie in the range of several electron volts around the Fermi level can participate in the molecular adsorption and reaction on the metal surface.[47,48] Recently, Linic and co-workers have extended this explanation to the small diatomic molecules that undergo a dissociation reaction on the metal surfaces explaining the differences between the thermal- and electron-driven paths.[19,44] However, it is still challenging to predict the paths of more complex reactions such as the coupling

reaction performed by relatively large molecules (e.g 4-nitrothiophenol and 4-aminothiophenol).

Generally, in the electron-driven reactions, the energetic charge/carriers (electron/holes) generated at the surface of the nanoparticles will transiently occupy an empty orbital of the adsorbed molecules before their energy is dissipated.[44] As a result, a transient ion (for the case of the adsorbate) or an excited state (for the whole adsorbate-metal complex) is formed in a new potential energy surface (PES) as shown in figure (2.5 B), where activation of chemical bonds and chemical transformations of the adsorbate would occur. It is worth noting that the energy of the charge carrier is converted into kinetic energy, by which the entire complex is moved along the reaction coordinate. Thus, this mechanism mainly depends on the charge transfer between the metal and the adsorbed molecule. This charge transfer has been classified into direct and indirect charge transfer.[36] The direct transfer is where the electrons are directly excited from near the Fermi level of the metal to the unoccupied orbital of the adsorbate (LUMO). Thus, the direct charge transfer does not include the formation of the energetic charge/carriers (hot electron/hole), which resembles the CID mechanism.[44] On the other hand, the indirect charge transfer includes the formation of the energetic charge carriers first, which are then scattered to occupy an empty orbital of the adsorbate resembling the Landau damping mechanism. Accordingly, the photocatalysis has been classified into direct and indirect photocatalysis. Several reactions have been related to the charge-mediated pathway. For instance, energetic electrons were reported to induce dissociation reaction of the H_2 molecules adsorbed on 5-20 nm gold nanostructures at light intensity of 2 W/cm^2.[49,50] Moreover, production of ethyl benzoate has been performed using esterification of the benzaldehyde on sub- 10 nm gold nanoparticles using a charge-driven reaction induced by visible light as the illumination source at room temperature.[51]

2.4. Phonon/heat-driven chemical reactions

Plasmon-induced heating represents another important application of the LSPR properties taking advantage of the efficient light absorption to locally increase the temperature at the targeted volume. This might locally induce chemical reactions triggered by the thermal

activation. Furthermore, the local high temperature might change the phases of the reacting mixture, thereby offering efficient mixing of the reacting molecules which enhances the reaction probability.[52,53] In these reactions, the electron-phonon coupling would distribute the energy of the energetic electrons to the phonon modes of the nanoparticles. Therefore, the energetic electrons act as a vehicle for transferring the energy to the nanoparticle, and heating it up. Such increase of the local temperature might induce chemical transformation of the adsorbed molecules.

The mechanism of these reactions starts with excitation of the phonon modes of the nanoparticles via electron-phonon coupling, which is then coupled with the vibrational modes of the adsorbate. As a result, the adsorbate is transformed from the reactant state into the product state on the same ground potential energy surface (i.e the molecule is not moved to an excited PES).[44] This can be simply explained as the adsorbate climbing a ladder of vibrational levels under the thermal excitation until it reaches the product state as shown in figure (2.5 A). Thus, the vibrational states of the molecules are more important than the electronic states in this mechanism since the reaction does not include any charge-transfer processes, and the ground potential energy surface of the reactant is not modified. It is worth mentioning a few examples of the reactions that were reported to be driven by heating generated via the plasmon excitation. For example, reformation of ethanol into CO_2, H_2, and CO has been observed on spherical 10-20 nm gold nanoparticles.[18] In this experiment, the LSPR excitation increased the temperature of the nanoparticles and induced formation of gas bubbles surrounding the nanoparticles. The reaction is likely to occur at the interface between the nanoparticles and the gas bubbles. In a similar way, the decomposition of dicumyl peroxide to 2-phenyl-2-propanol and acetophenone has been reported in an aqueous solution of 13 nm gold nanoparticles,[54] while the particle temperature was found to increase above 500 ^{o}C upon light excitation, which is enough for the cleavage of the peroxide bond. The plasmon-induced heating has been also used in the medical field, where the photothermal destruction of various carcinomas has been reported.[55,56]

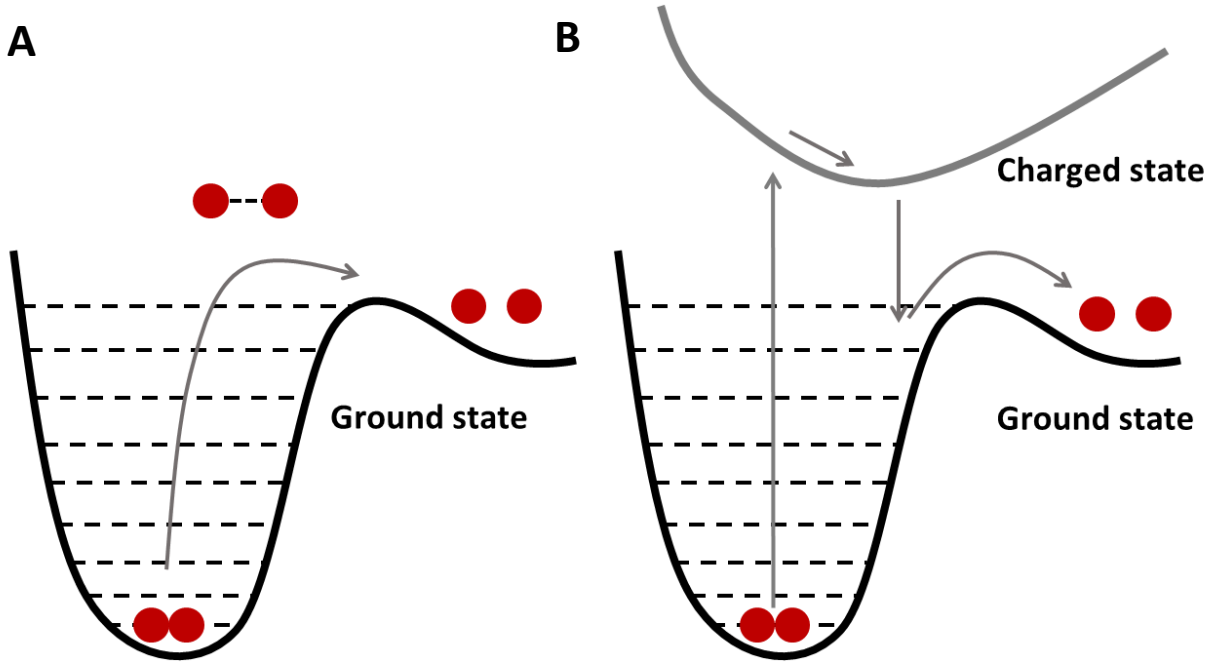

Figure 2.5. Schematics show the mechanisms of the phonon (A) and the electron-driven reaction (B) as described for the dissociation of a diatomic molecule shown in ref [43].

2.5. SERS monitoring of the plasmon-induced chemistry

Understanding the reaction mechanism and the structure-reactivity relationships are considered to be the first step towards the rational design of highly efficient catalysts. Therefore, a suitable technique is needed to provide information of where and how the reaction takes place, giving the priority to the molecular-elucidating spectroscopic techniques. Thus, owing to their pioneering advantages in this area, surface-enhanced Raman scattering and tip-enhanced Raman scattering have been commonly used to study a variety of the plasmonic reactions, opening a new pathway of in-situ monitoring and controlling the reaction on a single particle and single molecule level. Furthermore, SERS enables the detection and characterization of the surface species with high sensitivity up to the level of single molecules, and when combined with scanning probe microscopy, the spatial resolution is greatly enhanced reaching the nanoscale range.[57,58] On the other hand,

the high signal enhancement of SERS enables detection of the adsorbate with shorter acquisition times, allowing capturing of possible reaction intermediates.

In this direction, SERS has the first credits in the discovery of one of the important plasmonic reactions, where the 4-aminothiophenol molecules adsorbed on gold or silver dimerize into their azo-dimer form (DMAB) without the assistance of any chemical reagents. The story began in 1994 when Osawa observed that three new Raman peaks appear at 1143, 1390, and 1432 cm^{-1} when 4-aminothiophenol (4-APT) adsorbs on a silver electrode as shown in figure (2.6).[59] He first interpreted these peaks as an evidence of the chemical enhancement mechanism of SERS, however, the simulations failed to reproduce these peaks from 4-APT. In 2010, Wu and coworkers have shown theoretically that p,p'-dimercaptoazobenzene (DMAB) has the same Raman spectrum including these new peaks, predicting that 4-APT may undergo photo-coupling reaction into DMAB.[60] Since then, several experiments have been reported to confirm the photo-dimerization of 4-APT into DMAB describing the reaction as a plasmon-driven reaction.[61,62] Furthermore, the molecular mass of DMAB was detected by surface mass spectrometry after irradiating 4-APT adsorbed on a silver electrode a providing strong evidence of the photo-coupling reaction.[63] Later on, photodimerization of 4-nitrothiophenol (4-NTP) into DMAB was also reported.[64,65]

From the chemical point of view, the transformation of 4-ATP to DMAB is an oxidation process, while transformation of 4-NTP to DMAB is a reduction process, which implies that the surface plasmon plays different roles in inducing chemical reactions of the adsorbed molecules. In these reactions, SERS played an important role in driving and monitoring the reaction, where the light is used to initiate the reaction and to monitor the reaction on a time-resolved mode, while the plasmonic particles acted as a sensor as well as a catalyst. Overall, SERS and TERS have made tremendous progress and became mature spectroscopic techniques covering several advantages for the field of the heterogeneous catalysis. On the one hand, it makes it possible to monitor chemical reactions at a molecular level in real time, with the potential of observing reaction intermediates. On the other hand, the combination of SERS with a catalytically active material opens up the door to conduct a wealth of chemical reactions. Furthermore, the heat being generated from the plasmonic

materials upon illumination could create the proper conditions for triggering new reactions.

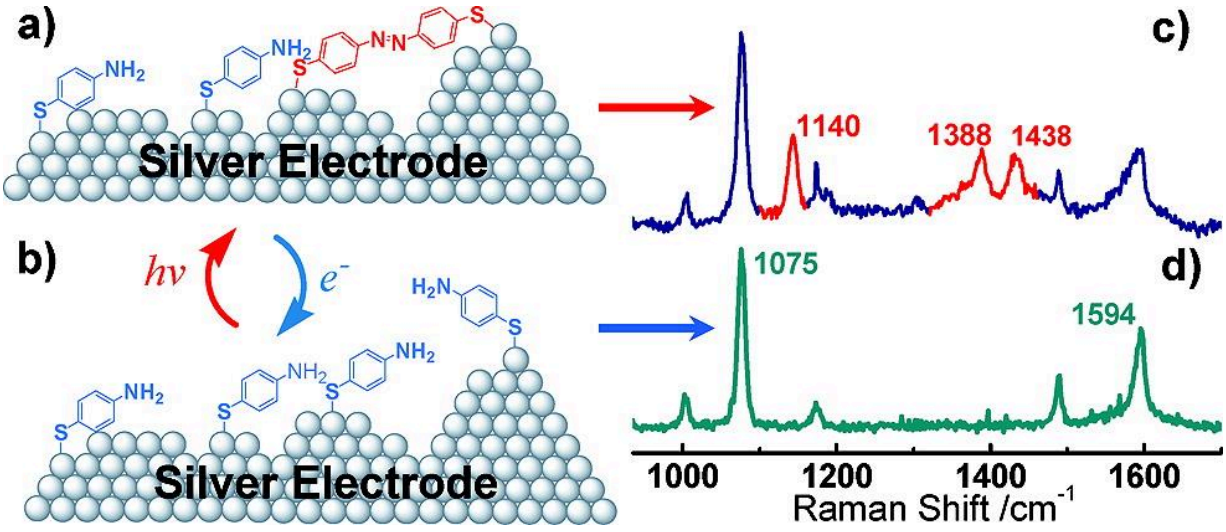

Figure 2.6. Schematic depictions of 4-ATP molecules adsorbed on silver electrodes (a, b) and their Raman signatures with (c) and without (d) the photo-product signature reproduced from ref [41].

2.6. Raman scattering

Raman spectroscopy (RS) is the main technique used in this dissertation to study the plasmon-driven chemical reactions. It is based on the inelastic scattering of the incident light by the molecular system and it was first discovered by the Indian physicist Sir. Raman in 1928.[66] RS is a vibrational spectroscopic technique used to gain "vibrational fingerprint" of the molecular system. Typically, when light interacts with the molecule, the electron cloud is distorted forming a short-lived state called "virtual state". This state is not stable and decays very quickly with light being scattered. The scattered photons can be of lower or higher energy than the incident photons and being called Stokes and anti-Stokes Raman scattering, respectively, as shown in figure (2.7 A). Nevertheless, the Raman scattering is a very weak process (only 1 photon of 10^7 of the scattered photons is Raman scattered) compared to the intense Rayleigh scattering (when the scattered photons have the same energy as the incident ones) as schematically illustrated in figure (2.7 B). At room temperature, the Stokes Raman scattering is more intense than the anti-Stokes scattering,

since only a few molecules are initially excited (exist in the vibrational state with a higher energy). The population of the states (N) can be estimated by the Boltzmann distribution as shown in equation (2.2):

$$\frac{N_{(v=1)}}{N_{(v=2)}} = e^{-\frac{\Delta E}{k_B T}} \tag{2.2}$$

Where k_B is the Boltzmann constant, ΔE is the energy difference between the states and T is the temperature.

When an oscillating electric field (light) interacts with the molecule, the electron cloud is displaced inducing a dipole moment (μ), which is linearly proportional to the strength of the electric field (E) and the polarizability of the material (α) as shown in equation (2.3):

$$\mu = \alpha E \tag{2.3}$$

The polarizability (α) describes how strong the electron cloud is distorted in response to the applied electric field. Furthermore, the changes of the polarizability should not cancel out for a mode to be a Raman active mode (i.e $\frac{d\alpha}{dQ} \neq 0$, where Q is the normal coordinate of the vibration), which is considered as the selection rule of the Raman scattering. Moreover, the intensity of the scattered light is directly proportional to the square of the magnitude of the induced dipole moment.

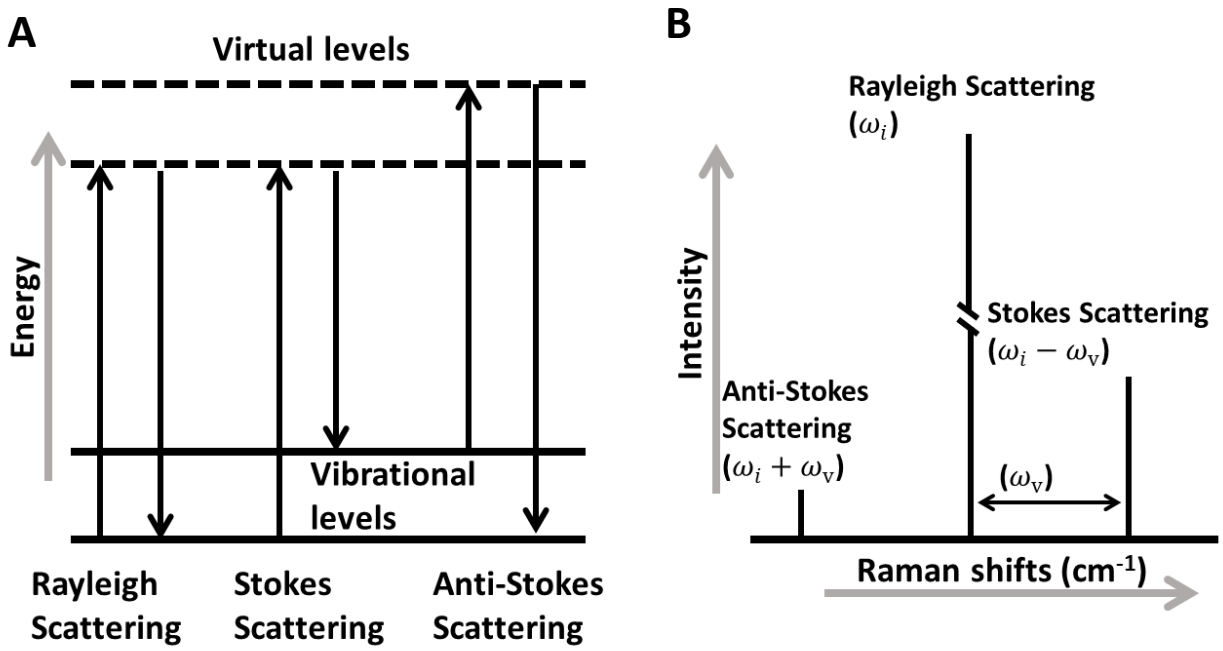

Figure 2.7. Schematics of the different light scattering with respect to the photon energy (A) and light intensity (B) showing both the Stokes and the anti-Stokes Raman scattering.

2.7. Surface Enhanced Raman Scattering (SERS)

As mentioned above, Raman spectroscopy has been underestimated for years, owing to its low sensitivity and the weak Raman cross-section of most of the molecules. However, it was observed that the Raman signal is strongly enhanced when the molecules come in the close vicinity of the metal surface, and termed SERS,[67,68] reviving the Raman spectroscopy again. As Raman spectroscopy, SERS is a very specific technique providing "fingerprint" information of the analyte. Moreover, SERS is not only sensitive but also selective for molecules that are close to or adsorbed on the surface of the metal nanoparticles.[69] SERS was first reported in 1974 for pyridine adsorbed on a rough silver electrode.[70] It is known now that SERS enhancement is a product of two contributions: electromagnetic- and chemical-enhancement.[71,72] The electromagnetic enhancement mechanism (EM) involves a resonant excitation of the LSPR, which results in an extraordinary enhancement of the electric field near the particle surface and experienced by the analyte molecules. As a result, a strong SERS signal enhancement of the adsorbate is produced. Furthermore, the

SERS enhancement (EF) depends on both the incident $[E(\omega_i)]$ and the scattered field [E $(\omega_i \pm \omega_v)$], where ω_i and ω_V are the incident light and the vibrational frequencies, repectively.

$$EF = |E(\omega_i)|^2 * |E(\omega_i \pm \omega_v)|^2 \quad (2.4)$$

For $\omega_i \gg \omega_V$, the common $|E|^4$ approximation can be used and therefore, $EF = |E(\omega_i)|^4$ is produced, which means that the SERS intensity scales to the fourth power of the incident electric field. A schematic depiction of the chemical enhancement mechanism (CM) in SERS is presented in figure (2.8). In short, the CM is based on the charge transfer between the metal and the analyte molecules, which might change the polarizability and enhance the Raman cross section of the adsorbed molecules.[73] The enhancement of the electric field and the molecular polarizability directly influence the intensity of the Raman scattering as shown in equation (2.3). Moreover, adsorption of the analyte on the metal surface might induce electronic coupling resulting in new intermediate electronic states that might coincide with the laser excitation wavelength. Resonant excitation of such states enhances the Raman scattering and is called resonance Raman scattering (RR).

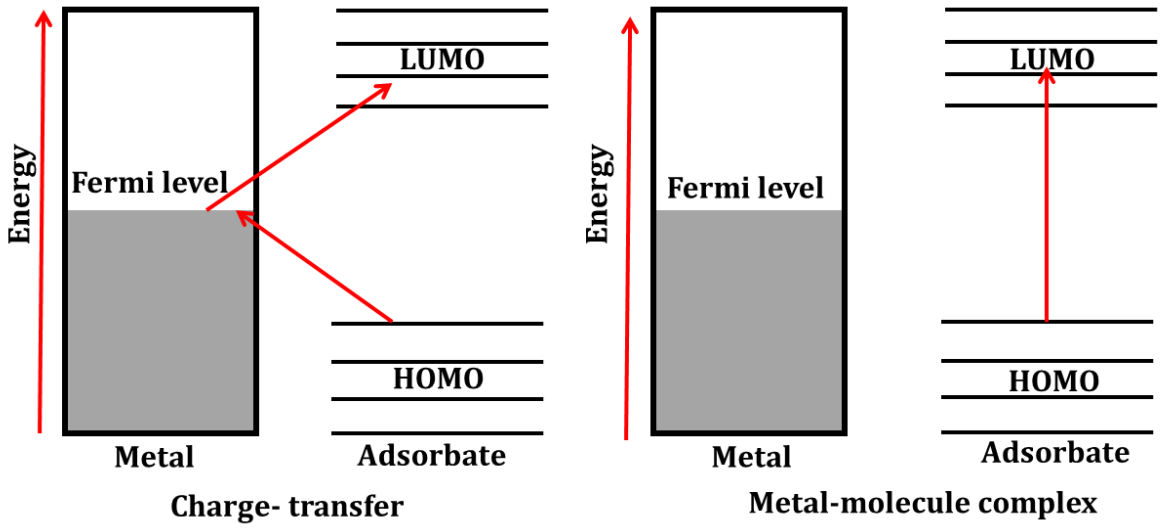

Figure 2.8. A schematic depiction of the chemical enhancement mechanisms in SERS as described in ref [53].

The dependence of SERS on the excitation wavelength was also discussed,[74–77] where the laser wavelength that coincides with the surface plasmon displayed the best signal enhancement. This results in the maximum field enhancement. It is worth noting that the plasmon resonance of the nanoparticles strongly depends on the size, shape and the surrounding environment as well as the nature of the nanoparticles.[78–82] Therefore, the plasmon band of the nanoparticles can be tuned to be in a maximum resonance with the excitation wavelength, resulting in extreme electric field enhancement and therefore extraordinary enhanced SERS signal. The EM is mainly based on the enhancement of the local electric field and a moderate increase of the local electric field leads to a remarkable SERS enhancement since the SERS intensity scales to the fourth power of the electric fields; SERS EF α $(E_{loc})^4$. For example, imagine a small increase of the local electric field so that $E_{loc}/E_{inc} = 10^2$, this will lead to a huge SERS enhancement by a factor of $(E_{loc}/E_{inc})^4 = (10^2)^4 = 10^8$. Overall, both the electromagnetic and the chemical mechanisms contribute to the SERS. However, the EM represents the majority of SERS intensity and can scale up to 10^{12}, while the relative CM enhancement is usually in the range of 10-100.[83,84] Moreover, the SERS enhancement was reported to be distance-dependent, since the electric field strength scales with the distance from the particle surface by a factor of $E(r) \sim 1/r^3$ and therefore the SERS intensity scales with a factor of $I_{SERS} \sim 1/r^{12}$.[85] This property makes SERS to be very selective for the molecules that are close to or adsorbed on the surface.

Controlling the shape of the particles enables the optical excitation of a specific LSPR, and finally optimizing the SERS enhancement. Additionally, the particle shape can enhance the SERS signal at specific locations, where the curvatures and the tips of the nanoparticles exhibit a strong electromagnetic enhancement and therefore Raman scattering. This enhancement is referred to as the lightning rod effect,[86–88] which allows the nanoparticles to act as optical antennas to concentrate the incident electromagnetic field. These locations are known as SERS hot spots. The influence of SERS hot spots on the signal enhancement was further studied, where dimers of silver nanocubes with a narrow gap formed between two nearly touching cubes have been chosen as the model system.[89] The dimers are covered with a self-assembled monolayer of 4-methylbenzenethiol (4-MBT). The authors showed that the 4-MBT molecules located in the nanogaps resist and take a much longer

time to be removed by the plasma etching compared to the molecules located at the surface. So as shown in the figure (2.9 A and B), plasma etching of the 4-MBT molecules located at the surface of the dimer resulted only in a slight reduction of SERS signal, which means that most of the SERS signal comes from the molecules located at SERS hot spots.

The SERS hot spots are considered to be the positions that exhibit an extreme field enhancement such as nano-gaps and nano-tips. However, the size of the nanogaps also influences the SERS enhancement. As shown in figure (2.9 C), the gold dimer with smallest interparticle distance (7.8 nm) exhibited the highest Raman signal. The probability of finding the molecules exactly in the interparticle-gap is extremely small compared to the high probability of finding the molecule at the particle surface (positions that exhibit moderate field enhancement). These probabilities (p(F)) were explained in terms of probabilities of finding a certain enhancement factor (EF) which exhibits a typical long-tail behavior as shown in figure (2.9 D).[69] The figure, moreover, shows that the signal enhancement depends on the Raman cross section of the probed molecules. For example, the molecules that have a high Raman cross-section require an enhancement factor of 10^7-10^8 for detection of single-molecule SERS, while other molecules that have a relatively small Raman cross-section might require a high EF of 10^{11}.

The sharp tips have been also considered as SERS hot spots, where they act as nanoantennas to enhance the electric field and hence the SERS signal.[90] For instance, gold nanostars with sharp tips have been used as a SERS substrate and have shown a SERS signal intensity of 7.4 and 3.4 times stronger than that of the spherical gold and silver spherical particles, respectively. Likewise, the silver nanoprisms prepared with sharp edges showed a higher SERS enhancement compared to those prepared with truncated edges.[91,92] Finally, SERS can be considered as a very sensitive technique reaching down to single-molecule detection depending on the efficiency of SERS substrate.[93–95]

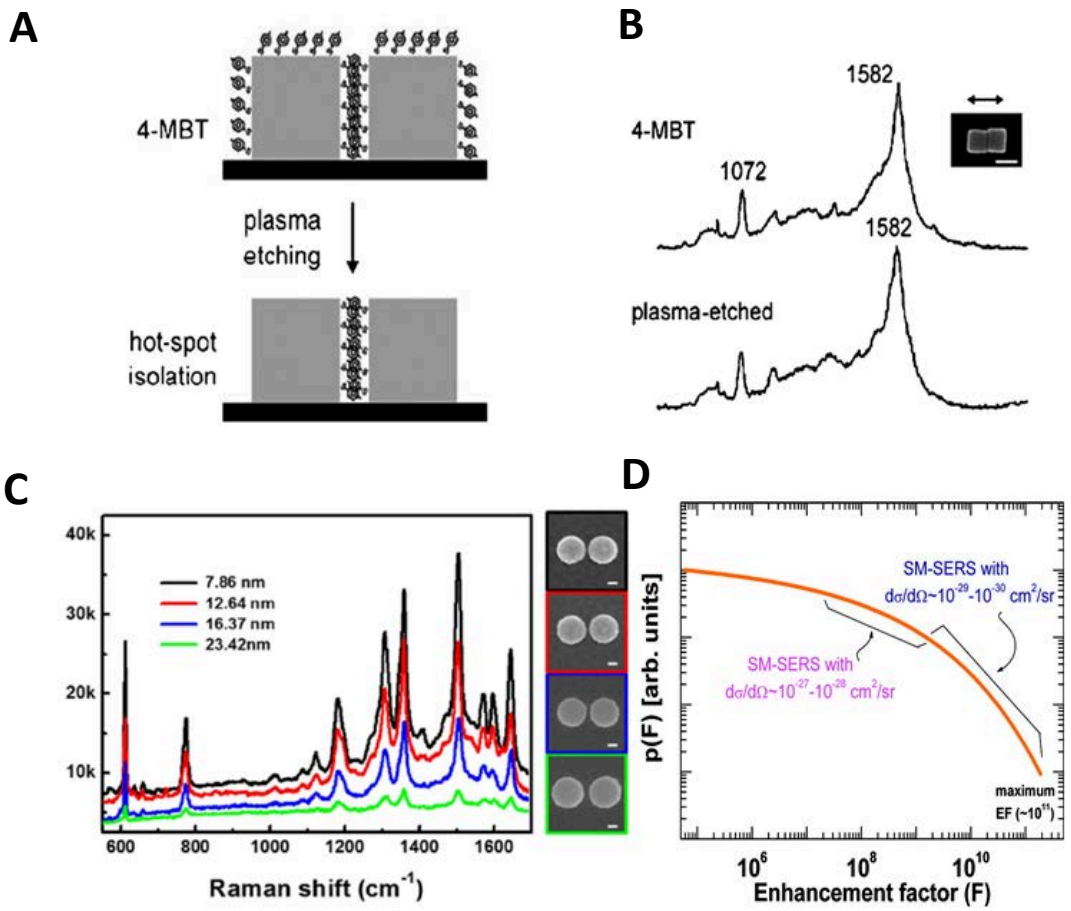

Figure 2.9. Schematic shows the plasma etching of the surface-adsorbed molecules (A) and their SERS spectra (B). SERS spectra of R6G adsorbed on gold dimers with different gap sizes (C) and the typical probability distribution for SERS enhancement factors (D), collected and adapted from ref [49,64, and 65].

On the other hand, the SERS enhancement factor (EF) is an estimation of how much the Raman scattering of the analyte is enhanced when deposited on a SERS substrate. It is difficult to compare the EF for different analytes since the Raman cross-section of the analyte would influence the final EF. However, two common equations have been used to estimate the EF of the analyte deposited on the SERS substrate (a) or dissolved in the nanoparticle solution (b):

$$EF = \frac{I_{SERS}}{I_{bulk}} \cdot \frac{N_{bulk}}{N_{SERS}} \text{ (a)} \qquad \text{or} \qquad EF = \frac{I_{SERS}}{I_{analyte}} \cdot \frac{C_{analyte}}{C_{SERS}} \text{ (b)} \qquad (2.5)$$

Where I_{SERS} , I_{bulk} and $I_{analyte}$ are the Raman scattering intensities of the selected mode of the probed analyte for the SERS, bulk samples and the aqueous solution, respectively. N_{SERS} is the number of analyte molecules in the laser spot, which are adsorbed on the SERS substrate, while N_{bulk} is the number of the probed molecules in the bulk sample. For the SERS in solution, $C_{analyte}$ and C_{SERS} are used representing the concentration of the analyte in absence and presence of the metal nanoparticles, respectively. Additionally, Several theoretical simulations such as discrete dipole approximation (DDA),[96] the multipole-multipole method,[97] and the time-domain finite-element method,[98] have been used to predict and explain the SERS enhancement factors of the complex-shaped plasmonic nanoparticles. For instance, the finite element method has been employed to show the plasmonic coupling between the 20 nm gold nanoshperes as the satellite particles and the 80 nm gold core of the 3D superstructures,[99] visualizing the hot spots that exist between the small particles and the core as well as between the satellites.

2.8. SERS substrates

Most of the SERS signal comes from molecules located in the SERS hot spots such as the nanogaps. Therefore, it is difficult to have a high and reproducible SERS enhancement from nanoparticles dispersed in a solution. Thus, development of highly uniform SERS substrates with SERS hot spots homogeneously distributed over the whole substrate is highly appreciated. Generally, the SERS substrate is prepared either by immobilization of the nanoparticles on a substrate or by the direct fabrication of the nanoparticles on a substrate, resembling the bottom-up and the top-down strategies, respectively. In the next section, I will briefly explain the principle of each type with few examples.

2.8.1. Direct SERS substrates

Lithography is a common example for the direct fabrication of SERS substrates, which is a multi-step fabrication method to produce nanoparticles directly on a substrate. It allows

the formation of well-ordered 2D arrays of nanoparticles as an efficient SERS substrate.[100–102] Lithography can be divided into three categories; nanosphere lithography, electron beam lithography, and nanoimprint lithography. In nanosphere lithography, spherical nanoparticles have been used as a template to engineer the SERS substrate as shown in figure (2.10 A),[103] where it starts with a drop casting of monodisperse polystyrene or SiO_2 nanosphere with the desired diameter on a clean substrate. After evaporation, the nanospheres are self-assembled into an ordered monolayer template for the metal deposition. Afterwards, several methods such as electrochemical deposition and physical evaporation methods can be employed to deposit a metal film over the nanoshere template (FON). On the one hand, this can be used as SERS substrate, where a film of the silver or the gold is deposited over the nanosphere template with narrow nanogaps. On the other hand, the nanosphere template can be removed by sonication leaving behind an ordered array of nanotriangular or nanovoid shape. The shape and the size of the nanogap can be controlled by adjusting the size of the nanosphere template as well as the thickness of the deposited metal film to increase SERS efficiency.

On the other side, electron beam lithography uses a focused beam of electrons to engineer the shape of interest with capabilities of producing of sub-10 nm nanogaps with controlled morphologies. As shown in figure (2.10 B), a gold-coated silicon substrate was covered with an electron-sensitive film called a resist and used for the e-beam writing process,[104] where the focused beam is used to draw the desired shape. Afterwards, the exposed or non-exposed parts of the resist are removed by immersing the substrate in a solvent producing the required shape on the resist. Finally, the SERS substrate is formed by either formation of another layer of gold on the shaped resist followed by lifting-off the resist. The other way uses plasma etching of the first gold layer, which directly forms the SERS substrate. Both ways produce well-ordered structures such as gold nanodiscs, nanogratings, and nanoholes with high enhancement factor. However, the substrates produced by e-beam lithography combined with lift-off tend to show higher SERS enhancements than those produced by plasma etching owing to their sharp edges. Recently, another type of lithography called nanoimprint lithography (NIL) was developed aiming at the formation of a large scale of uniform nanostructure arrays on a flexible

substrate,[105,106] which can be used as a flexible SERS active substrate to detect traces of the chemical samples from real surfaces in real time.

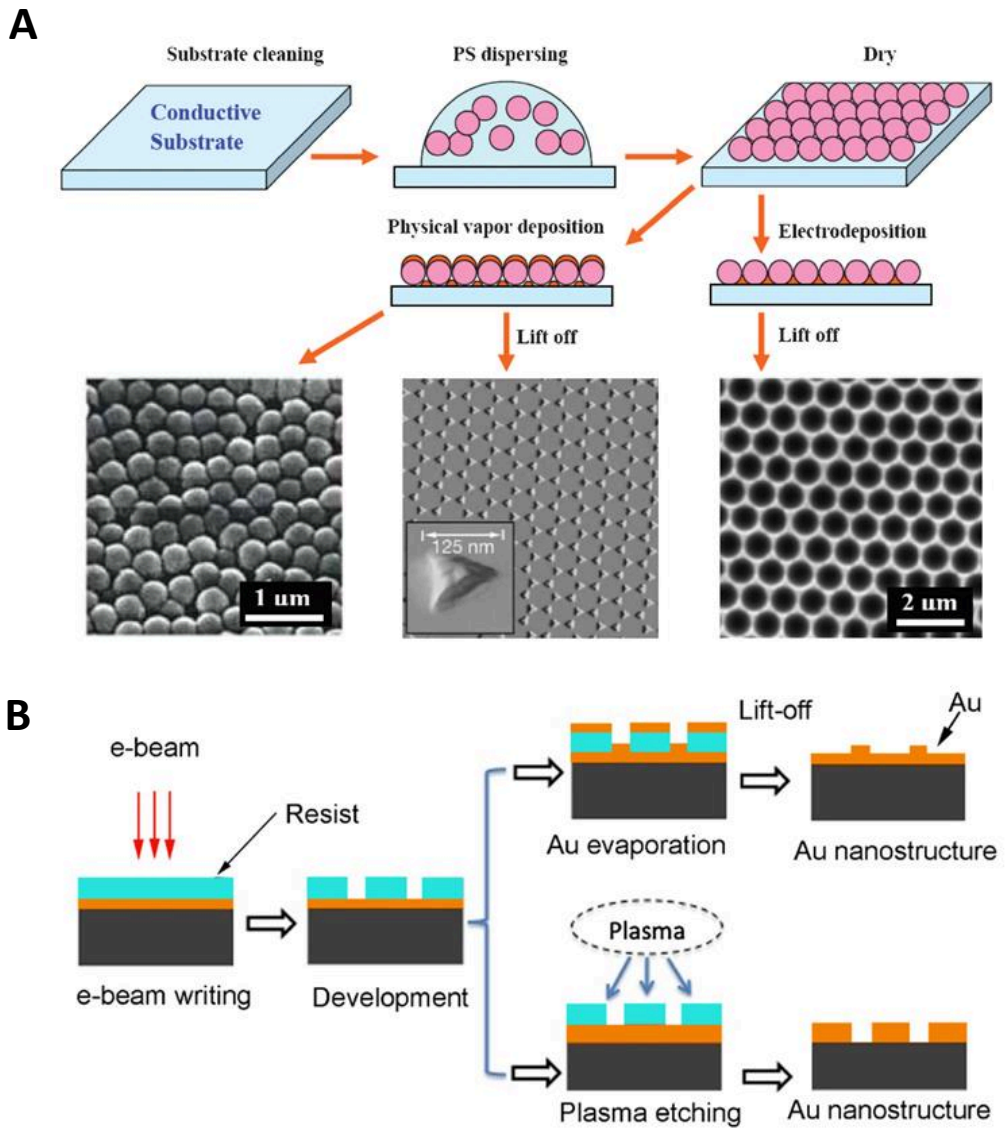

Figure 2.10. Schematic depictions of the nanoshere (A) and the electron beam lithography (B) adapted from ref [75 and 76].

2.8.2. SERS by nanoparticle immobilization

In this way, the SERS substrates are produced by forming first the nanoparticles, usually by wet chemical methods. The produced nanoparticles are then deposited on the substrate by several ways including chemical modification of the substrate and/or the particles, self –

assembly, and drop-casting of the nanoparticles. Drop casting of the nanoparticles on solid substrates such as silicon wafer and glass usually results in aggregations of the nanoparticles owing to the uncontrolled liquid drying. Such aggregations are beneficial for Raman enhancement which results from the SERS hot spots that formed between the particles in the aggregated form. However, the SERS signal is not reproducible since the aggregates are usually not homogeneous.

Various strategies have been performed to form a reproducible, homogeneous and efficient SERS substrates. For instance, self-assembly of gold nanostars has been performed using the electrostatic interaction between the particles and the substrate.[107] As shown in figure (2.11 A), the assembly of nanostars started with chemical modification of the substrate, where the ITO-glass was functionalized with APTES molecules in a process called silanization. The modification provided the substrates with positive charges that will electrostatically bind the negatively-charged gold nanostars allowing the formation of a homogeneous SERS substrate over several square centimeters. This substrate allowed detection of a low concentration of R6G with an enhancement factor of 2×10^5. The same protocol was employed to immobilize gold nanoparticles to the quartz substrate, where MPTMS was used to functionalize the substrate.[108,109] The modified substrate has a free thiol group provided by the MPTMS molecules that will capture and covalently bind the gold nanoparticles from the aqueous solution. In a different configuration, the gold nanostars have been embedded into a patterned PDMS film offering ultrasensitive, flexible and transparent SERS substrate.[110] As shown in figure (2.11 B), the gold nanostars monolayer was first developed onto the silicon substrate by electrostatic interaction followed by pouring the aqueous mixture of the PDMS and the curing agent. The gold nanostars-PDMS film was then detached from the solid substrate. The substrate was found to be stable against stretching, bending, and torsion with reproducible signal enhancement toward the benzenethiol molecules over 100 cycles with an enhancement factor of about 2×10^8. Furthermore, the nanoparticle-coated PDMS thin film can be used in a simple and efficient way,[111,112] where the probed surface is covered by the nanoparticle/PDMS film enabling high signal enhancement for Raman imaging.

Relatively speaking, the direct fabrication of SERS substrates might produce a highly homogeneous substrate but requires relatively expensive devices. On the other hand, the SERS substrate produced by immobilizing the nanoparticles does not need such complex steps. However, it is difficult to produce highly homogeneous substrates over a large scale.

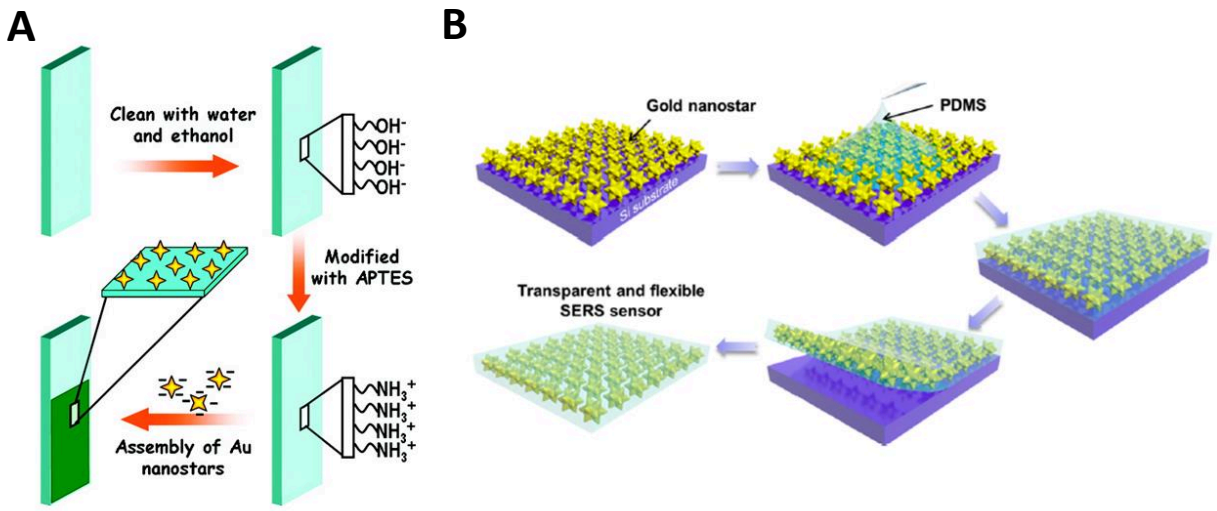

Figure 2.11. Schematic depictions of self-assembled gold nanostars on quartz substrate (A) and inside a polymer film (B) adapted from ref [79 and 82].

2.9. Case study of plasmon-driven dimerization reactions

Dimerization of 4-nitrothiophenol (4-NTP) or 4-aminothiophenol (4-ATP) into 4,4'-dimercaptoazobenzene (DMAB) is an important model example of the plasmon-driven reactions owing to the ambiguity accompanied with the nature and the mechanism of this reaction. As previously mentioned, when these molecules adsorb on metal nanoparticles, they display different Raman signatures.[63] It took around 15 years to unfold the ambiguity accompanied with this behavior, where the molecules were found to exhibit a dimerization reaction (figure 2.12) and not as believed, that these peaks were the evidence of the chemical-enhancement mechanism of SERS.[113] However, these reactions are still a point of debate, since the contributions of the surface plasmon to the reaction is still unclear. Typically, the 4-NTP and 4-ATP have been chosen as ideal candidates for SERS and catalysis owing to their high affinity to the metal surfaces driven by their thiol groups, guaranteeing their fixed and close contact to the SERS substrate. This would enables

studying the kinetics of the reactions with minor interference of the diffusion and desorption mechanisms. Furthermore, the molecules with the combination of nitro- or amino groups with the aromatic ring were found to have a relatively high Raman cross-section, enabling the observation of the reaction with a shorter acquisition time.

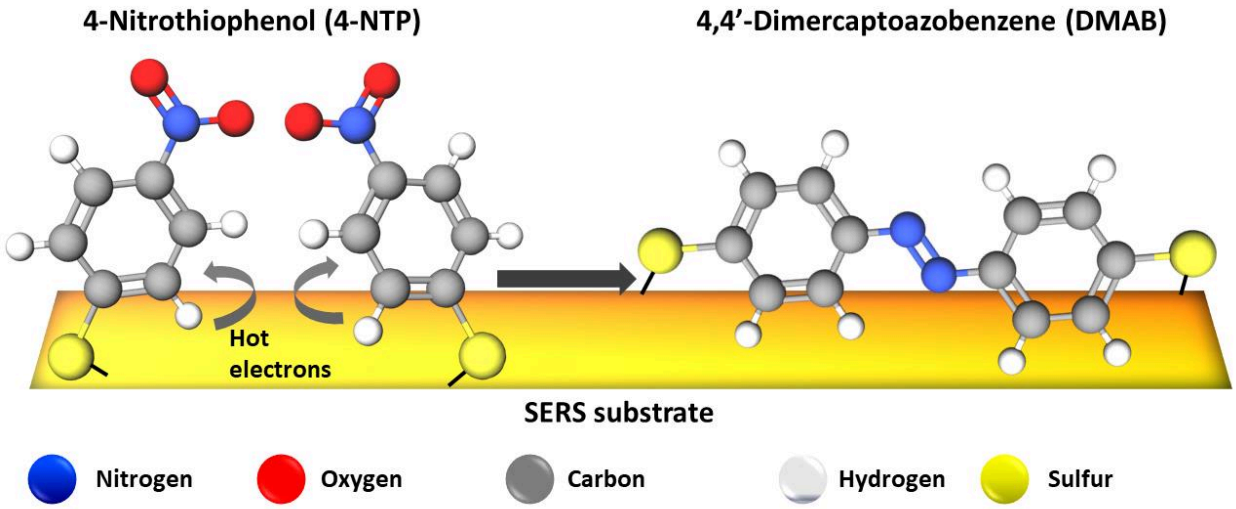

Figure 2.12. Schematic illustration of the plasmon-driven dimerization of 4-NTP to DMAB on the SERS substrate.

The plasmonic nature of the reaction was studied based on the surface plasmon resonance. In other words, tuning the resonance between the surface plasmon of the nanoparticles and the laser excitation is used to show the performance of such reactions towards the surface plasmon, since more resonance would lead to more generated hot electrons and higher nanoparticle temperatures which affect the reaction rate.[114] Several strategies have been employed to control this resonance. One technical way is to use different laser wavelengths that hit different regions of the surface plasmon band of the nanoparticles. However, this requires multiple lasers with high costs. Another way is to chemically control the position of the plasmon band of the nanoparticles with respect to the used laser wavelength. For instance, this was achieved by changing the aspect ratio of the gold

nanorods or by using different particle morphology such as gold nanostars.[115–120] Overall, the surface plasmon resonance has been shown to play the most important role in these surface-reactions, where the coupling reaction of 4-NTP into DMAB was found to depend on several factors, such as the laser wavelength, the laser power, and the substrate.

Briefly, The dimerization of 4-NTP was reproduced on the surface of silver microflowers, where the reaction rate was found to proceed faster when the sample was irradiated by 532 nm laser compared to 633 nm.[121] Furthermore, the dimerization process did not occur on the surface of a Cu film using 633 nm laser as the light source, while the reaction proceeded dramatically when the light source was changed to 514.5 nm confirming the laser wavelength dependence of the reaction.[122] Moreover, the laser power dependence of the reaction on aggregated gold nanoparticles was also reported, where the reaction did not proceed using a laser power lower than 1.2 mW.[123] However, with increasing the laser power, DMAB peaks were observed and increased in intensity. Moreover, an important control experiment was performed, where the 4-NTP solution without plasmonic nanoparticles was irradiated for a much longer time, however, the DMAB peaks were not observed providing a clear evidence for the importance of the surface plasmon for the reaction. The laser wavelength-, laser power-, time-, substrate dependences of the dimerization reaction were considered to be strong pieces of evidence for "the electron-driven" nature of the reaction, since using more resonant laser or substrate with a plasmon resonance located near to the used wavelength or more powered laser would strongly excite the surface plasmon of the metal, and therefore more hot electrons are generated and become available for the reaction as shown in figure (2.13).[114] However, the same factors were reported to increase the local temperature of the plasmonic nanoparticles via the plasmonic heating effect.[124–128] Such heat was used to drive and/or to enhance different chemical reactions. Therefore, the exact role of the energetic electrons or the plasmonic heating cannot be validated, while the plasmonic nature of the reaction can be confirmed.

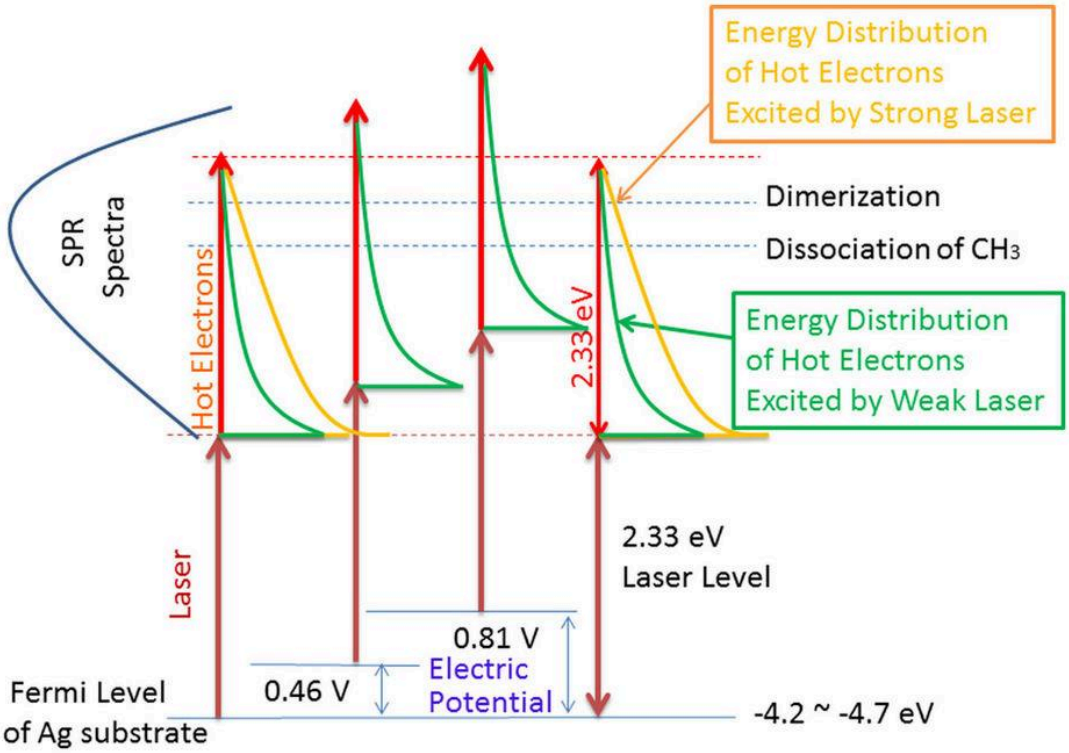

Figure 2.13. Schematic depictions describe the dependence of the plasmonic reaction on the laser intensity and the electric potential adapted from ref [86].

Owing to the high signal enhancement, SERS has been additionally used to monitor such coupling reactions in aqueous media. This possibility allowed controlling several parameters regarding the reaction environments such as the atmosphere and the pH of the reaction media. Interestingly, controlling the atmosphere of the experiment through a home-built cell was found to control the reaction rate.[129] For instance, the oxygen-saturated atmosphere was found to inhibit the dimerization reaction of 4-NTP, while the nitrogen-saturated atmosphere was used to enhance the reaction rate. This suggests the importance of the energetic electrons for the reaction since the oxygen is known to be an electron capturer and therefore inhibiting the reaction. This conclusion was supported by another investigation where an electron and a hole capturer have been introduced to the reaction medium. For instance, when an electron capturer ($AgNO_3$) was subjected to the reaction, the dimerization reaction rate was retarded while introducing a hole capturer (ammonium oxalate) into the reaction led to improving the reaction rate by preventing electron/hole recombination and making the electrons more available for the reaction.

These can be considered as a strong evidence of "the electron-driven" nature of the coupling reaction of 4-NTP.

On the other side, Kwan Kim and co-workers have measured SERS spectra of 4-NTP adsorbed on silver nanoparticle-substrates at liquid nitrogen temperature (77 K).[130] The authors showed that hot electrons were efficiently generated at this temperature while they did not observe any reaction signatures confirming an important role of the plasmonic heating. Moreover, Ping Xu and co-workers have proposed the plasmonic heating mechanism to be the driving mechanism of the dimerization reaction of 4-ATP with the assistance of the oxygen as an oxidizing agent. The authors suggested that the local temperature at the surface of the silver nanoparticles could exceed 150 ^{0}C, which might be enough to initiate the reaction. Likewise, Golubev and co-workers have proposed the high local temperature to be the key to the dimerization of the 4-NTP. Recently, we have detected an increase of the particle temperature up to 100 K during the reaction, which might support this hypothesis. Overall, these experiments show the importance of both the plasmonic heating and the charge-transfer mechanisms for the reaction, though their exact contributions in the reaction are still unclear. Therefore, in this thesis, a systematic study has been performed on the reaction and monitored by SERS for a deep understanding of the driving forces of such plasmonic reaction.

2.10. Concluding remarks

Plasmon-driven coupling reactions of 4-NTP or 4-ATP into DMAB have been confirmed theoretically and experimentally providing a new way to synthesize the azobenzene molecules. However, attempts to scale up this method have not been reported yet. Moreover, the reaction was found to depend on the different light, atmospheric, and chemical factors, while the exact role of the energetic electrons as well as the plasmonic heating is generally debated. SERS is an efficient tool for in-situ characterizing and monitoring these reactions. Taking this into consideration, here we use SERS as an analytical tool to further study the coupling reaction of 4-NTP to provide a fundamental and mechanistic explanation for the plasmonic reactions.

Chapter 3. Experiments and methods

3.1. Sample preparation

In this thesis, several gold nanoparticles with different morphology have been used as the reaction platform as well as the SERS template. For instance, the gold nanotriangles (AuNTs) and gold nanostars have been prepared and provided by the group of Prof. Koetz.[131,132] I used these structures as SERS substrates for the 4-NTP and R6G molecules.[133] For studying the dimerization reaction of 4-NTP, I further prepared gold nanoparticles with irregular shapes, generally termed gold nanoflowers (AuNFs) according to the published protocols.[134,135] Moreover, in papers G and H (presented in chapter 4 and 5), I deposited the AuNTs on the silicon wafers in a closed environment, enabling the formation of gold films with multilayers of the gold NTs. Before the deposition, the silicon substrates have been silanized with (3-Mercaptopropyl)trimethoxysilane to provide free thiol groups to bind the gold particles. In a different deposition method, the AuNTs formed a large scale monolayer on silicon and glass substrates with the assistance of an oil mixture of toluene and ethanol. I prepared some samples by this way and some were provided by the group of Prof. Koetz. In all experiments, I incubated the SERS substrates with a low concentration of the probed analyte (4-NTP or R6G), allowing the formation of a monolayer of the molecules on the particle surface. The unattached molecules were washed away by immersing the substrates in water and ethanol several times. Finally, the prepared substrates were used by me to further investigate the model plasmonic reaction of 4-NTP by various Raman microscopes. In a recent unpublished data, I used the gold nanostars dispersed in an aqueous solution for SERS properties, showing the direct influence of the plasmonic particles on the SERS signals without the need of depositing the particles. It is worth noting that all the particles were characterized by several microscopic and spectroscopic techniques as shown in the attached publications.

3.2. Experimental set-ups

3.2.1. UV-Vis-NIR spectroscopy

It is a routinely used technique in the field of analytics and it always refers to the extinction or the reflection properties of the sample in these regions of the electromagnetic spectrum. The absorption of light is associated with electronic transitions of both atoms and molecules, since the energy levels are quantized and only light with certain energy can, therefore, cause such transitions. In this thesis, we used this technique to define the location of the plasmon band of the gold nanoparticles, and the spectrum was then used to select a resonant excitation wavelength for Raman spectroscopy experiments. For instance, figure 3.1 shows the extinction spectrum of a monolayer of the gold NTs deposited on a glass substrate displaying a broad extinction band in the range of 500 – 2500 nm measured by the UV-VIS-NIR spectrometer (VIRIAN CARY 5000). Therefore, lasers with excitation wavelengths of 785 and 920 nm were used throughout the thesis to excite the localized surface plasmon for the catalytic and SERS purposes (shown as a red arrow in figure 3.1). It is worth noting that, the spectrum is called an extinction spectrum since both the absorption and the scattering of light were measured.

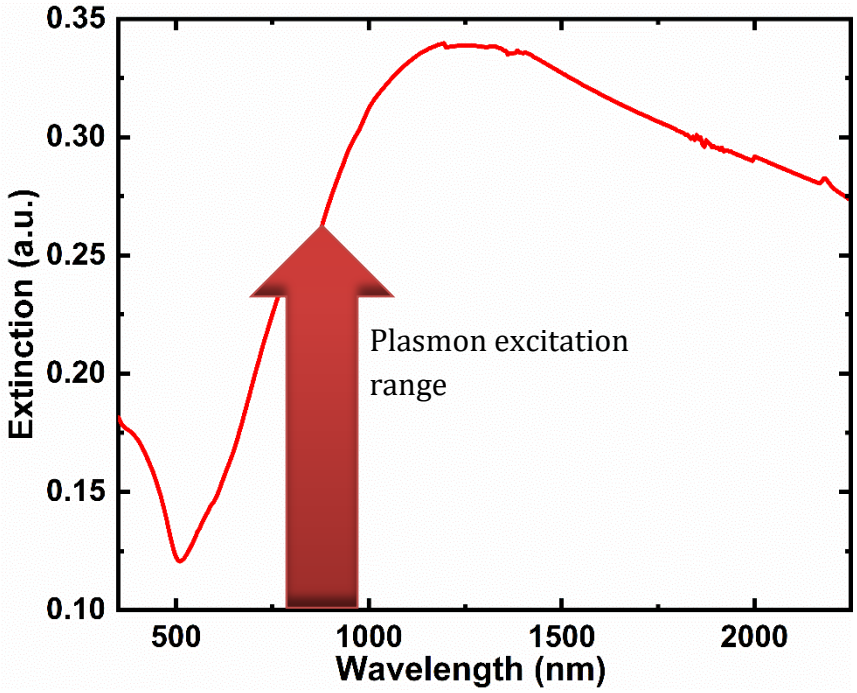

Figure 3.1. The extinction spectrum of a monolayer of gold NTs adsorbed on a glass substrate.

3.2.2. Raman spectroscopy experiments

Vibrational signatures can provide "fingerprint" information on the molecular structure of the sample and how it might change with time. Therefore, Raman spectroscopy is considered to be the main technique used in this dissertation to probe the vibrational modes of our molecular system. Typically, the incident photons exchange energy with the molecular vibrations. As a result, vibrations of the molecule are initiated and changes in the energy of the photons are observed.[136,137] For instance, the photon scattered with a lower energy than the incident photon is referred to as the "Stokes Raman scattering", while the photon scattered with higher energy is referred to as the "anti-Stokes Raman scattering". Schematically, as shown in figure (3.2 B), Raman scattering is collected by the same objective lens and filtered out from the incident light by a specific notch filter. The scattered light is then focused into the spectrometer, where the light is dispersed into different energies by specific gratings and being detected by the CCD detector.

Two Raman microscopes have been used in the work implemented in this thesis. For instance, the confocal Raman microscope alpha 300 from WITec was used in the Max Planck Institute of Colloids and Interfaces located in Golm, Potsdam. This microscope allowed monitoring the reaction in a time-resolved mode with using wide range of the laser powers. For the typical Raman experiments, the sample was put directly under the objective lens of the Raman microscope, and the measurement modes (single spectrum or time-dependent series), and the acquisition time were directly inserted into the software. For some Raman experiments, it was necessary to control the operating temperature during the measurements to show the importance of the plasmon-heating effect for the reaction. Therefore, we used a Linkam stage (THMS600 from Linkam), which provides a reaction chamber with a controllable temperature in a range from 298 K to 573 K as shown in figure (3.2 A). The sample was held inside the chamber and the light was focused onto the sample through a transparent window under a constant temperature. The temperature within the chamber is controlled by an external controller coupled with a thermocouple and a heater. The chamber also allows controlling of the operating atmosphere through an external gas inlet and outlet. In this thesis, controlling the operating temperature was chosen to study the properties of the plasmon-driven 4-NTP dimerization reaction towards what is called the plasmon-heating effect. In a different experiment, where the molecular temperatures were discussed, I used the confocal Raman microscope (JASCO NRS-4100) provided by the School of Analytical Science Adlershof, Humboldt University, which is located in Adlershof, Berlin. This microscope was used for detecting the Stokes and the anti-Stokes signatures of the probed molecules. From these measurements, the molecular temperature was estimated from the intensity ratio of the anti-Stokes and the Stokes Raman signal.

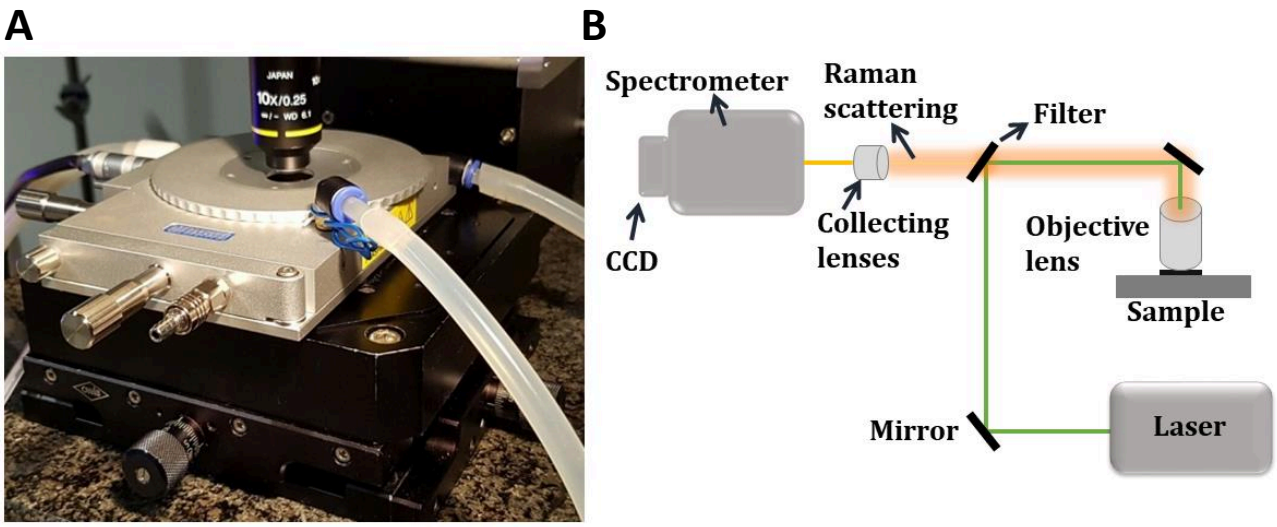

Figure 3.2. A photograph of the used Raman microscope with a heating stage (A) and its laser pathway (B).

3.2.3. X-ray diffraction experiments

X-ray diffraction is a powerful technique primarily used to study the crystal structure of the crystalline samples.

X-rays are a highly energetic electromagnetic radiation with a short wavelength (0.15 nm), which is in the same order of magnitude as the spacing between the planes in the crystal. Therefore, a specific diffraction pattern of the probed crystal can be produced. When the x-rays impinge on the sample, the diffraction only occurs if their path differences are equal to an integer multiple of the wavelength, which fulfills the conditions of Bragg's law shown in equation 3.1:

$$2d\ sin\ \theta = n\lambda \tag{3.1}$$

Here d is the spacing between the planes, ϴ is the incidence angle, n is the diffraction order and λ is the wavelength. Therefore, the diffraction from any set of the planes can only occur at certain angles predicted by Bragg's law. Now, considering the crystal as an ordered and regular array of atoms, we can study the changes of the inter-planar spacing in response to an external stimulus since the XRD selectively probes the crystal lattice. In our experiment, we have determined the temperature of the gold nanotriangles deposited as a flat

monolayer on a silicon wafer and resonantly irradiated by light. The laser and the x-ray (in-house and at the KMC3-XPP endstation of the Berlin synchrotron radiation facility BESSY II) were concentrated on the same spot on the nanotriangles-substrate as shown in figure (3.3). The temperature changes of the nanotriangles (ΔT) were determined by the relative changes of the out-of-plane lattice constant upon continuous light illumination and detected by the <111> Bragg peak of the nanotriangles.[138] We found that as the temperature of the particle increases (driven by high laser powers) the Bragg peak shifts to a lower angle. Finally, the particle temperature was determined from the shift of the Bragg peak using the following equation:

$$cot\theta\ \Delta\theta = \frac{\Delta c}{c} = -\alpha\ \Delta T \qquad (3.2)$$

Where Δθ is the shift of the Bragg peak, $\frac{\Delta c}{c}$ is the relative change of the out-of-plane lattice constant, and α is the linear thermal expansion coefficient of the gold.

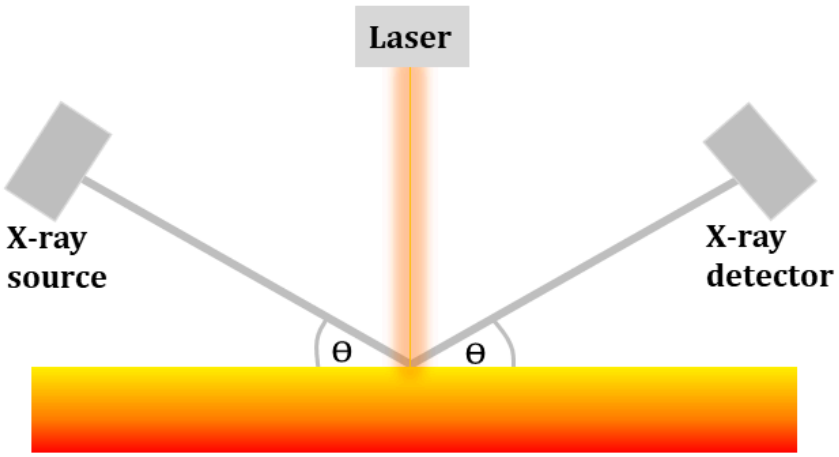

Figure 3.3. A schematic of the set up in the X-ray experiment.

Chapter 4. Manuscripts

In this chapter, I present my manuscripts that constitute my cumulative thesis. I further highlight my contribution in these manuscripts. It is worth noting that the data presented in all manuscripts were discussed and reviewed by all authors.

[A] **Radwan M. Sarhan**, Wouter Koopman, Jan Pudell, Felix Stete, Marc Herzog, Ferenc Liebig, Joachim Koetz, and Matias Bargheer: Scaling-up nano-plasmon catalysis: role of heat dissipation, J. Phys. Chem. C 2019, 123, 9352−9357.

This manuscript discusses the possibility of scaling up the nanoplasmonic catalysis, where the laser spot size is simply increased. I used the dimerization reaction of the 4-nitrothiophenol as a model example of the plasmonic reactions. I showed the importance of the heat dissipation from the reaction substrate for a successful dimerization reaction. In this manuscript, I designed and performed the Raman measurements. Analysis and presentation of these data were done by me under the guidance of Dr. Wouter Koopman and Prof. Matias Bargheer. Finally, the manuscript was written by me and reviewed by Dr. Wouter Koopman and Prof. Matias Bargheer.

[B] **Radwan M. Sarhan**, Wouter Koopman, Roman Schuetz, Thomas Schmid, Joachim Koetz, and Matias Bargheer: Importance of plasmonic heating for the plasmon-driven photodimerization of 4-nitrothiophenol, Sci. Rep., 2019, 9, 3060.

This study shows the role of the photons as well as the plasmonic heating for the plasmonic-driven dimerization reaction, where the plasmonic heating was shown to enhance the reaction rate, whereas the reaction is only driven in the presence of many photons. Herein, I designed the manuscript, where all the Raman measurements and the sample preparation were done by me. Analysis and presentation of the data were done by me together with Dr. Wouter Koopman and Prof. Matias Bargheer. The manuscript was

written by me and further enhanced and reviewed by Dr. Wouter Koopman and Prof. Matias Bargheer.

[C] Ferenc Liebig, **Radwan M. Sarhan**, Claudia Prietzel, Clemens N.Z. Schmitt, Matias Bargheer, Joachim Koetz. Tuned SERS Performances of undulated Au@Ag Triangles, ACS Appl. Nano Mater., 2018, 1, 1995–2003.

In this manuscript, undulated gold/silver nanotriangles have been developed by in situ reduction of the silver ions on the surface of the gold NTs. As a result, the location of the LSPR band has been shifted to be in a good resonance with the excitation laser, which results in obtaining a high SERS signal enhancement as compared with the bare particles. In this study, I performed several SERS experiments to show the dependence of the SERS signal intensity on the resonance between the excitation wavelength and the plasmon of the gold particles. Moreover, I designed and wrote the SERS part of the manuscript, where the presentation and the analysis of the data were performed by me.

[D] Ferenc Liebig, **Radwan M. Sarhan**, Claudia Prietzel, Matias Bargheer, Joachim Koetz. Undulated gold nanoplatelets. In situ growth of hemispherical gold nanoparticles onto the surface of gold nanotriangles, Langmuir, 2018, 34, 4584–4594.

This manuscript discusses the formation of the undulated gold nanoplatelets with zigzag-shaped edges for the first time. In this work, I have shown that the undulated nanoplatelets exhibit a high catalytic and SERS activity as compared with the normal unmodified triangles. I performed and designed the SERS experiments. The presentation of the data was done by me. The SERS part of the manuscript was written by me and reviewed by all authors.

[E] Ferenc Liebig, **Radwan M. Sarhan**, Mathias Sander, Wouter Koopman, Roman Schuetz, Matias Bargheer, and Joachim Koetz. Deposition of Gold Nanotriangles in Large Scale Close-Packed Monolayers for X-ray-Based Temperature Calibration and SERS Monitoring of Plasmon-Driven Catalytic Reactions, ACS Appl. Mater. Interfaces, 2017.

In this study, the formation of a large scale monolayer of the gold NTs has been discussed. The X-ray was further applied to show the high temperature of the nanotriangles as a result of the light irradiation needed for the plasmonic reaction. In this article, I designed and wrote the manuscript with Ferenc Liebig. I showed that the dimerization reaction of 4-NTP might benefit from the high temperature generated upon light irradiation. Moreover, the SERS measurements were performed and presented by me.

[F] Ferenc Liebig, Ricky Henning, **Radwan M Sarhan**, Claudia Prietzel, Matias Bargheer and Joachim Koetz: A new route to gold nanoflowers, Nanotechnology, 2018, 29, 185603.

This manuscript shows the formation of the gold nanoflowers by the vesicular-template method, where AOT/CTAB-based vesicle is used. The nanoflowers were shown to have a good SERS enhancement factor. Herein, I designed and wrote the SERS part of the article. The SERS measurements were performed by me, where I deposited the rhodamine dye on the surface of the SERS substrate as the probe. Finally, analysis and presentation of the SERS data were done by me.

[G] Alexander. Von Reppert, **Radwan M. Sarhan**, Felix Stete, Jan Pudell, Natalia Del Fatti, Aurelien Crut, Joachim Koetz, Ferenc Liebig, Claudia Prietzel, Matias Bargheer: Watching the Vibration and Cooling of Ultrathin Gold Nanotriangles by Ultrafast X-ray Diffraction, J. Phys. Chem. C., 2016, 120, 28894.

This study applies the ultrafast X-ray diffraction method to study the vibrations of the gold nanotriangles as a result of their optical excitation. In this work, I prepared the sample, where the gold nanotriangles were deposited in a flat gold film on silicon substrates after

functionalizing the substrates with (3-mercaptopropyl)triethoxysilane molecules in a process called silanization process.

[H] Ferenc. Liebig, **Radwan. M. Sarhan**, Claudia Prietzel, Antjie Reinecke, Joachim Koetz: "Green" Gold Nanotriangles: Synthesis, Purification by Polyelectrolyte/Micelle Depletion Flocculation and Performance in Surface-Enhanced Raman Scattering, RSC adv., 2016, 6, 33561.

This article shows the formation of the gold nanotriangles and their deposition as flat multilayers on the silicon wafers for the SERS applications. In this work. I deposited the nanotriangles on the silicon wafers and used them as the SERS substrate. I further designed and wrote the SERS part of the article. The SERS measurements and the data presentation were performed and presented by me.

Chapter 5. Discussion

5.1. Surface –enhanced Raman Scattering [C, D, F, H]

As was mentioned earlier, metal nanostructures exhibit unique optical and physicochemical properties that can be controlled by tuning their size, shape, and surroundings. This property can be used to maximize their interaction with light, which is beneficial for various applications such as nanophotonics, cancer therapy, and SERS. Typically, the anisotropic gold nanoparticles such as gold nanostars and gold nanotriangles have been extensively utilized for SERS applications.[139–141] Their nanotips act as nanoantennas enhancing the electromagnetic field and thus the Raman signals under resonant excitation of their LSPR ("lightning-rod effect").[142,143]

In manuscript H, we developed a SERS substrate based on the gold nanotriangles (AuNTs) for few molecule Raman analysis. The AuNTs were prepared in a facile one-step method in the presence of mixed phospholipid vesicles, followed by a separation step of the NTs from the spherical particles in a process called depletion flocculation.[131] For SERS applications, the NTs were deposited onto silicon substrate in a flat film. The deposition process started with silanization of the silicon wafers with 3-mercaptopropyltriethoxysilane, which was consequently functionalized with free thiol groups that bind the gold NTs.[144] This method resulted in the formation of a golden film deposited on the substrates and composed of flat multilayers of the gold NTs. I used this SERS substrate as a platform for detecting 4-NTP molecules. Moreover, in manuscript G, this configuration of the substrates has been successfully used to study the vibrational motions of the gold layer after optical excitation with ultrafast laser using ultrafast X-rays.

In different experiments, assembly of the particles at the water/air interface has been used to have a well-ordered assembly of the NTs as presented in manuscript E. In this method, the NTs were deposited in a large scale of closely packed monolayer on a solid substrate using a mixture of organic solvents.[138] In our system, a gold film was observed to form when an oil mixture of ethanol and toluene is applied to the aqueous solution of the gold

NTs. However, transferring this film to a solid substrate by horizontal lifting resulted in deformation of the monolayer. Therefore, an on-chip experiment was performed, where a drop of the aqueous solution of the gold NTs was set on the substrate, and the oil mixture (ethanol/toluene, 5:1) was then applied to form a golden film at the air-liquid interface. The film was then transferred to the solid surface after the water was evaporated, yielding a large scale of gold NTs monolayer as shown in figure (5.1A), which showed a good SERS performance for the self-assembled 4-NTP molecules (EF $\sim 2 \cdot 10^4$). In contrast to the assembly methods used in literature to form monolayers of gold NTs, this method does not require pre-functionalization of the particles with a specific surfactant and the monolayer is formed directly on the substrate without any transferring steps. Moreover, this assembly method was extended to include different shapes of the gold particles such as the gold nanostars as shown in manuscript F.

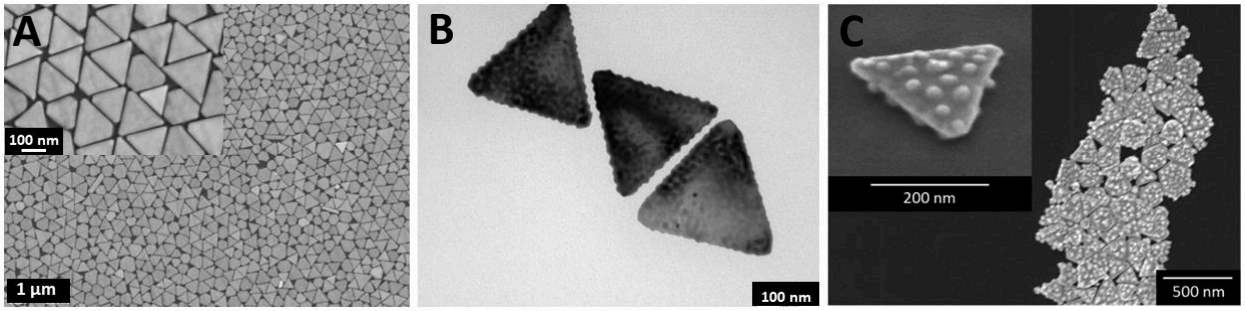

Figure 5.1. SEM images of the gold nanotriangles (A) and their complex structures of undulated gold nanotriangles (B) and gold/silver nanotriangles (C).

The morphology of the pristine AuNTs has been modified to further enhance the SERS signal as shown in figure (5.1B and C). For instance, in one direction, the in-situ reduction of the gold ions on the surface of the gold NTs has led to the formation of hemispherical gold nanoparticles on the surface of the NTs, while the NT edges were transformed into zigzag-shaped edges forming what is called "undulated gold nanotriangles" as shown in manuscript D.[132] This was achieved by covering the NTs with a shell of a cationic polymer (Polyethylenimine, PEI). Upon reduction of the chloroauric acid, the gold ions were reduced inside the shell and grown on the NT surface forming hemispherical particles with a diameter of 6 nm on both sides.

Such changes of the morphology increased the SERS signal enhancement of the main Raman peaks of 4-NTP compared to the bare gold NTs as shown in figure (5.2 A). The SERS spectrum is dominated by the main three Raman peaks of the 4-NTP at 1077, 1332, and 1575 cm^{-1}, which are assigned to the C-H bending, NO_2, and the C=C stretching modes, respectively. An enhancement factor of $\sim 6 \cdot 10^4$ was calculated for the strongest NO_2 vibrational mode. This enhancement was explained as a result of the roughened surface and edges of the undulated NTs since the changes in the morphology of NTs did not significantly influence the location of their LSPR band.

Besides the creation of large scale SERS substrates, the formation of complex structures of small nanoparticles on large plasmonic particles is of a great importance, for combining the catalytic activity of small particles with the SERS activity of the larger particles.[145,146] In paper D, the presence of small hemispherical nanoparticles on the NT surfaces increased the catalytic activity, as demonstrated by appearance of the plasmonically generated DMAB. As shown in figure (5.2 A), Raman peaks appeared at 1134, 1387, and 1434 cm^{-1} , which were assigned to the C-N and N=N stretching modes of DMAB molecules. However, it required higher laser intensity to drive the reaction on the bare NTs. Furthermore, the SERS spectrum displayed several small peaks at 1010, 1150-1210, and 1610 cm^{-1}, which were not observed in the SERS spectrum on bare NTs. These peaks were assigned to the very week C-H bending and ring deformation modes of the 4-NTP, since the 4-NTP molecules might be tilted on the roughened surface towards the gold NTs making their ring and C-H modes selectively enhanced.

In paper C, we show that the in-situ reduction of the silver ions on the gold NT surface resulted in the formation of silver nanoparticles (AgNPs) adsorbed on the gold naotriangles (Au@ Ag NTS).[133] Such changes in the morphology greatly influence the spectral location of the LSPR band of NTs. For instance, when the concentration of the silver nanoparticles on the NT surface was gradually increased, the LSPR band was stepwise shifted from 1300 to 800 nm. As a result, the SERS dependence on the resonance between the surface plasmon and the excitation wavelength was observed. The sample with the highest concentration of silver NPs exhibited a LSPR band at 800 nm, which is located close to the wavelength of the Raman laser (785 nm). Such sample, therefore, displayed the highest SERS signal

enhancement for the Rhodamine dye (R6G) as compared with the other off-resonant samples as shown in figure (5.2B).

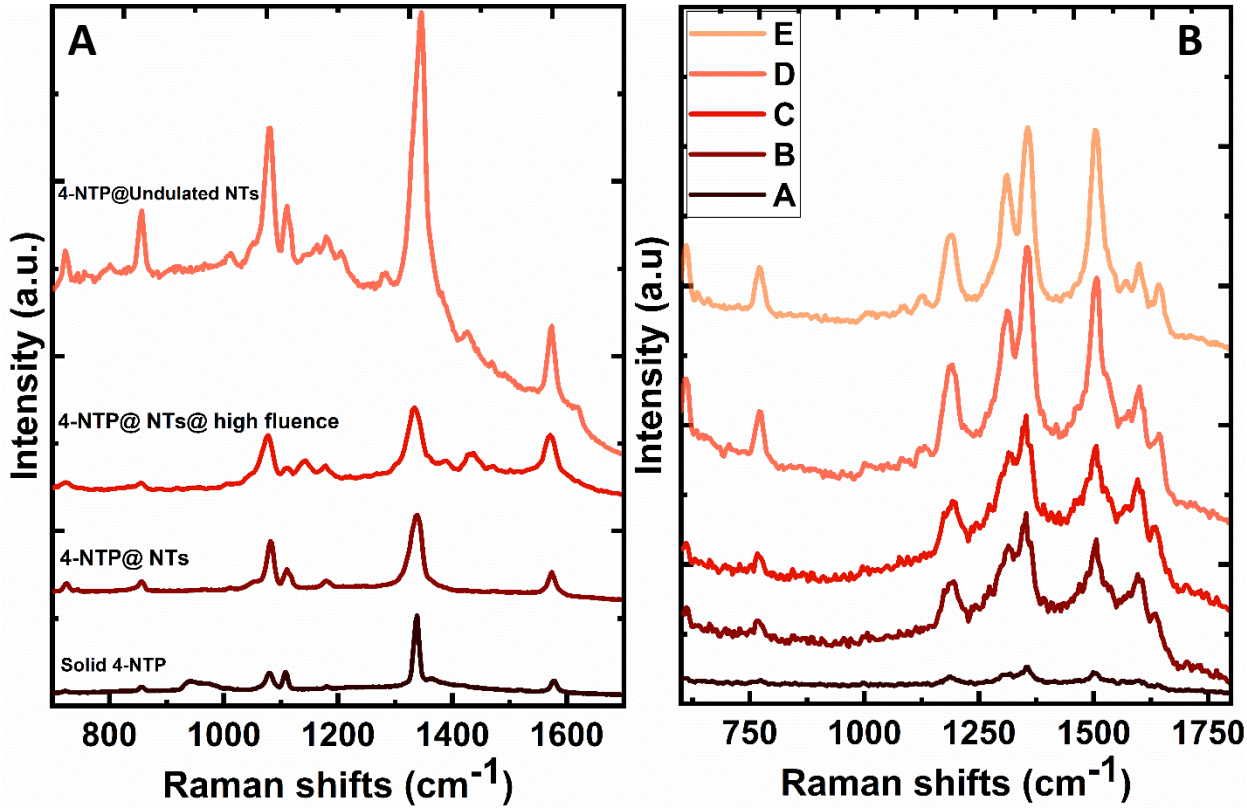

Figure 5.2. SERS performance of the bare and the undulated gold nanotriangles for the 4-NTP molecules (A) and the SERS signatures of R6G molecules adsorbed on gold/silver nanotriangles prepared with different concentrations of silver (B)

We explain this enhancement as a result of the plasmon resonance as well as the nanogaps formed between the AgNPs, which can be considered as new SERS hot spots. To further confirm the dependence of the SERS enhancement on the plasmon resonance, we used another excitation wavelength (532 nm) to record the SERS spectrum of the same sample. The Raman signature of the R6G molecules was barely visible in this case, confirming our explanation.

The high signal enhancement encouraged us to further decrease the concentration of the dye to 10^{-5} M. Interestingly, the SERS signature of the R6G molecule was clearly visible even after lowering the integration time to 1 second. These measurements were performed

using a relatively low laser power (2 mW) and a very short integration time (1 sec), which implies the high SERS activity of our sample for measuring low concentrations of the analyte under these conditions. It is worth noting that measuring under high laser intensities and/or long integration time may induce chemical changes of the analyte, ending up with detecting SERS signal from a different molecule.[63]

5.2 Plasmon-driven dimerization of 4-NTP [A, B, E, G]

As a result of the high signal enhancement of the plasmonic gold NTs, an excellent SERS spectrum of the analyte can be detected within a short integration time. Therefore, the chemical reactions occurring on the particle's surface can be monitored by SERS in real time scale. In paper E, static experiments have been performed to study the plasmon-driven dimerization of 4-NTP into DMAB, where the 4-NTP molecules are chemisorbed via Au-S bond on the surface of the gold NTs monolayer (inset of figure 5.3). Figure 5.3 shows the differences in the Raman signatures of the bulk 4-NTP and the 4-NTP chemisorbed on AuNFs, where three new Raman peaks appear in the fingerprint region of the adsorbed 4-NTP. These Raman peaks at 1134, 1387, and 1434 cm^{-1} were assigned to the C-N and N=N vibrational modes of the photo-product (DMAB).[138] A complete peak assignment is presented in table 5.1. The same behavior was observed for 4-NTP molecules being adsorbed on the monolayer of the gold NTs. Clearly, at low laser power (0.5 mW), the spectrum was found to be dominated by 4-NTP Raman peaks, while no signature of the DMAB was observed. However, increasing the laser power to 5 mW resulted in the formation of the dimerization product (DMAB) in a considerable amount as evidenced by its Raman peaks. These data confirm that the reaction is intensity-dependent. Moreover, time-dependent SERS measurements were performed to show the evolution of the DMAB Raman peaks in real time, where a considerable amount of DMAB was obtained after 200 seconds displaying that the reaction also depends on the laser exposure time.

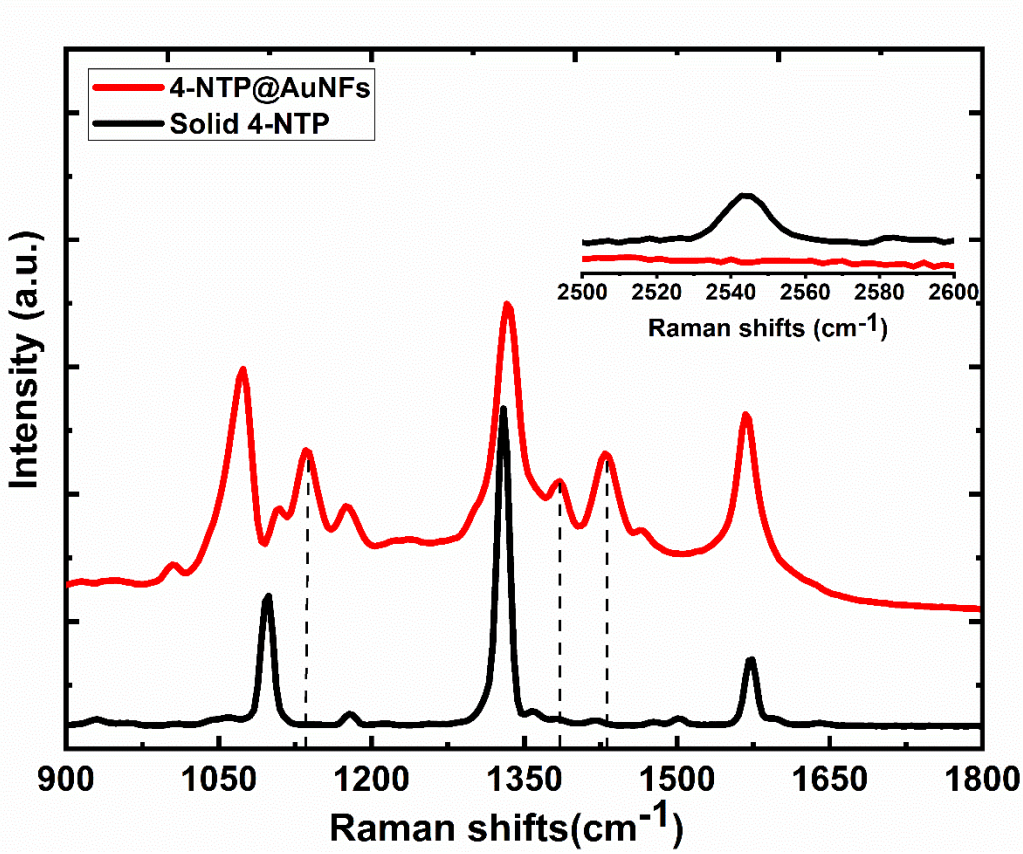

Figure 5.3. Raman spectra of neat 4-NTP molecules (black) and 4-NTP adsorbed on gold nanoflowers (red).

Typically, the reaction was explained to be driven as a result of the plasmon excitation, where energetic electrons as well as an increase of the particle's temperature are generated.[147–149] Consequently, two possible mechanisms have been proposed, where the electrons may scatter to populate the empty orbitals of the adsorbed 4-NTP molecules initiating the reaction, or the high temperature triggered by the light may directly induce the chemical transformation of the 4-NTP molecules. Therefore, at high excitation powers (e.g 5 mW), these effects are higher than those at low power (e.g 0.5 mW). This would increase the probability of the dimerization reaction that might be in need of a certain threshold of simultaneously excited hot electrons or a certain temperature, while increasing the irradiation time would linearly increase the reaction yield.

SERS assignments of the peaks[63,150,151]		
Peak position (cm^{-1})	**4-NTP**	**DMAB**
2545	S-H stretch.	-
1570	C=C stretch.	
1505	NO_2 antisym stretch.	-
1434		N=N stretch.
1387		N=N stretch.
1332	NO_2 sym stretch.	
1173	C-H bending.	
1134		C-N stretch.
1108	C-H bending.	
1075	Ring breath and C-S stretch.	

Table 5.1. Complete SERS assignments of 4-NTP and DMAB peaks.

The direct contribution of the local high temperature to the plasmon-driven dimerization of 4-NTP has caught our interest, since the role of the temperature in the plasmonic chemistry has been often ignored.[18,129,130,152] Calculating the local temperature is challenging particularly in presence of gradients, however, this is necessary to understand the mechanisms and pathways of the plasmon-induced reactions. Therefore, the nanoparticles and the molecular temperatures have been investigated during the reaction in order to find out whether or not the temperature's contribution plays a role regarding this reaction.

In paper E, X-ray diffraction experiments were performed to reveal the particle's temperature during the photocatalytic reaction, where the crystal lattice of the gold NTs is selectively probed.[138] In this experiment, several spots of the gold monolayer were irradiated with different laser intensities and the X-ray diffraction was simultaneously recorded to measure the temperature changes via the thermal expansion of the lattice. Moreover, to check the photocatalytic reaction, the SERS spectra of the irradiated spots

were then recorded by a Raman microscope. The gold <111> Bragg peak was found to shift to lower diffraction angles during the laser irradiation implying an increase of the temperature of the gold NTs. This shift was then translated into temperature changes of NTs, where the temperature of the gold particles was observed to linearly increase as the laser power increases, exceeding 100 K. However, SERS spectra did not show any signature of DMAB formation since the laser intensity was 5 order of magnitudes lower than the one being typically used under the microscope. It is worth to mention that the laser power was high enough to initiate the reaction, while it was necessary to pump a large area as probed by the X-rays. This data confirms that the reaction might occur at a very high temperature, where a specific laser intensity is reached.

In paper B, Raman spectroscopy has been used to probe the temperature of the adsorbed molecules. Basically, the incident photons would plasmonically excite the formation of the energetic electrons that will later couple to the phonon mode of the gold particles and heat up their crystal lattice.[37,153] Such heat can, therefore, excite the adsorbed molecules to a higher vibrational energy state and consequently evolving their anti-stokes Raman signature. Therefore, the anti-Stokes peaks can be used as a sign of the hot molecules, whereas the anti-Stokes/Stokes ratio can be used to obtain the temperature of such hot molecules. For this purpose, we measured full SERS spectra of 4-NTP adsorbed on a gold nanoflower-modified substrate, where the light intensity was tuned to be 2.4 and 127 kW/cm^2 resembling the non-reacting and reacting conditions, respectively. In figure 5.4, the DMAB peaks are shown to be clearly visible in both the Stokes and the anti-Stokes portions of the Raman spectrum attained after irradiating the sample with the high intensity. Interestingly, the anti-stoke Raman peaks of DMAB were observed to be more intense than those at the stokes part, which reveals a high temperature of the product DMAB molecules ($\Delta T_{vib,DMAB} = 350K$) as compared to the reactant 4-NTP molecules ($\Delta T_{vib,4NTP} = 200K$). The reason behind this might be that the DMAB molecules tend to form at the locations where the temperature is relatively high (hot spots). In this direction, we noticed in our measurements that approximately 70% of the 4-NTP peak intensity remains even after the intensity of the DMAB peak is saturated. This might corroborate our

argument that a small fraction of 4-NTP molecules, which exists in the hot spots could participate in the reaction.

Recently, Boerigter and co-workers have shown that the electron temperature of the particles can be determined from the intensity of the anti-Stokes background,[154] which measures the rate of the anti-Stokes shifted photons scattered from the Fermi-Dirac distributed electrons in the particles. Interestingly, following their procedures, we calculate a temperature rise of the particles of $\Delta T_{NP} \approx 150\ K$, which is significantly lower than the molecular temperature measured for the 4-NTP and DMAB molecules but in a good agreement with the particle temperature measured with X-ray diffraction. The relative low temperature of the particles could be attributed to the dissipation of the heat from the particles to the substrate, which results in a thermal equilibrium between them.

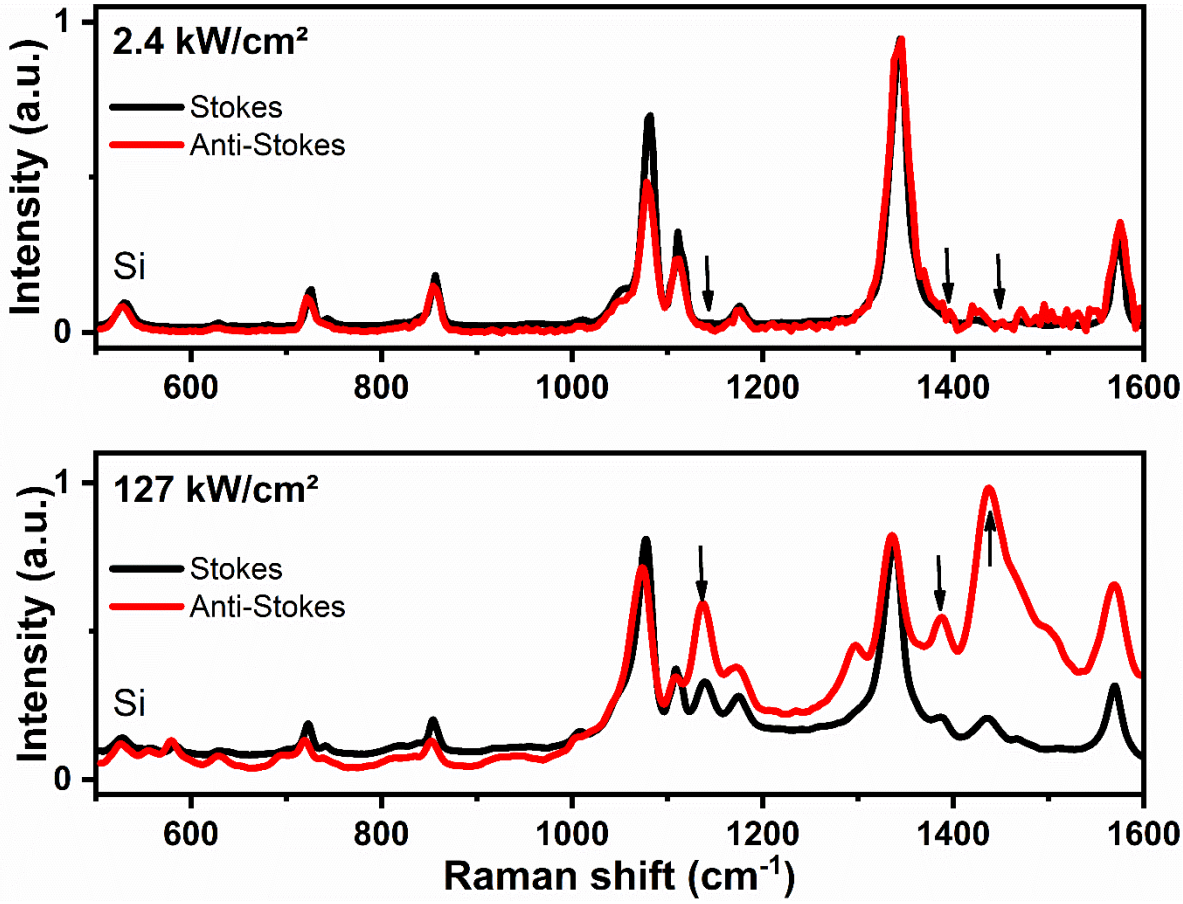

Figure 5.4. Complete SERS spectra of 4-NTP adsorbed on gold nanflowers at different light intensities showing the Stokes (black) and the anti-Stokes (red) portions of the spectra.

Overall, we have shown the temperature rise of the plasmonic particles and their adsorbates under the reaction conditions of 4-NTP dimerization. This high temperature might influence the reaction rate as most of the chemical reactions follow the Arrhenius law,[13] where the reaction rate (K) increases with the temperature (T) as shown in equation:

$$K(T) = A\ exp\ (-\frac{E_a}{RT}) \tag{5.1}$$

Where E_a is the activation energy per mole, A is a constant and R is the ideal gas constant. However, the common view is that the dimerization reaction of the 4-NTP is solely driven by the plasmonically generated energetic electrons.

To reveal the effect of the plasmonic heating on the reaction, the sample was put inside a temperature-controlled chamber, where the laser is focused onto the sample through a transparent window and the operating temperature was automatically controlled. Furthermore, the light intensity was tuned so that the reaction dynamic can be recorded in real time as shown in Figure 5.5A, where the evolution of DMAB Raman peaks at 1134, 1382, and 1434 cm^{-1} is clearly visible.

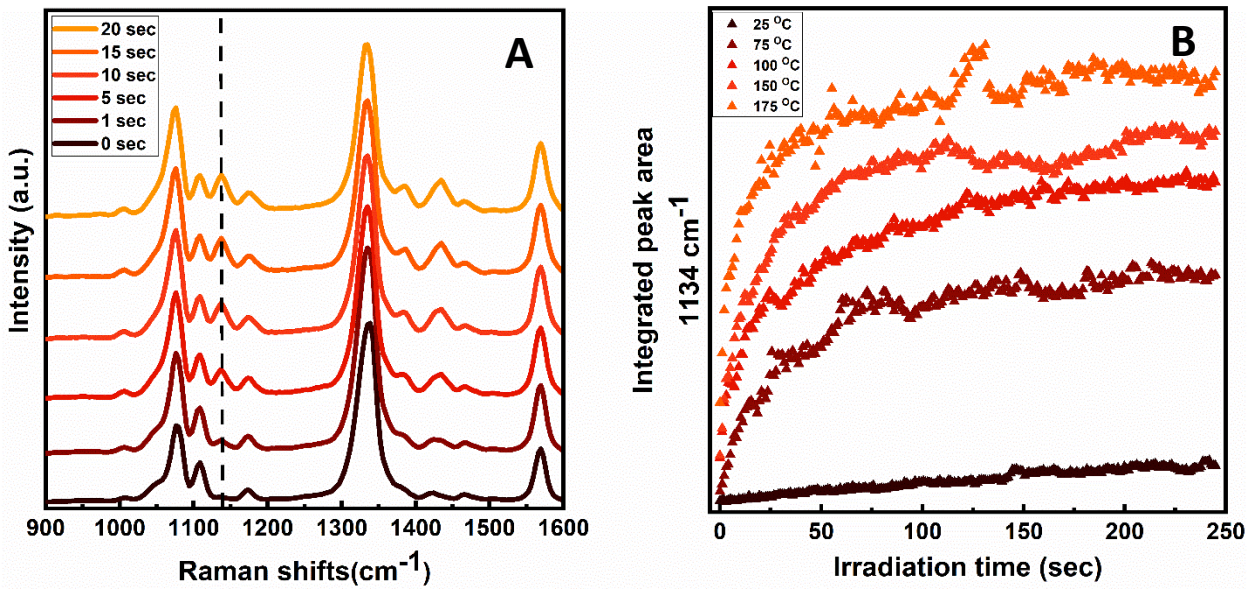

Figure 5.5. Time-dependent SERS performance of the reaction showing the time evolution of the main peak (dashed line) of the product DMAB (A), and its dynamic behavior at different operating temperatures (B).

In paper B, the reaction was performed under different temperatures, while the plasmonic heating effect is minimized by applying very low laser intensity. In this way, we mimicked the light induced heating effect by external heating. Furthermore, to display the reaction performance with the temperature, the area under the peak at 1134 cm^{-1} is integrated to show the amount of DMAB formed over time under different operating temperatures. As shown in figure 5.5B, the amount of DMAB increases as the operating temperature increases compared to the reaction performance at room temperature, showing that the reaction rate is influenced by the operating temperature. This suggests that the reaction indeed benefits from the high temperature generated by the plasmonic heating effect and that such dimerization reaction is driven by the thermal mechanism.

Indeed, Kwan Kim and co-workers have measured SERS spectra of 4-NTP adsorbed on silver nanoparticle-substrate at liquid nitrogen temperature (77 K).[130] The authors showed that the hot electrons were efficiently generated at this temperature while they did not observe any reaction signatures implying the importance of the heat for the reaction. Moreover, Golubev and co-workers have proposed the thermal mechanism triggered by the

plasmonic heating effect to be the driving force of the dimerization of 4-nitrothiophenol (4-NTP).[152] To end this controversy, we performed several temperature-dependent SERS spectra of 4-NTP adsorbed on gold nanoflowers, where the temperature was increased gradually in the range of 25-200 ^{o}C. It is worth to mention that the light was used here to probe the sample with very low laser power and short integration time (0.5 mW and 1 sec) to mimic the dark environment (no probabilities for photo-driven reactions). Concisely, no DMAB Raman peaks were observed in the dark environment regardless of the high temperature. Increasing the temperature was found to enhance the DMAB Raman peaks under illuminating the sample with constant laser intensity. It is important to note that increasing the temperature beyond 473 K used in paper B evaporates the 4-NTP molecules and only spectral noises can be detected. Moreover, the reaction was not observed in the absence of the gold nanoflowers regardless the high light intensity. Therefore, we can conclude that the reaction is mainly initiated by the photons needed for the plasmon excitation of the nanoparticles, while the reaction rate is enhanced by the plasmon-induced heat.

Additionally, the dependence of the reaction on the light intensity was checked, where the spots with a similar field enhancement have been hit with similar number of photons as shown in figure 5.6. In other words, we used different light intensities to irradiate the spots over different time so that the total number of photons are similar for all of the spots. Interestingly, the spots irradiated with low light intensity (0.01% of the laser power) showed the absence of the product DMAB even after irradiation for 60 minutes. In contrast, increasing the light intensity (1% of the laser power) resulted in the formation of well-resolved DMAB peaks after one second, although the same number of integral photons would be only reached after 30 seconds. This experiment shows the non-linearity of the reaction, where the reaction is driven as a result of the collective action of the photons which keep the crystal lattice and the adsorbate hot for the subsequent photons as well as for the subsequent energetic electron. However, a systematic study of the intensity dependence could not be performed owing to the non-homogeneity of the hot spots and therefore the field enhancement.

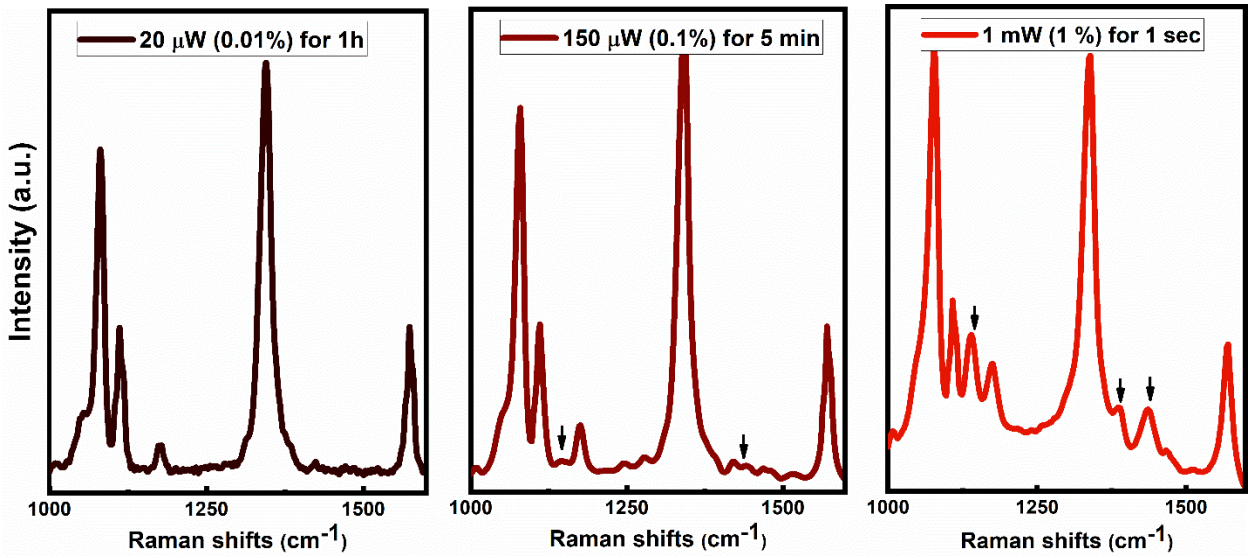

Figure 5.6. SERS spectra of 4-NTP adsorbed on gold nanoflowers irradiated with different laser intensities for different time.

Now, it is clear that the dimerization reaction of 4-NTP is plasmonically driven, where both the energetic electron and the plasmonic heating contribute to the reaction. However, heating by plasmonic NPs is different from the conventional macroscopic heating.[13] Plasmonic heating is highly confined to a nanometric volume, while the conventional heating distributes the temperature of the whole sample homogenously. Therefore, unlike the conventional macroscopic heating, heating by plasmonic NPs enables the formation of certain products at specific locations down to the nanometer scale. The reason behind this can be attributed to the difference in the heating and cooling dynamics over different heated areas, where the dynamics are thought to be enhanced over small areas. In paper A, we studied our model reaction with the primary aim of scaling up the nanoplasmonic catalysis, where an external laser was tuned to irradiate spots with different sizes and the reaction was then probed by a conventional Raman microscope. As shown in figure 5.7, Raman spectra taken from spots irradiated through the 30 and 50 mm focusing lenses (70 and 115 μm spots sizes) seem to be more typical with DMAB Raman peaks being observed. On the other hand, Raman spectra taken from spots irradiated through the 75 and 100 mm lenses (175 and 230 μm) seem to originate from molten NPs with only the Raman peak of

the silicon substrate being observed. This is confirmed by SEM images. This might show, on one hand, the advantages of the nanoplasmonics for chemistry as driven by the fast heat dissipation rate, where the small spots display a fast heating and cooling dynamics and therefore, enabling formation of DMAB molecules. The large spots display slow dynamics with heat being trapped in the substrate for much longer time, which results in melting of the NTs. On the other hand, this finding shows the challenges of scalling up the plasmonic catalysis, where a certain light intensity is needed and a high temperature should be simultaneously dissipated.

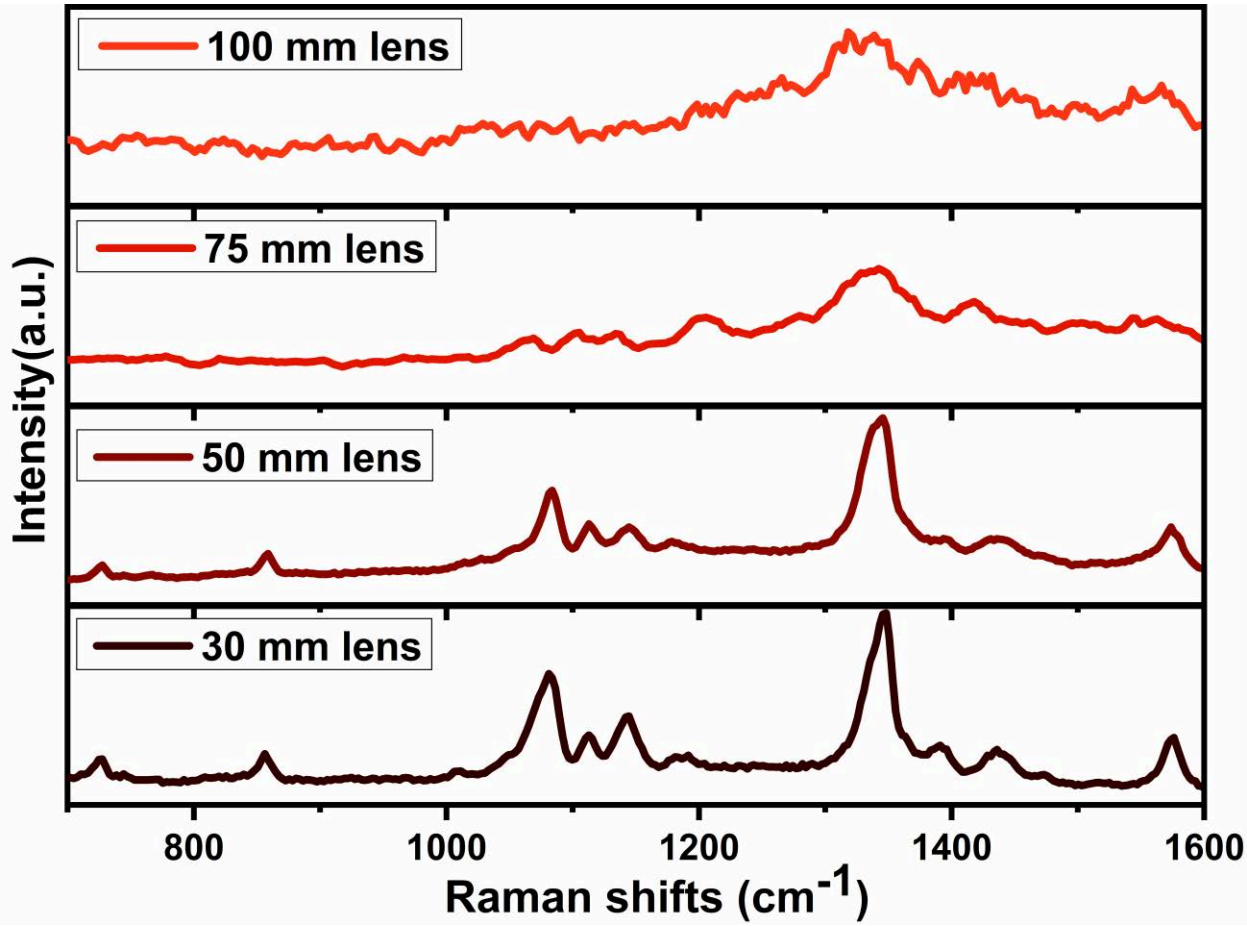

Figure 5.7. SERS spectra of 4-NTP adsorbed on gold NTs irradiated with approximately same intensity throught different spot sizes.

Finally in paper A, X-ray measurements were performed to measure the temperature over spots with different sizes. Interestingly, the temperature measured over large spot (500

μm) increased very significantly reaching 100 K after irradiating with a laser intensity of approximately 10 KW/cm^2, indicating a very low rate of cooling. On the other hand, the temperature detected over small spot (100 μm) displayed an increase of 70 K after irradiating the spot with a laser intensity of approximately 200 KW/cm^2, indicating a fast cooling dynamics over small spots as suggested by the 3D thermal transport. These experiments confirm the important role of the heat dissipation in the nanoplasmonics that has to be taken into account. As an example, we found that the gold NTs deposited on a glass substrate melted upon irradiation with a lower laser power as compared to those deposited on silicon substrate. The reason for that can be explained in terms of the heat dissipation, where the glass substrate is not a good thermal conductor compared to the silicon substrate. This assumption was evidenced by X-ray measurements being performed on gold NTs deposited on glass and silicon substrates. As expected, the particles deposited on the glass substrate displayed a higher temperature (>120 K) under irradiation with nearly 2 W compared to the particles deposited on the silicon substrate, which displayed a temperature of nearly 100 K under irradiation with 15 W laser power. Overall, we have shown that the in situ-generated heat enhances the reaction dynamics. However, this heat needs to be quickly dissipated from the reaction substrate.

5.3 Unpublished work

During our measurement, we observed that the reaction depends on the light intensity, where the reaction seems to proceed above a certain light intensity threshold. In attempts to describe this behavior, I measured several SERS spectra after irradiating the sample with certain laser powers seeking the signature of the reaction product DMAB. Figure 5.8, shows the measured SERS spectra after irradiating the same sample spot with different laser powers (1- 60 mW) for fixed exposure time (5 minutes). As shown, the spectra taken from the sample being irradiated with laser powers of 1- 4 mW did not show any formation of the DMAB product. The reaction started to occur using a laser power of 5 mW as evidenced by the observation of relative small peaks of the DMAB molecules. Increasing the laser power gradually increases the signal intesity of the reaction product. It is worth noting that the use of extremly high powers (80 and 100 mW) resulted in evaporation of the molecules, showing a relatively low Raman signal. This can be attributed to the laser-induced heating, which could be high enough to initiate a dissociation reaction of the 4-NTP by breaking the Au-S bond. Overall, these results might suggest that the reaction requires a threshold of the light intensity to initiate the dimerization process.

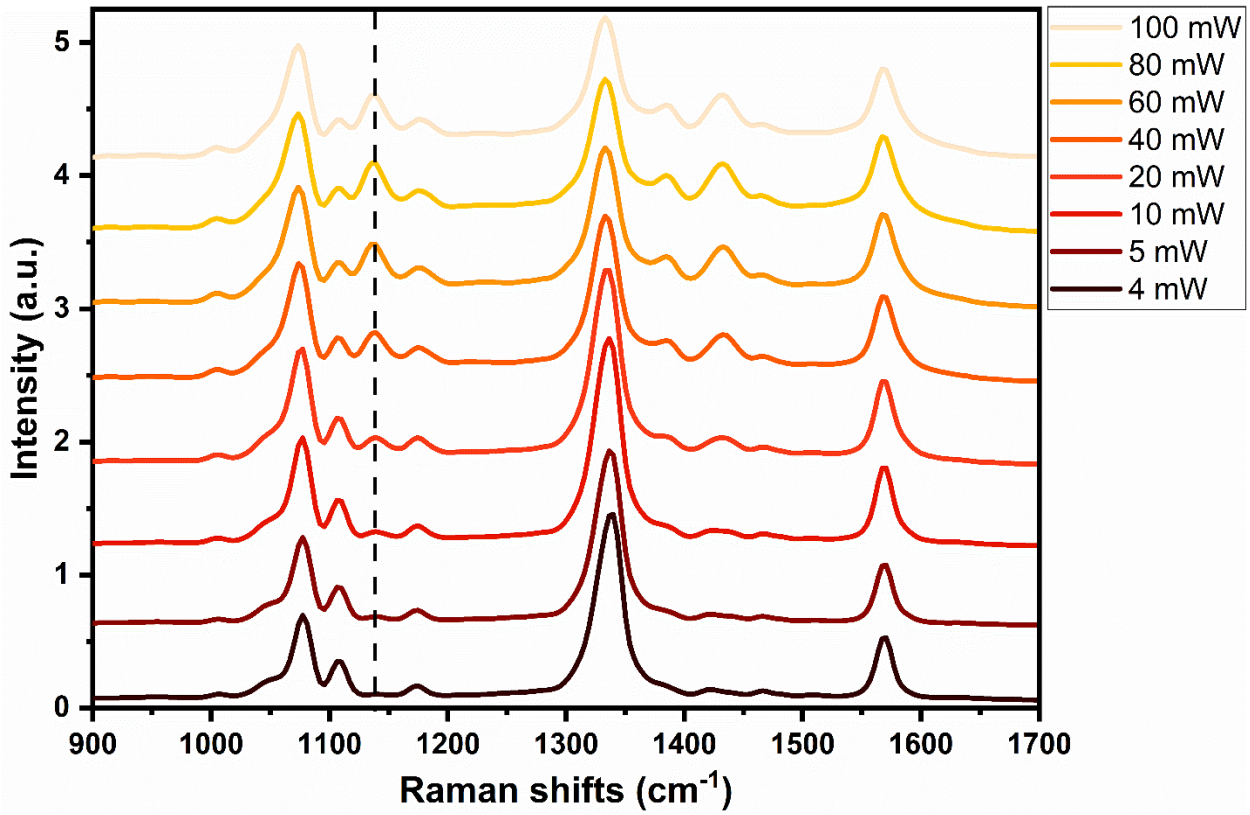

Figure 5.8. SERS spectra of 4-NTP molecules adsorbed on gold nanoflowers showing the intesity dependence performance of their chemical transformation. The spectra are measured using a laser power of 1 mW for 5 seconds as the integration time after irradiating the sample with the indicated power for 5 minutes.

On the other hand, as previously mentioned, the SERS enhancement is particularly strong in areas called "hot spots", e.g., in nano-sized gaps between the plasmonic particles or at nano-tips with high aspect ratios. Therefore, SERS experiments are often performed on a solid substrate, where the hot spots are generated from the aggregation of the particles or engineered by lithography. On the contrary, several applications require the measurements to be performed in an aqueous solution. For example, the ultrafast spectroscopy requires a fresh sample spot each measurement since the ultrafast laser could melt the particles.[155,156] The photothermal cancer therapy as well as the bioimaging require the injection of the sample into the biological fluids,[157,158] therefore, SERS investigations in solution are of special interest. I recently used SERS to show the performance of the gold nanostars prepared with different surfactants dispersed in an aqueous solution. The thiolated

molecules such as the 4-nitrothiophenol molecules (4-NTP) were used as a model probe in SERS application, owing to their high affinity to the metal particles. The particle solution was mixed with 1 mM of the 4-NTP and trapped in a closed glass vial to avoid its evaporation during the light irradiation.

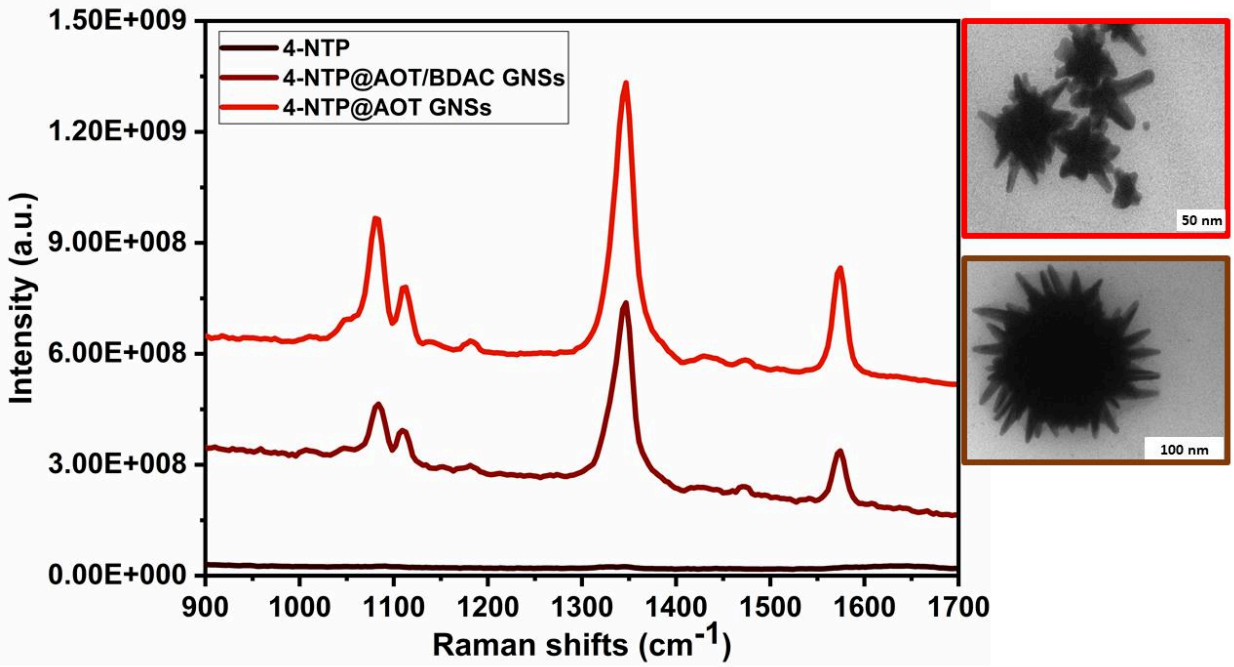

Figure 5.9 Raman spectra of 4-NTP molecules dissolved in an aqueous solution in presence (brown and red spectra) and in absence (black) of the gold nanostars.

Figure 5.9 shows the SERS performance of the gold nanostars prepared with different surfactants (e.g AOT and AOT/BDAC mixture). The SERS spectra are dominated by the main three Raman peaks of the 4-NTP at 1077, 1332, and 1575 cm^{-1}, assigned to the C-H bending, NO_2, and the C=C stretching modes, respectively. The SERS spectra of the prepared gold stars (red and brown spectra)are further compared with the Raman spectrum of the 4-NTP at a ten times higher concentration (black spectrum) as shown. Both types of the gold nanostars displayed a well-resolved Raman signature of the 4-NTP, whereas the Raman spectrum of 4-NTP without the gold stars displayed a very weak signal showing the direct influence of SERS.

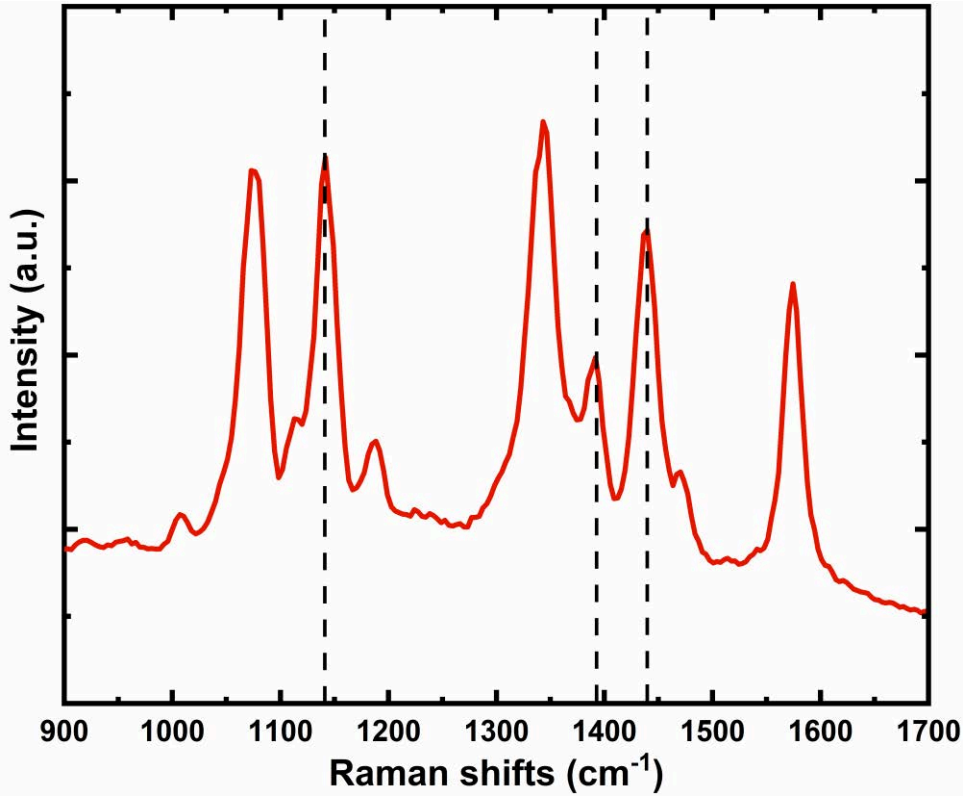

Figure 5.10 Raman spectra of 4-NTP molecules dissolved in an aqueous solution in presence of the AOT gold nanostars showing the presence of plasmonically generated DMAB product.

To give an estimation of the enhancement factor, the intensity of the strongest vibrational mode (NO_2) of the 4-NTP is further compared according to the following formula;

$$EF = \frac{I_{SERS}}{I_{Raman}} \cdot \frac{C_{Raman}}{C_{SERS}} \tag{5.2}$$

where I_{SERS} and I_{Raman} are the intensities of the NO_2 vibrational mode (vibrational mode at 1332 cm^{-1}) of the 4-NTP molecule in presence and absence of the gold nanostars, respectively. C_{SERS} and C_{Raman} are the concentrations of the 4-NTP solution in presence and absence of the gold particles, respectively. The enhancement factors were estimated to be $1.5 \cdot 10^3$ and $9.5 \cdot 10^2$ for the AOT (red spectrum) and AOT/BDAC-coated gold nanostars (brown spectrum), respectively. Generally, the gold nanostars are shown to be good

candidates for the signal enhancement owing to their long nano-tips. However, the difference in the signal enhancement could be attributed to their plasmon resonance, where the AOT/gold stars exhibit a plasmon band located more in resonance with the excitation wavelength as compared to the mixed AOT/BDAC/gold stars. Moreover, the SERS signal seems to be stable and reproducible over several measurements. The reproducibility of the SERS spectra was measured after refreshing the solution several times before each measurement, confirming the homogeneity of the hot spots as well as the dispersity of the particles. Therefore, we believe that our gold nanostars might be useful for several applications.

Finally, I reproduced the reaction in an aqueous solution, where the 4-NTP molecules are dissolved in the aqueous dispersion of the AOT/gold nanostars. The DMAB Raman peaks are observed at 1134, 138, and 1434 cm^{-1} as shown in figure 5.10 (marked with dashed lines). This is an important experiment showing that the reaction can also proceed in the liquid state. This opens the way for further work using ultrafast spectroscopy to study the reaction mechanism in femto- and picosecond time scale. In ultrafast spectroscopy, a flow of the reaction solution might be needed as a strategy to aviod melting of the metal nanoparticle by the ultrafast laser as seen in paper G.

Chapter 6. Summary and future perspectives

6.1. Summary

This dissertation is set out to show the fundamentals of the plasmon-induced chemical reactions in plasmonic nanoparticles-adsorbate systems. Raman spectroscopy was used as the main technique among other experimental tools, for being able to probe the vibrational modes of the molecules adsorbed on the surface of the plasmonic gold nanoparticles. The anti-Stokes part of the Raman spectrum is typically weak and often ignored in the data analysis compared to the intense Stokes part. However, in the thesis, the anti-Stokes to Stokes ratio has been used to determine the high temperature generated during the resonant excitation of the plasmonic nanoparticles, which influences the reaction rate.

SERS has shown a high efficiency in probing several analytes, where the analyte is adsorbed on the surface of the plasmonic nanoparticles. The SERS signal enhancements were shown to be influenced by many factors. For instance, existence of a roughened particle's surface and a resonant excitation wavelength have produced a high signal enhancement of the 4-NTP and R6G molecules, enabling monitoring of possible chemical transformation of the adsorbed molecules in real time. Surface reactions in this sense have been commonly referred to as "plasmonic reactions". The driving force of the reaction is mainly based on the resonant interaction between the incident photons and the oscillations of the free electrons of the metallic nanoparticles, which commonly refers to the localized surface plasmon resonance (LSPR). The decay of the LSPR would lead to the formation of energetic charge/carriers and high local temperature, which might induce chemical reactions of the adsorbed molecules.

In this thesis, the plasmon-driven dimerization of 4-NTP was used as a model reaction monitored and studied using SERS, where the 4-NTP molecules are chemically adsorbed on the gold nanoparticles via the covalent Au-S bond. Systematic experiments have been performed so that the intensity of the incident light and the operating temperature are controlled. On the one hand, within the mechanistic frame, the reaction was found to be only photo-driven since the photons were necessary to initiate the reaction. On the other

hand, conventional heating in a dark environment has failed to initiate the reaction, whereas heating under continuous irradiation of the sample was found to enhance the reaction rate following the Arrhenius behavior. In our experiments, we mimicked the plasmon-heating effect with an external heating under very low excitation powers where this effect is minimized. Unlike reported in the literature , our results show the importance of the light for initiating the reaction and the plasmon-heating for enhancing the reaction rate.

The local heating of the nanoparticles induced by the light is proved by X-ray and Raman spectroscopy measured in a reactive environment. A temperature increase of the gold nanotriangles of about 100 K has been measured by X-ray under continuous irradiation with CW laser, which was confirmed by measuring the intensity of the anti-Stokes background. The intensity ratio between the Stokes and the anti-Stokes signal have been applied to measure the molecular temperature of the adsorbed molecules. The temperature of the DMAB molecules was found to be higher than that of the 4-NTP molecules, suggesting that the reaction only proceeds at the hot spots. Furthermore, the temperature of the particles was found to be lower than the vibrational temperature of the adsorbed molecules, owing to the thermal equilibrium between the particles and the substrate phonons.

On the other hand, we took the first step towards scaling up the plasmonic catalysis. By scaling up the irradiated area, our experiments showed the importance of heat dissipation from the reaction substrate as a crucial factor. The dynamics of the heating and cooling on small irradiated spots has been shown to be different from those on large spots. The reaction was only observed on the small spots since the heat is efficiently dissipated from the substrate in a 3D way. In contrast, the large spots irradiated with approximately the same light intensity have resulted in melting of the metal NPs , since the heat is dissipated in a less efficient 1D way. Moreover, the silicon substrates have been shown to be more suited for the reaction as compared to the microscopic glass, owing to their high thermal conductivity. Conclusively, the high temperature resulting from light/particle interaction needs to be quickly dissipated from the reaction substrate, otherwise, the reaction platform (plasmonic particle) is melted, and the adsorbed reactants are destructed.

6.2. Future perspectives

This dissertation showed the fundamental mechanistic concepts of plasmonic chemistry and the factors that could influence the plasmonic reactions. Performing a systematic study for the 4-NTP dimerization reaction has now cleared the picture of the photo-driven nature of the reaction and the importance of the plasmonic heating. Based on the findings reported in this dissertation for such reaction (e.g the light intensity, spot size, and nanoscale heating), we can move forward with the time resolution of the experiments to enable monitoring possible reaction intermediates. This would allow studying the reaction mechanism and the reaction pathway by ultrafast laser spectroscopy.

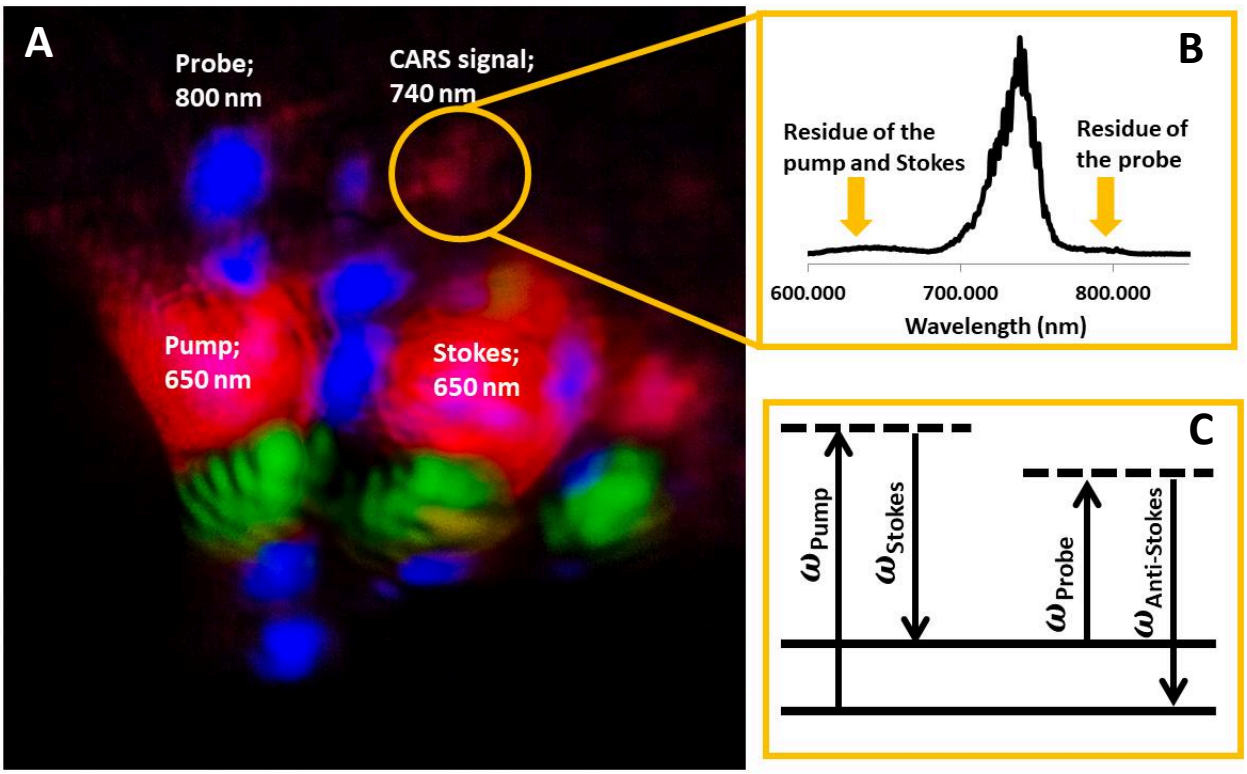

Figure 6.1. Photograph of the siganl outcomes from the coherent anti-Stokes Raman scattering set up (A) showing the anit-Stokes signal of the BBO crystal (B). A presentation of CARS energy diagram (C) .

Indeed, a coherent anti-stokes Raman scattering (CARS) setup was built in a box-CARS geometry, where the three incident beams were fixed to represent three corners of a box, while the beam in the fourth corner is generated from the sample as the anti-stokes Raman signal. CARS is a nonlinear four-wave mixing process used as a way to enhance the weak spontaneous Raman signal. In the CARS process, the pump and the Stokes beams are used to drive a coherent vibrational excitation of the molecular system. In contrast, a coherent anti-Stokes beam is generated by applying the probe beam as shown in figure (6.1C). In this way, the time resolution may be enhanced to the picosecond time scale, while the spectral resolution was achieved by detecting only the isolated Raman signal. In our CARS setup, I used two spectrally broadband laser beams centered at 650 nm as the pump/Stokes pair to excite the vibrational modes of the 4-NTP molecule. A narrow band beam was then used as the probe beam (~ 800 nm). It is important to mention that the spectral width of the probe beam should be equal to or less than the Raman line width of the probed molecule. A preliminary experiment has shown the presence of the anti-Stoke signal from the BBO crystal at 740 nm as shown in figure (6.1B). As seen, the interference of probe beam to the signal was avoided using a short-pass filter, while the pump/stokes pair is easily cut by a normal blocker since it is well isolated from the signal as shown in figure (6.1A). Finally, incorporation of the surface-enhanced Raman concepts into the setup is required for driving the chemical reaction and enhancement of the signal.

Bibliography

(1) Zhu, S.; Wang, D. Photocatalysis: Basic Principles, Diverse Forms of Implementations and Emerging Scientific Opportunities. *Adv. Energy Mater.* **2017**, *7*, 1700841, DOI: 10.1002/aenm.201700841.

(2) Remiro-Buenamañana, S.; García, H. Photoassisted CO 2 Conversion to Fuels. *ChemCatChem* **2018**, *110*, 288, DOI: 10.1002/cctc.201801409.

(3) Wang, Y.; Wei, Y.; Song, W.; Chen, C.; Zhao, J. Photocatalytic Hydrodehalogenation for the Removal of Halogenated Aromatic Contaminants. *ChemCatChem* **2018**, *822*, 83, DOI: 10.1002/cctc.201801222.

(4) Zhang, X.; Ke, X.; Yao, J. Recent development of plasmon-mediated photocatalysts and their potential in selectivity regulation. *J. Mater. Chem. A* **2018**, *6*, 1941–1966, DOI: 10.1039/C7TA10375A.

(5) Schneider, J.; Matsuoka, M.; Takeuchi, M.; Zhang, J.; Horiuchi, Y.; Anpo, M.; Bahnemann, D. W. Understanding TiO2 photocatalysis: mechanisms and materials. *Chemical reviews* **2014**, *114*, 9919–9986, DOI: 10.1021/cr5001892.

(6) Shaik, F.; Peer, I.; Jain, P. K.; Amirav, L. Plasmon-Enhanced Multicarrier Photocatalysis. *Nano letters* **2018**, *18*, 4370–4376, DOI: 10.1021/acs.nanolett.8b01392.

(7) Wang, P.; Huang, B.; Dai, Y.; Whangbo, M.-H. Plasmonic photocatalysts: harvesting visible light with noble metal nanoparticles. *Physical chemistry chemical physics : PCCP* **2012**, *14*, 9813–9825, DOI: 10.1039/c2cp40823f.

(8) Zhang, L.; Ding, N.; Lou, L.; Iwasaki, K.; Wu, H.; Luo, Y.; Li, D.; Nakata, K.; Fujishima, A.; Meng, Q. Localized Surface Plasmon Resonance Enhanced Photocatalytic Hydrogen Evolution via Pt@Au NRs/C 3 N 4 Nanotubes under Visible-Light Irradiation. *Adv. Funct. Mater.* **2018**, *8*, 1806774, DOI: 10.1002/adfm.201806774.

(9) Xiao, Y.; Chen, M.; Zhang, M. Improved Utilization of Sunlight Through the Incidence Dependence of the Photonic Stop Band: A g-C 3 N 4 -Embedded Fluorine-Doped Tin Oxide (FTO) Photonic Crystal Film. *ChemPhotoChem* **2018**, *38*, 253, DOI: 10.1002/cptc.201800198.

(10) Zrimsek, A. B.; Wong, N. L.; van Duyne, R. P. Single Molecule Surface-Enhanced Raman Spectroscopy: A Critical Analysis of the Bianalyte versus Isotopologue Proof. *J. Phys. Chem. C* **2016**, *120*, 5133–5142, DOI: 10.1021/acs.jpcc.6b00606.

(11) Abadeer, N. S.; Murphy, C. J. Recent Progress in Cancer Thermal Therapy Using Gold Nanoparticles. *J. Phys. Chem. C* **2016**, *120*, 4691–4716, DOI: 10.1021/acs.jpcc.5b11232.

(12) Jørgensen, J. T.; Norregaard, K.; Tian, P.; Bendix, P. M.; Kjaer, A.; Oddershede, L. B. Single Particle and PET-based Platform for Identifying Optimal Plasmonic Nano-Heaters for Photothermal Cancer Therapy. *Scientific reports* **2016**, *6*, 30076, DOI: 10.1038/srep30076.

(13) Baffou, G.; Quidant, R. Nanoplasmonics for chemistry. *Chemical Society reviews* **2014**, *43*, 3898–3907, DOI: 10.1039/c3cs60364d.

(14) Tatsuma, T.; Nishi, H.; Ishida, T. Plasmon-induced charge separation: chemistry and wide applications. *Chemical Science* **2017**, *8*, 3325–3337, DOI: 10.1039/c7sc00031f.

(15) Grzelczak, M.; Liz-Marzán, L. M. Colloidal nanoplasmonics: from building blocks to sensing devices. *Langmuir : the ACS journal of surfaces and colloids* **2013**, *29*, 4652–4663, DOI: 10.1021/la4001544.

(16) Stockman, M. I. Applied optics. Nanoplasmonic sensing and detection. *Science (New York, N.Y.)* **2015**, *348*, 287–288, DOI: 10.1126/science.aaa6805.
(17) Araújo, A.; Caro, C.; Mendes, M. J.; Nunes, D.; Fortunato, E.; Franco, R.; Águas, H.; Martins, R. Highly efficient nanoplasmonic SERS on cardboard packaging substrates. *Nanotechnology* **2014**, *25*, 415202, DOI: 10.1088/0957-4484/25/41/415202.
(18) Adleman, J. R.; Boyd, D. A.; Goodwin, D. G.; Psaltis, D. Heterogenous catalysis mediated by plasmon heating. *Nano letters* **2009**, *9*, 4417–4423, DOI: 10.1021/nl902711n.
(19) Christopher, P.; Xin, H.; Linic, S. Visible-light-enhanced catalytic oxidation reactions on plasmonic silver nanostructures. *Nature chemistry* **2011**, *3*, 467–472, DOI: 10.1038/nchem.1032.
(20) Climent, M. J.; Corma, A.; Iborra, S.; Sabater, M. J. Heterogeneous Catalysis for Tandem Reactions. *ACS Catal.* **2014**, *4*, 870–891, DOI: 10.1021/cs401052k.
(21) Zhang, Z.; Gernert, U.; Gerhardt, R. F.; Höhn, E.-M.; Belder, D.; Kneipp, J. Catalysis by Metal Nanoparticles in a Plug-In Optofluidic Platform: Redox Reactions of p- Nitrobenzenethiol and p-Aminothiophenol. *ACS Catal.* **2018**, *8*, 2443–2449, DOI: 10.1021/acscatal.8b00101.
(22) Yu, R.; Mazumder, P.; Borrelli, N. F.; Carrilero, A.; Ghosh, D. S.; Maniyara, R. A.; Baker, D.; García de Abajo, F. J.; Pruneri, V. Structural Coloring of Glass Using Dewetted Nanoparticles and Ultrathin Films of Metals. *ACS photonics* **2016**, *3*, 1194–1201, DOI: 10.1021/acsphotonics.6b00090.
(23) Lambertson, R. H.; Lacy, C. A.; Gillespie, S. D.; Leopold, M. C.; Coppage, R. H. Gold nanoparticle colorants as traditional ceramic glaze alternatives. *J Am Ceram Soc* **2017**, *100*, 3943–3951, DOI: 10.1111/jace.14928.
(24) Schaming, D.; Remita, H. Nanotechnology: from the ancient time to nowadays. *Found Chem* **2015**, *17*, 187–205, DOI: 10.1007/s10698-015-9235-y.
(25) Faraday, M. The Bakerian Lecture: Experimental Relations of Gold (and Other Metals) to Light. *Philosophical Transactions of the Royal Society of London* **1857**, *147*, 145–181, DOI: 10.1098/rstl.1857.0011.
(26) Reddy, V. Gold Nanoparticles: Synthesis and Applications. *Synlett* **2006**, *2006*, 1791–1792, DOI: 10.1055/s-2006-944219.
(27) *The mie theory: Basics and applications;* Hergert, W., Ed.; Springer Series in Optical Sciences 169; Springer: Berlin, 2012.
(28) Wriedt, T. Mie Theory: A Review. In *The mie theory: Basics and applications*; Hergert, W., Ed.; Springer Series in Optical Sciences 169; Springer: Berlin, 2012; pp 53–71.
(29) Mie, G. Beiträge zur Optik trüber Medien, speziell kolloidaler Metallösungen. *Ann. Phys.* **1908**, *330*, 377–445, DOI: 10.1002/andp.19083300302.
(30) Yu, K.; Kelly, K. L.; Sakai, N.; Tatsuma, T. Morphologies and surface plasmon resonance properties of monodisperse bumpy gold nanoparticles. *Langmuir* **2008**, *24*, 5849–5854, DOI: 10.1021/la703903b.
(31) Tanabe, I.; Tatsuma, T. Plasmonic manipulation of color and morphology of single silver nanospheres. *Nano letters* **2012**, *12*, 5418–5421, DOI: 10.1021/nl302919n.
(32) Jiang, G.; Baba, A.; Ikarashi, H.; Xu, R.; Locklin, J.; Kashif, K. R.; Shinbo, K.; Kato, K.; Kaneko, F.; Advincula, R. Signal Enhancement and Tuning of Surface Plasmon Resonance in Au Nanoparticle/Polyelectrolyte Ultrathin Films. *J. Phys. Chem. C* **2007**, *111*, 18687–18694, DOI: 10.1021/jp075986e.

(33) Mitsuishi, M.; Koishikawa, Y.; Tanaka, H.; Sato, E.; Mikayama, T.; Matsui, J.; Miyashita, T. Nanoscale actuation of thermoreversible polymer brushes coupled with localized surface plasmon resonance of gold nanoparticles. *Langmuir* **2007**, *23*, 7472–7474, DOI: 10.1021/la701215t.

(34) Agrawal, A.; Cho, S. H.; Zandi, O.; Ghosh, S.; Johns, R. W.; Milliron, D. J. Localized Surface Plasmon Resonance in Semiconductor Nanocrystals. *Chemical reviews* **2018**, *118*, 3121–3207, DOI: 10.1021/acs.chemrev.7b00613.

(35) Petryayeva, E.; Krull, U. J. Localized surface plasmon resonance: Nanostructures, bioassays and biosensing--a review. *Analytica chimica acta* **2011**, *706*, 8–24, DOI: 10.1016/j.aca.2011.08.020.

(36) Kale, M. J.; Avanesian, T.; Christopher, P. Direct Photocatalysis by Plasmonic Nanostructures. *ACS Catal.* **2013**, *4*, 116–128, DOI: 10.1021/cs400993w.

(37) Keller, E. L.; Brandt, N. C.; Cassabaum, A. A.; Frontiera, R. R. Ultrafast surface-enhanced Raman spectroscopy. *The Analyst* **2015**, *140*, 4922–4931, DOI: 10.1039/c5an00869g.

(38) Miranda-Andrades, J. R.; Pérez-Gramatges, A.; Pandoli, O.; Romani, E. C.; Aucélio, R. Q.; da Silva, A. R. Spherical gold nanoparticles and gold nanorods for the determination of gentamicin. *Spectrochimica acta. Part A, Molecular and biomolecular spectroscopy* **2017**, *172*, 126–134, DOI: 10.1016/j.saa.2016.04.023.

(39) Xia, H.; Bai, S.; Hartmann, J.; Wang, D. Synthesis of monodisperse quasi-spherical gold nanoparticles in water via silver(I)-assisted citrate reduction. *Langmuir : the ACS journal of surfaces and colloids* **2010**, *26*, 3585–3589, DOI: 10.1021/la902987w.

(40) Kozek, K. A.; Kozek, K. M.; Wu, W.-C.; Mishra, S. R.; Tracy, J. B. Large-Scale Synthesis of Gold Nanorods through Continuous Secondary Growth. *Chem. Mater.* **2013**, *25,* DOI: 10.1021/cm402277y.

(41) Nikoobakht, B.; El-Sayed, M. A. Preparation and Growth Mechanism of Gold Nanorods (NRs) Using Seed-Mediated Growth Method. *Chem. Mater.* **2003**, *15*, 1957–1962, DOI: 10.1021/cm020732l.

(42) Stete, F.; Koopman, W.; Bargheer, M. Signatures of Strong Coupling on Nanoparticles: Revealing Absorption Anticrossing by Tuning the Dielectric Environment. *ACS photonics* **2017**, *4*, 1669–1676, DOI: 10.1021/acsphotonics.7b00113.

(43) Long, R.; Li, Y.; Song, L.; Xiong, Y. Coupling Solar Energy into Reactions: Materials Design for Surface Plasmon-Mediated Catalysis. *Small (Weinheim an der Bergstrasse, Germany)* **2015**, *11*, 3873–3889, DOI: 10.1002/smll.201403777.

(44) Linic, S.; Aslam, U.; Boerigter, C.; Morabito, M. Photochemical transformations on plasmonic metal nanoparticles. *Nature materials* **2015**, *14*, 567–576, DOI: 10.1038/nmat4281.

(45) Kazuma, E.; Jung, J.; Ueba, H.; Trenary, M.; Kim, Y. Real-space and real-time observation of a plasmon-induced chemical reaction of a single molecule. *Science (New York, N.Y.)* **2018**, *360*, 521–526, DOI: 10.1126/science.aao0872.

(46) Fukui, K.; Yonezawa, T.; Shingu, H. A Molecular Orbital Theory of Reactivity in Aromatic Hydrocarbons. *The Journal of Chemical Physics* **1952**, *20*, 722–725, DOI: 10.1063/1.1700523.

(47) Fukui, K. The Role of Frontier Orbitals in Chemical Reactions (Nobel Lecture). *Angew. Chem. Int. Ed. Engl.* **1982**, *21*, 801–809, DOI: 10.1002/anie.198208013.

(48) Cortés, E. Efficiency and Bond Selectivity in Plasmon-Induced Photochemistry. *Advanced Optical Materials* **2017**, *5*, 1700191, DOI: 10.1002/adom.201700191.

(49) Mukherjee, S.; Libisch, F.; Large, N.; Neumann, O.; Brown, L. V.; Cheng, J.; Lassiter, J. B.; Carter, E. A.; Nordlander, P.; Halas, N. J. Hot electrons do the impossible: Plasmon-induced dissociation of H2 on Au. *Nano letters* **2013**, *13*, 240–247, DOI: 10.1021/nl303940z.

(50) Mukherjee, S.; Zhou, L.; Goodman, A. M.; Large, N.; Ayala-Orozco, C.; Zhang, Y.; Nordlander, P.; Halas, N. J. Hot-electron-induced dissociation of H2 on gold nanoparticles supported on SiO2. *J. Am. Chem. Soc.* **2014**, *136*, 64–67, DOI: 10.1021/ja411017b.

(51) Zhang, Y.; Xiao, Q.; Bao, Y.; Zhang, Y.; Bottle, S.; Sarina, S.; Zhaorigetu, B.; Zhu, H. Direct Photocatalytic Conversion of Aldehydes to Esters Using Supported Gold Nanoparticles under Visible Light Irradiation at Room Temperature. *J. Phys. Chem. C* **2014**, *118*, 19062–19069, DOI: 10.1021/jp505552v.

(52) Hogan, N. J.; Urban, A. S.; Ayala-Orozco, C.; Pimpinelli, A.; Nordlander, P.; Halas, N. J. Nanoparticles heat through light localization. *Nano letters* **2014**, *14*, 4640–4645, DOI: 10.1021/nl5016975.

(53) Fang, Z.; Zhen, Y.-R.; Neumann, O.; Polman, A.; García de Abajo, F. J.; Nordlander, P.; Halas, N. J. Evolution of light-induced vapor generation at a liquid-immersed metallic nanoparticle. *Nano letters* **2013**, *13*, 1736–1742, DOI: 10.1021/nl4003238.

(54) Fasciani, C.; Bueno Alejo, C. J.; Grenier, M.; Netto-Ferreira, J. C.; Scaiano, J. C. High-temperature organic reactions at room temperature using plasmon excitation: Decomposition of dicumyl peroxide. *Organic letters* **2011**, *13*, 204–207, DOI: 10.1021/ol1026427.

(55) Chen, J.; Wang, D.; Xi, J.; Au, L.; Siekkinen, A.; Warsen, A.; Li, Z.-Y.; Zhang, H.; Xia, Y.; Li, X. Immuno gold nanocages with tailored optical properties for targeted photothermal destruction of cancer cells. *Nano Lett.* **2007**, *7*, 1318–1322, DOI: 10.1021/nl070345g.

(56) Lin, J.-T.; Chiang, Y.-S.; Lin, G.-H.; Lee, H.; Liu, H.-W. In Vitro Photothermal Destruction of Cancer Cells Using Gold Nanorods and Pulsed-Train Near-Infrared Laser. *Journal of Nanomaterials* **2012**, *2012*, 1–6, DOI: 10.1155/2012/861385.

(57) Gao, C.; Lin, W.; Wang, J.; Wang, R.; Wang, J. Principle and Application of Tip-enhanced Raman Scattering. *Plasmonics* **2018**, *13*, 1343–1358, DOI: 10.1007/s11468-017-0638-6.

(58) Latorre, F.; Kupfer, S.; Bocklitz, T.; Kinzel, D.; Trautmann, S.; Gräfe, S.; Deckert, V. Spatial resolution of tip-enhanced Raman spectroscopy - DFT assessment of the chemical effect. *Nanoscale* **2016**, *8*, 10229–10239, DOI: 10.1039/c6nr00093b.

(59) Osawa, M.; Matsuda, N.; Yoshii, K.; Uchida, I. Charge transfer resonance Raman process in surface-enhanced Raman scattering from p-aminothiophenol adsorbed on silver: Herzberg-Teller contribution. *J. Phys. Chem.* **1994**, *98*, 12702–12707, DOI: 10.1021/j100099a038.

(60) Wu, D.-Y.; Liu, X.-M.; Huang, Y.-F.; Ren, B.; Xu, X.; Tian, Z.-Q. Surface Catalytic Coupling Reaction of p -Mercaptoaniline Linking to Silver Nanostructures Responsible for Abnormal SERS Enhancement: A DFT Study. *J. Phys. Chem. C* **2009**, *113*, 18212–18222, DOI: 10.1021/jp9050929.

(61) Merlen, A.; Chaigneau, M.; Coussan, S. Vibrational modes of aminothiophenol: A TERS and DFT study. *Phys. Chem. Chem. Phys.* **2015**, *17*, 19134–19138, DOI: 10.1039/C5CP01579K.

(62) Zhang, Z.; Kinzel, D.; Deckert, V. Photo-Induced or Plasmon-Induced Reaction: Investigation of the Light-Induced Azo-coupling of Amino Groups. *J. Phys. Chem. C* **2016,** DOI: 10.1021/acs.jpcc.6b03233.

(63) Huang, Y.-F.; Zhu, H.-P.; Liu, G.-K.; Wu, D.-Y.; Ren, B.; Tian, Z.-Q. When the signal is not from the original molecule to be detected: Chemical transformation of para-aminothiophenol on Ag during the SERS measurement. *J. Am. Chem. Soc.* **2010**, *132*, 9244–9246, DOI: 10.1021/ja101107z.

(64) Lin, T.-W.; Tasi, T.-T.; Chang, P.-L.; Cheng, H.-Y. Reversible Association of Nitro Compounds with p -Nitrothiophenol Modified on Ag Nanoparticles/Graphene Oxide Nanocomposites through Plasmon Mediated Photochemical Reaction. *ACS Appl. Mater. Interfaces* **2016**, *8*, 8315–8322, DOI: 10.1021/acsami.6b01522.

(65) Zhang, J.; Winget, S. A.; Wu, Y.; Su, D.; Sun, X.; Xie, Z.-X.; Qin, D. Ag@Au Concave Cuboctahedra: A Unique Probe for Monitoring Au-Catalyzed Reduction and Oxidation Reactions by Surface-Enhanced Raman Spectroscopy. *ACS nano* **2016**, *10*, 2607–2616, DOI: 10.1021/acsnano.5b07665.

(66) RAMAN, C. V.; KRISHNAN, K. S. A New Type of Secondary Radiation. *Nature* **1928**, *121*, 501–502, DOI: 10.1038/121501c0.

(67) Ladouceur, H. D.; Tevault, D. E.; Smardzewski, R. R. Surface-enhanced Raman scattering from vapor-deposited copper, silver, and gold. Excitation profiles and temperature dependence. *The Journal of Chemical Physics* **1983**, *78*, 980–985, DOI: 10.1063/1.444802.

(68) Nguyen, T. B.; Thu Vu, T. K.; Nguyen, Q. D.; Nguyen, T. D.; Nguyen, T. A.; Trinh, T. H. Preparation of metal nanoparticles for surface enhanced Raman scattering by laser ablation method. *Adv. Nat. Sci: Nanosci. Nanotechnol.* **2012**, *3*, 25016, DOI: 10.1088/2043-6262/3/2/025016.

(69) Blackie, E. J.; Le Ru, E. C.; Etchegoin, P. G. Single-molecule surface-enhanced Raman spectroscopy of nonresonant molecules. *J. Am. Chem. Soc.* **2009**, *131*, 14466–14472, DOI: 10.1021/ja905319w.

(70) Fleischmann, M.; Hendra, P. J.; McQuillan, A. J. Raman spectra of pyridine adsorbed at a silver electrode. *Chemical Physics Letters* **1974**, *26*, 163–166, DOI: 10.1016/0009-2614(74)85388-1.

(71) Sanchez-Gil, J.; Garcia-Ramos, J.; Mendez, E. Electromagnetic mechanism in surface-enhanced Raman scattering from Gaussian-correlated randomly rough metal substrates. *Optics express* **2002**, *10*, 879–886.

(72) Wang, J.; Li, Y.; Wu, S.; Song, P.; Xia, L. Chemical mechanism of surface-enhanced Raman scattering via charge transfer in fluorenone-Ag complex. *Journal of physics. Condensed matter : an Institute of Physics journal* **2016**, *28*, 214002, DOI: 10.1088/0953-8984/28/21/214002.

(73) Chu, H.; Song, S.; Li, C.; Des Gibson. Surface Enhanced Raman Scattering Substrates Made by Oblique Angle Deposition: Methods and Applications. *Coatings* **2017**, *7*, 26, DOI: 10.3390/coatings7020026.

(74) Lim, J. K.; Joo, S.-W. Excitation-wavelength-dependent charge transfer resonance of bipyridines on silver nanoparticles: Surface-enhanced Raman scattering study. *Surf. Interface Anal.* **2007**, *39*, 684–690, DOI: 10.1002/sia.2577.

(75) Álvarez-Puebla, R. A. Effects of the Excitation Wavelength on the SERS Spectrum. *The journal of physical chemistry letters* **2012**, *3*, 857–866, DOI: 10.1021/jz201625j.

(76) Samanta, A.; Jana, S.; Das, R. K.; Chang, Y.-T. Wavelength and shape dependent SERS study to develop ultrasensitive nanotags for imaging of cancer cells. *RSC Adv.* **2014**, *4*, 12415, DOI: 10.1039/c3ra46208k.

(77) Ye, J.; Hutchison, J. A.; Uji-i, H.; Hofkens, J.; Lagae, L.; Maes, G.; Borghs, G.; van Dorpe, P. Excitation wavelength dependent surface enhanced Raman scattering of 4-aminothiophenol on gold nanorings. *Nanoscale* **2012**, *4*, 1606–1611, DOI: 10.1039/c2nr11805j.

(78) Gu, G. H.; Kim, J.; Kim, L.; Suh, J. S. Optimum Length of Silver Nanorods for Fabrication of Hot Spots. *J. Phys. Chem. C* **2007**, *111*, 7906–7909, DOI: 10.1021/jp070384g.

(79) Maillard, M.; Giorgio, S.; Pileni, M.-P. Tuning the Size of Silver Nanodisks with Similar Aspect Ratios: Synthesis and Optical Properties. *J. Phys. Chem. B* **2003**, *107*, 2466–2470, DOI: 10.1021/jp022357q.
(80) Li, M.; Cushing, S. K.; Zhang, J.; Lankford, J.; Aguilar, Z. P.; Ma, D.; Wu, N. Shape-dependent surface-enhanced Raman scattering in gold-Raman probe-silica sandwiched nanoparticles for biocompatible applications. *Nanotechnology* **2012**, *23*, 115501, DOI: 10.1088/0957-4484/23/11/115501.
(81) Abdallah, T.; El-Brolosy, T. A.; Mohamed, M. B.; Easawi, K.; Negm, S.; Talaat, H. Effect of shape and interstice on surface enhanced Raman scattering (SERS) of molecules adsorbed on gold nanoparticles in the near-dipole and quadrupole regions. *J. Raman Spectrosc.* **2012**, *43*, 1924–1930, DOI: 10.1002/jrs.4131.
(82) Quester, K.; Avalos-Borja, M.; Vilchis-Nestor, A. R.; Camacho-López, M. A.; Castro-Longoria, E. SERS properties of different sized and shaped gold nanoparticles biosynthesized under different environmental conditions by Neurospora crassa extract. *PloS one* **2013**, *8*, e77486, DOI: 10.1371/journal.pone.0077486.
(83) Campion, A.; Ivanecky, J. E.; Child, C. M.; Foster, M. On the Mechanism of Chemical Enhancement in Surface-Enhanced Raman Scattering. *J. Am. Chem. Soc.* **1995**, *117*, 11807–11808, DOI: 10.1021/ja00152a024.
(84) Ko, H.; Singamaneni, S.; Tsukruk, V. V. Nanostructured surfaces and assemblies as SERS media. *Small (Weinheim an der Bergstrasse, Germany)* **2008**, *4*, 1576–1599, DOI: 10.1002/smll.200800337.
(85) Schlücker, S. Surface-enhanced Raman spectroscopy: Concepts and chemical applications. *Angewandte Chemie (International ed. in English)* **2014**, *53*, 4756–4795, DOI: 10.1002/anie.201205748.
(86) Ermushev, A. V.; Mchedlishvili, B. V.; Oleĭnikov, V. A.; Petukhov, A. V. Surface enhancement of local optical fields and the lightning-rod effect. *Quantum Electron.* **1993**, *23*, 435–440, DOI: 10.1070/QE1993v023n05ABEH003090.
(87) Liao, P. F.; Wokaun, A. Lightning rod effect in surface enhanced Raman scattering. *The Journal of Chemical Physics* **1982**, *76*, 751–752, DOI: 10.1063/1.442690.
(88) Grand, J.; La Chapelle, M. L. de; Bijeon, J.-L.; Adam, P.-M.; Vial, A.; Royer, P. Role of localized surface plasmons in surface-enhanced Raman scattering of shape-controlled metallic particles in regular arrays. *Phys. Rev. B* **2005**, *72,* DOI: 10.1103/PhysRevB.72.033407.
(89) Camargo, P. H. C.; Rycenga, M.; Au, L.; Xia, Y. Isolating and probing the hot spot formed between two silver nanocubes. *Angewandte Chemie (International ed. in English)* **2009**, *48*, 2180–2184, DOI: 10.1002/anie.200806139.
(90) Lai, C.-H.; Wang, G.-A.; Ling, T.-K.; Wang, T.-J.; Chiu, P.-K.; Chou Chau, Y.-F.; Huang, C.-C.; Chiang, H.-P. Near infrared surface-enhanced Raman scattering based on star-shaped gold/silver nanoparticles and hyperbolic metamaterial. *Scientific reports* **2017**, *7*, 5446, DOI: 10.1038/s41598-017-05939-0.
(91) Jin, R.; Cao, Y.; Mirkin, C. A.; Kelly, K. L.; Schatz, G. C.; Zheng, J. G. Photoinduced conversion of silver nanospheres to nanoprisms. *Science (New York, N.Y.)* **2001**, *294*, 1901–1903, DOI: 10.1126/science.1066541.
(92) Sun, Y.; Mayers, B.; Xia, Y. Transformation of Silver Nanospheres into Nanobelts and Triangular Nanoplates through a Thermal Process. *Nano Lett.* **2003**, *3*, 675–679, DOI: 10.1021/nl034140t.
(93) Mosier-Boss, P. A. Review of SERS Substrates for Chemical Sensing. *Nanomaterials* **2017**, *7,* DOI: 10.3390/nano7060142.

(94) Sharma, Y.; Dhawan, A. Novel SERS substrates for chemical and biological sensing. In *2017 Opto-Electronics and Communications Conference (OECC) and Photonics Global Conference (PGC)*; IEEE: [Piscataway, New Jersey], 2017?; pp 1–6.
(95) Solís, D. M.; Taboada, J. M.; Obelleiro, F.; Liz-Marzán, L. M.; García de Abajo, F. J. Optimization of Nanoparticle-Based SERS Substrates through Large-Scale Realistic Simulations. *ACS photonics* **2017**, *4*, 329–337, DOI: 10.1021/acsphotonics.6b00786.
(96) Yang, W.-H.; Schatz, G. C.; van Duyne, R. P. Discrete dipole approximation for calculating extinction and Raman intensities for small particles with arbitrary shapes. *The Journal of Chemical Physics* **1995**, *103*, 869–875, DOI: 10.1063/1.469787.
(97) Hafner, C. Multiple multipole program computation of periodic structures. *J. Opt. Soc. Am. A* **1995**, *12*, 1057, DOI: 10.1364/JOSAA.12.001057.
(98) Martin, Y. C.; Hamann, H. F.; Wickramasinghe, H. K. Strength of the electric field in apertureless near-field optical microscopy. *Journal of Applied Physics* **2001**, *89*, 5774–5778, DOI: 10.1063/1.1354655.
(99) Gellner, M.; Steinigeweg, D.; Ichilmann, S.; Salehi, M.; Schütz, M.; Kömpe, K.; Haase, M.; Schlücker, S. 3D self-assembled plasmonic superstructures of gold nanospheres: Synthesis and characterization at the single-particle level. *Small (Weinheim an der Bergstrasse, Germany)* **2011**, *7*, 3445–3451, DOI: 10.1002/smll.201102009.
(100) Bryche, J.-F.; Tsigara, A.; Bélier, B.; La Chapelle, M. L. de; Canva, M.; Bartenlian, B.; Barbillon, G. Surface enhanced Raman scattering improvement of gold triangular nanoprisms by a gold reflective underlayer for chemical sensing. *Sensors and Actuators B: Chemical* **2016**, *228*, 31–35, DOI: 10.1016/j.snb.2016.01.018.
(101) Haynes, C. L.; van Duyne, R. P. Nanosphere Lithography: A Versatile Nanofabrication Tool for Studies of Size-Dependent Nanoparticle Optics. *J. Phys. Chem. B* **2001**, *105*, 5599–5611, DOI: 10.1021/jp010657m.
(102) Hulteen, J. C.; Treichel, D. A.; Smith, M. T.; Duval, M. L.; Jensen, T. R.; van Duyne, R. P. Nanosphere Lithography: Size-Tunable Silver Nanoparticle and Surface Cluster Arrays. *J. Phys. Chem. B* **1999**, *103*, 3854–3863, DOI: 10.1021/jp9904771.
(103) Wu, D.-Y.; Li, J.-F.; Ren, B.; Tian, Z.-Q. Electrochemical surface-enhanced Raman spectroscopy of nanostructures. *Chemical Society reviews* **2008**, *37*, 1025–1041, DOI: 10.1039/b707872m.
(104) Yue, W.; Wang, Z.; Yang, Y.; Chen, L.; Syed, A.; Wong, K.; Wang, X. Electron-beam lithography of gold nanostructures for surface-enhanced Raman scattering. *J. Micromech. Microeng.* **2012**, *22*, 125007, DOI: 10.1088/0960-1317/22/12/125007.
(105) Zhang, C.; Yi, P.; Peng, L.; Lai, X.; Chen, J.; Huang, M.; Ni, J. Continuous fabrication of nanostructure arrays for flexible surface enhanced Raman scattering substrate. *Scientific reports* **2017**, *7*, 39814, DOI: 10.1038/srep39814.
(106) Liu, L.; Zhang, Q.; Lu, Y.; Du, W.; Li, B.; Cui, Y.; Yuan, C.; Zhan, P.; Ge, H.; Wang, Z. *et al.* A high-performance and low cost SERS substrate of plasmonic nanopillars on plastic film fabricated by nanoimprint lithography with AAO template. *AIP Advances* **2017**, *7*, 65205, DOI: 10.1063/1.4985270.
(107) Su, Q.; Ma, X.; Dong, J.; Jiang, C.; Qian, W. A reproducible SERS substrate based on electrostatically assisted APTES-functionalized surface-assembly of gold nanostars. *ACS applied materials & interfaces* **2011**, *3*, 1873–1879, DOI: 10.1021/am200057f.

(108) Ben Haddada, M.; Blanchard, J.; Casale, S.; Krafft, J.-M.; Vallée, A.; Méthivier, C.; Boujday, S. Optimizing the immobilization of gold nanoparticles on functionalized silicon surfaces: Amine- vs thiol-terminated silane. *Gold Bull* **2013**, *46*, 335–341, DOI: 10.1007/s13404-013-0120-y.

(109) Péron, O.; Rinnert, E.; Lehaitre, M.; Crassous, P.; Compère, C. Detection of polycyclic aromatic hydrocarbon (PAH) compounds in artificial sea-water using surface-enhanced Raman scattering (SERS). *Talanta* **2009**, *79*, 199–204, DOI: 10.1016/j.talanta.2009.03.043.

(110) Park, S.; Lee, J.; Ko, H. Transparent and Flexible Surface-Enhanced Raman Scattering (SERS) Sensors Based on Gold Nanostar Arrays Embedded in Silicon Rubber Film. *ACS applied materials & interfaces* **2017**, *9*, 44088–44095, DOI: 10.1021/acsami.7b14022.

(111) Lu, G.; Li, H.; Zhang, H. Nanoparticle-coated PDMS elastomers for enhancement of Raman scattering. *Chemical communications (Cambridge, England)* **2011**, *47*, 8560–8562, DOI: 10.1039/c1cc12027a.

(112) Lu, G.; Li, H.; Zhang, H. Gold-nanoparticle-embedded polydimethylsiloxane elastomers for highly sensitive Raman detection. *Small (Weinheim an der Bergstrasse, Germany)* **2012**, *8*, 1336–1340, DOI: 10.1002/smll.201102258.

(113) Sun, M.; Xu, H. A novel application of plasmonics: Plasmon-driven surface-catalyzed reactions. *Small (Weinheim an der Bergstrasse, Germany)* **2012**, *8*, 2777–2786, DOI: 10.1002/smll.201200572.

(114) Zhang, X.; Wang, P.; Zhang, Z.; Fang, Y.; Sun, M. Plasmon-driven sequential chemical reactions in an aqueous environment. *Scientific reports* **2014**, *4*, 5407, DOI: 10.1038/srep05407.

(115) Carattino, A.; Khatua, S.; Orrit, M. In situ tuning of gold nanorod plasmon through oxidative cyanide etching. *Physical chemistry chemical physics : PCCP* **2016**, *18*, 15619–15624, DOI: 10.1039/c6cp01679k.

(116) Kedia, A.; Kumar, P. S. Gold nanostars reshaping and plasmon tuning mechanism. In ; AIP, 2013; pp 232–233.

(117) Liu, X.-L.; Wang, J.-H.; Liang, S.; Yang, D.-J.; Nan, F.; Ding, S.-J.; Zhou, L.; Hao, Z.-H.; Wang, Q.-Q. Tuning Plasmon Resonance of Gold Nanostars for Enhancements of Nonlinear Optical Response and Raman Scattering. *J. Phys. Chem. C* **2014**, *118*, 9659–9664, DOI: 10.1021/jp500638u.

(118) Qin, L.; Zhang, C.; Li, R.; Li, X. Silicon-gold core-shell nanowire array for an optically and electrically characterized refractive index sensor based on plasmonic resonance and Schottky junction. *Optics letters* **2017**, *42*, 1225–1228, DOI: 10.1364/OL.42.001225.

(119) Shajari, D.; Bahari, A.; Gill, P.; Mohseni, M. Synthesis and tuning of gold nanorods with surface plasmon resonance. *Optical Materials* **2017**, *64*, 376–383, DOI: 10.1016/j.optmat.2017.01.004.

(120) Shi, W.; Sahoo, Y.; Swihart, M. T.; Prasad, P. N. Gold nanoshells on polystyrene cores for control of surface plasmon resonance. *Langmuir : the ACS journal of surfaces and colloids* **2005**, *21*, 1610–1617, DOI: 10.1021/la047628y.

(121) Kang, L.; Xu, P.; Zhang, B.; Tsai, H.; Han, X.; Wang, H.-L. Laser wavelength- and power-dependent plasmon-driven chemical reactions monitored using single particle surface enhanced Raman spectroscopy. *Chemical communications (Cambridge, England)* **2013**, *49*, 3389–3391, DOI: 10.1039/c3cc40732b.

(122) Dong, B.; Fang, Y.; Chen, X.; Xu, H.; Sun, M. Substrate-, wavelength-, and time-dependent plasmon-assisted surface catalysis reaction of 4-nitrobenzenethiol dimerizing to p,p'-

dimercaptoazobenzene on Au, Ag, and Cu films. *Langmuir : the ACS journal of surfaces and colloids* **2011**, *27*, 10677–10682, DOI: 10.1021/la2018538.

(123) Ren, X.; Tan, E.; Lang, X.; You, T.; Jiang, L.; Zhang, H.; Yin, P.; Guo, L. Observing reduction of 4-nitrobenzenthiol on gold nanoparticles in situ using surface-enhanced Raman spectroscopy. *Physical chemistry chemical physics : PCCP* **2013**, *15*, 14196–14201, DOI: 10.1039/c3cp51385h.

(124) Baffou, G.; Quidant, R.; Girard, C. Heat generation in plasmonic nanostructures: Influence of morphology. *Appl. Phys. Lett.* **2009**, *94*, 153109, DOI: 10.1063/1.3116645.

(125) Coppens, Z. J.; Li, W.; Walker, D. G.; Valentine, J. G. Probing and controlling photothermal heat generation in plasmonic nanostructures. *Nano letters* **2013**, *13*, 1023–1028, DOI: 10.1021/nl304208s.

(126) Yeshchenko, O. A.; Kutsevol, N. V.; Naumenko, A. P. Light-Induced Heating of Gold Nanoparticles in Colloidal Solution: Dependence on Detuning from Surface Plasmon Resonance. *Plasmonics* **2016**, *11*, 345–350, DOI: 10.1007/s11468-015-0034-z.

(127) Huang, X.; El-Sayed, M. A. Plasmonic photo-thermal therapy (PPTT). *Alexandria Journal of Medicine* **2011**, *47*, 1–9, DOI: 10.1016/j.ajme.2011.01.001.

(128) Qiu, J.; Wei, W. D. Surface Plasmon-Mediated Photothermal Chemistry. *J. Phys. Chem. C* **2014**, *118*, 20735–20749, DOI: 10.1021/jp5042553.

(129) Xu, P.; Kang, L.; Mack, N. H.; Schanze, K. S.; Han, X.; Wang, H.-L. Mechanistic understanding of surface plasmon assisted catalysis on a single particle: Cyclic redox of 4-aminothiophenol. *Scientific reports* **2013**, *3*, 2997, DOI: 10.1038/srep02997.

(130) Kim, K.; Choi, J.-Y.; Shin, K. S. Surface-Enhanced Raman Scattering of 4-Nitrobenzenethiol and 4-Aminobenzenethiol on Silver in Icy Environments at Liquid Nitrogen Temperature. *J. Phys. Chem. C* **2014**, *118*, 11397–11403, DOI: 10.1021/jp5015115.

(131) Liebig, F.; Sarhan, R. M.; Prietzel, C.; Reinecke, A.; Koetz, J. “Green” gold nanotriangles: synthesis, purification by polyelectrolyte/micelle depletion flocculation and performance in surface-enhanced Raman scattering. *RSC Adv.* **2016**, *6*, 33561–33568, DOI: 10.1039/C6RA04808K.

(132) Liebig, F.; Sarhan, R. M.; Prietzel, C.; Thünemann, A. F.; Bargheer, M.; Koetz, J. Undulated Gold Nanoplatelet Superstructures: In Situ Growth of Hemispherical Gold Nanoparticles onto the Surface of Gold Nanotriangles. *Langmuir : the ACS journal of surfaces and colloids* **2018**, *34*, 4584–4594, DOI: 10.1021/acs.langmuir.7b02898.

(133) Liebig, F.; Sarhan, R. M.; Prietzel, C.; Schmitt, C. N. Z.; Bargheer, M.; Koetz, J. Tuned Surface-Enhanced Raman Scattering Performance of Undulated Au@Ag Triangles. *ACS Appl. Nano Mater.* **2018**, *1*, 1995–2003, DOI: 10.1021/acsanm.8b00570.

(134) Xie, J.; Zhang, Q.; Lee, J. Y.; Wang, D. I. C. The synthesis of SERS-active gold nanoflower tags for in vivo applications. *ACS nano* **2008**, *2*, 2473–2480, DOI: 10.1021/nn800442q.

(135) Cui, Q.; Yashchenok, A.; Zhang, L.; Li, L.; Masic, A.; Wienskol, G.; Möhwald, H.; Bargheer, M. Fabrication of bifunctional gold/gelatin hybrid nanocomposites and their application. *ACS applied materials & interfaces* **2014**, *6*, 1999–2002, DOI: 10.1021/am5000068.

(136) Dietzek, B.; Cialla, D.; Schmitt, M.; Popp, J. Introduction to the Fundamentals of Raman Spectroscopy. In *Confocal raman microscopy*; Dieing, T., Hollricher, O., Toporski, J., Eds.; Springer Series in Optical Sciences 158; Springer: Heidelberg, London, 2011; pp 21–42.

(137) Butler, H. J.; Ashton, L.; Bird, B.; Cinque, G.; Curtis, K.; Dorney, J.; Esmonde-White, K.; Fullwood, N. J.; Gardner, B.; Martin-Hirsch, P. L. *et al.* Using Raman spectroscopy to characterize biological materials. *Nature protocols* **2016**, *11*, 664–687, DOI: 10.1038/nprot.2016.036.

(138) Liebig, F.; Sarhan, R. M.; Sander, M.; Koopman, W.; Schuetz, R.; Bargheer, M.; Koetz, J. Deposition of Gold Nanotriangles in Large Scale Close-Packed Monolayers for X-ray-Based Temperature Calibration and SERS Monitoring of Plasmon-Driven Catalytic Reactions. *ACS applied materials & interfaces* **2017**, *9*, 20247–20253, DOI: 10.1021/acsami.7b07231.

(139) Fortuni, B.; Fujita, Y.; Ricci, M.; Inose, T.; Aubert, R.; Lu, G.; Hutchison, J. A.; Hofkens, J.; Latterini, L.; Uji-I, H. A novel method for in situ synthesis of SERS-active gold nanostars on polydimethylsiloxane film. *Chemical communications (Cambridge, England)* **2017**, *53*, 5121–5124, DOI: 10.1039/c7cc01776f.

(140) Schwenk, N.; Mizaikoff, B.; Cárdenas, S.; López-Lorente, Á. I. Gold-nanostar-based SERS substrates for studying protein aggregation processes. *The Analyst* **2018**, *143*, 5103–5111, DOI: 10.1039/c8an00804c.

(141) He, S.; Chua, J.; Tan, E. K. M.; Kah, J. C. Y. Optimizing the SERS enhancement of a facile gold nanostar immobilized paper-based SERS substrate. *RSC Adv.* **2017**, *7*, 16264–16272, DOI: 10.1039/C6RA28450G.

(142) Yan, Z.; Du, W.; Tu, L.; Gu, P.; Huang, Z.; Zhan, P.; Liu, F.; Wang, Z. A facile high-performance SERS substrate based on broadband near-perfect optical absorption. *J. Raman Spectrosc.* **2015**, *46*, 795–801, DOI: 10.1002/jrs.4721.

(143) Chattopadhyay, S.; Lo, H.-C.; Hsu, C.-H.; Chen, L.-C.; Chen, K.-H. Surface-Enhanced Raman Spectroscopy Using Self-Assembled Silver Nanoparticles on Silicon Nanotips. *Chem. Mater.* **2005**, *17*, 553–559, DOI: 10.1021/cm049269y.

(144) Reppert, A. von; Sarhan, R. M.; Stete, F.; Pudell, J.; Del Fatti, N.; Crut, A.; Koetz, J.; Liebig, F.; Prietzel, C.; Bargheer, M. Watching the Vibration and Cooling of Ultrathin Gold Nanotriangles by Ultrafast X-ray Diffraction. *J. Phys. Chem. C* **2016**, *120*, 28894–28899, DOI: 10.1021/acs.jpcc.6b11651.

(145) Yang, Y.; Zhu, J.; Zhao, J.; Weng, G.-J.; Li, J.-J.; Zhao, J.-W. A growth of spherical gold satellites on the surface of Au@Ag@SiO2 core-shell nanostructures used for an ultrasensitive SERS immunoassay of alpha-fetoprotein. *ACS applied materials & interfaces* **2019,** DOI: 10.1021/acsami.8b21238.

(146) Pazos-Perez, N.; Fitzgerald, J. M.; Giannini, V.; Guerrini, L.; Alvarez-Puebla, R. A. Modular assembly of plasmonic core–satellite structures as highly brilliant SERS-encoded nanoparticles. *Nanoscale Adv.* **2019**, *1*, 122–131, DOI: 10.1039/C8NA00257F.

(147) Kang, L.; Han, X.; Chu, J.; Xiong, J.; He, X.; Wang, H.-L.; Xu, P. In Situ Surface-Enhanced Raman Spectroscopy Study of Plasmon-Driven Catalytic Reactions of 4-Nitrothiophenol under a Controlled Atmosphere. *ChemCatChem* **2015**, *7*, 1004–1010, DOI: 10.1002/cctc.201403032.

(148) Qiao, P.; Sun, B.; Li, H.; Pan, K.; Tian, G.; Wang, L.; Zhou, W. Surface Plasmon Resonance-Enhanced Visible-NIR-Driven Photocatalytic and Photothermal Catalytic Performance by Ag/Mesoporous Black TiO2 Nanotube Heterojunctions. *Chemistry, an Asian journal* **2018,** DOI: 10.1002/asia.201801428.

(149) Cho, F.-H.; Kuo, S.-C.; Lai, Y.-H. Surface-plasmon-induced azo coupling reaction between nitro compounds on dendritic silver monitored by surface-enhanced Raman spectroscopy. *RSC Adv.* **2017**, *7*, 10259–10265, DOI: 10.1039/C7RA00374A.

(150) Osawa, M.; Matsuda, N.; Yoshii, K.; Uchida, I. Charge transfer resonance Raman process in surface-enhanced Raman scattering from p-aminothiophenol adsorbed on silver: Herzberg-Teller contribution. *J. Phys. Chem.* **1994**, *98*, 12702–12707, DOI: 10.1021/j100099a038.

(151) Skadtchenko, B. O.; Aroca, R. Surface-enhanced Raman scattering of p-nitrothiophenol. *Spectrochimica Acta Part A: Molecular and Biomolecular Spectroscopy* **2001**, *57*, 1009–1016, DOI: 10.1016/S1386-1425(00)00415-7.

(152) Golubev, A. A.; Khlebtsov, B. N.; Rodriguez, R. D.; Chen, Y.; Zahn, D. R. T. Plasmonic Heating Plays a Dominant Role in the Plasmon-Induced Photocatalytic Reduction of 4-Nitrobenzenethiol. *J. Phys. Chem. C* **2018**, *122*, 5657–5663, DOI: 10.1021/acs.jpcc.7b12101.

(153) Gruenke, N. L.; Cardinal, M. F.; McAnally, M. O.; Frontiera, R. R.; Schatz, G. C.; van Duyne, R. P. Ultrafast and nonlinear surface-enhanced Raman spectroscopy. *Chemical Society reviews* **2016**, *45*, 2263–2290, DOI: 10.1039/c5cs00763a.

(154) Boerigter, C.; Aslam, U.; Linic, S. Mechanism of Charge Transfer from Plasmonic Nanostructures to Chemically Attached Materials. *ACS nano* **2016**, *10*, 6108–6115, DOI: 10.1021/acsnano.6b01846.

(155) Cheng, C.-W.; Chang, C.-L.; Chen, J.-K.; Wang, B. Femtosecond laser melting of silver nanoparticles: comparison of model simulations and experimental results. *Appl. Phys. A* **2018**, *124*, 10232, DOI: 10.1007/s00339-018-1792-1.

(156) Li, R.; Ashour, O. A.; Chen, J.; Elsayed-Ali, H. E.; Rentzepis, P. M. Femtosecond laser induced structural dynamics and melting of Cu (111) single crystal. An ultrafast time-resolved x-ray diffraction study. *Journal of Applied Physics* **2017**, *121*, 55102, DOI: 10.1063/1.4975198.

(157) Yin, D.; Li, X.; Ma, Y.; Liu, Z. Targeted cancer imaging and photothermal therapy via monosaccharide-imprinted gold nanorods. *Chemical communications (Cambridge, England)* **2017**, *53*, 6716–6719, DOI: 10.1039/c7cc02247f.

(158) Moon, H. J.; Ku, M.; Lee, H.; Yoon, N.; Yang, J.; Bong, K. W. Implantable Photothermal Agents based on Gold Nanorods-Encapsulated Microcube. *Scientific reports* **2018**, *8*, 13683, DOI: 10.1038/s41598-018-31793-9.

Chapter 7. Appendix

This chapter presents the publications that constitute my thesis together with their supporting materials.

RSC Advances

PAPER

View Article Online
View Journal | View Issue

Cite this: *RSC Adv.*, 2016, **6**, 33561

"Green" gold nanotriangles: synthesis, purification by polyelectrolyte/micelle depletion flocculation and performance in surface-enhanced Raman scattering†

Ferenc Liebig,[a] Radwan M. Sarhan,[b] Claudia Prietzel,[a] Antje Reinecke[c] and Joachim Koetz*[a]

Received 23rd February 2016
Accepted 23rd March 2016

DOI: 10.1039/c6ra04808k

www.rsc.org/advances

The aim of this study was to develop a one-step synthesis of gold nanotriangles (NTs) in the presence of mixed phospholipid vesicles followed by a separation process to isolate purified NTs. Negatively charged vesicles containing AOT and phospholipids, in the absence and presence of additional reducing agents (polyampholytes, polyanions or low molecular weight compounds), were used as a template phase to form anisotropic gold nanoparticles. Upon addition of the gold chloride solution, the nucleation process is initiated and both types of particles, *i.e.*, isotropic spherical and anisotropic gold nanotriangles, are formed simultaneously. As it was not possible to produce monodisperse nanotriangles with such a one-step procedure, the anisotropic nanoparticles needed to be separated from the spherical ones. Therefore, a new type of separation procedure using combined polyelectrolyte/micelle depletion flocculation was successfully applied. As a result of the different purification steps, a green colored aqueous dispersion was obtained containing highly purified, well-defined negatively charged flat nanocrystals with a platelet thickness of 10 nm and an edge length of about 175 nm. The NTs produce promising results in surface-enhanced Raman scattering.

1. Introduction

Monodisperse gold nanoparticles (NPs) are of increasing interest due to their shape and size-dependent optical properties,[1,2] which are of enormous interest for many applications in photonics,[3] catalysis,[4] electronics[5] and biomedicine.[6] It is already well established from Turkevich *et al.* that monodisperse spherical NPs can be synthesized by adding sodium citrate as a reducing agent to a highly diluted aqueous gold chloride solution.[7] The nucleation process in the presence of sodium citrate was than further refined by Frens, as a bottom up strategy to build up monodisperse spherical NPs of different sizes.[8]

Recently, it was shown that asymmetric shaped NPs are formed by using special reduction agents, like lemongrass,[9] or tryptophan.[10] Other strategies towards the development of anisotropic nanoparticles include templates,[11] such as dendrimers,[12] microemulsions,[13,14] or polyelectrolyte micelles.[15]

Current seeding-mediated synthesis methods are very efficient in controlling the size and shape of anisotropic gold nanoparticles and, especially, those of nanorods. Over a decade ago, Jana *et al.* had already proposed a seed-mediated, surfactant-assisted two-step approach involving the use of the cationic surfactant, CTAB.[16] The seed-mediated synthesis, in presence of CTAB, is very sensitive to halide ions,[10,17,18] meaning that nanorods are only formed in absence of iodide ions. Furthermore, the shape of gold crystals can be dramatically changed upon addition of trace amounts of iodide ions, resulting in the formation of gold nanoprisms.[19] Mirkin and co-workers studied the growth of nanoparticles on CTAC-capped seeds containing iodide ions in the absence or presence of silver cations and reported that the anisotropic growth only occurs in absence of silver cations.[20] Kinetically controlled reaction paths are dependent on the addition rate of ascorbic acid. Hong *et al.* demonstrated that nanoplates are predominantly formed in presence of iodide ions at the lowest addition rate of the mild reducing agent ascorbic acid.[21]

Nevertheless, an efficient synthetic method to produce exclusively monodisperse anisotropic gold nanoparticles of defined shape is still lacking. As a result, different attempts have been made to separate anisotropic NPs from spherical

[a]University of Potsdam, Institute for Chemistry, Karl-Liebknecht-Str. 24-25, 14476 Potsdam, Germany. E-mail: koetz@uni-potsdam.de; Fax: +493319775054; Tel: +493319775220

[b]University of Potsdam, Institute for Physics, Karl-Liebknecht-Str. 24-25, 14476 Potsdam, Germany

[c]Max Planck Institute of Colloids and Interfaces, Am Mühlenberg 1, 14476 Potsdam, Germany

† Electronic supplementary information (ESI) available. See DOI: 10.1039/c6ra04808k

ones. However, a separation of the anisotropic particles from the spherical ones is not trivial. The most attractive separation approach was initially developed by Park *et al.* through the application of a method involving depletion-induced shape and size selection of gold nanoparticles.[22] These authors were able to show that rod-like NPs preferential aggregate and sediment in the presence of numerous micelles. Scarabelli *et al.* used this method very successfully to separate and purify gold nanotriangles (NTs) in presence of CTAC micelles.[23]

In previous work, different template phases, *i.e.* mixed phospholipid-based vesicles, were used to build up anisotropic gold nanoparticles in a one-step process.[24–26] Applying a strongly alternating polyampholyte, *i.e.*, PalPhBisCarb, and through the variation of the reaction conditions and composition of the template phase, more than 60% of the AuNPs were found to be anisotropic gold nanoplatelets.

The mechanism by which the one-step process leads to the formation of nanotriangles on the surface of mixed vesicles remains unknown. Therefore, the present work is focused, on the one hand, on the growth mechanism of triangular gold nanoplatelets on the surface of vesicles in presence of different reducing agents, *i.e.*, polyelectrolytes and low molecular reducing agents. On the other hand, the depletion flocculation process of the nanotriangles was investigated through the addition of the anionic surfactant AOT in excess. As a result of our research, purified negatively charged nanoplatelets with a yield of 99.8% after several purification steps and a polydispersity of 10% were obtained, which can be used for SERS measurements or as a nano-platform for the construction of superstructures, for instance, with oppositely charged spherical nanoparticles.

2. Experimental details

2.1. Materials

The phospholipid PL90G (purity > 97.3%) was obtained from PHOSPHOLIPID GmbH. The surfactant dioctyl sodium sulfosuccinate (AOT) with a purity of 98%, hydrogen tetrachloroaurate(III) trihydrate ($HAuCl_4 \cdot 3H_2O$), 4-nitrothiophenol (4-NTP), the commercially available polymers PDADMAC (<100 000 g mol^{-1}, 35 wt% in H_2O), poly(acrylic acid) sodium salt (PAA) (60 000 g mol^{-1}) and alginic acid from brown algae (AlgA) (64 000 g mol^{-1}) were purchased from Sigma-Aldrich. Lemon grass oil, lactic acid (≥98%) and L(+)-ascorbic acid (≥99%) were obtained from Roth. Molecular biology grade trisodium citrate dehydrate was obtained from Electran. All chemicals were used as received. The strongly alternating copolymer poly(*N*,*N*′-diallyl-*N*,*N*′-dimethylammonium-*alt*-3,5-bis-carboxyphenyl-maleamic carboxylate (PalPhBisCarb) was synthesized by free radical polymerization according to the procedure described by Fechner and Koetz.[27] The molecular weight (15 000 g mol^{-1}) was determined viscometrically by using available constants of the homopolymer poly(diallyldimethylammonium chloride) (PDADMAC) for the Kuhn–Mark–Houwink–Sakurada equation. Only distilled water, which had passed through a Milli-Q Reference A+ water purification system from Millipore, was used in all of the described experiments.

2.2. Characterization methods

UV-vis absorption measurements were carried out with an Agilent 8453 UV-vis-NIR spectrometer covering the wavelength range 200 to 1100 nm. The shape and size of the gold nanoparticles were determined by transmission electron microscopy (TEM). Samples were dropped on carbon-coated copper grids. Upon air drying (using a suspension preparation procedure), the samples were examined using either one of two TEMs, mainly with a JEOL JEM-1011 at an acceleration voltage of 80 kV, or with a JEOL JEM-2200 FS to obtain higher resolution TEM (HRTEM) images, at an acceleration voltage of 200 kV. For the statistical evaluation (yield and polydispersity) of each sample more than 600 particles were analysed. The polydispersity was determined regarding the average edge length. The characterization of the thickness of the gold nanotriangles was performed on PicoScan-AFM from Agilent. In order to obtain the zeta potential, the Malvern Nano Zetasizer 3600, based on the principle of electrophoretic light scattering, was employed. In addition to TEM, a Hitachi S-4800 scanning electron microscope (SEM) was used to analyze the coating layer of the silica wafer for the SERS measurements. Raman spectra were recorded using a confocal Raman Microscope alpha300 from WITec equipped with laser excitation at wavelength of 785 nm. The laser beam was focused through a Nikon 20× microscope objective with a NA of 0.4. The spectra were acquired with a thermoelectrically cooled Andor CCD detector DU401A-BV placed behind the spectrometer UHTS 300 from WITec with a spectral resolution of 3 cm^{-1}. The Raman band of a silicon wafer at 520 cm^{-1} was used to calibrate the spectrometer.

2.3. Synthesis of nanotriangles (NTs)

PL90G (0.5 wt%) and AOT (0.5 wt%) in addition to one of the applied added agents (0.01 wt%) were dispersed together in water and stirred for 24 hours at room temperature. The resulting turbid vesicle dispersion was mixed with the freshly prepared aqueous 2 mM tetrachloroaurate precursor solution. The mixtures were stirred at 45 °C for 45 minutes resulting in a purple colored clear dispersion.

2.4. Purification of the NTs by depletion flocculation

As a result of the diversity in shape and size, a separation method was considered necessary in order to obtain pure NTs. Such a separation procedure can be achieved through the use of depletion flocculation, in the presence of polymers or micelles. The separation effect is dependent on the amount of surfactant used for the vesicle phase and the reducing agent. Once separation of triangular gold nanoparticles from the spherical ones had occurred, the dispersion was washed by centrifugation.

The depletion flocculation was performed in presence of AOT micelles. The results show that only a combined polyelectrolyte/micelle depletion flocculation process leads to a complete separation of the triangles. The optimum concentration of the added AOT solution was found at 0.02 M.

2.5. Preparation of SERS substrate

For the immobilization of the nanotriangles on the substrate, a silicon wafer was purified in a solution of 30 wt% H_2O_2 and 30 wt% H_2SO_4 for 1 h. It was rinsed in deionized water and dried before being used. The wafer was immersed in an aqueous solution of 2% 3-MPTMS ethanol for 6 h, rinsed in ethanol and dried. 100 μl of the gold nanotriangles dispersion were assembled on the wafer surface and the unattached nanotriangles were removed by washing the surface with deionized water. The gold nanotriangle-coated silicon wafer was immersed in 10 mM solution of 4-NTP in ethanol overnight. The wafer was washed with ethanol and deionized water before being measured.

3. Results and discussion

3.1 Template phase characterization

A turbid dispersion of negatively charged vesicles was generated under the described conditions. Dynamic light scattering (DLS) experiments of this dispersion showed that there was a very broad particle size distribution (ranging from 50 nm to 5000 nm). The intensity plot revealed a maximum at 450 nm and the number plot had a maximum at around 50 nm (Fig. 1A). The corresponding cryo-SEM micrographs (Fig. 1B) highlighted the presence of small unilamellar vesicles (SUV) of about 50 nm in size, which is in good agreement with the number plot obtained from the DLS data, in addition to the significantly larger giant unilamellar vesicles (GUV). A more detailed inspection of the interior of the GUVs by Cryo-SEM (see Fig. 1B) suggests that these are in fact multivesicular vesicles (MVV). Note, that these GUVs, with diameters up to 50 μm, can be visualized by light microscopy, as shown in Fig. 1C.

This means that the template phase is a polydisperse vesicle phase containing SUVs that are partly incorporated in GUVs.

3.2. One-step gold nanotriangle formation process

By using the mixed vesicle template phase, in the absence of any additional reducing components, an increase in the UV absorption at higher wavelengths around the peak maximum of 520 nm was observed. The plasmon resonance frequency and, thereby, the position of the localized surface plasmon resonance (LSPR) band is appreciably influenced by the size, shape, dielectric constant of the metal particle and its surroundings. A characteristic plasmon absorption band at about 525 nm can be assigned to spherical gold nanoparticles with a particle diameter between 5 and 40 nm,[16] whereas anisotropic nanoparticles like nanorods exhibit two absorption peaks, mainly the transverse plasmon band at 520 nm and the longitudinal band between 700 and 1300 nm, depending on the aspect ratio.[28] Asymmetric gold nanoplatelets also absorb in this region, that is between 650 and 1300 nm.[9,10,29]

Applying this knowledge to the UV-vis spectrum shown in Fig. 2, suggests that the formation of anisotropic gold nanoparticles, as well as spherical isotropic gold nanoparticles, has occurred. To get a more detailed understanding about the shape of the nanoparticles, TEM experiments were carried out. In addition to spherical particles of around 20 nm in size, nanotriangles with edge lengths varying between 20 nm and 200 nm were visualized (Fig. 2).

When template phases were generated in the presence of macromolecular components, quite different effects were observed.

In case of the polycation PDADMAC, only spherical isotropic gold nanoparticles were formed. This conclusion, based on the TEM micrographs (Fig. S1†) is in good agreement with the corresponding UV-vis spectrum, which showed that there was only a broad peak maximum that was shifted to lower wavelengths (Fig. 3).

By adding the polyanions PAA and AlgA, nanotriangles were formed in addition to spherical nanoparticles. The TEM micrographs as well as the UV-vis spectra indicate an enhancing effect with regard to the formation of NTs. Table 1 shows that the edge length of the NTs increases and the polydispersity decreases, in the same order of magnitude.

The use of PalPhBisCarb leads to NTs with an edge length of about 60 nm, representing 33% of all particles, with a slightly lower polydispersity of 33% and a corresponding UV-vis maximum at 950 nm. This can be explained by the fact that PalPhBisCarb behaves like a polyanion at pH 9.

Following experiments in presence of low molecular reducing components containing carboxylic moieties were performed under the same conditions as mentioned before. Table 2 shows the TEM analysis results concerning the triangular structures. The associated TEM micrographs could be

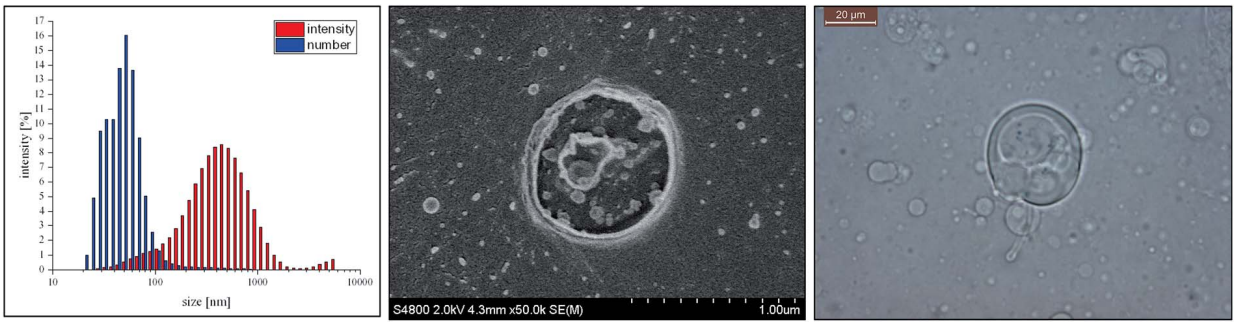

Fig. 1 Analysis of the turbid vesicle template phase *via* DLS intensity and number plot (left), the corresponding Cryo-SEM micrograph (center), and the image of light microscopy (right).

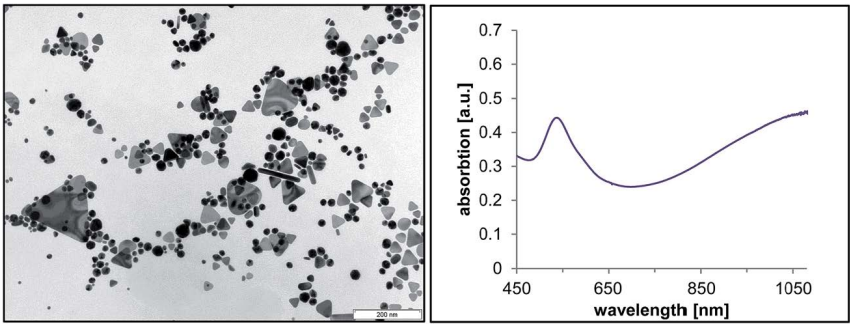

Fig. 2 TEM micrograph (left) and corresponding UV-vis spectrum (right) of the gold nanoparticles formed in the template phase without further reducing components.

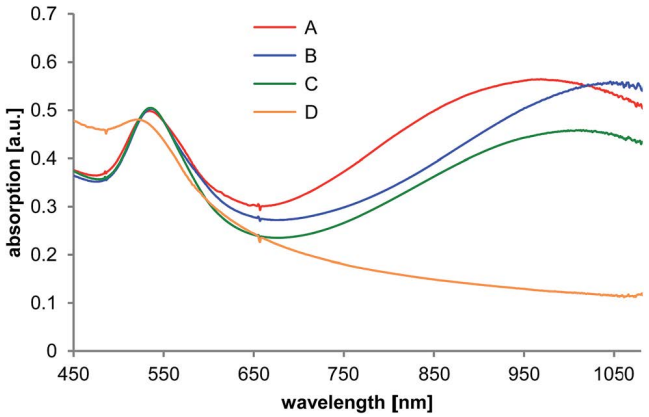

Fig. 3 UV-vis absorption spectra of the gold nanoparticles formed in the template phase in presence of PalPhBisCarb (A), PAA (B), AlgA (C) and PDADMAC (D).

Table 1 TEM analysis of gold nanotriangles

Vesicle phase	Yield (%)	Edge length (nm)	Polydispersity (%)
Without additional compounds	30	44 ± 25	56.1
+PalPhBisCarb (A)	33	59 ± 19	33.3
+Poly(acrylic acid) (B)	31	90 ± 32	35.9
+Alginic acid (C)	30	85 ± 32	38.1
+PDADMAC (D)	0	—	—

found in the ESI (Fig. S2†). Experiments by adding ascorbic acid show that 24% of all particles are triangles permitting a shoulder at 630 nm in the UV-vis spectrum. By replacing ascorbic acid with sodium citrate, larger NTs of about 42 nm in size with a corresponding UV-vis peak at about 720 nm can be observed (Fig. 4). The use of L-lactic acid resulted in the UV-vis maximum being shifted to 820 nm accompanied by the formation of triangles with an average edge length of 68 nm. Under these conditions, deformed nanoplatelets were also generated. In the presence of lemon grass oil, the individual NTs are more uniform with more defined sharp corners resulting in an absorption maximum at 900 nm.

In conclusion, the reducing agents used here show both size and shape-dependent effects. The addition of polyanions, as reducing agents, lead to an increase of nanotriangles, whereas low molecular weight compounds decrease the amount of NTs (Table 2).

3.3. Mechanism of the NT formation process

To achieve a better understanding of the NT formation process, some additional time-dependent experiments were performed in presence of PalPhBisCarb. Time-dependent UV-vis absorption spectra (Fig. 5) show once a growing peak at 520 nm, which can be directly correlated to the formation of spherical gold nanoparticles, and an appearing peak at 970 nm, which can be attributed to the formation of anisotropic particles. This peak increased over time and shifted towards the resulting absorption maximum at 1050 nm. As a result, the UV short wavelength at 520 nm, as well as the long wavelength absorption at about 1000 nm increased simultaneously with time. Thus, the formation of anisotropic nanotriangles starts isochronously with the formation of isotropic spherical nanoparticles.

Additional experiments performed by using light microscopy show a color change to red and green at the same time scale with the rising UV-vis absorption peak. These color effects were detected inside of the giant multivesicular vesicles, where the local concentration of AOT/phospholipon bilayer structures is at its highest.

From a mechanistic point of view one can conclude that one part of the critical nuclei started to grow up until the spherical particles reached a size of about 20 nm in a "classical" nucleation process according to the La Mer diagram. Another part of the critical nuclei grow up until anisotropic NTs were formed

Table 2 TEM analysis of gold nanotriangles

Vesicle phase	Yield (%)	Edge length (nm)	Polydispersity (%)
+L-Ascorbic acid (E)	24	26 ± 6	23.6
+Sodium citrate (F)	25	42 ± 16	39.7
+L-Lactic acid (G)	19	68 ± 21	31.2
+Lemon grass oil (H)	27	72 ± 18	25.1

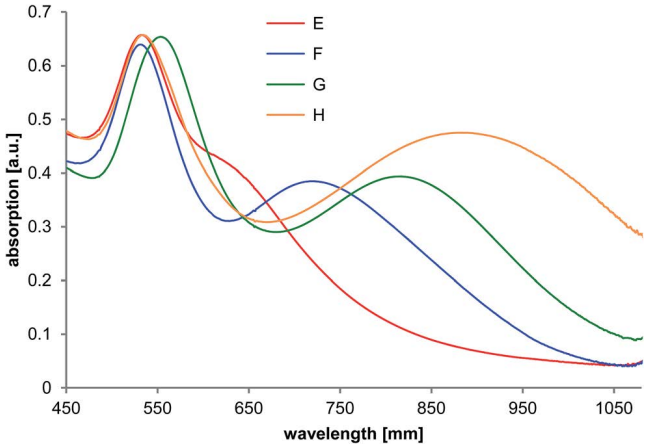

Fig. 4 UV-vis absorption spectra of the gold nanoparticles formed in the template phase in presence of L-ascorbic acid (E), sodium citrate (F), L-lactic acid (G) and lemon grass oil (H).

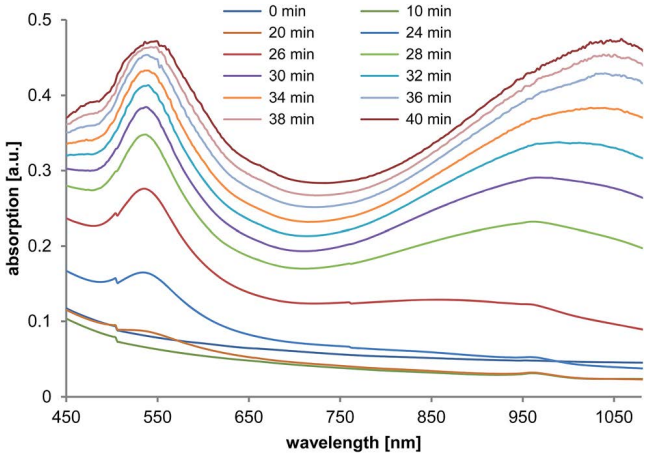

Fig. 5 Time-dependent UV-vis measurements during gold nanoparticle synthesis in the presence of PalPhBisCarb.

due to the symmetry-breaking effects of the template phase, which was influenced by the inner network structure inside of the multivesicular giant vesicles. Recently, we have shown that PalPhBisCarb can transform a mixed AOT vesicle phase into a tubular network structure,[30] which is a preferred weak template phase for making nanotriangles. Therefore, one can assume that the nanotriangles are predominantly formed at the junction points inside of the giant multivesicular vesicles.[25] Anisotropic crystals can only be formed when the cubic lattice symmetry is interrupted, *e.g.*, by stacking faults. Crystal nuclei with stacking faults can grow to form thin plates with {111} facets on the upper and lower side, *e.g.*, by adding ligands with the affinity for {111} faces. Such ligands can be surfactants as well as polymers. For example alkylated poly(ethyleneimines) and the cationic surfactant CTAB adsorb selective on gold or silver {111} facets.[31,32]

The growth process of the nanoparticles leads to a decomposition of the giant vesicles and the system becomes optically clear. Attempts to suppress the formation of spherical particles in such a one-step process failed. Therefore, a procedure to separate the anisotropic NTs from the isotropic spherical particles was required.

3.4. Gold nanotriangle separation process

Recently, Scarabelli *et al.* showed that the initial shape-yield of 50% nanotriangles, produced by a seed-mediated synthesis, can be elevated to 95% by a depletion induced separation process in presence of an excess of CTAC micelles.[23] Related experiments with CTAC showed the principal suitability of this procedure to separate our NTs. However, a quantitative and qualitative separation with CTAC micelles was unsuccessful. A reason for that could be the opposite charge of the NTs and CTAC micelles. Therefore, we used in the following experiments an AOT-based depletion flocculation process for our NTs.

To verify the quantity and quality of the shape controlled separation process in presence of AOT micelles in excess, TEM analysis and UV-Vis spectroscopy were performed. In the absence of a reducing agent (mixed vesicle template phase without additional components) only an incomplete separation process (NT yield < 50%) was observed. In presence of the low molecular reducing components, the separation procedure proved unsuccessful, too. That means the weak reducing low molecular weight compounds with carboxylic groups do not improve the AOT micelle based depletion flocculation process. Much better results were obtained upon addition of the polyelectrolytes PAA, AlgA, and PalPhBisCarb. The TEM micrographs (Fig. 6) demonstrated that the efficiency of the separation process in the presence of the polyelectrolytes was related to an enforced depletion flocculation. In that case negatively charged NTs with a zeta potential of about −75 mV and non-adsorbing negatively charged polyelectrolytes were combined. Consequently, the AOT micelle-based depletion flocculation process is enhanced by a polymer-based depletion flocculation leading to a quantitative separation of nanoplatelets (NPLs) in the presence of PalPhBisCarb (>99%) and AlgA (>99%), and an almost complete separation in the presence of PAA (96%), taking into account that the amount of well defined nanotriangles with pronounced corners is lower (Table 3). In addition to the NTs, the dispersion contains hexagonal structures, which are incompletely crystallized triangles in different growth phases. UV-vis measurements confirm the TEM analysis, meaning that the peak at around 525 nm, which is usually caused by spherical particles, disappears after three purification (washing and centrifugation) steps (compare Fig. S3†). Compared to the TEM analysis before the separation procedure, the average size of the NTs is increased drastically. This implies that the polyelectrolyte/micelle depletion flocculation affect only the fraction of larger sized NTs.

The shape-controlled depletion flocculation process showed only efficient results in presence of macromolecules, and seemed to be unaffected by AOT micelles alone. Hence, the depletion flocculation of larger NTs is mainly driven by the polymer, which can act as a reducing agent and is displaced on the particle surface by AOT. By investigating the influence of the

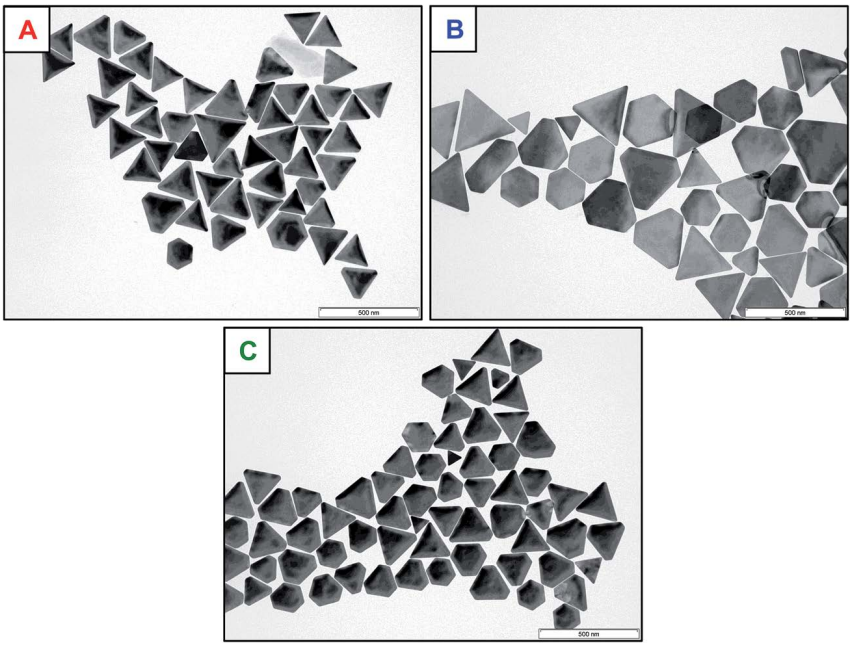

Fig. 6 TEM micrographs of the gold nanoparticles in presence of a PalPhBisCarb (A), PAA (B) and AlgA (C).

Table 3 TEM analysis of anisotropic gold nanoplatelets (NPLs) and nanotriangles (NTs)

Vesicle phase	Yield of NPLs (%)	Yield of NTs (%)	Edge length (nm)	Polydispersity (%)
PalPhBisCarb (A)	99.7	79	175 ± 17	10.1
Poly(acrylic acid) (B)	96	59	254 ± 50	20.0
Alginic acid (C)	99.8	73	169 ± 24	14.2

molar mass of PAA no significant effect on the NT formation process could be detected.

In summary, our results show that a combined polyelectrolyte/micelle depletion flocculation process is a sensitive and efficient procedure for the separation of larger anisotropic flat nanoplatelets. The highest amount of triangles can be observed in presence of PalPhBisCarb. Surprisingly, the edge length of the isolated NTs (listed in Table 3) is significantly larger in comparison to the initial ones (compare Table 1). Recently, Zhang *et al.* have shown that the micelle depletion flocculation strongly depends on the type of micelles.[29] Therefore, a stepwise flocculation with CTAB and CTAC micelles leads to a size-dependent separation of NTs. Hence, our combined polyelectrolyte/micelle depletion flocculation is even a size-selective process, yielding only the fraction of larger NTs.

3.5. Gold nanotriangle characterization

For a more comprehensive characterization, the resulting green colored dispersions were examined by means of AFM and HRTEM.

The AFM measurement in Fig. 7 shows that the nanotriangles were indeed flat nanoplatelets with a thickness of 10 nm. HRTEM micrographs (compare Fig. 8) confirmed the crystalline nature of the flat nanoplatelets with the top and bottom surfaces being composed of {111} facets. The triangles were single crystalline face-centered cubic (fcc) structured and as observed from the fast Fourier transform (FFT) (see inset in the HRTEM micrograph) orientated in the [111] direction. The forbidden 1/3 {422} reflections indicates the presence of twin planes parallel to the (111) surface and perpendicular to the electron beam.[33] Thus, the symmetry-braking effects of the AOT/phospholipon bilayer was enhanced in presence of PalPhBisCarb due to the adsorption of the amphoteric polymer on the

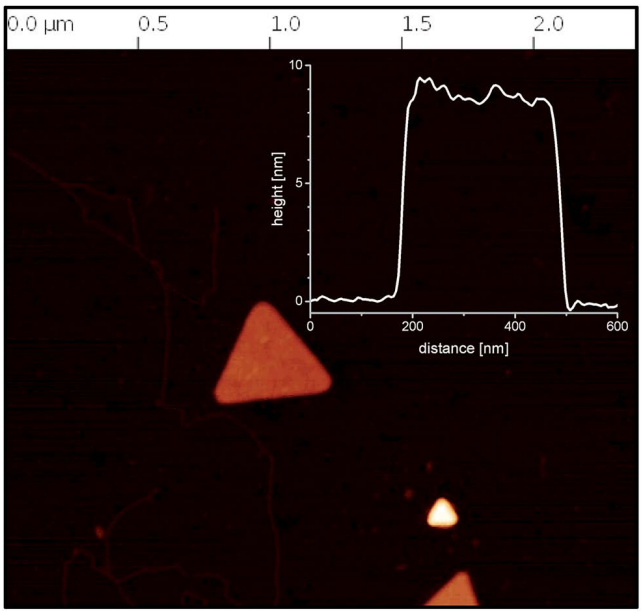

Fig. 7 Analysis of the triangle thickness by AFM.

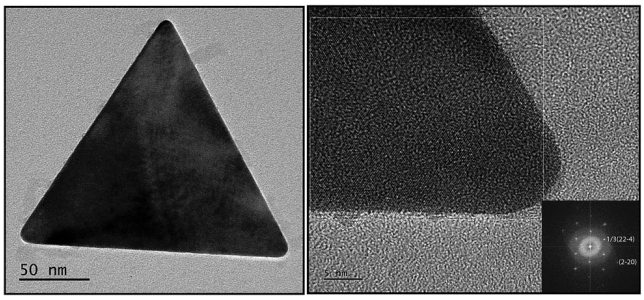

Fig. 8 Analysis of the triangle crystallinity by HRTEM; the inset (right) shows the fast Fourier transform (FFT) of the single crystal with the six-fold symmetry of the fcc lattice of gold.

{111} facets. The special performance of PaPhBisCarb in relation to the polyanions PAA and AlgA can be related to the cationic functional groups of the polyampholyte. The quaternary *N*-functions may play a similar role to that of the head group of the alkylated PEI samples in the selective adsorption of gold facets.[31]

3.6. SERS performance

The SERS effectiveness of the gold nanotriangles synthesized with PalPhBisCarb was studied using 4-nitrothiophenol as a probe, which can be easily chemisorbed on the gold nanoparticles by S–Au covalent bond. First experiments with a highly diluted sample show no significant effect. Therefore, the gold nanotriangle concentration was increased resulting in a completely covered SERS substrate (compare SEM micrograph in Fig. 9). Furthermore, Fig. 9 shows the comparison between Raman spectra of the solid 4-NTP molecules and the adsorbed 4-NTP molecules on SERS substrate. The enhancement of Raman scattering can be directly noticed from the spectra.

The Raman spectrum of 4-NTP showed the characteristic symmetric stretching of the NO_2 group at 1327 cm^{-1} and the C=C stretching of the phenyl ring at 1568 cm^{-1}.

On the gold nanotriangles, new peaks appeared at 1381 cm^{-1} and 1429 cm^{-1} due to the plasmon-assisted chemical dimerization of the 4-NTP to 4,4′-dimercaptoazobenzene (DMAB).

The SERS enhancement factor of the 4-NTP on the nanotriangles-fabricated SERS substrate was estimated using the equation:

$$\mathrm{EF} = \frac{I_{\mathrm{SERS}}}{I_{\mathrm{bulk}}} \frac{N_{\mathrm{bulk}}}{N_{\mathrm{ads}}}$$

where I_{SERS} and I_{bulk} are the Raman intensity at a certain vibration for the 4-NTP molecules adsorbed on the SERS substrate and solid 4-NTP molecules, respectively. The strongest NO_2 vibration at 1327 cm^{-1} was chosen to calculate the SERS enhancement factor. N_{ads} and N_{bulk} are the number of the probed adsorbed and solid 4-NTP molecules, respectively.[34]

To calculate N_{ads}, formation of a monolayer of 4-NTP on the SERS substrate was assumed.[35] Knowing the area occupied by an adsorbed 4-NTP molecule and the laser spot size, the N_{ads} was calculated to be 5.65×10^6. For N_{bulk}, the irradiated volume was considered as a cylinder with a waist diameter of ~1.2 μm and a depth of ~11.5 μm. So N_{bulk} was calculated to be 1.39×10^{11}. For the vibration at 1327 cm^{-1}, the SERS enhancement factor was estimated to be $\sim 2.76 \times 10^4$. We have repeated the measurements on three different batches of the nanotriangles and nearly the same signal enhancement was obtained. Control experiments performed at lower nanoparticle density show a lower signal enhancement.

The high SERS enhancement on the gold nanotriangles-fabricated substrate is mainly attributed to the junctions between the particles and the sharp edges of the nanotriangles, which they have been widely studied as "SERS hot spots", where the local electromagnetic field and therefore the Raman scattering is enhanced.[36]

4. Conclusions

A one-step synthesis of gold nanotriangles in a mixed AOT/phospholipon vesicle phase in the presence of different reducing components with size-dependent properties was developed.

This NT formation process can be suppressed by polycations and enhanced by polyanions. The initiation of the growing process, that leads to the formation of flat nanotriangles, starts at the bilayer interface facing the inside of giant multivesicular vesicles. In the case of the non-adsorbing polyanions and AOT micelles, a combined polyelectrolyte/micelle depletion flocculation process was used for the complete removal of the byproducts. The green colored, highly purified and long time stable (>3 month) dispersions of 10 nm thin nanotriangles used

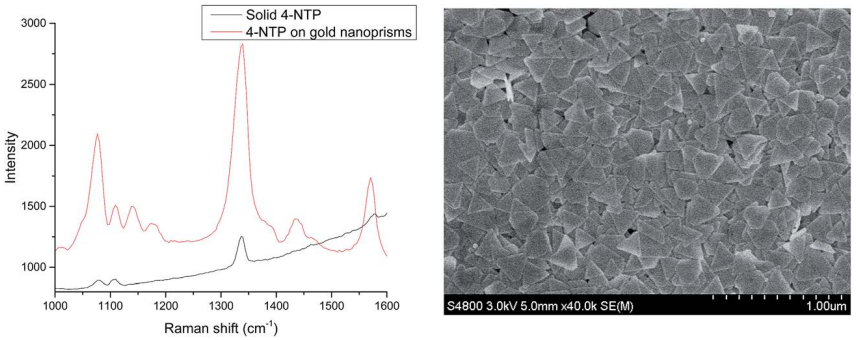

Fig. 9 Raman spectrum of 4-nitrothiophenol in absence and presence of gold nanotriangles (left), SEM micrograph of the according substrate (right).

for SERS measurements show an enhancement factor of 2.76×10^4 for the detection of 4-NTP, and will be served as a basis for building blocks for supramolecular stacking structures.

Acknowledgements

We would like to thank Dr Alexey Kopyshev and Prof. Svetlana Santer (University of Potsdam) for the AFM images.

References

1 M. Tréguer-Delapierre, J. Majimel, S. Mornet, E. Duguet and S. Ravaine, *Gold Bull.*, 2008, **41**, 195–207.
2 J. Aizpurua, P. Hanarp, D. S. Sutherland, M. Käll, G. W. Bryant and F. J. García de Abajo, *Phys. Rev. Lett.*, 2003, **90**, 057401.
3 X. Wang, R. Morea, J. Gonzalo and B. Palpant, *Nano Lett.*, 2015, **15**, 2633–2639.
4 A. Corma and H. Garcia, *Chem. Soc. Rev.*, 2008, **19**, 2096–2126.
5 G. Schmid and B. Corain, *Eur. J. Inorg. Chem.*, 2003, **17**, 3081–3098.
6 M. C. Daniel and D. Astruc, *Chem. Rev.*, 2004, **104**, 293–346.
7 J. Turkevich, P. C. Stevenson and J. Hillier, *Discuss. Faraday Soc.*, 1951, **11**, 55–75.
8 G. Frens, *Nature, Phys. Sci.*, 1973, **241**, 20–22.
9 A. Rai, A. Singh, A. Ahmad and M. Sastry, *Langmuir*, 2006, **22**, 736–741.
10 M. Kasture, M. Sastry and B. L. V. Prasad, *Chem. Phys. Lett.*, 2010, **484**, 271–275.
11 R. McCaffrey, H. Long, Y. Jin, A. Sanders, W. Park and W. Zhang, *J. Am. Chem. Soc.*, 2014, **136**, 1782–1785.
12 R. W. Scott, O. M. Wilson and R. M. Crooks, *J. Phys. Chem. B*, 2005, **109**, 692–704.
13 C. Note, S. Kosmella and J. Koetz, *Colloids Surf., A*, 2006, **290**, 150–156.
14 C. Note, J. Koetz, L. Wattebled and A. Laschewsky, *J. Colloid Interface Sci.*, 2007, **308**, 162–169.
15 W. Ding, J. Lin, K. Yao, J. W. Mays, M. Ramanathan and K. Hong, *J. Mater. Chem. B*, 2013, **1**, 4212–4216.
16 N. R. Jana, L. Gearheart and C. J. Murphy, *Langmuir*, 2001, **17**, 6782–6786.
17 S. E. Lohse, N. D. Burrows, L. Scarabelli, L. M. Liz-Marzan and C. J. Murphy, *Chem. Mater.*, 2014, **26**, 34–43.
18 A. Filankembo, S. Giorgio, I. Lisiecki and M. P. Pileni, *J. Phys. Chem.*, 2003, **107**, 7492–7500.
19 T. H. Ha, H.-J. Koo and B. H. Chung, *J. Phys. Chem. C*, 2007, **111**, 1123–1130.
20 M. R. Langille, M. L. Personick, J. Zhang and C. A. Mirkin, *J. Am. Chem. Soc.*, 2012, **134**, 14542–14554.
21 S. Hong, J. A. I. Acapulco Jr, H.-J. Jang, A. S. Kulkarni and S. Park, *Bull. Korean Chem. Soc.*, 2014, **35**, 1737–1742.
22 K. Park, H. Koerner and R. A. Vaia, *Nano Lett.*, 2010, **10**, 1433–1439.
23 L. Scarabelli, M. Coronado-Puchau, J. J. Giner-Casares, J. Langer and L. M. Liz-Marzan, *ACS Nano*, 2014, **6**, 5833–5842.
24 D. Robertson, B. Tiersch, S. Kosmella and J. Koetz, *J. Colloid Interface Sci.*, 2007, **305**, 345–351.
25 A. Köth, D. Appelhans, D. Robertson, B. Tiersch and J. Koetz, *Soft Matter*, 2011, **7**, 10581–10584.
26 A. Köth, D. Appelhans, C. Prietzel and J. Koetz, *Colloids Surf., A*, 2012, **414**, 50–56.
27 M. Fechner and J. Koetz, *Macromol. Chem. Phys.*, 2011, **212**, 2691–2699.
28 D. K. Smith and B. A. Korgel, *Langmuir*, 2008, **24**, 644–649.
29 F. Zhang, J. Zhu, H.-Q. An, J.-J. Li and J.-W. Zhao, *J. Mater. Chem. C*, 2016, **4**, 568.
30 N. Schulze, D. Appelhans, B. Tiersch and J. Koetz, *Colloids Surf., A*, 2014, **457**, 326–332.
31 C. C. Chen, C. H. Hsu and P. L. Kuo, *Langmuir*, 2007, **23**, 6801–6806.
32 S. Chen and D. L. Charoll, *J. Phys. Chem. B*, 2004, **108**, 5500–5506.
33 A. I. Kirkland, D. A. Jefferson, D. G. Duff, P. P. Edwards, I. Gameson, B. F. G. Johnson and D. J. Smith, *Proc. R. Soc. London, Ser. A*, 1993, **440**, 589–609.
34 Q. Cui, A. Yashchenok, L. Zhang, L. Lidong, A. Masic, G. Wienskol, H. Möhwald and M. Bargheer, *ACS Appl. Mater. Interfaces*, 2014, **6**, 1999–2002.
35 A. S. D. S. Indrasekara, S. Meyers, S. Shubeita, L. C. Feldman, T. Gustafsson and L. Fabris, *Nanoscale*, 2014, **6**, 8891–8899.
36 B. Xue, D. Wang, J. Zuo, X. Kong, Y. Zhang, X. Liu, L. Tu, Y. Chang, C. Li, F. Wu, Q. Zeng, H. Zhao, H. Zhao and H. Zhang, *Nanoscale*, 2015, **7**, 8048–8057.

SUPPLEMENTARY PART

FIGURES

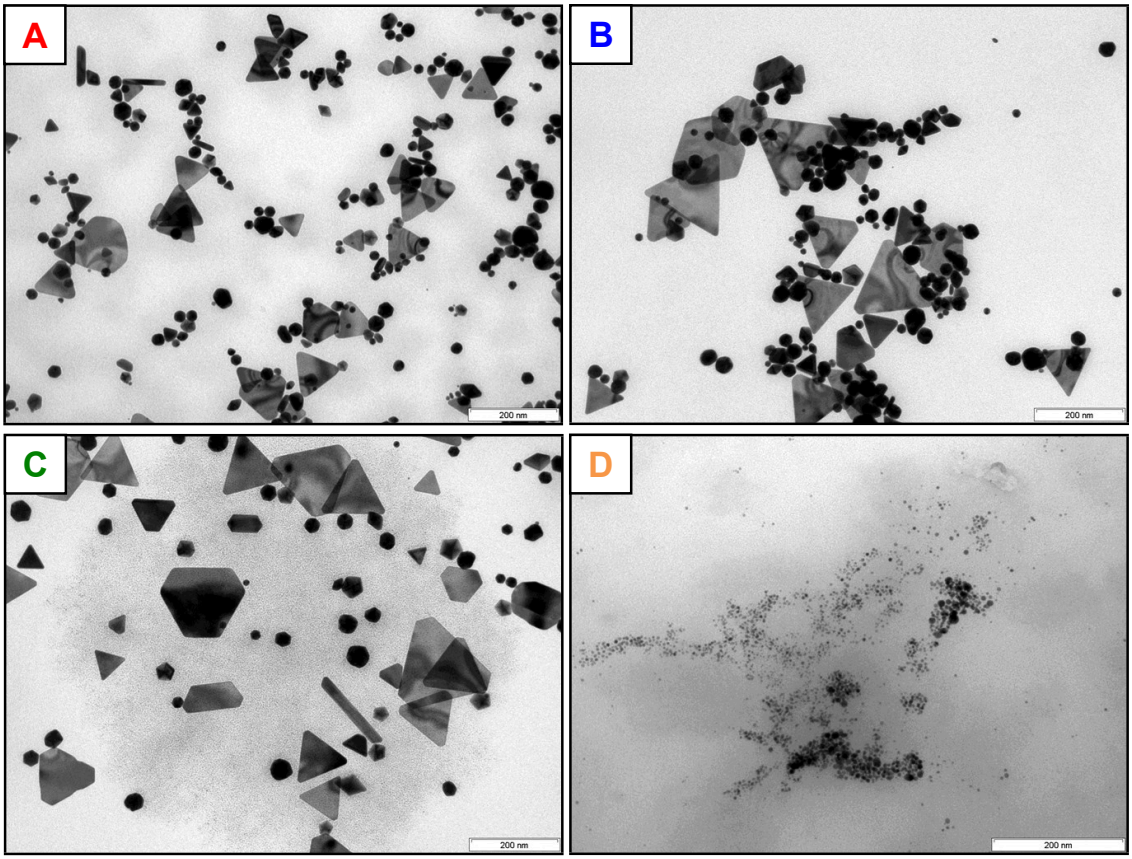

Fig. S1 TEM micrographs of the gold nanoparticles formed in the template phase in presence of PalPhBisCarb (A), PAA (B), AlgA (C) and PDADMAC (D)

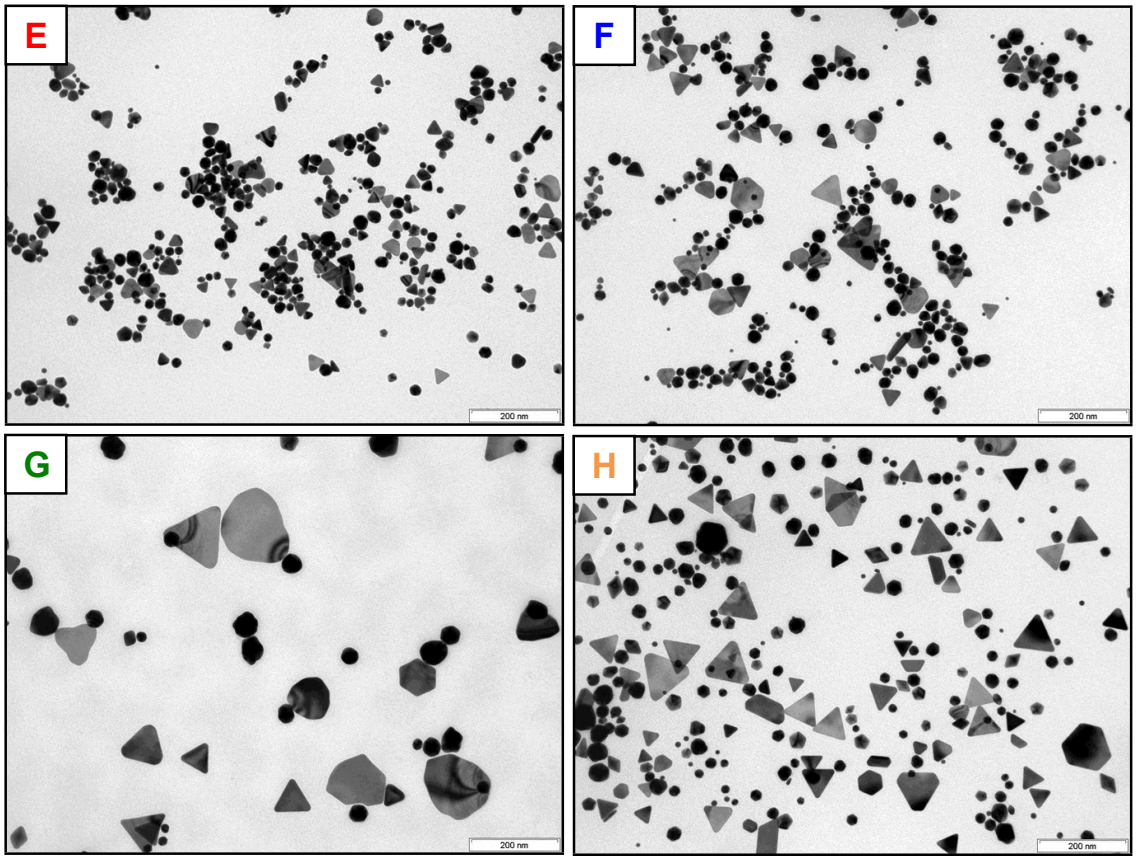

Fig. S2 TEM micrographs of the gold nanoparticles formed in the template phase in presence of L-ascorbic acid (E), sodium citrate (F), L-lactic acid (G) and lemon grass oil (H)

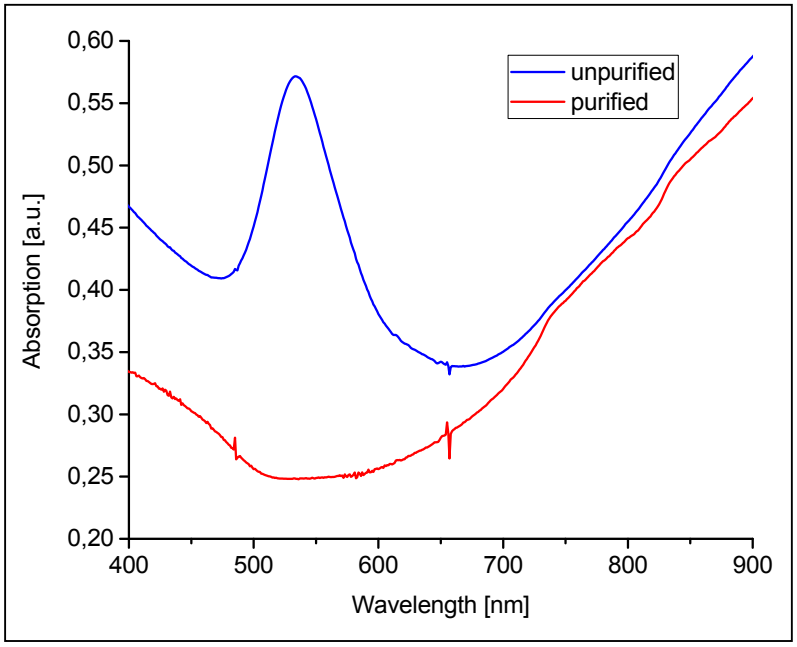

Fig. S3 UV-vis absorption spectra before separation and after three purification steps

LANGMUIR Article
Cite This: Langmuir 2018, 34, 4584−4594
pubs.acs.org/Langmuir

Undulated Gold Nanoplatelet Superstructures: In Situ Growth of Hemispherical Gold Nanoparticles onto the Surface of Gold Nanotriangles

Ferenc Liebig,[†] Radwan M. Sarhan,[‡,§] Claudia Prietzel,[†] Andreas F. Thünemann,[∥] Matias Bargheer,[‡] and Joachim Koetz*[,†]

[†]Institute for Chemistry and [‡]Institute for Physics, University of Potsdam, 14476 Potsdam, Germany
[§]School of Analytical Sciences Adlershof (SALSA), Humboldt-Universität zu Berlin, 10099 Berlin, Germany
[∥]Bundesanstalt für Materialforschung und -prüfung (BAM), Unter den Eichen 87, 12205 Berlin, Germany

Supporting Information

ABSTRACT: Negatively charged flat gold nanotriangles, formed in a vesicular template phase and separated by an AOT-micelle-based depletion flocculation, were reloaded by adding a cationic polyelectrolyte, that is, a hyperbranched polyethylenimine (PEI). Heating the system to 100 °C in the presence of a gold chloride solution, the reduction process leads to the formation of gold nanoparticles inside the polymer shell surrounding the nanoplatelets. The gold nanoparticle formation is investigated by UV−vis spectroscopy, small-angle X-ray scattering, and dynamic light scattering measurements in combination with transmission electron microscopy. Spontaneously formed gold clusters in the hyperbranched PEI shell with an absorption maximum at 350 nm grow on the surface of the nanotriangles as hemispherical particles with diameters of ∼6 nm. High-resolution micrographs show that the hemispherical gold particles are crystallized onto the {111} facets on the bottom and top of the platelet as well as on the edges without a grain boundary. Undulated gold nanoplatelet superstructures with special properties become available, which show a significantly modified performance in SERS-detected photocatalysis regarding both reactivity and enhancement factor.

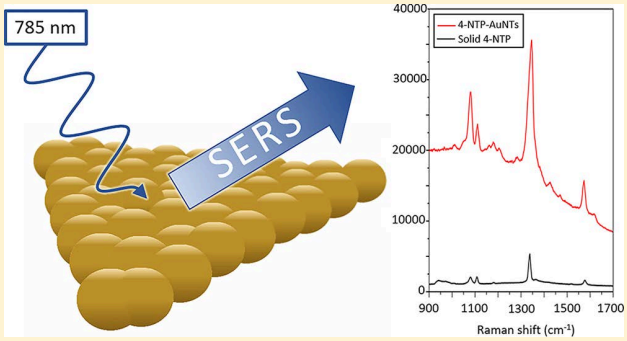

1. INTRODUCTION

Gold nanoparticle dispersions with their size-dependent optical properties are one of the oldest colloidal model systems, opening a door to many fields of application in catalysis, photonics, drug delivery, and medicine.[1−7] The classical way to achieve monodisperse spherical gold nanoparticles on the nanometer scale due to a nucleation process was established by Turkevich et al. by using sodium citrate as a reducing organic agent.[8] A characteristic feature of spherical gold nanoparticles in the size range between 5 and 50 nm is the strong absorption band between 520 and 530 nm due to the localized surface plasmon resonance (LSPR).[9] Using polyelectrolytes as reducing and stabilizing component the stability of gold nanoparticles can be improved. We have already shown that polyethylenimine (PEI) can play this role very well.[10] In this way electrosterically stabilized particles can be obtained. However, to the best of our knowledge time-dependent investigations of the growth mechanism in the presence of polyelectrolytes have not been reported up to now.

Another topic of increasing interest regards asymmetric gold nanoplatelets because of their shape-dependent optical properties[11−14] and their promising results in surface-enhanced Raman scattering (SERS).[15−17] Flat nanoplatelets exhibit a more intensive longitudinal absorption band in the near-infrared (NIR) region between 700 and 1400 nm,[16,18] a wavelength region of special interest for tissue imaging.[1] The absorption maximum in the NIR region can be tuned by controlling the size and thickness of the individual nanotriangles.[19,20]

One possibility to produce asymmetric gold nanoparticles is the seed-mediated synthesis in the presence of the cationic surfactant CTAB and iodide ions as symmetry-breaking components.[15,21−23] Furthermore, the crystallization process is linked to the kinetically controlled formation of nanoplatelets at a slow reaction rate.[24] Nevertheless, the seed-mediated synthesis leads only to a shape yield of nanotriangles of ∼50%.[15]

Another strategy to synthesize nanotriangles is based on the addition of size-controlling agents, for example, lemon grass extracts[25] or tryptophan,[26] but also the confinement of dendrimers, block copolymer micelles, or vesicles leads to the formation of asymmetric nanoplatelets.[27−29] A halide-free

Received: August 17, 2017
Revised: February 20, 2018
Published: March 27, 2018

DOI: 10.1021/acs.langmuir.7b02898
Langmuir 2018, 34, 4584−4594

synthesis of Au nanoplates was demonstrated by Chen et al. in the presence of Au/Ag nanorings and polyvinylpyrrolidone (PVP).[30] By using mixed vesicles as a template phase, the amount of nanotriangles can be increased by adding polymers as symmetry-breaking components, for example, a maltose-modified polyethylenimine[31] or polyampholytes.[16] By using small-angle X-ray scattering (SAXS) and UV−vis spectroscopy in combination with TEM micrographs, we recently demonstrated that the nanotriangle growth process starting inside of multivesicular vesicles can be described by an Ostwald ripening mechanism at the periphery of loosely packed gold nanoparticle aggregates.[32] Under optimized conditions the amount of anisotropic particles does not exceed 60%, and the corresponding amount of nanotriangles (NTs) is 30%.[16] Therefore, in all cases an additional separation step to purify the gold nanoplatelets is needed. Park et al. proposed a surfactant micelle-induced separation process for nanoparticles of different size and shape.[33] A simple purification method based on the nanoparticle surface area discrepancy, which separates particles with the same mass but different shapes, was reported by Lui and coworkers.[34] Scarabelli et al. have shown that a CTAC-micelle-based depletion flocculation is useful to separate gold nanoplatelets from spherical gold nanoparticles.[15] A shape- and size-selective separation of gold nanotriangles in a two-step approach using CTAB and CTAC micelles was presented by Zhang et al.[35]

Our recently published separation technique by a polyelectrolyte/AOT-micelle-based depletion flocculation is a successful way to isolate very stable negatively charged gold nanoplatelets that have been used in ultrafast X-ray diffraction studies and for SERS.[16,36] The advantage of the AOT/phospholipid-based one-step procedure is the formation of long-time stable nanoplatelets that are not only form-stable for more than a month but also can even be irradiated with laser fluences up to F = 2.9 mJ/cm^2.[36] Very recently, close-packed large area monolayers (>1 cm^2) of highly ordered nanoplatelets have been formed on different substrates, that is, silicon wafer and quartz glass, after adding ethanol−toluene mixtures.[37]

The idea of the present study is to build up colloidal superstructures that combine properties of nanoplatelets with the catalytic properties of small spherical nanoparticles, which also enhances the SERS performance due to increased surface roughness. To the best of our knowledge, time-dependent studies of oriented overgrowth of gold clusters onto the surface of gold nanoplatelets have not been reported up to now.

In this paper, we describe the synthesis of spherical gold nanoparticles in a polymer shell surrounding the nanotriangles. At first the negatively charged nanoplatelets were reloaded by adding the polycation polyethylenimine (PEI), before gold chloride was added to the PEI-entrapped nanoplatelets, and the system was heated to 100 °C. The time-dependent process of nanoparticle formation in the PEI shell was investigated by UV−vis spectroscopy, TEM, SAXS, and DLS measurements.

For a more comprehensive interpretation of these results the time-dependent gold nanoparticle formation was analyzed in pure PEI solution (reference system) before starting the experiments in the presence of the gold nanoplatelets.

2. EXPERIMENTAL SECTION

2.1. Chemicals. The tetrachloroauric(III)acid ($HAuCl_4 \cdot 3H_2O$) was purchased from Sigma-Aldrich. The hyperbranched polyethylenimine with a molar mass of 25 000 g/mol was obtained from the BASF (Lupasol G100). Milli-Q Reference A+ water was used in all experiments.

2.2. Methods. UV−vis absorption measurements were performed with a Shimadzu UV−2600 spectrophotometer in the wavelength range between 200 and 1400 nm. Shape and size of the gold nanoparticles were determined by using the transmission electron microscope JEM-1011 (JEOL) at an acceleration voltage of 80 kV as well as the JEM-2200 FS (JEOL) at 200 kV for high resolution (HRTEM) and fast Fourier transformation (FFT). For tomographic reconstruction at the HRTEM a tilt series from −62 to +50° was recorded with a step width of 2°. Samples were dropped on carbon-coated copper grids and quickly dried by removing the excess liquid with filter paper. SEM micrographs were obtained using a ZEISS Supra 55PV scanning electron microscope at an acceleration voltage of 4 kV. Dynamic light scattering (DLS) and zeta potential measurements were performed with the Malvern Nano Zetasizer 3600. In situ small-angle X-ray scattering (SAXS) measurements were performed with a slit-focus instrument (SAXSess from Anton Paar) as described in detail in our recent study on the formation of gold nanotriangles.[32] In the present study the temperature of the samples was 100 °C and the measurement time for collecting scattering data was 1 min.

A confocal Raman microscope (JASCO NRS-4100) equipped with laser excitation at wavelength of 785 nm was used to investigate the SERS performance. The laser beam was focused on the sample through 100× objective lens. The laser power was 2 mW and the Raman band of the silicon wafer at 520 cm^{-1} was used to calibrate the spectrometer.

2.3. Experimental Part. The nanotriangles were synthesized according to the protocol in ref 16. This means a 0.5 wt % phospholipid and 0.5 wt % AOT solution was stirred for 24 h at room temperature in the presence of the strongly alternating polyampholyte (0.01 wt %) poly(*N*,*N*-diallyl-*N*,*N*-dimethylammonium-*alt*-3,5-bis-carboxyphenyl-maleamic carboxylate) to produce the vesicular template dispersion, which was mixed with a freshly prepared 2 mM tetrachloroaureate precursor solution. After 45 min at 45 °C, a purple-colored gold nanoparticle solution was obtained. The produced nanotriangles were separated from spherical gold nanoparticles via a depletion flocculation by adding a 0.02 M AOT solution. After several washing and centrifugation steps (8 min at 13 000 rpm) the resulting gold nanotriangle stock solution was characterized by TEM (compare Figure S3) and DLS measurements (Figure S2) before being used in the following experiments.

Zeta potential measurements verify the reloading process of the negatively charged nanotriangles in the stock solution by adding a 2 wt % PEI solution.

The gold nanotriangle stock solution was mixed together with the 2 wt % PEI solution and the 2 mM gold chloride precursor solution in a volume ratio of 1:1:1. The resulting aqueous solution was heated to 100 °C. For the time-dependent measurements, every 5 min a sample was taken from the hot solution and cooled in an ice bath to stop the gold growing process immediately. Subsequently the samples were characterized by UV−vis spectroscopy, DLS measurements, TEM microscopy, and SAXS experiments.

To prepare a sample for SERS measurements, a droplet of the aqueous dispersion was placed on a silicon wafer, and after adding an ethanol−toluene mixture with a volume ratio 5:1 a film casting was observed similar to the procedure previously described by us.[37] After solvent evaporation the silicon wafer was immersed in 10 mM 4-nitrothiophenol (4-NTP) ethanolic solution for 6 h and washed in ethanol before starting SERS experiments.

3. RESULTS AND DISCUSSION

3.1. Time-Dependent Gold Nanoparticle Formation in PEI Solution. We first report the growth of spherical nanoparticles in PEI solution in the absence of gold nanotriangles. Previous investigations have shown the best nanoparticle stabilization with gold reduction via PEI of the molar mass of 25 000 g/mol, which proceeded rapidly at 100 °C.[10,38] About 5 min after adding the gold chloride solution to

DOI: 10.1021/acs.langmuir.7b02898
Langmuir 2018, 34, 4584−4594

the 2 wt % PEI solution at 100 °C, the peak at 330 nm in the UV−vis spectrum (Figure 1) can be related to the formation of

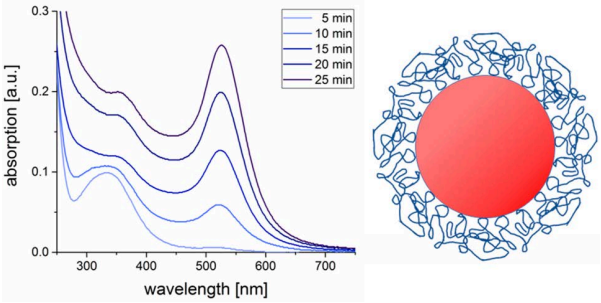

Figure 1. Gold nanoparticle formation in a PEI solution investigated by time dependent UV−vis measurements with a scheme of a PEI-entrapped gold nanoparticle.

very small gold nanoparticles or gold clusters. Previously, we have shown that fluorescent gold clusters, synthesized in PEI-containing microemulsion droplets, with particle dimensions smaller than 2 nm absorb at 350 nm.[39] For example, Au_{11} clusters produce absorption peaks in the same range between 370 and 416 nm, which strongly depends on the components stabilizing the Au clusters.[40,41] While small particles <2 nm are above the limit where the crystal field levels split, they are not large enough to express a coherent surface plasmon resonance (SPR). In addition to the cluster absorption peak at 334 nm a second peak at 526 nm was observed, indicating the existence of a second particle generation showing surface plasmon resonance. This SPR peak was clearly visible after 10 min and increased on the time scale of minutes step by step. The first cluster peak shifts from 349 nm (after 15 min) to finally 358 nm, verifying that over the whole time period new clusters are formed, which grow up to colloidal dimensions.

Complementary DLS experiments performed with the Nano Zetasizer underline the UV−vis statements and are discussed in the Supporting Information in more detail (Section SI.1). We conclude that the confinement effect of the hyperbranched PEI is not strong enough to terminate the formation of gold particles on the cluster level. In consequence, larger colloidal particles are produced.

3.2. Time-Dependent Gold Nanoparticle Formation in PEI Solution in the Presence of Gold Nanotriangles. The green-colored aqueous dispersion containing gold nanoplatelets with a platelet thickness of 7.5 ±1.5 nm and an edge length of ∼175 nm was synthesized in a vesicular template phase, according to the procedure previously described by us.[16] The nanoplatelets were separated by a polyelectrolyte/AOT micelle-based depletion flocculation and redispersed in water and characterized by electrophoretic light scattering. After washing, the zeta potential of the negatively charged nanoplatelets in the nanotriangle stock solution is −34 ± 1 mV. The negative zeta potential indicates that AOT micelles are adsorbed on the gold surface,[42−44] by analogy to adsorbed CTAB micelles on gold nanorods.[45] Therefore, polycations can attach onto the negatively charged AOT layer, resulting in a reloading of the zeta potential. Zeta potential measurements by adding polyethylenimine to the stock solution (in comparison to the reference system discussed above) show a shift to a positive mean value of +12 ± 0.5 mV, indicating the PEI adsorption. On the basis of these experimental data we can conclude that an AOT/PEI bilayer was formed on the surface of the nanotriangles, schematically shown in Scheme 1.

Scheme 1. Au^{3+} Ion Penetration and Reduction Process in the AOT/PEI Bilayer Embedding the Gold Nanotriangles

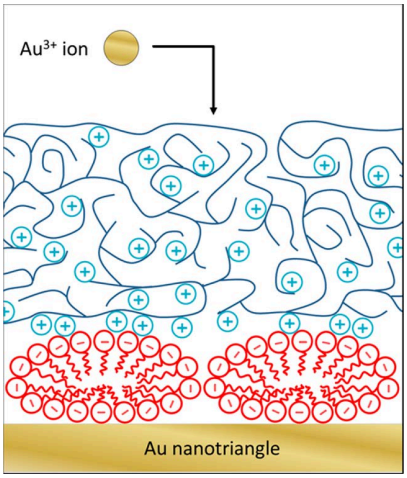

A TEM micrograph of the nanotriangle stock solution is shown in Figure S3 (Supporting Information). After mixing the nanotriangle stock solution with the 2 wt % PEI solution and the 2 mM gold chloride precursor solution in volume ratio 1:1:1 and heating the system to 100 °C the gold reduction process starts immediately.

Initially, the UV−vis experiments recorded in the presence of the PEI-entrapped gold nanoplatelets show an absorption maximum at 1310 nm (Figure 2). After 5 min this peak shifted to 1243 nm as the dielectric function of the platelets' environment changed with the cluster formation, evidenced by the cluster peak at 330 nm. After 10 min, the cluster peak broadened, and the SPR peak at 526 nm was detected, which evidences the formation of colloidal spherical particles, which are not attached to the nanotriangles. The peak associated with the triangles is shifted to even lower wavelength of ∼1183 nm. Recently, a blue shift with increasing thickness of nanoprisms was shown by other authors.[46] In our system the blue shift can be explained by an increase in the platelet thickness. In the following time period between 15 and 25 min a small shift of the cluster peak from 350 to 360 nm can be seen, which is in agreement with the reference system discussed above. At the same time the SPR peak at 526 nm increased and the nanotriangle peak broadened and developed a shoulder at ∼800 nm. We emphasize that the shoulder reached a maximum after 10 min. Simulations of optical spectra of spherical particles have shown the appearance of an absorption peak between 700 and 800 nm after incorporating tips in full agreement with the experimental spectra of nanostars.[46] Senthil Kumar et al.[47] have already shown that there is a good agreement with the tip, defined by a 3 nm rounding radius, and the calculated spectra by means of the boundary element method.[48] On the basis of this data the shoulder at 800 nm can be considered as a first hint to the undulated surface of our triangles, but for a more comprehensive discussion the nanotriangles must be investigated in more detail. Time-dependent DLS experiments (shown in Section SI.2) are insensitive to the surface modification of the nanotriangles, but they show a similar formation of spherical nanoparticles, as observed without NTs.

DOI: 10.1021/acs.langmuir.7b02898
Langmuir 2018, 34, 4584−4594

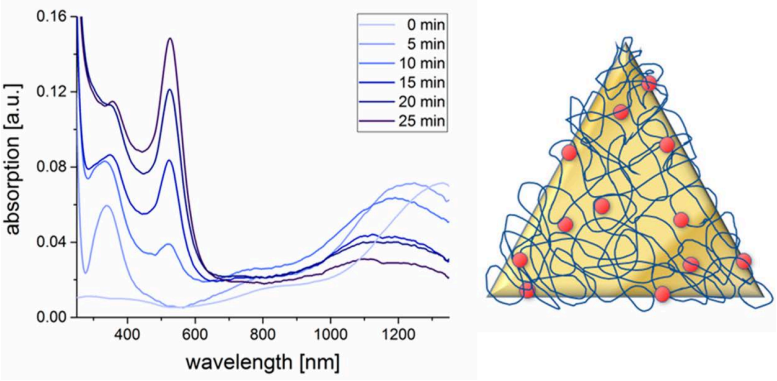

Figure 2. Gold nanoparticle formation in a PEI solution in the presence of gold nanotriangles investigated by time-dependent UV–vis measurements with a scheme of gold nanoparticles formed in the PEI-shell surrounding the gold nanotriangle.

Time-dependent TEM and SAXS experiments, however, clearly show the growth of hemispherical particles on the NT.

The TEM micrographs already show the formation of cluster-like nanoparticles embedded into the PEI shell on the surface of the nanoplatelets after 5 min. TEM tomographic experiments, by tilting the stage, underline these results (Figure 3). This means that the Au^{3+} reduction process, performed in

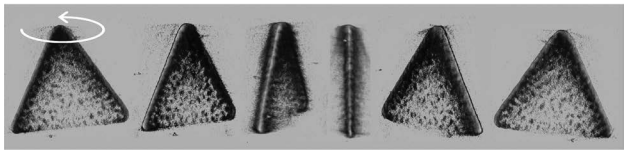

Figure 3. Reconstructed tomography images of asymmetric nanoplatelets with embedded gold clusters after 5 min.

the PEI shell surrounding the nanoplatelets, leads to the formation of gold clusters, which grow up to half-spherical particles on the top or bottom of the platelets with undulatory shaped edges (Figure 4, Figure S4). In the following 15 min, the edge-decorated NTs become more indistinct; this means that the undulation of the edges is decreased again, resulting in more rounded triangles. This is in good agreement with the decrease in the absorption shoulder at 800 nm previously discussed. Two micrographs with a number of undulated platelets are shown in the Supporting Information (Figure S4).

The HRTEM micrographs in the JEM 2200 FS confirmed the hemispherical gold nanoparticles that grow onto the surface of the NT platelets (compare Figure 5). Corresponding fast Fourier transformation (FFT) of the whole region and the marked region in Figure 5 shows that the hemispherical nanoparticles have the same orientation as the triangles. The {220} reflections in both FFTs correspond to a lattice distance of 0.144 nm. The six-fold symmetry of these reflections indicates a <111> orientation of an fcc single crystal, and the flat facets of the triangle are parallel to the {111} plane. This means that the "half-spheres" grow onto the {111} facets at the nanotriangle surface without a grain boundary. The resulting undulated superstructure is formed at top and bottom as well as at the edges of the triangles.

By tilting the stage, the side projection of the triangles was visualized (compare Figure 5c). The profile of the undulated triangles, schematically demonstrated in Figure 5, shows a minimum value of the platelet thickness of ~11 nm and a maximum value of ~15 nm. Considering that the thickness of

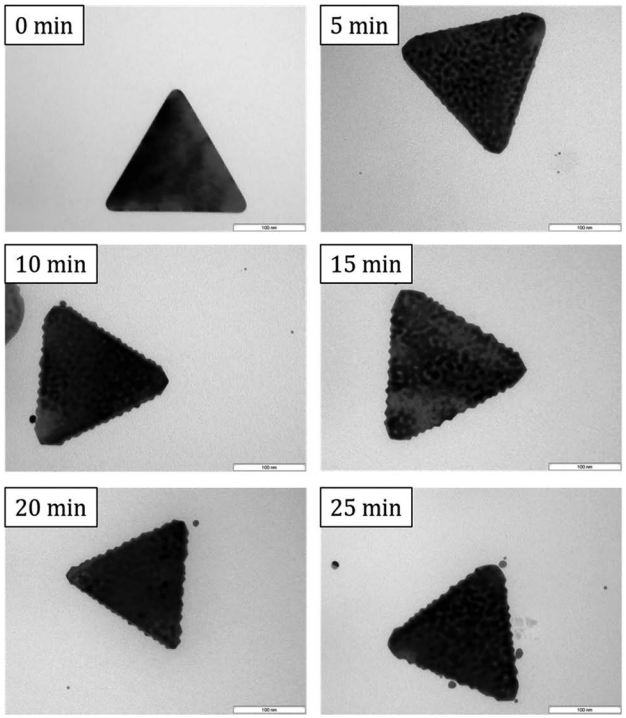

Figure 4. Time-dependent TEM micrographs of the gold nanoparticle formation onto the nanotriangles.

the platelet at the beginning is 8 nm and the diameter of the sphere is 7 nm, it can be concluded that on both sides of the platelet "half-spheres" grow on the NT surface. Such a "half-sphere" is shown in the magnified micrograph in Figure S5 (Supporting Information). It has to be stated here that the platelet thickness obtained by TEM side projection should be larger than that by other methods (e.g., SAXS) due to deviations of the tilting angle from exactly 90°.

The crystallization process of our "half-spheres" in the PEI shell is quite different from the spike formation process in a concentrated PVP solution in DMF, reported by the Liz-Marzán group.[47] In the presence of PVP as reducing agent the rapid growth along the [110] direction leads to the formation of room-temperature stable nanostars,[47,49] or spiked gold nanorods.[50] This means the type of polymer, used as reducing agent, strongly influences the crystallization process. Our platelets consist of {111} facets, which are embedded in an

DOI: 10.1021/acs.langmuir.7b02898
Langmuir 2018, 34, 4584–4594

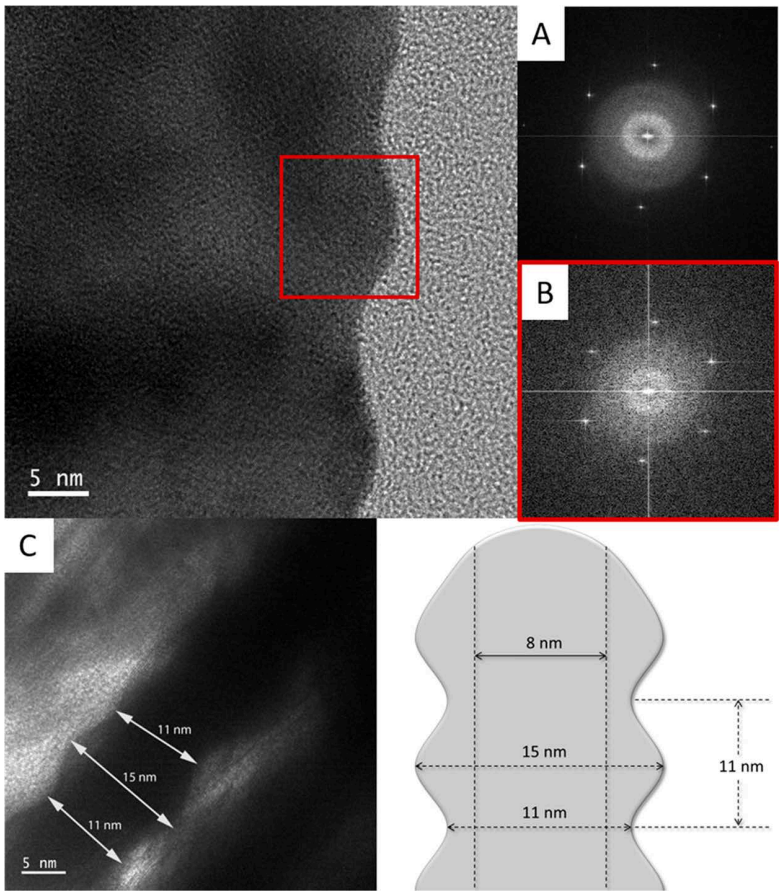

Figure 5. HRTEM micrograph of the nanotriangle edge region with the corresponding FFTs: FFT of the whole region (A) and FFT of the marked region (B). HRTEM micrograph of the side projection of a nanotriangle superstructure after tilting the stage (C) and the corresponding scheme showing the triangle profile.

AOT/PEI bilayer (compare Scheme 1). The diffusion of Au^{3+} ions through the AOT/PEI bilayer seems to slow down the penetration of Au (ions/clusters) to the NT surface.

We conclude that in a first step the Au^{3+} ions are transported to the AOT/PEI bilayer, schematically shown in Scheme 1. In the next step the Au^{3+} ions penetrate into the PEI layer. Inside of the PEI layer the reduction process starts and gold clusters are formed in the first 5 min. In the following time period the clusters diffuse and grow on the (111) facets of the gold nanotriangle surface to become half-spheres. This process can be understood only by a hindered transportation of Au^{3+} ions through the AOT/PEI bilayer. The slow penetration of Au^{3+} ions through the electrostatically stabilized micelle/polycation bilayer leads to the formation of individual gold seeds, which grow up very slowly and are separated from each other on the <111> facets of the gold nanotriangle surface. This is in contrast with the fast transport of metal ions through an isolated polymer or surfactant bilayer shell, resulting in both cases in a layer overgrowth.[50,51]

We performed in situ SAXS measurements during gold nanoparticle formation at 100 °C to check the results from TEM. The "Guinier" term for the nanotriangles should only change if something is added or removed on their surfaces. The formation of the "free" gold nanoparticles in solution is added as a separate term with different q-dependency. Thus it can be seen that the surfaces of the nanotriangles grow in their thickness or spherical gold nanoparticles grow up in solution, separately. Examples of scattering curves measured at reaction times of 1 and 5 min are shown in Figure 6 (symbols). For clarity, t = 1 and 5 min mean that the SAXS data were collected for 1 min, that is, between 0 and 1 min and from 4 to 5 min,

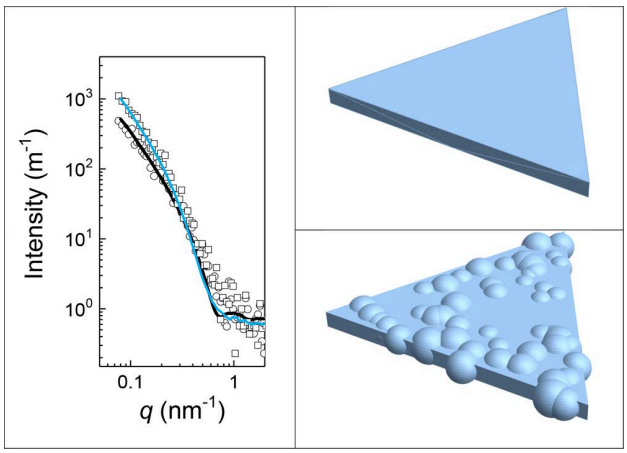

Figure 6. (Left) Scattering intensity of the nanotriangles after 1 and 5 min of reaction (spheres and squares, respectively). Curve simulations are from models of a nanotriangle with a flat surface and an undulated surface (black and blue solid line). (Right) Corresponding structures used for calculation of the scattering curves.

DOI: 10.1021/acs.langmuir.7b02898
Langmuir 2018, 34, 4584−4594

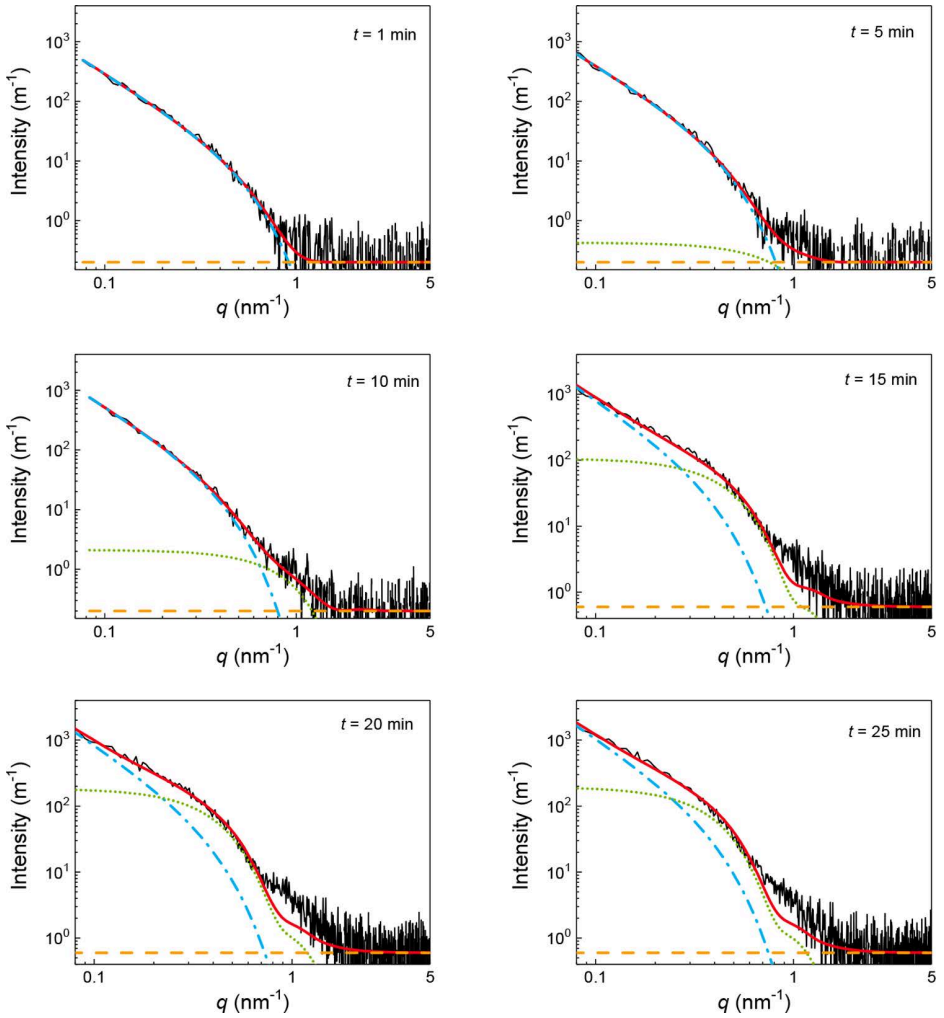

Figure 7. SAXS curve at reaction times of t = 1, 5, 10, 15, 20, and 25 min and corresponding curve fits (red solid lines). The individual contribution of the curve fitting, consisting of the Guinier model for platelets (nanotriangles including hemispheres on them), additional gold spheres not in contact with the nanotriangles, and a scattering background are given (blue dashed-dotted, green dotted, and yellow dashed lines, respectively).

respectively. It can be seen that the scattering intensity of the t = 5 min curve is higher than that of the t = 1 min measurement in a q range of 0.08 to 0.4 nm^{-1}. Such finding has to be expected if hemispheres grow on the surfaces of the nanotriangles. Simulations of the scattering of a nanotriangle with a flat surface and with hemispheres on the surface were performed. Cartoons of the two structures are shown in Figure 6. These Figures were generated by randomly positioning spheres within the nanotriangle. Calculations of the corresponding SAXS curves were performed by applying the Debye formula with the technique used by Hansen.[52]

A visual comparison of the measured SAXS data and these simulations indicates a qualitative agreement of the proposed structure models and the corresponding scattering curves. Unfortunately, a quantitative application of the Hansen approach is not possible in our study because the signal-to-noise ratio is relatively low due to the short measurement time of 1 min.

For a more quantitative evaluation we tentatively assume that the scattering curves in different stages of the reaction can be sufficiently described by the sum of the scattering from the nanotriangle with the hemispheres thereon $I_{\text{Guinier}}(q)$ and the scattering of "free" spheres $I_{\text{sphere}}(q)$. Our hypothesis is that the spheres are separated from the nanotriangles and formed predominantly in later stages of the reaction. Under these assumptions, the entire scattering is given by

$$I(q) = I_{\text{Guinier}}(q) + I_{\text{sphere}}(q) + b$$

where b represents a constant background.

The Guinier approximation of sheet-like structures according to Hjelm et al.[53] can be applied to the nanotriangles because the edge length of about 175 nm is much larger than the thickness of 7.5 ± 1.5 nm as

$$I_{\text{Guinier}}(q) = \frac{2\pi}{q^2}\Delta\mu \exp(-R_d^2 q^2)$$

The $\Delta\mu$ is the excess cross section per unit area of the plate over that of an equivalent volume. The transverse radius of gyration R_d is taken in the direction normal to the nanotriangles' surface. For a flat surface of the triangle its thickness is calculated as $d = \sqrt{12}\,R_d$; that is, a thickness of 7.5 ± 1.5 nm corresponds to an R_d value of 2.17 ± 1.5 nm. The Guinier law is independent of the details of the structure and therefore applicable for flat and undulated structures. Note that

DOI: 10.1021/acs.langmuir.7b02898
Langmuir 2018, 34, 4584−4594

the d value is an apparent thickness for undulated nanotriangles when calculated from R_d.

The formula for curve fitting of spheres $I_{sphere}(q,R,\Delta\eta)$ with Gaussian number-weighted size distribution $Gauss(R,N,\sigma,R_0)$ is

$$I_{sphere}(q) = \int_0^\infty Gauss(R, N, \sigma, R_0) \left[\frac{4}{3}\pi R^3 \Delta\eta \left(3\frac{\sin(qR) - qR\cos(qR)}{(qR)^3}\right)\right]^2 dR$$

where the Gaussian size distribution is defined as

$$\text{Gauss}(R, N, \sigma, R_0) = N[\sqrt{\pi/2}\,\sigma(1 + \text{erf}(R_0/(\sqrt{2}\sigma)))]^{-1} e^{-(R-R_0)^2/2\sigma^2}$$

Examples for measured curves, curve fits, and the contributions of the nanotriangles, spheres, and background at reaction times of t = 1, 5, 10, 15, 20, and 25 min are shown in Figure 7. The scattering results exclusively from the nanotriangles at 1 min, as expected (blue dashed-dotted line). At 5 min the scattering is dominated by the nanotriangles, while a very small contribution of free spheres is visible (blue dashed-dotted and green dotted line, respectively). In later stages of the reaction the relative amount of the scattering of the spheres increase successively in relation to the scattering of the nanotriangles.

The increase in the apparent height of the nanotriangles and the radii of the free spheres are shown in Figure 8 (blue squares and green spheres, respectively). It can be seen there that heights increase monotonously from 1 to 10 min and become constant at larger reaction times. By contrast, no spheres were found for reaction times smaller than 5 min (indicated as (a) in Figure 8). A growing number of free gold spheres with a mean radius of 2 nm develop between 5 and 10 min (indicated as (b)). Their radii grow to ~5 nm between 10 and 25 min (indicated as (c)).

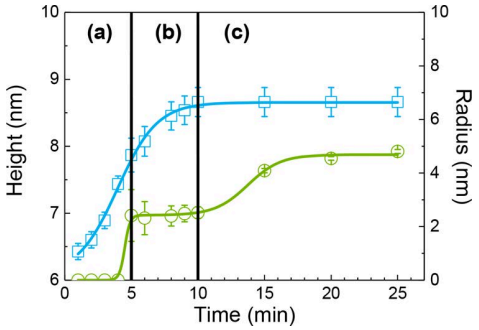

Figure 8. Changes of the apparent height of the gold triangles (triangle height plus hemispheres on the triangle surface) and radii of spheres formed in solution (blue and green symbols, respectively). Solid lines are curve fits using a single Boltzmann growth function for the apparent height of the nanotriangles and a bimodal Boltzmann growth function for the spheres (blue and green lines, respectively). The three stages of the reaction are indicated by (a), (b), and (c).

We employed a single and double Boltzmann equation[54] for quantitative description of the growth kinetics of the nanotriangles heights and the radii of the spheres. Therefore, the heights are described by

$$d(t) = \frac{d_1 - d_2}{1 + \exp[(t - t_0)/k]} + d_2$$

where d_1 and d_2 are the initial and final height, respectively, t_0 is the inflection point of the curve with $d(t) = (d_1 - d_2)/2$, and k is the slope factor. The best-fit curve for quantification of $d(t)$ is shown in Figure 8 (blue solid curve) with parameter values of d_1 = 6.08 ± 0.14 nm, d_2 = 8.65 ± 0.03 nm, t_0 = 4.0 ± 0.2 min, and k = 1.5 ± 0.2 min.

The double Boltzmann function for quantification of the increase in the radii of the free spheres $R(t)$ is given by

$$R(t) = R_f\left[\frac{p}{1 + \exp[(t - t_1)/k_1]} + \frac{1 - p}{1 + \exp[(t - t_2)/k_2]}\right]$$

R_f is the radius at the end of the measurement, p and $1 - p$ are the radii fraction of R_f in growth steps 1 and 2, t_1 and t_2 are the centers of the reaction steps, and $k_1$and k_2 are the corresponding slope factors. The fit result applying $R(t)$ is shown in Figure 8 (green solid curve). Best-fit parameters are R_f = 4.69 ± 0.09 nm, p = 0.52 ± 0.03 nm, t_1 = 4.5 ± 0.1 min, t_2 = 13.7 ± 0.6 min, k_1 = −0.2 min, and k_1 = −1.2 min.

These SAXS results support the conclusions drawn from TEM investigations and provide quantitative parameters about the reaction kinetics. Furthermore, SAXS allows us to distinguish between particles formed in solution and in the PEI shell surrounding the nanotriangles.

3.3. Separation of the PEI-Modified Gold Nanotriangles and Their SERS Performance. To separate the undulated gold nanotriangles (AuNTs) from the spherical particles in solution, the sample after 15 min of growth was centrifuged two times for 8 min at 13 000 rpm. UV−vis measurements clarify the successful separation (Figure 9). The absorption peak of the spherical particles at 526 nm is no longer present for the purified sample. It has to be mentioned here that a similar UV−vis spectrum (compare Figure S6) can be obtained by decreasing the PEI concentration, indicating the predominant formation of gold nanoparticles in the PEI shell surrounding the nanotriangles. This means that the purification process can be avoided by optimizing the PEI concentration, which is needed only for the nanotriangle coating; however, the nanotriangle concentration has to be determined very exactly. This will be possible by additional SAXS experiments. The processed undulated AuNTs were deposited on a silicon wafer by a recently described technique.[36] A droplet of the dispersion was set on the surface of the substrate. Then, an ethanol−toluene (5:1) mixture was added to the droplet, which leads to

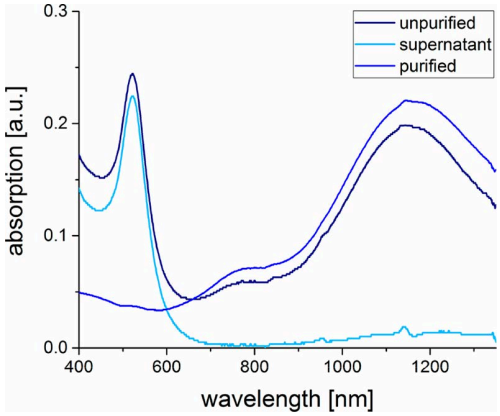

Figure 9. UV−vis spectra of the unpurified and the purified AuNT sample.

DOI: 10.1021/acs.langmuir.7b02898
Langmuir 2018, 34, 4584−4594

a complete wetting of the substrate and a close-packed layer formation at the interface. After the evaporation of the liquid, the close-packed layer (shown in Figure 10) remains on the substrate.

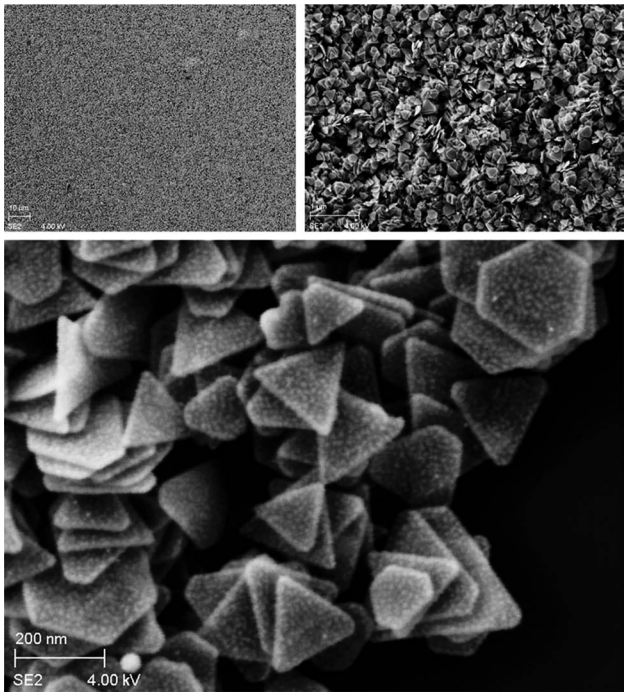

Figure 10. SEM micrographs at different magnifications of the close-packed gold nanotriangle layer on the surface of the silicon wafer.

To study the SERS performance, these AuNTs-fabricated silicon wafers were immersed in 10 mM ethanolic solution of 4-nitrothiophenol (4-NTP) for 6 h to ensure a complete coverage of the sample with 4-NTP that binds to the Au surface via the thiol group.[55,56] The substrate was then washed several times in water and ethanol to guarantee the removal of the physiosorbed excess molecules. Subsequently, the wafers were dried in air before being used. In Figure 11, the SERS spectra of this undulated gold nanotriangle film (blue) using 4-NTP molecules as the analyte are compared with SERS spectra obtained from nanotriangles without undulation[36] (red) and to Raman spectra of 4-NTP powder (black). These three spectra were recorded under identical settings of the Raman microscope. The spectra are dominated by three main peaks at 1077, 1332, and 1575 cm^{-1} assigned to the C−H bending, NO_2, and C═C stretching modes of 4-NTP, respectively. The blue spectrum recorded on undulated NT shows additional lines, which are not observed in the red and black spectra. Some of them can be attributed to the product of a photoinduced dimerization of 4-NTP to DMAB: Peaks at 1134, 1387, and 1434 cm^{-1} are assigned to the C−N symmetric stretching and N═N stretching vibrational modes of DMAB. As a confirmation, we added the magenta line, which shows a SERS spectrum obtained from nonundulated Au-NTs illuminated with a larger fluence, which is known to drive this reaction.[37] This suggests an increased photocatalytic activity of the undulated Au surfaces because the photocatalytic reaction can be driven at lower light intensity. Additional peaks in the range 1150 to 1210 cm^{-1} and at 1610 cm^{-1} can be assigned to vibrational modes of the analyte including C−H bending and

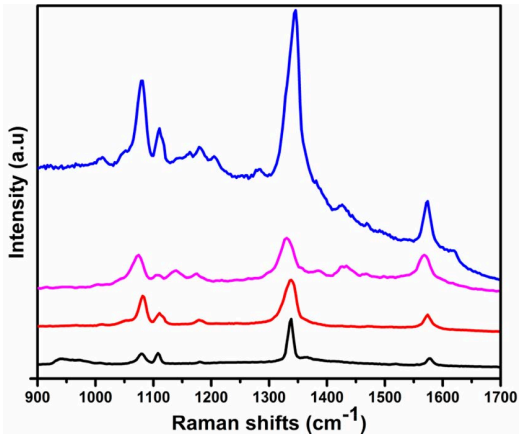

Figure 11. Raman spectra of 4-NTP recorded under identical conditions: 4-NTP powder (black), 4-NTP on nonmodified GNTs (red), and 4-NTP on undulated GNTs (blue). The magenta line was recorded under a higher fluence for the nonmodified GNTs to drive the dimerization reaction to DMAB.

ring deformation motions,[57] which are enhanced by the rough surface of the undulated Au-NTs. The enhancement of such weak modes probably originates from a symmetry breaking on the rough surface or because molecules can be tilted toward the gold surface so that the C−H groups approach the metal surface.

The SERS performance was estimated by the enhancement factor EF, which is the ratio of SERS intensity to Raman intensity for a selected vibrational mode of the analyte under the same conditions (laser and sample conditions) using the following equation

$$EF = \frac{I_{SERS}}{N_{SERS}} / \frac{I_{normal}}{N_{normal}}$$

where I_{SERS} and I_{normal} are the Raman intensity of the NO_2 vibrational mode at 1332 cm^{-1} for the 4-NTP molecules adsorbed on the gold nanotriangles and solid 4-NTP, respectively. N_{SERS} and N_{Normal} are the number of the 4-NTP molecules adsorbed on the gold nanotriangles and solid 4-NTP in the laser spot, respectively. For the characteristic Raman peaks of 4-NTP, the enhancement of Raman scattering can be directly seen from the spectra in Figure 11 because they were recorded under identical conditions in the microscope. In particular, the relative scattering intensity of undulated NTs is about four times larger than the intensity for flat NTs. This is mainly due to the stacking of the undulated NTs, which could not be avoided for the undulated NTs. The SERS substrate with flat NTs is a monolayer.[37] Each gold platelet has a thickness of ∼10 nm so that only about three platelets stacked on top of each other efficiently contribute to the SERS signal because the light intensity is attenuated with a penetration depth of ∼15 nm. Thus the SERS enhancement factor is only slightly larger for the undulated NTs.

If we assume a compact 4-NTP monolayer adsorbed on both surfaces of the platelets, we calculate $N_{SERS} = 8 \times 10^6$ from the laser spot with a diameter of 1 μm and the area of 0.2 nm^2 occupied by an adsorbed 4-NTP molecule. On the basis of the density of bulk 4-NTP, we estimated $N_{Normal} = 1 \times 10^{11}$ in the focal volume under the illuminated spot. Finally, the enhancement factor was found to be 6×10^4 (monolayer adsorption on both surfaces). Assuming two or three platelet layers that

DOI: 10.1021/acs.langmuir.7b02898
Langmuir 2018, 34, 4584−4594

contribute to the signal because the sample is not a monolayer, this enhancement factor is a bit overestimated. In any case, the direct comparison of the undulated and flat NTs shows an enhanced SERS performance. To check the uniformity of the SERS substrate, several spots were measured under the same conditions, and nearly the same signal enhancement was reproduced (compare Figure S7).

A small fluctuation of the intensity might be explained by different orientations of spots[58] and changes of the molecular orientation on the surface.[15] The enhancement factor is found to be somewhat larger than the value recorded by us for the unmodified gold nanotriangles under the same conditions with the same analyte,[16,37] as can be seen in Figure 11. Note that different EF values are reported in the literature depending on the type of analyte and SERS performance in solution or on different substrates.[59] In general, anisotropic gold nanoparticles such as gold nanotriangles and gold nanostars were reported to have high enhancement factors owing to their structures.[15,49−51,55−61] The high enhancement factor mainly originates from the tips of the particles where the local electromagnetic field and the Raman scattering are enhanced. Moreover, assembly of these nanostructures into closely packed monolayers may result in a higher Raman enhancement because new "tip to tip" nanogaps were produced. Hence, the enhancement of our undulated AuNTs can be related to the SERS hot spots provided by the rough surface due to the presence of the "half-spheres", curved edges, and the junctions formed between these edges and their neighbors.

4. CONCLUSIONS

When the hyperbranched PEI is used as a reducing and stabilizing agent for the gold nanoparticle formation at 100 °C, predominantly gold clusters with an UV−vis maximum at 330 nm are formed inside of the polymer network. In an aqueous PEI solution, the gold clusters located in the branched PEI network start to grow up to colloidal dimensions with a particle size of ∼6 nm. If this process is realized in a AOT/PEI bilayer shell surrounding gold nanoplatelets, then the clusters crystallize onto the {111} facets at the bottom and top surfaces of the platelets as well as the edges and build up "half-spheres" without a grain boundary in contrast with the gold nanostar formation observed in the presence of PVP. SAXS results show that undulated nanotriangles are preferentially formed in the first 10 min, before gold clusters in solution start to grow up to colloidal dimensions. In comparison with the unmodified gold nanotriangles, the undulated ones show significantly increased photocatalytic activity for the dimerization of 4-NTP and an increased enhancement factor in SERS.

■ ASSOCIATED CONTENT

Supporting Information

The Supporting Information is available free of charge on the ACS Publications website at DOI: 10.1021/acs.langmuir.7b02898.

DLS part, four TEM micrographs, one UV−vis spectrum, and several SERS spots (PDF)

■ AUTHOR INFORMATION

Corresponding Author

*E-mail: koetz@uni-potsdam.de. Phone: +49 331 977 5220.

ORCID

Andreas F. Thünemann: 0000-0002-9883-6134

Matias Bargheer: 0000-0002-0952-6602

Joachim Koetz: 0000-0001-9113-1337

Notes

The authors declare no competing financial interest.

■ ACKNOWLEDGMENTS

The financial support from the German Research Foundation (KO 1387/14-1; INST 336/64-1) is gratefully acknowledged. We thank Brian R. Pauw for simulation of the scattering curves of nanotriangles with flat surface and hemispherical caps on the nanotrinagles.

■ REFERENCES

(1) Daniel, M. C.; Astruc, D. Gold nanoparticles: assembly, supramolecular chemistry, quantum-size-related properties, and applications toward biology, catalysis, and nanotechnology. *Chem. Rev.* **2004**, *104*, 293−346.

(2) Millstone, J. E.; Park, S.; Shuford, K. L.; Qin, L.; Schatz, G. C.; Mirkin, C. A. Observation of a Quadrupole Plasmon Mode for a Colloidal Solution of Gold Nanoprisms. *J. Am. Chem. Soc.* **2005**, *127*, 5312−5313.

(3) Elghanian, R.; Storhoff, J. J.; Mucic, R. C.; Letsinger, R. L.; Mirkin, C. A. Selective Colorimetric Detection of Polynucleotides Based on the Distance-Dependent Optical Properties of Gold Nanoparticles. *Science* **1997**, *277*, 1078−1081.

(4) Perrault, S. D.; Walkey, C.; Jennings, T.; Fischer, H. C.; Chan, W. C. W. Mediating Tumor Targeting Efficiency of Nanoparticles Through Design. *Nano Lett.* **2009**, *9*, 1909−1915.

(5) Qian, X.; Peng, X.-H.; Ansari, D. O.; Yin-Goen, Q.; Chen, G. Z.; Shin, D. M.; Yang, L.; Young, A. N.; Wang, M. D.; Nie, S. In vivo tumor targeting and spectroscopic detection with surface-enhanced Raman nanoparticle tags. *Nat. Biotechnol.* **2008**, *26*, 83−90.

(6) Paciotti, G. F.; Myer, L.; Weinreich, D.; Goia, D.; Pavel, N.; McLaughlin, R. E.; Tamarkin, L. Colloidal Gold: A Novel Nanoparticle Vector for Tumor Directed Drug Delivery. *Drug Delivery* **2004**, *11*, 169−183.

(7) Duncan, B.; Kim, C.; Rotello, V. M. Gold Nanoparticle Platforms as Drug and Biomacromolecule Delivery Systems. *J. Controlled Release* **2010**, *148*, 122−127.

(8) Turkevich, J.; Stevenson, P. C.; Hillier, J. A study of nucleation and growth processes in the synthesis of colloidal gold. *Discuss. Faraday Soc.* **1951**, *11*, 55−75.

(9) Link, S.; El-Sayed, M. A. Size and temperature dependence of the plasmon absorption of colloidal gold nanoparticles. *J. Phys. Chem. B* **1999**, *103*, 4212−4217.

(10) Note, C.; Kosmella, S.; Koetz, J. Poly(ethyleneimine) as reducing and stabilizing agent for the formation of gold nanoparticles in w/o microemulsions. *Colloids Surf., A* **2006**, *290*, 150−156.

(11) Eustis, S.; El-Sayed, M. A. Why gold nanoparticles are more precious than pretty gold: Noble metal surface plasmon resonance and its enhancement of the radiative and nonradiative properties of nanocrystals of different shapes. *Chem. Soc. Rev.* **2006**, *35*, 209−217.

(12) Murphy, C. J.; Gole, A. M.; Hunyadi, S. E.; Orendorff, C. J. One-Dimensional Colloidal Gold and Silver Nanostructures. *Inorg. Chem.* **2006**, *45*, 7544−7554.

(13) Sun, M.; Ran, G.; Fu, Q.; Xu, W. The effect of iodide on the synthesis of gold nanoprisms. *J. Exp. Nanosci.* **2015**, *10*, 1309−1318.

(14) Malikova, N.; Pastoriza-Santos, I.; Schierhorn, M.; Kotov, N. A.; Liz-Marzan, L. M. Layer-by-Layer Assembled Mixed Spherical and Planar Gold Nanoparticles: Control of Interparticle Interactions. *Langmuir* **2002**, *18*, 3694−3697.

(15) Scarabelli, L.; Coronado-Puchau, M.; Giner-Casares, J. J.; Langer, J.; Liz-Marzan, L. M. Monodisperse Gold Nanotriangles: Size Control, Large-Scale Self-Assembly, and Performance in Surface-Enhanced Raman Scattering. *ACS Nano* **2014**, *8*, 5833−5842.

(16) Liebig, F.; Sarhan, R. M.; Prietzel, C.; Reinecke, A.; Koetz, J. "Green" gold nanotriangles: synthesis, purification by polyelectrolyte/

DOI: 10.1021/acs.langmuir.7b02898
Langmuir 2018, 34, 4584−4594

micelle depletion flocculation and performance in surface-enhanced Raman scattering. *RSC Adv.* **2016**, *6*, 33561−33568.
(17) Lee, Y. H.; Lee, C. K.; Tan, B.; Rui Tan, J. M.; Phang, I. Y.; Ling, X. Y. Using the Langmuir−Schaefer technique to fabricate large-area dense SERS-active Au nanoprism monolayer films. *Nanoscale* **2013**, *5*, 6404−6412.
(18) Smith, A. M.; Mancini, M. C.; Nie, S. Bioimaging: second window for in vivo imaging. *Nat. Nanotechnol.* **2009**, *4*, 710−711.
(19) Oldenburg, S. J.; Jackson, J. B.; Westcott, S. L.; Halas, N. J. Infrared extinction properties of gold nanoshells. *Appl. Phys. Lett.* **1999**, *75*, 2897−2895.
(20) Mayer, M.; Scarabelli, L.; March, K.; Altantzis, T.; Tebbe, M.; Kociak, M.; Bals, S.; García de Abajo, F. J.; Fery, A.; Liz-Marzan, L. M. Controlled living nanowire growth: precise control over the morphology and optical properties of AgAuAg bimetallic nanowires. *Nano Lett.* **2015**, *15*, 5427−5437.
(21) Sun, M. J.; Ran, G. J.; Fu, Q.; Xu, W. L. The effect of iodide on the synthesis of gold nanoprisms. *J. Exp. Nanosci.* **2015**, *10*, 1309−1318.
(22) Ha, T. H.; Koo, H.-J.; Chung, B. H. Shape-controlled synthesis of of gold nanoprisms and nanorods influenced by specific nadsorption of halide ions. *J. Phys. Chem. C* **2007**, *111*, 1123−1130.
(23) Jana, N. R.; Gearheart, L.; Murphy, C. J. Seeding Growth for Size Control of 5−40 nm Diameter Gold Nanoparticles. *Langmuir* **2001**, *17*, 6782−6786.
(24) Hong, S.; Acapulco, J. A. I.; Jang, H.-J.; Kulkarni, A. S.; Park, S. Kinetically Controlled Growth of Gold Nanoplates and Nanorods via a One-Step Seed-Mediated Method. *Bull. Korean Chem. Soc.* **2014**, *35*, 1737−1742.
(25) Shankar, S. S.; Rai, A.; Ahmad, A.; Sastry, M. Controlling the Optical Properties of Lemongrass Extract Synthesized Gold Nanotriangles and Potential Application in Infrared-Absorbing Optical Coatings. *Chem. Mater.* **2005**, *17*, 566−572.
(26) Kasture, M.; Sastry, M.; Prasad, B. L. V. Halide ion controlled shape dependent gold nanoparticle synthesis with tryptophan as reducing agent: Enhanced fluorescent properties and white light emission. *Chem. Phys. Lett.* **2010**, *484*, 271−275.
(27) Scott, R. W.; Wilson, O. M.; Crooks, R. M. Synthesis, characterization, and applications of dendrimer-encapsulated nanoparticles. *J. Phys. Chem. B* **2005**, *109*, 692−704.
(28) Ding, W.; Lin, J.; Yao, K.; Mays, J. W.; Ramanathan, M.; Hong, K. Building triangular nanoprisms from the bottom-up: a polyelectrolyte micellar approach. *J. Mater. Chem. B* **2013**, *1*, 4212−4216.
(29) Robertson, D.; Tiersch, B.; Kosmella, S.; Koetz, J. Preparation of crystalline gold nanoparticles at the surface of mixed phosphatidylcholine-ionic surfactant vesicles. *J. Colloid Interface Sci.* **2007**, *305*, 345−351.
(30) Chen, L.; Hu, H.; Liu, Q.; Ji, F.; Chen, S.; Xu, Y.; Zhang, Q. Halide-free synthesis of Au nanoplates and monitoring the shape evolution process through a marker experiment. *J. Mater. Chem. C* **2016**, *4*, 6457−6460.
(31) Köth, A.; Appelhans, D.; Prietzel, C.; Koetz, J. Asymmetric gold nanoparticles synthesized in the presence of maltose-modified poly(ethyleneimine). *Colloids Surf., A* **2012**, *414*, 50−56.
(32) Liebig, F.; Thünemann, A. F.; Koetz, J. Ostwald ripening growth mechanism of gold nanotriangles in vesicular template phase. *Langmuir* **2016**, *32*, 10928−10935.
(33) Park, K.; Koerner, H.; Vaia, R. A. Depletion-Induced Shape and Size Selection of Gold Nanoparticles. *Nano Lett.* **2010**, *10*, 1433−1439.
(34) Liu, R.; Zhou, J.-H.; Zhou, Z.-K.; Jiang, X.; Liu, J.; Liu, G.; Wang, X.-H. On-demand shape and size purification of nanoparticle based on surface area. *Nanoscale* **2014**, *6*, 13145−13153.
(35) Zhang, F.; Zhu, J.; An, H.-Q.; Li, J.-J.; Zhao, J.-W. A two-step approach to realize size- and shape-selective separation of crude gold nanotriangles with high purification. *J. Mater. Chem. C* **2016**, *4*, 568−580.
(36) Von Reppert, A.; Sarhan, R. M.; Stete, F.; Pudell, J.; Del Fatti, N.; Crut, A.; Koetz, J.; Liebig, F.; Prietzel, C.; Bargheer, M. Watching the vibration and cooling of ultrathin gold nanotriangles by ultrafast X-ray diffraction. *J. Phys. Chem. C* **2016**, *120*, 28894−28899.
(37) Liebig, F.; Sarhan, R. M.; Sander, M.; Koopman, W.; Schuetz, R.; Bargheer, M.; Koetz, J. Deposition of gold nanotriangles in large scale close-packed manolayers for X-ray-based temperature calibration and SERS monitoring of plasmon-driven catalytic reactions. *ACS Appl. Mater. Interfaces* **2017**, *9*, 20247−20253.
(38) Kosmella, S.; Venus, J.; Hahn, J.; Prietzel, C.; Koetz, J. Low-temperature synthesis of polyethyleneimine-entrapped CdS quantum dots. *Chem. Phys. Lett.* **2014**, *592*, 114−119.
(39) Lemke, K.; Prietzel, C.; Koetz, J. Fluorescent gold clusters synthesized in a polyethyleneimine modified reverse microemulsion. *J. Colloid Interface Sci.* **2013**, *394*, 141−146.
(40) Yang, Y.; Chen, S. Surface manipulation of the electronic energy of subnaometer-sized gold clusters: an electrochemical and spectroscopic investigation. *Nano Lett.* **2003**, *3*, 75−79.
(41) Bertino, M. F.; Sun, Z.-M.; Zhang, R.; Wang, L.-S. Facile synthesis of monodisperse ultrasmall Au clusters. *J. Phys. Chem. B* **2006**, *110*, 21416−21418.
(42) Schniepp, H. C.; Shum, H. C.; Saville, D. A.; Aksay, I. A. Surfactant Aggregates at Rough Solid-Liquid Interfaces. *J. Phys. Chem. B* **2007**, *111*, 8708−8712.
(43) Dey, J.; Bhattacharjee, J.; Hassan, P. A.; Aswal, V. K.; Das, S.; Ismail, K. Micellar shape drive in counterion binding. Small-angle neutron scattering study of AOT micelle. *Langmuir* **2010**, *26*, 15802−15806.
(44) Knock, M. M.; Sanii, L. S. Effect of Hydrophobization of Gold QCM-D Crystals on Surfactant Adsorption at the Solid-Liquid Interface. *ACS Symp. Ser.* **2011**, *1070*, 175−192.
(45) Meena, S. K.; Sulpizi, M. Understanding the Microscopic Origin of Gold Nanoparticle Anisotropic Growth from Molecular Dynamics Simulations. *Langmuir* **2013**, *29*, 14954−14961.
(46) Casado-Rodriguez, M. A.; Sanchez-Molina, M.; Lucena-Serrano, A.; Lucena-Serrano, C.; Rodriguez-Gonzalez, B.; Algarra, M.; Diaz, A.; Valpuesta, M.; Lopez-Romero, J. M.; Perez-Juste, J.; Contreras-Caceres, R. Synthesis of vinyl-terminated Au nanoprisms and nanooctahedra mediated by 3-butenoic acid: direct Au@pNIPAM fabrication with improved SERS capabilities. *Nanoscale* **2016**, *8*, 4557−4564.
(47) Senthil Kumar, P. S.; Pastoriza-Santos, I.; Rodríguez-González, B.; Javier García de Abajo, F.; Liz-Marzán, L. M. High-yield synthesis and optical response of gold nanostars. *Nanotechnology* **2008**, *19*, 015606.
(48) García de Abajo, F. J.; Howie, A. Retarded field calculation of electron energy loss in inhomogeneous dielectrics. *Phys. Rev. B: Condens. Matter Mater. Phys.* **2002**, *65*, 115418.
(49) Khoury, C. G.; Vo-Dinh, T. Gold Nanostars For Surface-Enhanced Raman Scattering: Synthesis, Characterization and Optimization. *J. Phys. Chem. C* **2008**, *112*, 18849−18859.
(50) Aldeanueva-Potel, P.; Carbo-Argibay, E.; Pazos-Perez, N.; Barbosa, S.; Pastoriza-Santos, I.; Alvarez-Puebla, R.; Liz-Marzan, L. M. Spiked gold beads as substrates for single-particle SERS. *ChemPhysChem* **2012**, *13*, 2561−2565.
(51) Tebbe, M.; Kuttner, C.; Mayer, M.; Maennel, M.; Pazos-Perez, N.; König, A. F.; Fery, A. Silver-overgrowth-induced changes in intrinsic optical properties of gold nanorods: From noninvasive monitoring of growth kinetics to tailoring internal mirror changes. *J. Phys. Chem. C* **2015**, *119*, 9513−9523.
(52) Hansen, S. Calculation of small-angle scattering profiles using Monte-Carlo simulation. *J. Appl. Crystallogr.* **1990**, *23*, 344−346.
(53) Hjelm, R. P.; Schteingart, C.; Hofmann, A. F.; Sivia, D. S. Form and structure of of self-assembling particles in monoolein-bile salt mixtures. *J. Phys. Chem.* **1995**, *99*, 16395−16406.
(54) Ibarra-Sánchez, J. J.; Fuentes-Ramírez, R.; Roca, A. G.; del Puerto Morales, M.; Cabrera-Lara, L. I. Parameters for scaling up the synthesis of magnetite nanoparticles in organic media: stirring rate and growth kinetic Ind. Eng. Chem. *Ind. Eng. Chem. Res.* **2013**, *52*, 17841−17847.

DOI: 10.1021/acs.langmuir.7b02898
Langmuir 2018, 34, 4584−4594

(55) Kim, K.; Choi, J.-Y.; Shin, K. S. Photoreduction of 4-Nitrobenzenethiol on Au by Hot Electrons Plasmonically Generated from Ag Nanoparticles: Gap-Mode Surface-Enhanced Raman Scattering Observation. *J. Phys. Chem. C* **2015**, *119*, 5187−5194.
(56) Osinkina, L.; Lohmüller, T.; Jackel, F.; Feldmann, J. Synthesis of Gold Nanostar Arrays as Reliable, Large-Scale, Homogeneous Substrates for Surface-Enhanced Raman Scattering Imaging and Spectroscopy. *J. Phys. Chem. C* **2013**, *117*, 22198−22202.
(57) Perry, D. A.; Son, H. J.; Cordova, J. S.; Smith, L. G.; Biris, A. S. Adsorption analysis of nitrophenol isomers on silver nanostructures by surface-enhanced spectroscopyemulsion. *J. Colloid Interface Sci.* **2010**, *342*, 311−319.
(58) Walker, D. A.; Browne, K. P.; Kowalczyk, B.; Grzybowski, B. A. Self-Assembly of Nanotriangle Superlattices Facilitated by Repulsive Electrostatic Interactions. *Angew. Chem., Int. Ed.* **2010**, *49*, 6760−6763.
(59) Le Ru, E. C.; Blackie, E.; Meyer, M.; Etchegoin, P. G. Surface Enhanced Raman Scattering Enhancement Factors: a comprehensive Study. *J. Phys. Chem. C* **2007**, *111*, 13794−13803.
(60) Saverot, S.; Geng, X.; Leng, W.; Vikesland, P. J.; Grove, T. Z.; Bickford, L. R. Facile, tunable, and SERS-enhanced HEPES gold nanostars. *RSC Adv.* **2016**, *6*, 29669−29673.
(61) He, S.; Kang, M. W. C.; Khan, F. J.; Tan, E. K. M.; Reyes, M. A.; Kah, J. C. Y. Optimizing gold nanostars as a colloid-based surface-enhanced Raman scattering (SERS) substrate. *J. Opt.* **2015**, *17*, 114013−114026.

DOI: 10.1021/acs.langmuir.7b02898
Langmuir 2018, 34, 4584−4594

Supporting Information

Undulated gold nanoplatelet superstructures: In situ growth of hemispherical gold nanoparticles onto the surface of gold nanotriangles

Ferenc Liebig,[a] Radwan M. Sarhan,[b,c,] Claudia Prietzel,[a] Andreas F. Thünemann,[d] Matias Bargheer,[b] Joachim Koetz[a*]

[a] Institute for Chemistry and [b] Institute for Physics, University of Potsdam, Karl-Liebknecht-Strasse 24-25, Haus 25, 14476 Potsdam, Germany

[c] School of Analytical Sciences Adlershof (SALSA), Humboldt-Universität zu Berlin, , Albert-Einstein-Str. 5-9, 10099 Berlin, Germany

[d] Bundesanstalt für Materialforschung und -prüfung (BAM), Unter den Eichen 87, 12205 Berlin, Germany

* Corresponding author: Joachim Koetz

E-mail: koetz@uni-potsdam.de

In this supplementary material we show time dependent DLS experiments and additional spectra and TEM images to illustrate analytic details to cross check the presumed mechanism for preparing undulated nanotriangles.

Section S.1: Time dependent DLS experiments in PEI solution in absence of nanotriangles

We performed DLS experiments during the growth of Au particles in the absence of AuNTs (Figure S1). In the first 10 minutes only clusters with dimensions ≤ 2nm were found, in full agreement with the UV-vis absorption maximum at 334 nm. After 15 minutes, a second larger particle fraction with diameter of about 10 nm becomes detectable. This fraction dominates after 25 minutes and the cluster peak disappear in the intensity plot. The number plot experiments show only the cluster peak after 5 minutes, and in all other experiments two peaks for both particle dimensions. Therefore, the UV-vis experiments are corroborated by the DLS experiments.

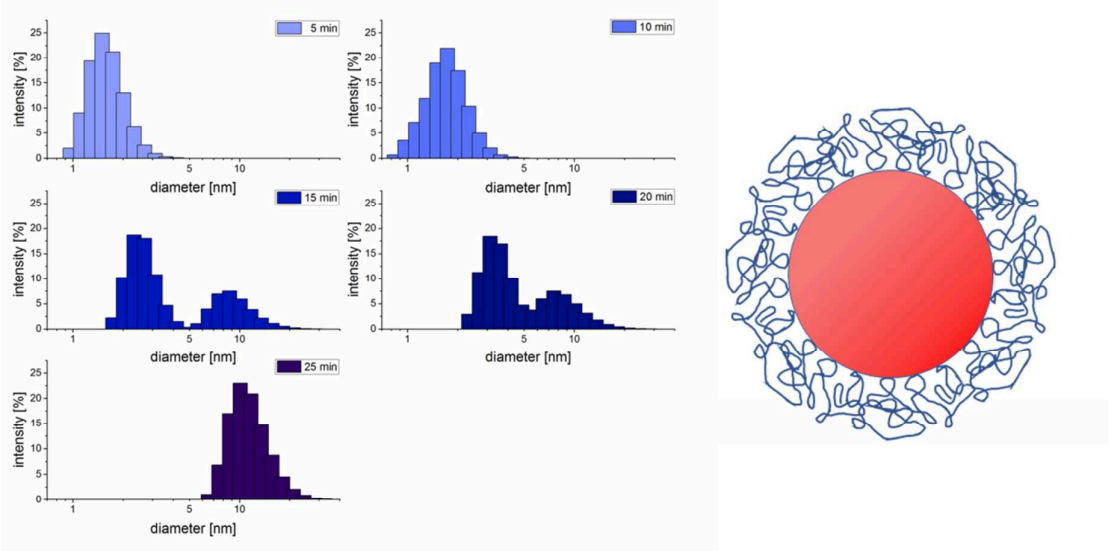

Figure S1. Gold nanoparticle formation in a PEI solution investigated by DLS measurements with a scheme of a PEI-entrapped gold nanoparticle.

Section S.2: Time dependent DLS experiments in PEI solution in presence of nanotriangles

For completeness we also performed DLS experiments during the growth of undulated NTs. Figure S2 shows a dominant peak between 100 and 300 nm which must be attributed to the presence of the AuNTs. We do not attempt to interpret the changes of this peak since DLS is designed for isotropic particles. However, this method enables tracing the particle growth in presence of the anisotropic platelets over time. The decisive factor is the differentiation between the large triangle fraction in comparison to the fraction of small spherical particles formed in solution. In contrast to the larger particle fraction > 100 nm, which can be attributed to the nanotriangles, the fraction of small nanoparticles of about 10-20 nm in diameter can be detected in the intensity plot only after a time period > 15 minutes. For shorter growth times, the small nanoparticle fraction is not strong enough to be visible next to the larger particle fraction. Potentially the particles form at the NT surface at the expense of “free” particles and the apparent larger size of the particles around 20 nm must be attributed to their reduced mobility in the presence of NTs. In any case spherical gold nanoparticles are formed in solution in analogy to the PEI reference system.

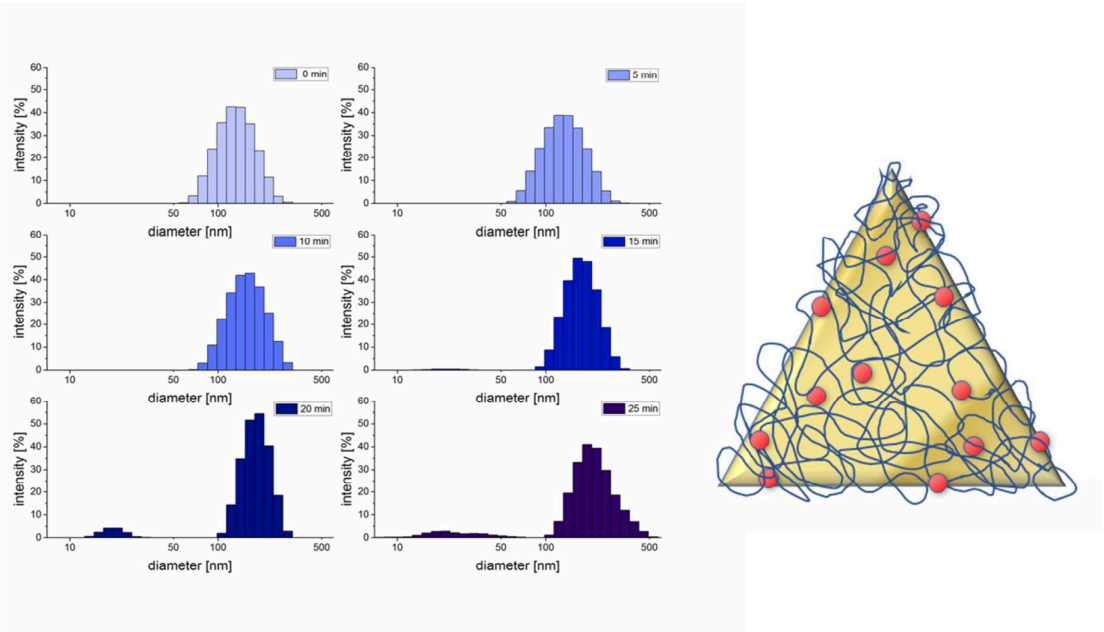

Figure S2. Gold nanoparticle formation in a PEI solution investigated by DLS measurements in the presence of gold nanotriangles with a scheme of gold nanoparticles formed in the PEI-shell surrounding the gold nanotriangle

Section S.3: Additional TEM and SEM micrographs, a UV-vis spectrum and SERS spots

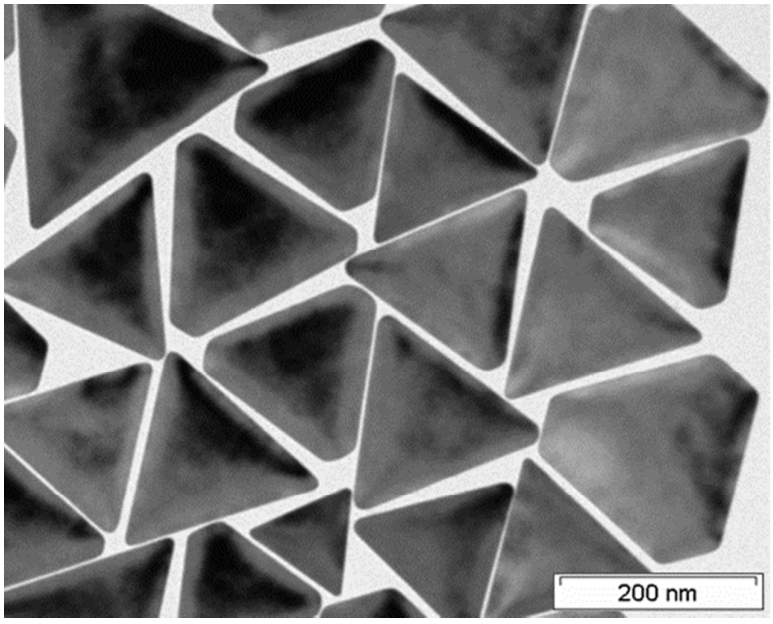

Figure S3. TEM micrograph of the gold nanotriangle stock solution

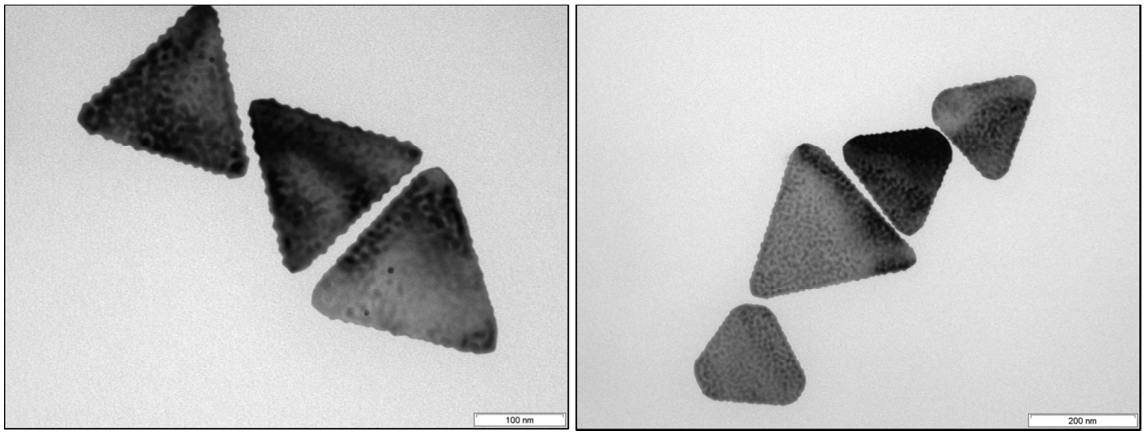

Figure S4. TEM micrographs of undulated gold nanotriangles after 10 minutes of heating

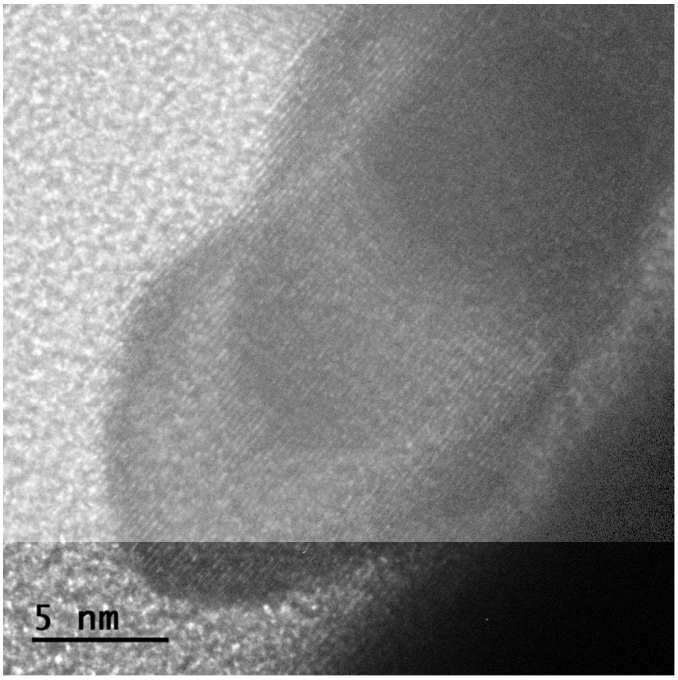

Figure S5. Magnified HRTEM micrograph of a "half sphere" at the nanotriangle edge

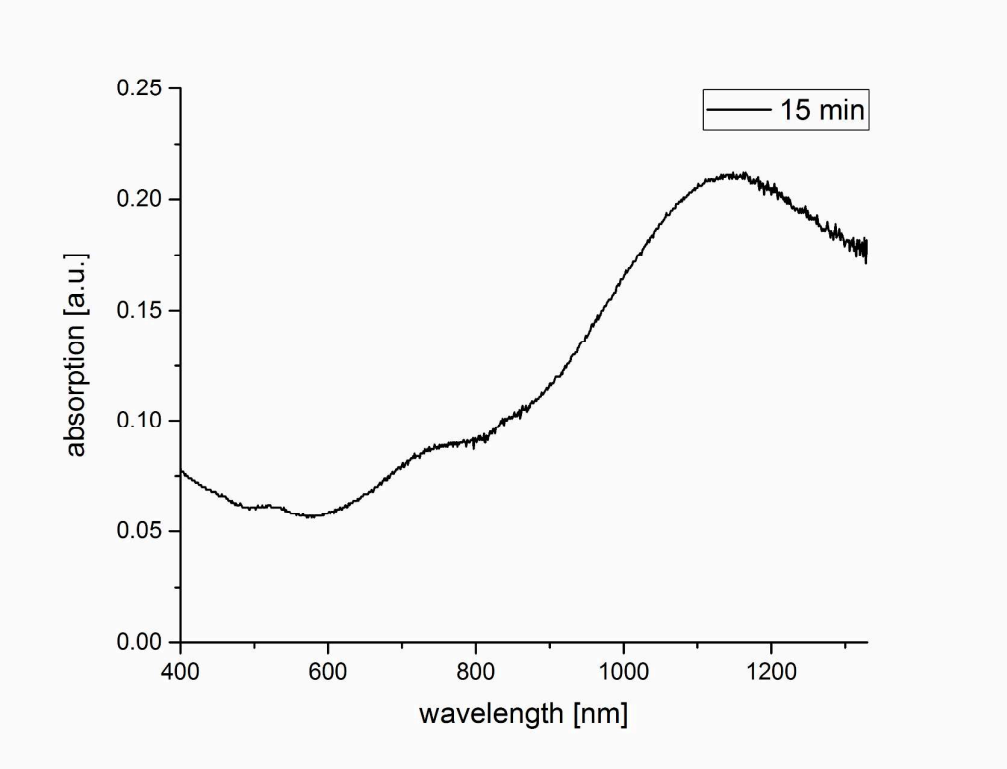

Figure S6. UV-vis spectrum of the unpurified AuNT sample at a lower PEI concentration (0.8 wt%) to show that the formation of spherical particles in solution can be minimized.

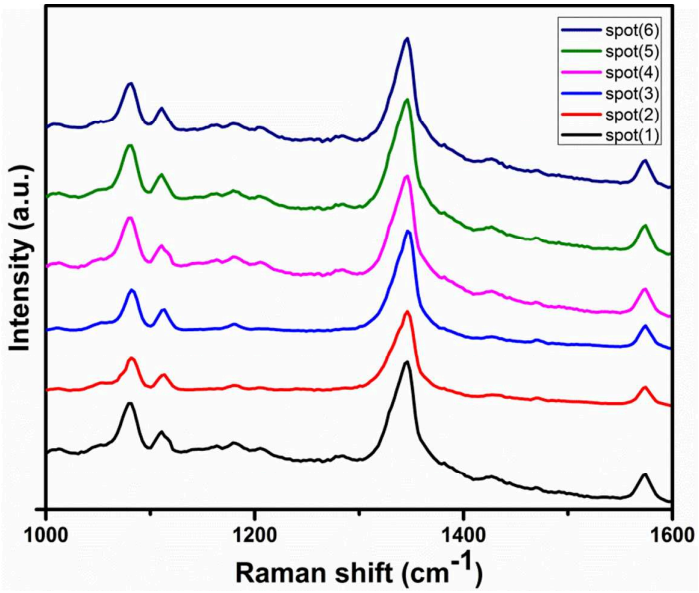

Figure S7. Several SERS spots measured on undulated nanotriangles under the same conditions as a cross-check of the uniformity of the SERS substrate.

ACS APPLIED NANO MATERIALS
Cite This: ACS Appl. Nano Mater. 2018, 1, 1995−2003
Article
www.acsanm.org

Tuned Surface-Enhanced Raman Scattering Performance of Undulated Au@Ag Triangles

Ferenc Liebig,[†] Radwan M. Sarhan,[‡,§,∥] Claudia Prietzel,[†] Clemens N. Z. Schmitt,[⊥] Matias Bargheer,[‡] and Joachim Koetz*[,†]

[†]Institute for Chemistry and [‡]Institute for Physics, University of Potsdam, 14476 Potsdam, Germany
[§]Chemistry Department, Faculty of Science, Cairo University, Cairo 12613, Egypt
[∥]School of Analytical Sciences Adlershof (SALSA), Humboldt-Universität of Berlin, 10099 Berlin, Germany
[⊥]Max Planck Institute of Colloids and Interfaces, 14476 Potsdam, Germany

Supporting Information

ABSTRACT: Negatively charged ultraflat gold nanotriangles (AuNTs) stabilized by the anionic surfactant dioctyl sodium sulfosuccinate (AOT) were reloaded with the cationic surfactant benzylhexadecyldimethylammonium chloride (BDAC). Because of the spontaneous formation of a catanionic AOT micelle/BDAC bilayer onto the surface of the reloaded AuNTs, a reduction of Ag^+ ions leads to the formation of spherical silver nanoparticles (AgNPs). With increasing concentration of AgNPs on the AuNTs, the localized surface plasmon resonance (LSPR) is shifted stepwise from 1300 to 800 nm. The tunable LSPR enables to shift the extinction maximum to the wavelength of the excitation laser of the Raman microscope at 785 nm. Surface-enhanced Raman scattering (SERS) experiments performed under resonance conditions show an SERS enhancement factor of the analyte molecule rhodamine RG6 of 5.1×10^5, which can be related to the silver hot spots at the periphery of the undulated gold nanoplatelets.

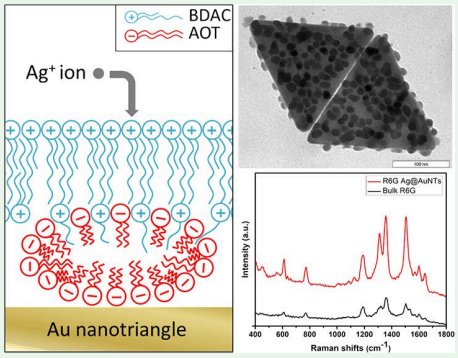

KEYWORDS: *gold nanotriangles, catanionic surfactant bilayer, undulated nanoplatelets, SERS, LSPR*

1. INTRODUCTION

The optical properties of metal nanoparticles can be controlled by changing their morphology or composition.[1] The tunable localized surface plasmon resonances (LSPR) enable a broad range of applications in biosensors,[2−5] imaging,[6−8] and surface-enhanced Raman scattering (SERS).[9−12] SERS facilitates the detection of analyte molecules deposited on metal nanoparticles, and the sensitivity depends on the nature of the nanoparticle as well as the distance between the analyte and the surface.[13−15] Spherical Au nanoparticles with diameter <50 nm exhibit an LSPR band in the range from 520 to 590 nm and Ag nanparticles of similar dimensions from 400 to 450 nm.[16−18] To improve the plasmon-enhanced spectroscopy and catalytic performance, the LSPR band has to be shifted toward the near-infrared regime. Using asymmetric nanoparticles, e.g., nanorods or nanotriangles, such a red-shift of the UV−vis absorption can be induced. Another approach combines the properties of Au and Ag. In comparison to gold nanoparticles (AuNPs), silver nanoparticles (AgNPs) provide stronger SERS signals.[19,20] Anisotropic silver nanoparticles can be synthesized by a seed-mediated growth strategy in the presence of polymers. Especially polyanions, e.g., sodium polyacrylates or sodium polystyrenesulfonates, direct the anisotropic growth of "stitched Ag seeds" to nanotriangles.[21] Jin et al. prepared Ag nanotriangles via photoinduced conversion of Ag seeds,[22] and Tsai et al. prepared gold-coated silver triangular platelets.[23] The formation of a Au−Ag shell is accompanied by a shift of the UV maximum to ca. 680 nm.[18,23]

In general, the synthesis of monodisperse gold nanoparticles with different shapes and sizes is easier to handle. To combine both advantages, it is possible to use well-defined gold nanoparticles as platform for coating with silver nanoparticles.[24−27] SERS measurements generally profit from so-called "hot spots" which help decreasing the acquisition time.[28] The very large shape anisotropy of ultrathin gold nanotriangles provides the special advantage that they can be self-assembled with crystalline facets aligned, e.g., for in situ X-ray diffraction measurements which calibrate the particle temperature in a plasmonically assisted catalytic reaction.[29,30] Based on these conditions, building block particles decorated with smaller nanoparticles make them ideal candidates for SERS experiments. The enhancement of the Raman signal of silver-coated gold nanoparticles was used in several applications.[31−33]

Anisotropic gold nanoparticles with a proven signal enhancement can be covered by silver shells of varied sizes. The morphology of the "core particle" can be influenced by many

Received: April 4, 2018
Accepted: April 9, 2018
Published: April 9, 2018

DOI: 10.1021/acsanm.8b00570
ACS Appl. Nano Mater. 2018, 1, 1995−2003

Scheme 1. Approach to Undulated Au@Ag Nanotriangles

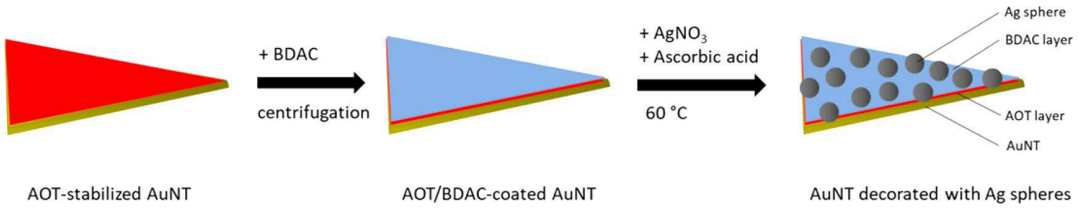

factors, for example, the type and the concentration of the reaction components, such as surfactants, reducing agents, and ancillary additives.[34−38] The counterion of the surfactant plays a key role because such halide ions have a strong tendency to adsorb on metallic surfaces as shape-directing agents.[39] To reduce silver on stabilized gold nanoparticle templates, usually an aqueous solution of $AgNO_3$ is added to the dispersion, followed by ascorbic acid (AA) to start the reduction of Ag^+. Type and concentration of the stabilizers are crucial for controlling the surface modification because they affect the preferred deposition on the Au crystallographic facets and the in situ formation of Ag complexes and Ag−Br nanoparticles.[40] For example, silver-overgrowth processes in the presence of the cationic surfactant benzylhexadecyldimethylammonium chloride (BDAC) leads to the formation of a silver shell on the surface of gold nanorods. Depending on the shell thickness the UV absorption can be tuned.[11] However, spherical Ag nanoparticles are not yet formed under such conditions.

Recently, we have shown that ultrathin gold nanotriangles can be synthesized in a vesicular template phase.[41] In contrast to the well-established seed-mediated, CTAB-assisted synthesis of positively charged anisotropic gold nanoparticles,[32,33,36,37] our template-directed one-step strategy leads to the formation of anionically charged ultrathin gold nanoplatelets with a platelet thickness of 7−8 nm according to an Ostwald ripening mechanism at the periphery of soft gold nanoparticle aggregates.[42]

In this work, we synthesize spherical silver nanoparticles directly on the surface of our ultrathin gold nanotriangles (AuNTs)after reloading the anionically charged AuNTs with the cationic surfactant BDAC according to Scheme 1.

The blue-shift of the LSPR frequency can be tuned via the concentration of AgNPs on the AuNT surface. The concomitant enhancement of the SERS signal can be correlated to the hot spots of the undulated structure of spherical silver nanoparticles attached to the platelet surface of the Au−Ag core−shell nanotriangles (Au@AgNTs).

2. EXPERIMENTAL SECTION

2.1. Chemicals. Silver nitrate ($AgNO_3$) and rhodamine RG6 were purchased from Sigma-Aldrich. Benzylhexadecyldimethylammonium chloride (BDAC) and L(+)-ascorbic acid (AA) were obtained from Roth. Milli-Q Reference A+ water was used in all preparations. Poly(*N*,*N*-diallyl-*N*,*N*-dimethylammonium-*alt*-3,5-bis-carboxyphenyl-maleamic carboxylate) (PalPhBisCarb) was synthesized by free radical polymerization.[41]

2.2. Characterization. The optical characterization was carried out by UV−vis−NIR spectroscopy performed with a Shimadzu UV-2600 spectrophotometer. Transmission electron microscopy (TEM) was performed on the JEM-1011 (JEOL) at an acceleration voltage of 80 kV. The micrographs of high-resolution TEM (HRTEM) and scanning transmission electron microscopy (STEM) in combination with energy-dispersive X-ray (EDX) spectroscopy were received with the JEOL JEM 2200FS at an acceleration voltage of 200 kV. For the EDX analysis a spot size of 0.5 nm was used. Scanning electron microscopy (SEM) micrographs were obtained with a Hitachi S-4800 and a ZEISS Supra 55PV. Zeta potential measurements were performed with the Malvern Nano Zetasizer 3600.

The Raman spectra were recorded using a confocal alpha 300 Raman microscope from WITec equipped with excitation laser at wavelength of 785 nm. The laser beam of 2 mW and penetration depth of 25 μm was focused through 100× (NA = 1) microscope objective. The spectra of different integration times were recorded with a thermoelectrically cooled CCD detector DU401A-BV from Andor placed behind the UHTS 300 spectrometer (WITec) with a spectral resolution of 3 cm^{-1}. The Raman band of a silicon wafer at 520 cm^{-1} was used to calibrate the spectrometer.

2.3. Synthesis. The gold nanotriangles (AuNTs) were synthesized in the vesicular template phase containing the phospholipid PL90G, AOT, and the strongly alternating polyampholyte PalPhBisCarb by the reduction of $HAuCl_4$. To separate the nanoplatelets from spherical gold nanoparticles, a depletion flocculation in the presence of AOT micelles was used according to the procedure described earlier by us.[41] The finally obtained nanoplatelets include to ca. 80% nanotriangles and 20% truncated triangles or hexagons[41] and will be called "gold nanotriangles" (AuNTs) in the following. Inspired by the silver overgrowth of CTAB-stabilized nanorods[11] and the protocol by Gomez-Graña et al.,[27] our negatively charged AuNTs were reloaded with the positively charged surfactant BDAC by adding 10 mM BDAC aqueous solution to our 0.9 mM AuNTs dispersion in a volume ratio of 0.3:1 and washing (six times) with the 10 mM BDAC surfactant solution by centrifugation at 13 000 rpm for 8 min. To verify the reloading process, zeta potential measurements were done. The BDAC-coated AuNTs were redispersed in water and show a zeta potential of +48 mV. In the next step, various volumes of a 0.1 M $AgNO_3$ were added. The obtained solution was heated up to 60 °C. After 5 min, 0.4 M ascorbic acid was added and maintained for 2 h.

For the preparation of the SERS substrate according to the protocol given by us earlier,[29] a droplet of the dispersion was deposited on glass. By adding an ethanol−toluene (5:1) mixture to the droplet in a ratio 1:2, a complete wetting of the substrate occurred. Simultaneously, a close-packed AgNP layer formation was observed at the AuNT interface, which remains after evaporation. The modified nanoparticle assembly was immersed in 1 mM aqueous solution of R6G for 6 h. The SERS substrates were washed several times with water to remove the unattached molecules and dried before being measured.

3. RESULTS AND DISCUSSION

3.1. Synthesis and Characterization of Au@Ag Triangles. The AuNTs prepared in the multivesicular template phase and separated from spherical nanoparticles form a green dispersion.[41] A TEM micrograph of the AuNTs can be seen in Figure S1. Tebbe et al. have outlined that for a defined Ag-film formation an excess of the cationic surfactant BDAC is required.[11] Therefore, we have reloaded our AOT-stabilized AuNTs with the cationic surfactant BDAC. To ensure a complete replacement of nonadsorbed surfactants, the sample was washed several times by centrifugation. Additionally, the zeta potential was controlled until it reached a constant value. Through the reloading, the zeta potential changes from −25 to +41 mV. A more detailed discussion of the reloading process

DOI: 10.1021/acsanm.8b00570
ACS Appl. Nano Mater. 2018, 1, 1995−2003

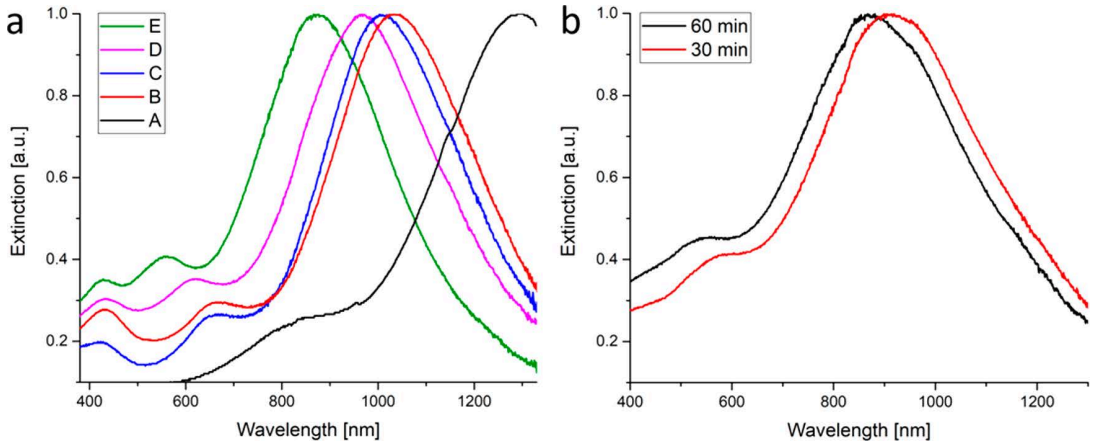

Figure 1. UV−vis extinction spectra of the AuNTs after 120 min at different amounts of a 0.1 M $AgNO_3$ solution (normalized at the LSPR maximum): (A) without $AgNO_3$, (B) 2.5 μL, (C) 5 μL, (D) 7.5 μL, and (E) 10 μL (a). The corresponding time-dependent spectra of sample E after 30 and 60 min (b).

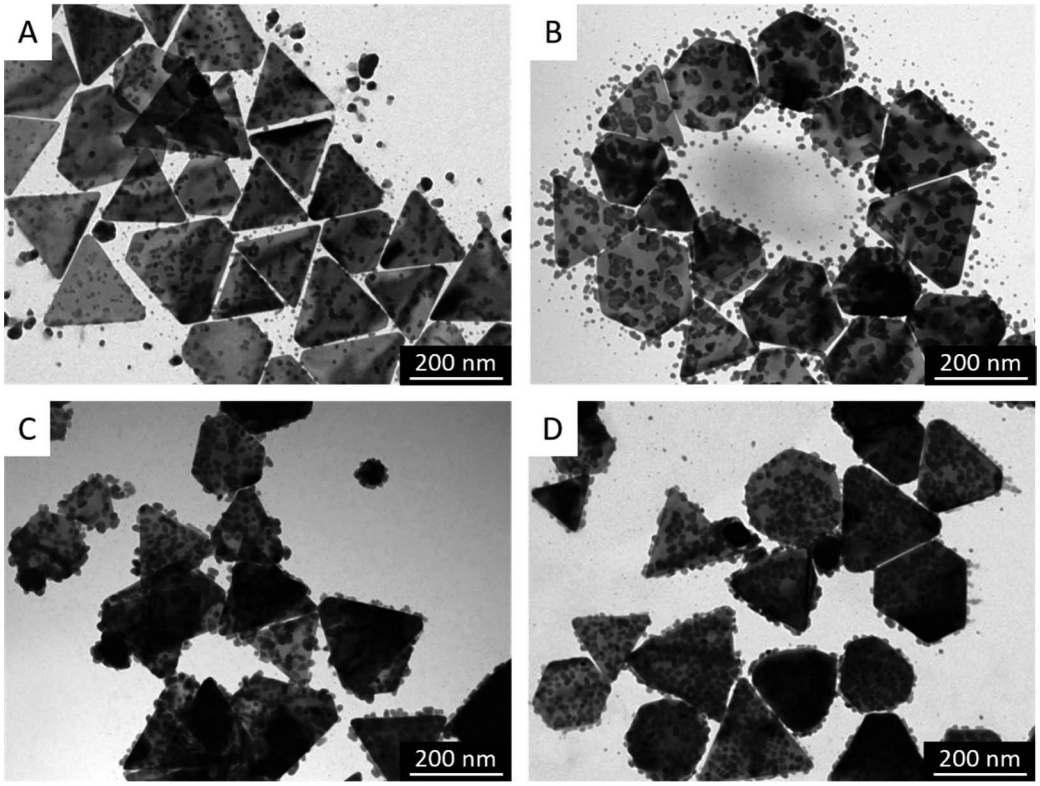

Figure 2. TEM micrographs of the AuNTs at different amounts of a 0.1 M aqueous $AgNO_3$ solution: (A) 2.5 μL, (B) 5 μL, (C) 7.5 μL, and (D) 10 μL. Scale bars: 200 nm.

will be given below. The chloride counterions of the BDAC strongly limit the growth process.[11,43,44] The nucleation rates of Ag on different Au crystal facets as well as the accessibility and reduction rate of the Ag precursors are important parameters to control the process.[11] This means that the formation of Ag crystal facets depends on the ratio of BDAC and $AgNO_3$, too.[45,46] For a controlled reduction of silver and an increased reduction power of ascorbic acid, the process was performed at 60 °C as suggested by the relevant literature.[11,47] To ensure an excess of 4 times molar ascorbic acid, the same amount of $AgNO_3$ was used.[11] After 2 h, the extinction spectrum of the solution stops changing, which indicates the termination of the synthesis. In Figure 1, the final blue-shifted extinction spectra of the different particle solutions from low silver concentration (B) to higher silver concentration (E) can be seen.

The black curve (A) of the unmodified AuNTs exhibits a maximum of the LSPR band at 1300 nm. To determine the edge length of the AuNTs (Figure S1), we analyzed TEM micrographs. The thickness of the AuNTs was determined by ultrafast X-ray diffraction (UXRD), where the out-of-plain strain oscillation period after a femtosecond pulse excitation is proportional to the thickness and the sound velocity.[30] AFM experiments confirmed the results found by UXRD.[41] With this combined analysis we assess the average shape of the AuNTs as

DOI: 10.1021/acsanm.8b00570
ACS Appl. Nano Mater. 2018, 1, 1995−2003

isosceles triangles with an edge length of 175 nm and a thickness of 7 nm.

The reduction of $AgNO_3$ on the AuNTs surface changes the position of the LSPR band (compare Figure 1). With increasing amount of $AgNO_3$ the extinction peak shifted from 1050 to 870 nm. A very large shift is observed between the pure AuNTs (sample A) and the sample B with few Ag particles covering the AuNT. This effect can be rationalized by a strongly changed dielectric function of the medium surrounding the AuNTs, so that the resonance condition of an effective medium theory is considerably changed. Upon deposition of more and more Ag on the AuNT the blue-shift continues. The deposition of spherical Ag nanoparticles onto the Au nanoplatelets leads to an increase of the platelet thickness, which is accompanied by a blue-shift of the LSPR band. For the densely packed sample structure E it is reasonable to attribute an additional contribution of the shift to the modified aspect ratio of the entire metallic particle structure. A second characteristic spectral modification is observed: With higher $AgNO_3$ concentration, the shoulder at 800 nm turns into a visible peak around 580 nm. This side peak and shoulders can be associated with the in-plane quadrupolar mode, whereas the strong peak at higher wavelength is the dipolar mode.[48,49] Both peaks are shifted to lower wavelength. Deviations between the two shifts can be related to a nonuniform deposition of Ag on the AuNT surface. At higher silver nitrate concentrations the Ag deposition on the nanotriangle surface is much higher and more homogeneous. The additional peak at about 420 nm indicates the formation of spherical Ag nanoparticles in solution after 2 h. Additional time-dependent measurements (compare Figure 1B) have shown that the UV peak at 420 nm does not exist up to 1 h, indicating that Ag nanoparticles are not formed in solution at the beginning. Therefore, one can conclude that the Ag nanoparticle formation process starts in the BDAC/AOT shell surrounding the AuNTs and not in solution. Control experiments (performed in the absence of AuNTs) show an extinction maximum at 420 nm for Ag nanoparticles in solution. However, these Ag nanoparticles in solution aggregate spontaneously and sedimentate. When this process is performed in the presence of AOT-stabilized AuNTs, the gold nanotriangles become instable and stick to the glass vessel. Only in the presence of BDAC/AOT-modified AuNTs can a stable colloidal dispersion be observed.

The TEM micrographs clarify that spherical silver nanoparticles are formed on the gold nanotriangle surfaces (Figure 2). Note that these important findings are in contrast to the formation of a closed silver shell surrounding gold nanorods.[11,26] This special behavior can be explained by the quite different surface modification of our AOT-stabilized AuNTs. Currently published MD simulations have shown that AOT micelles with an aggregation number of 20 strongly adsorb on the Au (111) facets, resulting in distorted cylindrical micelles attached to the gold surface.[50] Thus, the role of the added cationic surfactant has to be discussed in more detail. A hydrophobic dominated bilayer through interdigitated chains of AOT and BDAC on the gold surface can be discussed in this context, too. However, in the case of two oppositely charged surfactant molecules electrostatic interactions between the head groups mainly influence phenomena of self-assembly. It is well-known that oppositely charged surfactants can form different types of organized systems, including catanionic vesicles. Villa et al. have shown that AOT and BDAC can build up spontaneously unilamellar vesicles.[51] Therefore, it can be assumed that the cationic surfactant BDAC attaches to the AOT micelles at the surface of the AuNTs, which spontaneously form an alternating AOT/BDAC layer in between the AOT micelles and the BDAC bilayer, as schematically shown in Scheme 2. Our EDX experiments

Scheme 2. Representation of the Ag Reduction Process on the Surface of the Au Nanotriangles in the Presence of the AOT Micelle/BDAC Bilayer

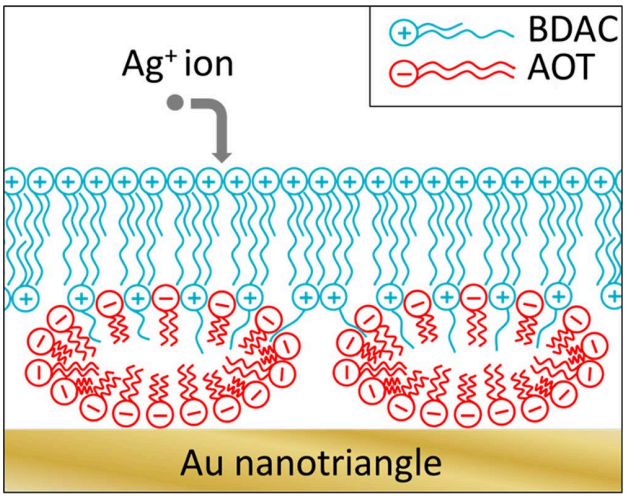

(shown later) underline this model of AOT micelles surrounded by a BDAC layer. Therefore, the transport process of individual Ag^+ ions to the AuNTs can be described in analogy to the schemata proposed by Tebbe et al.,[11] but due to the presence of the more stable AOT micelle/BDAC bilayer on the surface of the AuNTs, the transport of Ag^+ ions is hindered, and a quite different Ag crystallization of spherically particles take place. When we perform similar experiments in the absence of BDAC, this means by adding $AgNO_3$ to the AOT-modified AuNTs (in analogy to the experiments shown here), a silver film formation on the surface of the nanotriangles is observed, resulting in a broad extinction peak shifted to lower wavelength. The resulting Au@AgNTs are not stable and coagulate after several hours. These additional experiments clearly show that spherical nanoparticles are formed only in the presence of the AOT micelle/BDAC bilayer. On the one hand, the size of the "spheres" decreases with a higher concentration of silver, and at the same time the polydispersity of the individual "spheres" decreases. On the other hand, the density of the "spheres" increases. This behavior can be discussed on the basis of nucleation processes in the AOT micelle/BDAC bilayer. At a lower Ag^+ ion concentration the Ag clusters grow up to larger dimensions, and at higher Ag^+ ion concentration many more seeds are spontaneously formed, leading to a more homogeneous particle distribution on the AuNT surface (see Table 1). We have calculated the coverage ratio of spherical Ag nanoparticles (according to Table 1) on the surface of a standard AuNT with an edge length of 175 nm. Thus, sample E offers the most uniform coating by spherical particles and will be investigated in the following experiments in more detail. For analyzing, the standard deviation values of the iTEM software were taken. Because of the inhomogeneity of the spherelike silver particles, the average diameter was determined by the largest distance of the particles themselves, whereas the inner particle distance was measured by the shortest edge-to-edge

DOI: 10.1021/acsanm.8b00570
ACS Appl. Nano Mater. 2018, 1, 1995−2003

Table 1. TEM Analysis of the AgNPs on the AuNTs Surface Shown in Figure 2

sample	size [nm]	particle distance [nm]	number of particles	coverage ratio [%]
B	19 ± 9	24 ± 13	27 ± 11	4
C	21 ± 8	19.5 ± 9	38 ± 7	21
D	12.5 ± 3	6 ± 4	56 ± 10	42
E	12 ± 2	4 ± 2	81 ± 14	56

distance. To obtain representative results, approximately thousand particles were included to the calculations.

To get more information about the three-dimensional structure of the modified AuNTs, SEM measurements of the sample E were performed (Figure 3). The inset image of Figure 3 shows an SEM measurement at a tilting angle of 45°, where a part of the downside structure can be noticed. AgNPs grow as "spheres" on the side and surface facets of the AuNTs.

A more detailed characterization of the crystalline structure was obtained by using HRTEM. Furthermore, the decoration of the AgNPs was investigated by elemental analysis through STEM in combination with EDX. Figure 4 shows a HRTEM micrograph of a silver-coated gold nanotriangle tip with the fast Fourier transformation (FFT) of two areas. The FFT of the red marked area in the HRTEM micrograph shows the typical 6-fold symmetry of the gold triangle orientated in the ⟨111⟩-direction, in agreement with earlier experiments.[41] The spots marked by the squares correspond to the 1/3 {224} reflections, and the circles correspond to the {220} reflections of the gold nanotriangle. In the FFT of the blue marked area one can find additional spots, marked by the triangles corresponding to {111} reflections (green) and {200} reflections (blue). These extra reflections show that there are separate spherical particles on the surface of the gold triangle. Because of the similar lattice parameters, we cannot distinguish between gold and silver. Therefore, additional energy dispersive X-ray spectroscopy (EDX) analysis of the Ag-coated gold nanotriangles was performed.

Figure 5 shows different EDX measurements of sample E. For (1) and (2), we determine the material composition by a point analysis. The particle of spectrum 1 is recorded on a sphere which has grown over the edge of the triangle. Consistently, the EDX shows no gold atoms in this region. Besides the expected silver atoms in the spherical particle, the observation of a copper EDX signal can be assigned to the TEM grid and the sulfur to the surfactant AOT, which remains on the triangle facets. In addition to the clearly defined sulfur peak of the AOT one can find a significant smaller chlor peak characteristic for the chloride counterions of BDAC (compare Figure 5). This is an experimental evidence for both surfactants in the shell surrounding the AuNTs. The clear dominance of the sulfur peak in comparison to the chloride counterion peak of BDAC underlines the proposed model of AOT micelles (shown in Scheme 2) with an alternating AOT/BDAC layer (accompanied by a release of the counterions), in contrast to a model of interdigitated chains.

Point 2 shows the spectrum of a particle on the triangle surface. As expected, we find gold in the elemental analysis. The maximum for sulfur was overlaid by the more intense gold peak. To underpin these results, a line analysis was carried out along the line labled 3. Starting from outside the Au@AgNT, we first observe a pronounced smooth maximum of the Ag signal, where the intensity dependence is given by the thickness of the sphere as the line cuts through the ball-shaped Ag particle. By coincidence, the center of the Ag nanosphere lies on top of the AuNT's edge, giving rise to the sharp increase of the Au signal in the line analysis 3 in Figure 5.

3.2. SERS Performance of Au@Ag Triangles. For SERS measurements, the Au@AgNTs were self-assembled on glass in analogy to our former experiments.[41] To this end, an ethanol–toluene (5:1) mixture was added to a droplet of sample E deposited on glass. The oil mixture in a ratio 1:2 induces a complete wetting of the substrate, and a shimmering layer at the interface was seen. After evaporation a close-packed layer of Au@AgNTs remains on the substrate. In Figure S2, the layer formation of sample E with the highest Ag concentration can be seen at different magnifications of the SEM micrographs.

3.3. SERS Experiments. SERS was recently used as a promising analytical technique to identify traces of chemical

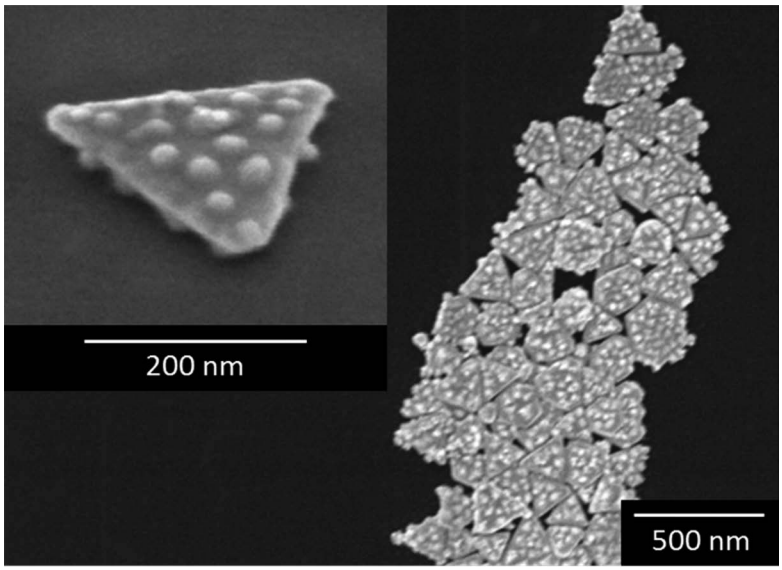

Figure 3. SEM micrographs of sample E. Inset: recording at tilting angle of 45°.

DOI: 10.1021/acsanm.8b00570
ACS Appl. Nano Mater. 2018, 1, 1995–2003

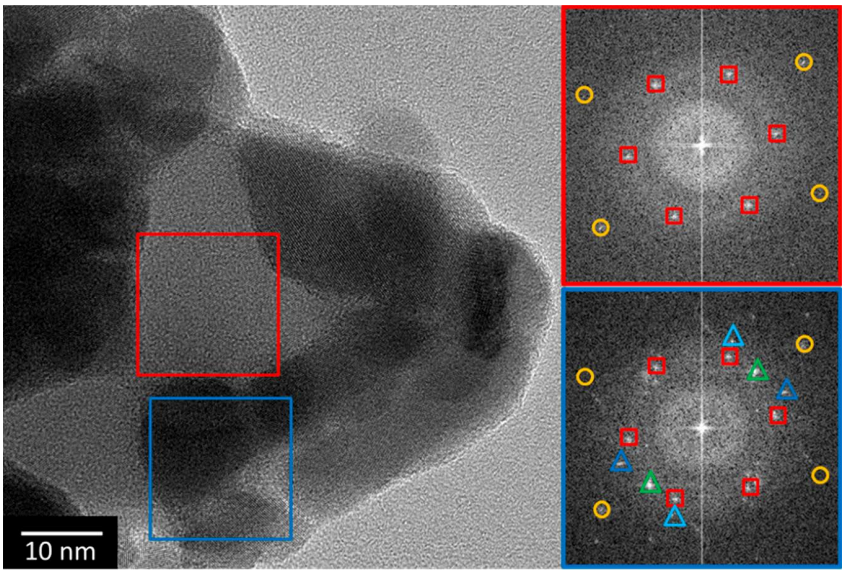

Figure 4. HRTEM micrograph of a gold nanotriangle tip decorated with silver nanoparticles and the fast Fourier transformation of two different areas.

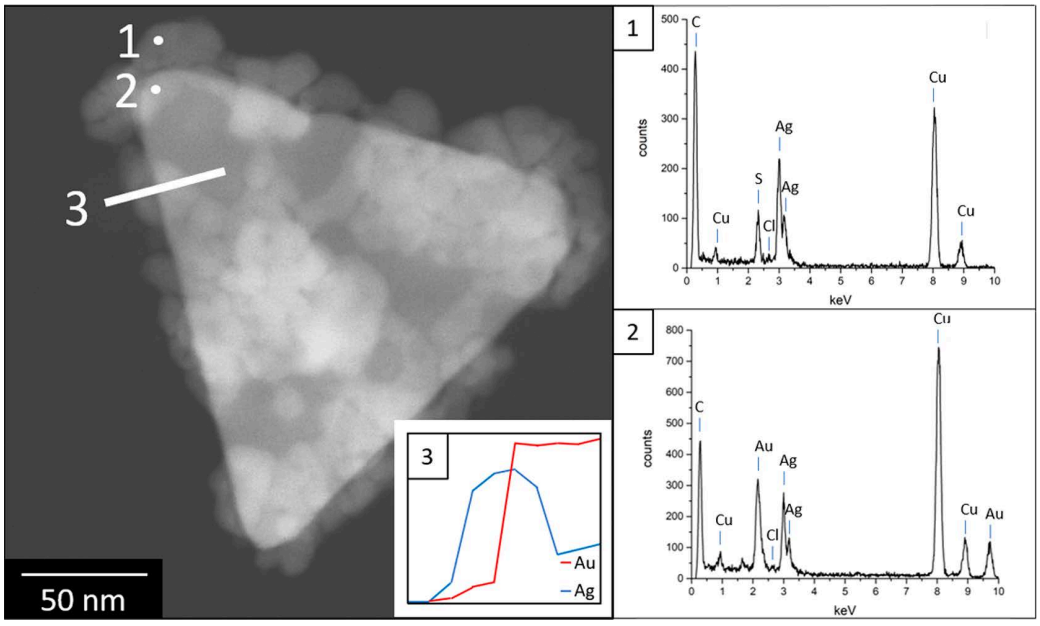

Figure 5. EDX measurements of sample E. (1) and (2): point analysis; (3): line analysis.

and biological samples, owing to the high signal enhancement provided by the metal nanoparticles. For instance, SERS helped to identify the missing colorant of the famous painting "For to be a farmer's boy" from traces of the dye left on the painting.[52] Here we demonstrate the SERS performance of the prepared particle-modified substrates with a low concentration of Rhodamine R6G dye (1 mM) as the probe molecule. R6G molecules were self-assembled on monolayers of the prepared nanostructures. Figure 6 shows a SERS spectrum of R6G, which matches the Raman spectrum of the bulk R6G molecules. The characteristic Raman bands at 610, 770, 1184, and 1307 cm^{-1} were assigned to the C−C−C ring in-plane bending, out-of-plane bending, C−C stretching vibrations, and C−O−C stretching, respectively. The vibrations at 1356 and 1504 cm^{-1} are assigned to the aromatic ring C−C stretching vibrations.[53]

Figure 7 displays SERS spectra of R6G adsorbed on the five substrates with different Ag "sphere" coverage of the AuNT (compare Figure 1). Sample E exhibited the highest signal enhancement compared to the other Au@Ag particles and the bare gold nanotriangles. Generally, the signal enhancement of SERS can originate from a chemical enhancement mechanism (CM) and an electromagnetic enhancement mechanism (EM). In our study the EM is mainly responsible for the SERS signal enhancement for varying Ag particle concentration. Furthermore, we measured SERS spectrum of the sample E using a different excitation wavelength (532 nm) under the same conditions of the Raman microscope. As a result, the characteristic Raman peaks of R6G were barely observed as

DOI: 10.1021/acsanm.8b00570
ACS Appl. Nano Mater. 2018, 1, 1995−2003

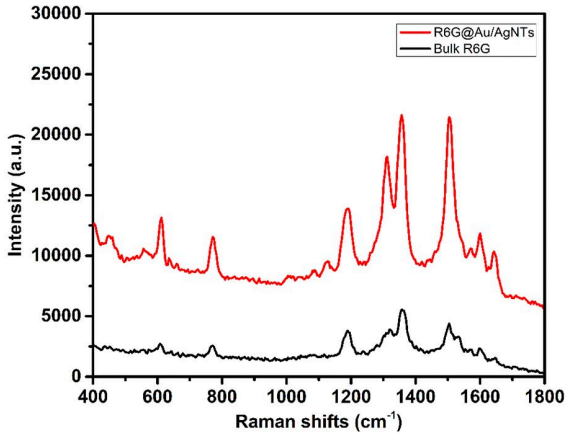

Figure 6. SERS performance of the bulk R6G molecules self-assembled on Au@AgNTs taken using 2 mW excitation power and 60 s integration time.

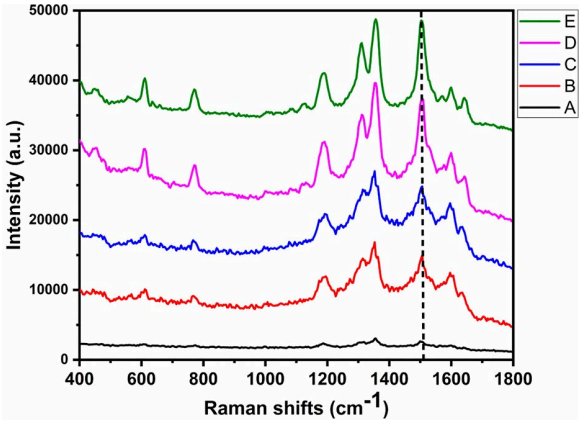

Figure 7. SERS performance of self-assembled R6G molecules on Au@AgNTs at different at different amounts of a 0.1 M aqueous $AgNO_3$ solution: (A) without $AgNO_3$, (B) 2.5 μL, (C) 5 μL, (D) 7.5 μL, and (E) 10 μL.

shown in Figure S3, which confirms the dependence of the SERS performance on the plasmon resonance. The presence of Ag "spheres" on the AuNTs considerably shifts the extinction (Figure 1) of the localized surface plasmon resonance (LSPR) of the particle.[54] Moreover, the silver nanoparticles surrounding the gold nanotriangles form good nanogaps as new SERS hot spots where the molecules exhibit extraordinary signal enhancement.

The signal enhancement factor (EF) is the ratio of the signal intensity of Raman from a bulk sample to the SERS intensity of a selected vibrational mode, normalized by the number of molecules in the excited laser spot. The EF was calculated from the formula

$$\mathrm{EF} = \frac{I_{\mathrm{SERS}}}{I_{\mathrm{bulk}}}\frac{N_{\mathrm{bulk}}}{N_{\mathrm{SERS}}}$$

where I_{SERS} and I_{bulk} are the Raman scattering intensities of the selected mode (peak at 1504 cm^{-1}) for the SERS and bulk samples, respectively. N_{SERS} is the number of R6G molecules in the laser spot, which are adsorbed on SERS substrate, while N_{bulk} is the number of the probed molecules in the bulk sample. We assumed that R6G molecules formed a compact monolayer on the surface of the particles. N_{SERS} was calculated to be 3.5 × 10^5 based on the laser spot size and the area occupied by an R6G molecule. Moreover, based on the density of the R6G bulk material, N_{bulk} was calculated to be 3 × 10^{10} within the illuminated volume. I_{SERS} and I_{bulk} were taken for Raman vibrational mode at 1504 cm^{-1} from the spectra shown in Figure 7. The enhancement factor was calculated to be 5.1 × 10^5. To study the capacity of the SERS substrate, we further decreased the concentration of the analyte (10^{-5} M). Figure 8

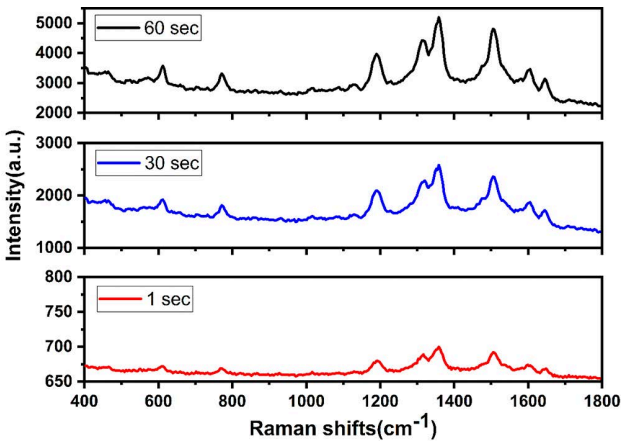

Figure 8. SERS spectra of 10^{-5} M R6G assembled on sample E recorded using different integration times.

shows SERS spectra of R6G molecules assembled on sample E and taken at different integration times. Interestingly, the Raman bands of the 10^{-5} M of R6G were clearly visible even using low excitation power (2 mW) and short integration time (1 s) which can be considered as the limit of detection at these conditions, since high excitation powers and/or longer irradiation time were reported to induce chemical changes of the analyte.[29,55] Finally, we attribute this high EF to the plasmon resonance as well as the newly formed nanogap between the gold NTs and the silver NPs.

4. CONCLUSIONS

The main advantage of our Au@Ag nanotriangles in contrast to gold nanoparticles covered by a closed silver shell is the controlled formation of undulated surfaces with tunable optical and photocatalytic properties by decorating the surface with spherical silver nanoparticles.

The growth of spherical Ag particles on the gold surface is induced by the templating effect of the AOT micelle/BDAC bilayer, spontaneously formed after reloading the AOT-stabilized AuNTs with the cationic surfactant BDAC. The catanionic AOT/BDAC layer hinders the transport of Ag^+ ions, which leads to the formation of spherical Ag nanoparticles in the surfactant bilayer shell. The overgrowth of gold nanotriangles with spherical silver nanoparticles opens a way of fine-tuning the optical properties of the resulting undulated Au@Ag NTs by varying the Ag nanoparticle concentration on the Au surface. The modulation of the surface plasmons leads to a significant blue-shift of the dipolar mode and an enhancement of the in-plane quadrupolar mode. With increasing $AgNO_3$, the decoration of the AuNTs by a nanoparticle monolayer is achieved. Additionally, EDX and HRTEM measurements of the Au@AgNTs clearly verify the growth of silver nanoparticles on the surface as well as on the edge of the platelets. The Au@AgNTs are efficient SERS substrates, which show an enhance-

DOI: 10.1021/acsanm.8b00570
ACS Appl. Nano Mater. 2018, 1, 1995−2003

ment factor of 5.1×10^5 for the highest amount of silver. This can be attributed to the amount of AgNPs and therefore to the amount of nanogaps and their homogeneity at the nanotriangle surface.

■ ASSOCIATED CONTENT

Supporting Information

The Supporting Information is available free of charge on the ACS Publications website at DOI: 10.1021/acsanm.8b00570.

One TEM micrograph and two SEM micrographs (PDF)

■ AUTHOR INFORMATION

Corresponding Author

*(J.K.) E-mail koetz@uni-potsdam.de; Ph +49 331 977 5220.

ORCID

Matias Bargheer: 0000-0002-0952-6602

Joachim Koetz: 0000-0001-9113-1337

Notes

The authors declare no competing financial interest.

■ ACKNOWLEDGMENTS

The financial support from the German Research Foundation (KO 1387/14-1; INST 336/64-1) is gratefully acknowledged.

■ REFERENCES

(1) Kalele, S.; Gosavi, S. W.; Urban, J.; Kulkarini, S. K. Nanoshell Particles: Synthesis, Properties and Applications. *Curr. Sci.* **2006**, *91*, 1038−1052.

(2) Zhao, J.; Zhang, X.; Yonzon, C. R.; Haes, A. J.; Van Duyne, R. P. Localized Surface Plasmon Resonance Biosensors. *Nanomedicine* **2006**, *1*, 219−228.

(3) Endo, T.; Ikeda, D.; Kawakami, Y.; Yanagida, Y.; Hatsuzawa, T. Fabrication of Core-Shell Structured Nanoparticle Layer Substrate for Excitation of Localized Surface Plasmon Resonance and Its Optical Response for DNA in aqueous Conditions. *Anal. Chim. Acta* **2010**, *661*, 200−205.

(4) Steinbrück, A.; Stranik, O.; Csaki, A.; Fritzsche, W. Sensoric Potential of Gold-Silver Core-Shell Nanoparticles. *Anal. Bioanal. Chem.* **2011**, *401*, 1241−1249.

(5) Anker, J. N.; Hall, W. P.; Lyan dres, O.; Shah, N. C.; Zhao, J.; Van Duyne, R. P. Biosensing with Plasmonic Nanosensors. *Nat. Mater.* **2008**, *7*, 442−453.

(6) Fu, Y. Q.; Zhou, W. Modulation of Main Lobe for Superfocusing Using Subwavelength Metallic Heterostructures. *Plasmonics* **2009**, *4*, 141−146.

(7) Wax, A.; Sokolov, K. Molecular Imaging and Darkfield Microspectroscopy of Live Cells Using Gold Plasmonic Nanoparticles. *Laser Photonics Rev.* **2009**, *3*, 146−158.

(8) Ando, J.; Yano, T.; Fujita, K.; Kawata, S. Metal Nanoparticles for Nano-Imaging and Nano-Analysis. *Phys. Chem. Chem. Phys.* **2013**, *15*, 13713−13722.

(9) Fernanda Cardinal, M.; Rodríguez-González, B.; Alvarez-Puebla, R. A.; Pérez-Juste, J.; Liz-Marzán, L. M. Modulation of Localized Surface Plasmons and SERS Response in Gold Dumbbells through Silver Coating. *J. Phys. Chem. C* **2010**, *114*, 10417−10423.

(10) Nima, Z. A.; Davletshin, Y. R.; Watanabe, F.; Alghazali, K. M.; Kumaradas, J. C.; Biris, A. S. Bimetallic Gold Core-Silver Shell Nanorod Performance for Surface Enhanced Raman Spectroscopy. *RSC Adv.* **2017**, *7*, 53164−53171.

(11) Tebbe, M.; Kuttner, C.; Mayer, M.; Maennel, M.; Pazos-Perez, N.; König, T. A. F.; Fery, A. Silver-Overgrowth-Induced Changes in Intrinsic Optical Properties of Gold Nanorods: From Noninvasive Monitoring of Growth Kinetics to Tailoring Internal Mirror Charges. *J. Phys. Chem. C* **2015**, *119*, 9513−9523.

(12) Gong, J.; Zhou, F.; Li, Z.; Tang, Z. Synthesis of Au@Ag Core-Shell Nanocubes Containing Varying Shaped Cores and Their Localized Surface Plasmon Resonances. *Langmuir* **2012**, *28*, 8959−8964.

(13) Schlücker, S. Surface-Enhanced Raman Spectroscopy: Concepts and Chemical Applications. *Angew. Chem., Int. Ed.* **2014**, *53*, 4756−4795.

(14) Tian, Z. Q.; Ren, B.; Wu, D. Y. Surface-Enhanced Raman Scattering: From Nobel to Transition Metals and From Rough Surfaces to Ordered Nanostructures. *J. Phys. Chem. B* **2002**, *106*, 9463−9483.

(15) Zrimsek, A. B.; Chiang, N.; Mattei, M.; Zaleski, S.; McAnally, M. O.; Chapman, C. T.; Henry, A.-I.; Schatz, G. C.; Van Duyne, R. P. Single-Molecule Chemistry with Surface- and Tip-Enhanced Raman Spectroscopy. *Chem. Rev.* **2017**, *117*, 7583−7613.

(16) Link, S.; El-Sayed, M. A. Size and Temperature Dependence of the Plasmon Absorption of Colloidal Gold Nanoparticles. *J. Phys. Chem. B* **1999**, *103*, 4212−4217.

(17) Kelly, K. L.; Coronado, E.; Zhao, L. L.; Schatz, G. C. The Optical Properties of Metal Nanoparticles: The Influence of Size, Shape, and Dielectric Environment. *J. Phys. Chem. B* **2003**, *107*, 668−677.

(18) Yang, W.; Wu, K.; Yang, W.; Wang, H.; Lv, X.; Qian, L.; Yu, T.; Li, Z.; Zhou, X.; Barasa, G. O.; Yuan, S.; Jiang, Y.; Yang, Z. Nanoporous Au-Ag shell with fast kinetics: Integrating Chemical and Plasmonic Catalysis. *Nanotechnology* **2017**, *28*, 425704.

(19) Etchegoin, P. G.; Le Ru, E. C. Basic Electromagnetic Theory of SERS. In *Surface Enhanced Raman Spectroscopy: Analytical, Biophysical and Life Science Applications*; Schlücker, S., Ed.; Wiley-VCH: Weinheim, 2010; pp 1−37.

(20) Zhao, J.; Pinchuk, A. O.; McMahon, J. M.; Li, S.; Ausman, L. K.; Atkinson, A. L.; Schatz, G. C. Methods for Describing, the Electromagnetic Properties of Silver and Gold Nanoparticles. *Acc. Chem. Res.* **2008**, *41*, 1710−1720.

(21) Kim, B.-H.; Oh, J.-H.; Han, S. H.; Yun, Y.-J.; Lee, J.-S. Combinatorial Polymer Library Approach for the Synthesis of Silver nanoplates. *Chem. Mater.* **2012**, *24*, 4424−4433.

(22) Jin, R.; Cao, Y. W.; Mirkin, C. A.; Kelly, K. L.; Schatz, G. C.; Zheng, J. G. *Science* **2001**, *294*, 1901.

(23) Tsai, D.-S.; Chen, C.-H.; Chou, C.-C. Preparation and Characterization of of gold-coated silver triangular platelets in nanometer scale. *Mater. Chem. Phys.* **2005**, *90*, 361−366.

(24) Xue, C.; Millstone, J. E.; Li, S.; Mirkin, C. A. Plasmon-Driven Synthesis of Triangular Core-Shell Nanoprisms from Gold Seeds. *Angew. Chem., Int. Ed.* **2007**, *46*, 8436−8439.

(25) Lui, M.; Guyot-Sionnest, P. Syntheis and Optical Characterization of Au/Ag Core/Shell nanorods. *J. Phys. Chem. B* **2004**, *108*, 5882−5888.

(26) Gómez-Graña, S.; Goris, B.; Altantzis, T.; Fernández-López, C.; Carbó-Argibay, E.; Guerrero-Martínez, A.; Almora-Barrios, N.; López, N.; Pastoriza-Santos, I.; Pérez-Juste, J.; Bals, S.; Van Tendeloo, G.; Liz-Marzán, L. M. Au@Ag Nanoparticles: Halides Stabilize {100} Facets. *J. Phys. Chem. Lett.* **2013**, *4*, 2209−2216.

(27) Hou, S.; Hu, X.; Wen, T.; Liu, W.; Wu, X. Core-Shell Noble Metal Nanostructures Templated by Gold Nanorods. *Adv. Mater.* **2013**, *25*, 3857−3862.

(28) Hartman, T.; Wondergem, C. S.; Kumar, N.; van den Berg, A.; Weckhuysen, B. M. Surface- and Tip-Enhanced Raman Spectroscopy in Catalysis. *J. Phys. Chem. Lett.* **2016**, *7*, 1570−1584.

(29) Liebig, F.; Sarhan, R. M.; Sander, M.; Koopman, W.; Schütz, R.; Bargheer, M.; Koetz, J. Deposition of Gold Nanotriangles in Large Scale Close-Packed Monolayers for X-Ray-Based Temperature Calibration and SERS Monitoring of Plasmon-Driven Catalytic Reactions. *ACS Appl. Mater. Interfaces* **2017**, *9*, 20247−20253.

(30) Von Reppert, A.; Sarhan, R. M.; Stete, F.; Pudell, J.; Del Fatti, N.; Crut, A.; Koetz, J.; Liebig, F.; Prietzel, C.; Bargheer, M. Watching the Vibraation and Cooling of Ultrathin Gold Nanotriangles by Ultrafast X-Ray Diffraction. *J. Phys. Chem. C* **2016**, *120*, 28894−28899.

DOI: 10.1021/acsanm.8b00570
ACS Appl. Nano Mater. 2018, 1, 1995−2003

(31) Lin, M.; Wang, Y.; Sun, X.; Wang, W.; Chen, L. Elastic" Property of Mesoporous Silica Shell: for Dynamic Surface Enhanced Raman Scattering Ability Monitoring of Growing Noble Metal Nanostructures via a Simplified Spatially Confined Growth Method. *ACS Appl. Mater. Interfaces* **2015**, *7*, 7516−7525.
(32) Zhang, Y.; Wang, Z.; Wu, L.; Pei, Y.; Chen, P.; Cui, Y. *Analyst* **2014**, *139*, 5148−5154.
(33) Contreras-Caceres, R.; Dawson, C.; Formanek, P.; Fischer, D.; Simon, F.; Janke, A.; Uhlmann, P.; Stamm, M. Polymers as Templates for Au and Au@Ag Bimetallic Nanorods: UV-Vis and Surface Enhanced Raman Spectroscopy. *Chem. Mater.* **2013**, *25*, 158−169.
(34) Gao, J.; Bender, C. M.; Murphy, C. J. Dependence of the Gold Nanorod Aspect Ratio on the Nature of the Directing Surfactant in Aqueous Solution. *Langmuir* **2003**, *19*, 9065−9070.
(35) Scarabelli, L.; Coronado-Puchau, M.; Giner-Casares, J. J.; Langer, J.; Lir-Marzan, L. M. Monodisperse Gold Nanotriangles: Size Control, Large-Scale Self-Assembly, and Performance in Surface-Enhanced Raman Scattering. *ACS Nano* **2014**, *8*, 5833−5842.
(36) Scarabelli, L.; Grzelczak, M.; Liz-Marzan, L. M. Tuning Gold Nanorod Synthesis through Prereduction with Salicylic Acid. *Chem. Mater.* **2013**, *25*, 4232−4238.
(37) Ye, X.; Jin, L.; Caglayan, H.; Chen, J.; Xing, G.; Zheng, C.; Doan-Nguyen, V.; Kang, Y.; Engheta, N.; Kagan, C. R.; Murray, C. B. Improved Size-Tunable Synthesis of Monodisperse Gold Nanorods through the Use of Aromatic Additives. *ACS Nano* **2012**, *6*, 2804−2817.
(38) Hong, S.; Acapulco, J. A. I.; Jang, H.-J.; Kulkarni, A. S.; Park, S. Kinetically Controlled Growth of Gold Nanoplates and Nanorods via a One-Step Seed-Mediated Method. *Bull. Korean Chem. Soc.* **2014**, *35*, 1737−1742.
(39) Lohse, S. E.; Burrows, N. D.; Scarabelli, L.; Liz-Marzan, L. M.; Murphy, C. J. Anisotropic Noble Metal Nanocrystal Growth: The Role of Halides. *Chem. Mater.* **2014**, *26*, 34−43.
(40) Park, K.; Drummy, L. F.; Vaia, R. A. Ag Shell Morphology on Au Nanorod Core: Role of Ag Precursor Complex. *J. Mater. Chem.* **2011**, *21*, 15608−15618.
(41) Liebig, F.; Sarhan, R. M.; Prietzel, C.; Reinecke, A.; Koetz, J. Green" Gold Nanotriangles: Synthesis, Purification by Polyelectrolyte/Micelle Depletion Flocculation and Performance in Surface-Enhanced Raman Scattering. *RSC Adv.* **2016**, *6*, 33561−33568.
(42) Liebig, F.; Thünemann, A. F.; Koetz, J. *Langmuir* **2016**, *32*, 10928−10935.
(43) Jing, H.; Zhang, Q.; Large, N.; Yu, C.; Blom, D. A.; Nordlander, P.; Wang, H. Tunable Plasmonic Nanoparticles with Catalytically Active High-Index Facets. *Nano Lett.* **2014**, *14*, 3674−3682.
(44) Jiang, R.; Chen, H.; Shao, L.; Li, Q.; Wang, J. Unraveling the Evolution and Nature of the Plasmons in (Au Core)-(Ag Shell) Nanorods. *Adv. Mater.* **2012**, *24*, OP200−OP207.
(45) Husein, M. M.; Rodil, E.; Vera, J. H. A Novel Approach for the Preparation of AgBr Nanoparticles from Their Bulk Solid Precursor Using CTAB Microemulsions. *Langmuir* **2006**, *22*, 2264−2272.
(46) Liu, X.-H.; Luo, X.-H.; Lu, S.-X.; Zhang, J.-C.; Cao, W.-L. A Novel Cetyltrimethyl Ammonium Silver Bromide Complex and Silver Bromide Nanoparticles Obtained by the Surfactant Counterion. *J. Colloid Interface Sci.* **2007**, *307*, 94−100.
(47) Okuno, Y.; Nishioka, K.; Kiya, A.; Nakashima, N.; Ishibashi, A.; Niidome, Y. Uniform and Controllable Preparation of Au-Ag Core-Shell Nanorods Using Anistropic Silver Shell Formation on Gold Nanorods. *Nanoscale* **2010**, *2*, 1489−1493.
(48) Mie, G. Beiträge zur Optik trüber Medien, speziell kolloidaler Metallösungen. *Ann. Phys.* **1908**, *330*, 377.
(49) Félidj, N.; Grand, J.; Laurent, G.; Aubard, J.; Lévi, G.; Hohenau, A.; Galler, N.; Aussenegg, F. R.; Krenn, J. R. Multipolar Surface Plasmon Peaks on Gold Nanotriangles. *J. Chem. Phys.* **2008**, *128*, 094702.
(50) Poghosyan, A.; Shahinyan, A. A.; Koetz, J. Self-assembled Monolayer Formation of Distorted Cylindrical AOT Micelles on Gold Surfaces. *Colloids Surf., A* **2018**, *546*, 20.
(51) Villa, C. C.; Correa, N. M.; Silber, J. J.; Moyano, F.; Falcone, R. D. Singularities in the Physicochemical Properties of Spontaneous AOT-BHD Unilamellar Vesicles in Comparison with DOPC Vesicles. *Phys. Chem. Chem. Phys.* **2015**, *17*, 17112−17121.
(52) Brosseau, C. L.; Casadio, F.; Van Duyne, R. P. Revealing the Invisible: Using Surface-Enhanced Raman Spectroscopy to Identify Minute Remnants of Color in Winslow Homer's Colorless Skies. *J. Raman Spectrosc.* **2011**, *42*, 1305−1310.
(53) Zhai, W.-L.; Li, D.-W.; Qu, L.-L.; Fossey, J. S.; Long, Y.-T. Multiple Depositions of Ag Nanoparticles on Chemically Modified Agarose Films for Surface-Enhanced Raman Spectroscopy. *Nanoscale* **2012**, *4*, 137−142.
(54) Sow, I.; Grand, J.; Lévi, G.; Aubard, J.; Félidj, N.; et al. Revisiting Surface-Enhanced Raman Scattering on Realistic Lithographic Gold Nanostripes. *J. Phys. Chem. C* **2013**, *117*, 25650−25658.
(55) Tesema, T. E.; Kafle, B.; Tadesse, M. G.; Habteyes, T. G. Plasmon-Enhanced Resonant Excitation and Demethylation of Methylene Blue. *J. Phys. Chem. C* **2017**, *121*, 7421−7428.

DOI: 10.1021/acsanm.8b00570
ACS Appl. Nano Mater. 2018, 1, 1995−2003

Supporting Information

Tuned Surface Enhanced Raman Scattering Performance of Undulated Au@Ag Triangles

Ferenc Liebig,[a] Radwan M. Sarhan,[b,c,d] Claudia Prietzel,[a] Clemens N.Z. Schmitt,[e] Matias Bargheer,[b] Joachim Koetz[a,*]

[a]Institute for Chemistry and [b]Institute for Physics, University of Potsdam, 14476 Potsdam, Germany

[c]Chemistry Department, Faculty of Science, Cairo University, Cairo 12613, Egypt

[d]School of Analytical Sciences Adlershof (SALSA), Humboldt-Universität of Berlin, 10099 Berlin, Germany

[e]Max Planck Institute of Colloids and Interfaces, 14476 Potsdam, Germany

* Corresponding author: Joachim Koetz

E-mail: koetz@uni-potsdam.de

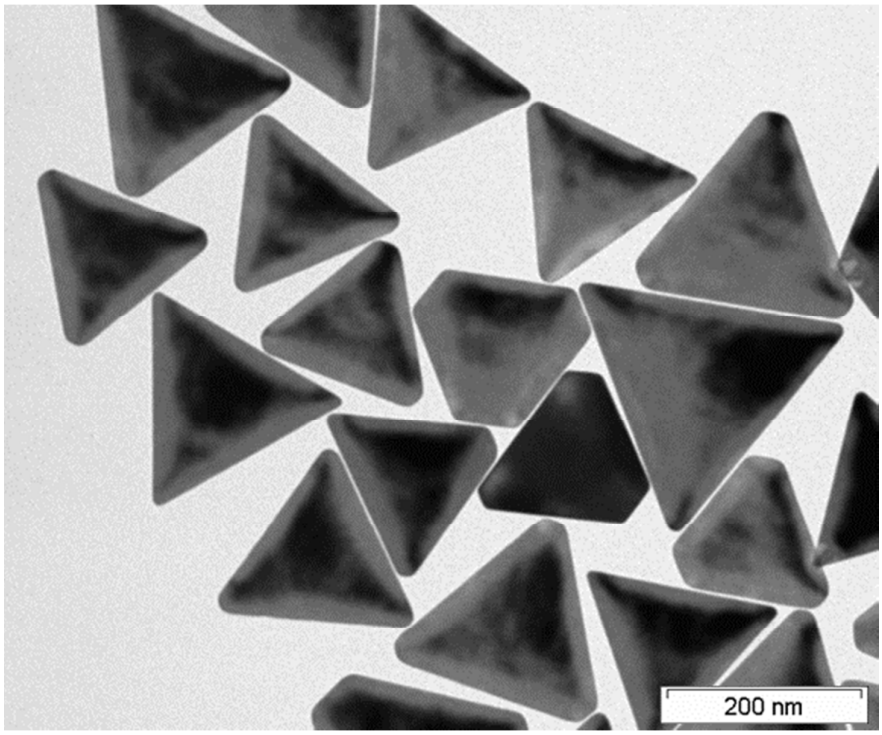

Figure S1. TEM micrographs of the purified gold nanotriangles.

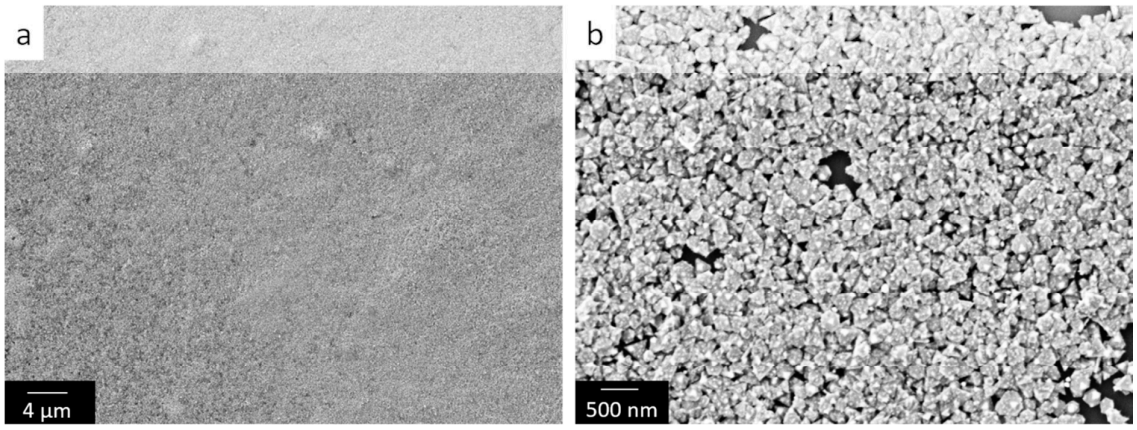

Figure S2. Representative SEM micrographs of self-assembled Ag@AuNTs of sample E deposit on glass at lower and higher magnification (b).

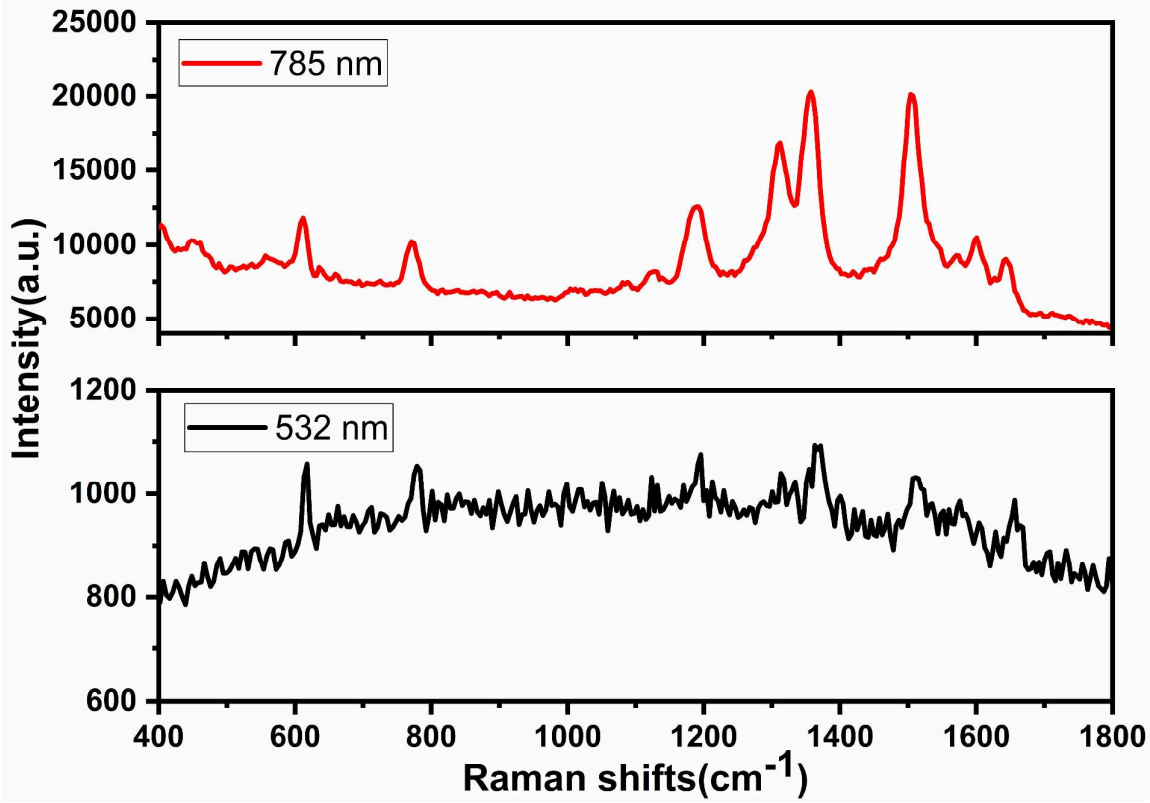

Figure S3. SERS spectra of 10^{-5} M of R6G assembled on sample E at the excitation wavelength of 532 nm and 785 nm.

OPEN ACCESS
IOP Publishing
Nanotechnology
Nanotechnology 29 (2018) 185603 (8pp)
https://doi.org/10.1088/1361-6528/aaaffd

A new route to gold nanoflowers

Ferenc Liebig[1], Ricky Henning[1], Radwan M Sarhan[2,3,4], Claudia Prietzel[1], Matias Bargheer[2] and Joachim Koetz[1]

[1] Institute for Chemistry, University of Potsdam, 14476 Potsdam, Germany
[2] Institute for Physics, University of Potsdam, 14476 Potsdam, Germany
[3] Chemistry Department, Faculty of Science, Cairo University, Cairo 12613, Egypt
[4] School of Analytical Sciences Adlershof (SALSA), Humboldt-Universität of Berlin, 10099 Berlin, Germany

E-mail: koetz@uni-potsdam.de

Received 21 December 2017, revised 13 February 2018
Accepted for publication 16 February 2018
Published 9 March 2018

Abstract

Catanionic vesicles spontaneously formed by mixing the anionic surfactant bis(2-ethylhexyl) sulfosuccinate sodium salt with the cationic surfactant cetyltrimethylammonium bromide were used as a reducing medium to produce gold clusters, which are embedded and well-ordered into the template phase. The gold clusters can be used as seeds in the growth process that follows by adding ascorbic acid as a mild reducing component. When the ascorbic acid was added very slowly in an ice bath round-edged gold nanoflowers were produced. When the same experiments were performed at room temperature in the presence of Ag^+ ions, sharp-edged nanoflowers could be synthesized. The mechanism of nanoparticle formation can be understood to be a non-diffusion-limited Ostwald ripening process of preordered gold nanoparticles embedded in catanionic vesicle fragments. Surface-enhanced Raman scattering experiments show an excellent enhancement factor of $1.7 \cdot 10^5$ for the nanoflowers deposited on a silicon wafer.

Supplementary material for this article is available online

Keywords: catanionic vesicles, gold cluster, gold nanoflowers, crystal growth, HRTEM, SEM

(Some figures may appear in colour only in the online journal)

1. Introduction

The size- and shape-dependent optical properties of gold nanoparticles are of special interest in different fields of catalysis [1], photonics [2], sensing [3], and for biomedical uses [4, 5]. In particular, asymmetric gold nanoparticles, such as nanorods [6], nanocages [7], nanopyramids [8], nanotriangles [9] and nanoprisms [10] offer great potential in biomedical applications such as photothermal cancer therapy [11] and imaging [12] due to their absorption in the near-infrared (tissue diagnostic window) range [13]. Furthermore, the localized surface plasmon resonance can be easily tailored by small changes to the morphology [9, 14, 15]. The presence of the sharp tips and spikes of those anisotropic particles leads in surface-enhanced Raman scattering (SERS) to an increased electromagnetic field, which enhances the Raman signal and enables the investigation of catalytic reactions [15–18]. Studies of facet-dependent catalytic activity showed that high-index faceted particles aid molecule adsorption and are most active for surface reactions [18, 19]. Thus, the more exotic nanostars turned into the focus of the relevant research [20, 21].

Various protocols have been reported to produce anisotropic metal nanoparticles. Template-based strategies [22, 23] and seed-mediated routes [24, 25] have been used. The procedure used most often is to obtain asymmetric particles based on a seed-mediated, two-step process in the presence of the cationic surfactant cetyltrimethylammonium bromide (CTAB) [24]. In the second step, the CTAB-based gold seeds are grown by adding ascorbic acid (AA) in the presence of silver ions. Nevertheless, for the synthesis of nanostars a modified procedure is needed, e.g., by performing the seed-mediated growth process in a concentrated dimethylformamide solution in the

presence of poly(vinyl pyrrolidone) (PVP) [21]. A surfactant-free synthesis of gold nanostars using citrate-based seeds was reported by Yuan *et al* [26]. In that case, the AA has to be added quickly in the presence of silver ions. Under defined pH conditions the presence of Ag^+ ions is necessary for the formation of nanostars [26].

Recently, we have shown that flat gold nanotriangles are formed in a multivesicular Bis(2-ethylhexyl) sulfosuccinate sodium salt (AOT)/phospholipid-based template phase [27, 28]. The mechanism of the one-step formation process can be described by a diffusion-limited Ostwald ripening on the periphery of soft gold nanoparticle aggregates [29]. The resulting nanoplatelets, separated from spherical particles by a polyelectrolyte/micelle-based depletion flocculation [28], are long time stable with special optical and vibratory properties [30]. Ultrathin nanotriangles deposited in large scale close-packed monolayers on Si wafers can be successfully used as a substrate for monitoring photocatalytic reactions by SERS [31].

In the present work, we tried to synthesize gold nanoparticles in another type of vesicular template phase. It is already well known that mixtures of oppositely charged surfactants can form different types of organized systems, including vesicles [32]. For example, AOT builds spontaneously unilamellar vesicles with the cationic surfactant benzyl-n-hexadecyldimethylammoniumchloride, which are of special relevance in the areas of pharmacology, cosmetics, and foods [33, 34]. CTAB can form vesicles with sodium dodecylsulfate (SDS) and AOT, too [35, 36], but to the best of our knowledge this kind of vesicle has not yet been used as a template phase for making gold nanoparticles. CTAB is well-known as a shape-directing agent for the seed-mediated synthesis of gold nanorods showing a high reproducibility [25, 37, 38]. By forming a bilayer, CTAB interacts with the gold nanoparticle surface as well as Au ions in the solution [39]. Thereby, the CTAB counterion bromide plays a key role in the formation of Au nanorods through adsorption onto the side facets of the seeds. Additionally, the long tail of the surfactant facilitates the anisotropic growth [40]. A further advantage is that a CTAB bilayer prevents aggregation, leading to more stabilized particles [41].

Surprisingly, our first experiments have shown that AOT/CTAB-based vesicles, in the absence of additional components, can reduce a gold chloride solution in contrast to the surfactant components alone. This is another example showing that mixtures of oppositely charged surfactants may have synergistic benefits in their properties and applications [42]. However, the nanoparticle formation process is terminated at very small particle dimensions on the gold cluster level. Therefore, we started to use the gold clusters as a new type of seed for the formation of anisotropic gold nanoparticles by adding a mild reducing agent, i.e., AA. By varying the reaction temperature or adding silver ions, spiked gold nanostars with a flower-like inner structure and special optical properties can be synthesized.

2. Experimental details

2.1. Materials and methods

Tetrachloroauric(III)acid ($HAuCl_4 \cdot 3H_2O$), AOT and natrium borohydride ($NaBH_4$) were purchased from Sigma-Aldrich. CTAB was obtained from Fluka and AA from Roth. In all experiments, Milli-Q Reference A+ water was used.

UV–vis absorption experiments were performed with a Shimadzu UV–2600 spectrophotometer. Light microscopic images were captured and analyzed by the Leica DMLB microscope. Transmission electron microscope (TEM) micrographs were obtained by using a JEM-1011 (JEOL) TEM at an acceleration voltage of 80 kV as well as a JEM-2200 FS (JEOL) at 200 kV for high resolution (HRTEM). Scanning electron microscopic (SEM) investigations were performed with a S-4800 from Hitachi. Dynamic light scattering (DLS) and zeta potential measurements were made with a Malvern Nano Zetasizer 3600. A confocal Raman microscope (alpha 300, WITec, Ulm, Germany) was used to record Raman spectra of the samples. The microscope was equipped with an excitation laser at a wavelength of 785 nm and the laser beam was focused through a 100× microscope objective. The spectra were recorded with a thermoelectrically cooled charge-coupled device detector (DU401A-BV, Andor, UK) placed behind the spectrometer (UHTS 300; WITec, Ulm, Germany) with a spectral resolution of 3 cm^{-1}. The Raman band of a silicon wafer at 520 cm^{-1} was used to calibrate the spectrometer.

2.2. Vesicle formation and nanoparticle formation

A 0.16 M aqueous AOT solution and a 0.1 or 0.01 M CTAB solution were mixed together to obtain an AOT/CTAB vesicle solution. The turbid dispersion was agitated by using an ultrasound finger. The resulting vesicular dispersion (template phase) was characterized by light microscopy and DLS.

The vesicular template phase was mixed with a 2 mM gold chloride ($HAuCl_4$) precursor solution at a mixing ratio of 1:3. The obtained aqueous 'seed' solution was characterized by UV–vis spectroscopy and TEM microscopy.

Reducing components, i.e., citric acid, $NaBH_4$ or AA were added to the 'seed' solution by varying the temperature, the rate of adding the reducing agent and the molar ratio of the components. The resulting colored gold dispersions were characterized by UV–vis spectroscopy and TEM microscopy.

2.3. SERS substrates

For the layer formation of gold nanoflowers, a droplet of the dispersion was set on the Si substrate. By adding an ethanol-toluene mixture in a ratio of 5:1 to the droplet, the particles build a shimmering film on the interface, which remains as a layer after solvent evaporation. The silicon wafer fabricated with gold nanoflower film was immersed in a 1 mM aqueous

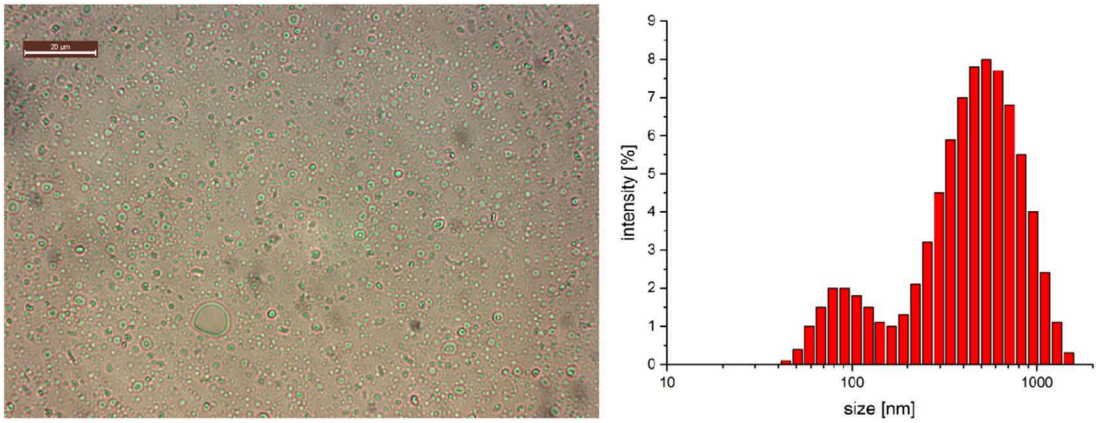

Figure 1. Light microscopic image of the vesicular template phase and the corresponding dynamic light scattering (DLS) plot.

solution of Rhodamine R6G for 6 h. The SERS substrates were washed with water several times to remove the unattached molecules and dried before being measured.

3. Results and discussion

By mixing adequate amounts of the 0.1 M CTAB solution with the 0.16 M AOT solution, the vesicle phase is formed after sonification. The resulting light microscopic image (figure 1) show well-distributed vesicles in a size range between 100 nm and 5 μm. The giant vesicles (GVs) in the μm range are surrounded by a shell, similar to the SDS/CTAB-based catanionic vesicles obtained by Tah *et al* [35]. DLS measurements reveal a bimodal size distribution on the nanometer scale, with a small vesicle (SV) fraction at about 85 nm and a second larger vesicle (LV) fraction at about 500 nm.

By adding a 2 mM $HAuCl_4$ solution (gold precursor solution) to the vesicle phase at volume rates of 3:1 and heating the mixtures for 45 min to 45 °C, a color change to yellow/orange can be observed. The UV–vis spectra show an UV absorption maximum at 380 nm and a shoulder between 450 and 500 nm (figure 2). Recently, we have shown by HRTEM and asymmetric flow field flow fractionation (AFFFF) that gold clusters of diameter $\leqslant$ 2 nm show an absorption maximum at 360 nm [43]. Thus, it can be assumed that very small gold clusters are formed.

The corresponding TEM micrograph of the SV fraction is shown in figure 3(A). By zooming into such a vesicle, individual gold nanoparticles in the size range between 2 nm and 5 nm can be detected at higher magnification (figure 3(B)). The gold cluster, well embedded into the vesicular template phase, with particle diameter $\leqslant$ 2 nm, corresponds to the UV–vis absorption at 380 nm, and the individual and somewhat larger particles (around 5 nm in size) correspond to the UV–vis shoulder at 450–500 nm (compare with figure 2).

Astonishingly, our results show that the AOT/CTAB-based catanionic unilamellar vesicles reduce a gold precursor solution in the absence of any additional reducing component. It has to be mentioned that neither of the surfactant

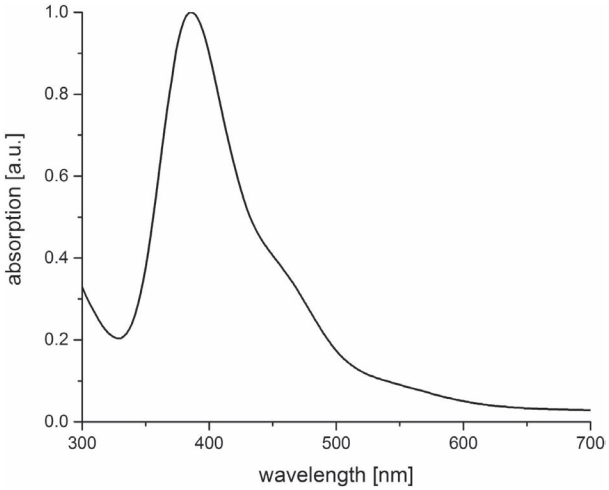

Figure 2. UV–vis spectra of the gold cluster 'seed' solution.

components, the CTAB solution or the AOT solution, can on its own reduce the gold chloride solution. Accordingly, electrostatic interactions between the functional head groups in the double layer are responsible for the reducing properties of the vesicular template phase. Due to the low reducing power accompanied by the template effect of the vesicles, the growth of gold crystals is already terminated at the cluster level. This interesting feature of the catanionic vesicles opens a door to the use of these gold clusters as 'seeds' for the seed-mediated synthesis of anisotropic gold nanoparticles.

Taking into account that there is still an excess of non-reduced Au^{3+} ions, we added three different reducing agents to our gold clusters embedded in the vesicular template phase, i.e., sodium borohydride, sodium citrate, and AA, respectively.

By using the strong reducing components $NaBH_4$ or sodium citrate, an optical color change to red and a spectroscopic shift of the cluster peak from 380 nm to 550 nm can be observed. Through the stepwise addition of a 0.1 M sodium borohydride solution to the seed solution, a stepwise degradation of the absorption cluster peak at 350 nm and a

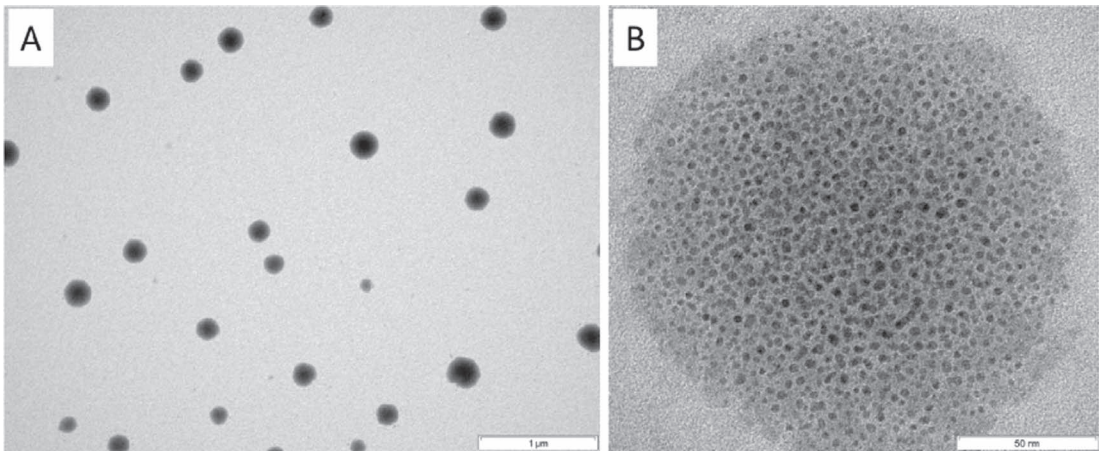

Figure 3. TEM micrographs of small vesicles after adding the gold precursor solution and heating the system to 45 °C for 45 min at lower (A) and higher (B) magnifications.

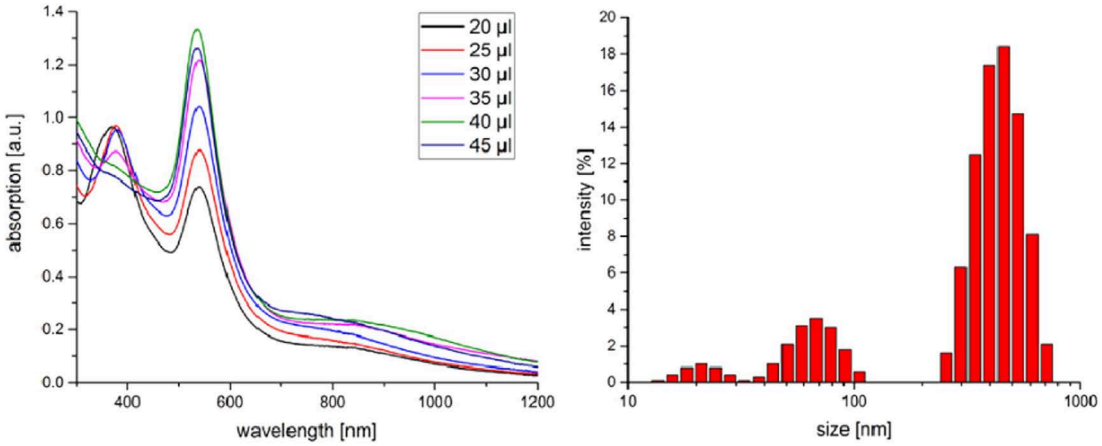

Figure 4. UV–vis spectra and DLS plot of the 'seed' solution after adding stepwise a 0.1 M ascorbic acid (AA) solution.

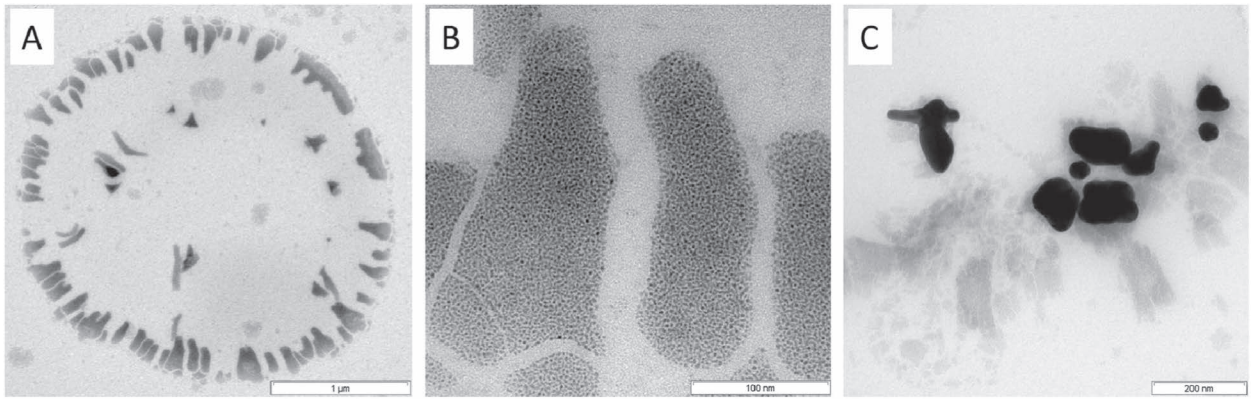

Figure 5. TEM micrograph of fragments of super large vesicles after adding stepwise a 0.1 M AA solution at room temperature (A); a magnified micrograph of the fragments with well-embedded small gold nanoparticles (B); and crystallized larger anisotropic gold nanoparticles (C).

corresponding increase of the surface plasmon resonance peak at 550 nm was noticed (figure S1 is available online at stacks.iop.org/NANO/29/185603/mmedia), which indicate the growth of gold clusters up to particle diameters $\geqslant$ 5 nm [44]. When the same experiments were performed with AA, similar results were observed, but in addition to the peak at 550 nm a further broad peak between 800 and 1000 nm was detected (figure 4). After a dosage of 40 μl the cluster peak

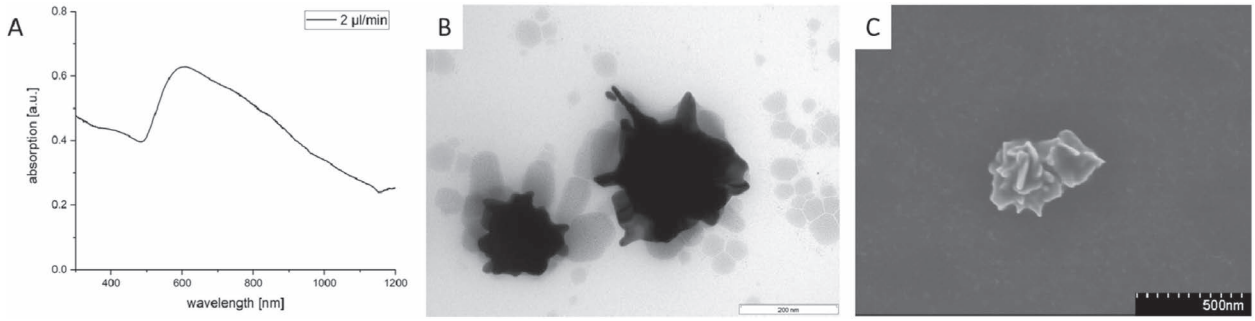

Figure 6. UV–vis spectra of the 'seed' solution after cooling in the ice bath and adding stepwise a 0.1 M AA solution with corresponding TEM and SEM micrographs of round-edged nanoflowers.

disappears and the UV maximum at 550 and 850 nm reaches a maximum. DLS experiments reveal a shift of the SV and LV peaks to smaller dimensions and the appearance of a new peak at about 20 nm. The peak shifts may be related to the decomposition of larger vesicles into fragments, and the new peak at about 20 nm to the formation of gold nanoparticles.

A corresponding TEM micrograph of the resulting system shows fragments of the GV template phase (figure 5(A)). A magnified picture of the irregular fragments (figure 5(B)) reveals well-embedded 5 nm sized gold nanoparticles, which are responsible for the UV absorption at 550 nm. Furthermore, anisotropic larger gold nanoparticles crystallize in the fragments (example shown in figure 5(C)), which seem to be responsible for the broad UV absorption in the near-infrared (NIR) range.

For a more controlled synthesis of such anisotropic gold nanoparticles, we varied the reaction conditions, i.e., the CTAB concentration was reduced to 0.01 M, the template was cooled in an ice bath, and the rate of silver nitrate addition was modified.

After cooling the 'seed' solution in an ice bath and adding the AA very slowly (2 μl/min), an UV absorption maximum between 580 and 620 nm (figure 6(A)) was observed. The corresponding TEM micrograph (figure 6(B)) shows spiked individual nanoparticles, which tend to aggregate at low temperatures (at 0 °C) and disaggregate at room temperature. In this case, a color change from blue to dark red can be observed. SEM micrographs show that round-edged nanoflowers or so-called nanostars are formed. It is noteworthy that the already well-established synthesis of spiked nanostars is performed at room temperature by the rapid addition of PVP-coated Au seeds to the gold chloride solution [21], or by the quick addition of a silver nitrate/AA solution to a citrate-stabilized seed solution [26]. In both cases, a fast addition at room temperature is realized, which is in contrast to our reaction conditions at low temperatures (0 °C) and slow addition rates.

It is already well known that Ag^+ ions are of special relevance by forming anisotropic gold nanoparticles in the second step of the seed-mediated synthesis, experimentally shown by the Liz-Marzan group [9, 20, 24]. Yuan *et al* have demonstrated that for the surfactant-free synthesis of nanostars, a fast addition of AA in the presence of Ag^+ ions is required [26]. Nevertheless, the role of Ag^+ ions in shape-controlled synthesis is not entirely understood. Inspired by these results, further experiments focused on the role of Ag^+ ions in the crystallization process. Gold nanostars can be described as having a branched structure with a metal core and protruding sharp spikes [45, 46]. Therefore, we propose that the Ag^+ ions could specifically block the growth on the long sides, as observed for the nanorod growth in [38]. The formation of the spikes can thus be roughly compared to the growth of nanorods. In previous investigation related to CTAB-protected gold nanorods synthesis, the presence of Ag^+ ions generated a high yield of rod-shaped nanostructures with Au{110} faces on the side of the rods and {100} on the top of the rods. This can be explained by a selective silver adsorption to {110} Au facets inhibiting Au deposition on those surfaces, but allowing Au deposition on {100} surfaces [47].

By adding AA at the same rate in the presence of Ag^+ ions to the 'seed' solution, spiked nanoparticles are already formed at room temperature. The UV absorption curve becomes more distinct, with a maximum at 680 nm (figure 7(A)). SEM micrographs at a tilting angle of 45° offer a possibility to investigate the inner structure of the nanoparticles. Figure 7(B) shows that the spiked nanoparticles are supramolecular structured platelet aggregates with a flower-like inner structure; this means that sharp-edged nanoflowers are formed. Additional HRTEM measurement of a gold nanoflower tip shows a single crystallinity with ⟨101⟩ zone axis (figure 7(C)), quite similar to the tips of gold nanostars shown by Kumar *et al* [21].

Up to now, only a limited number of papers have reported the formation of gold nanoflowers (NFs) [48–54]. Rod-like gold nanoparticles [49–51] and sheet-like gold nanoparticles [52–54] can assemble into nanoflower superstructures. Winkler *et al* [54] discussed a time-dependent two-step model of autocatalytic growth, from sharp-edged to round-edged large micro-flowers, by using hydroxylamine as the reducing agent in a one-step procedure. Wang *et al* [52] discussed self-assembly of gold sheet structures due to Van der Waals and anisotropic hydrophobic attraction forces of sheet-like gold nanoparticles in the presence of PVP and Ag^+ ions.

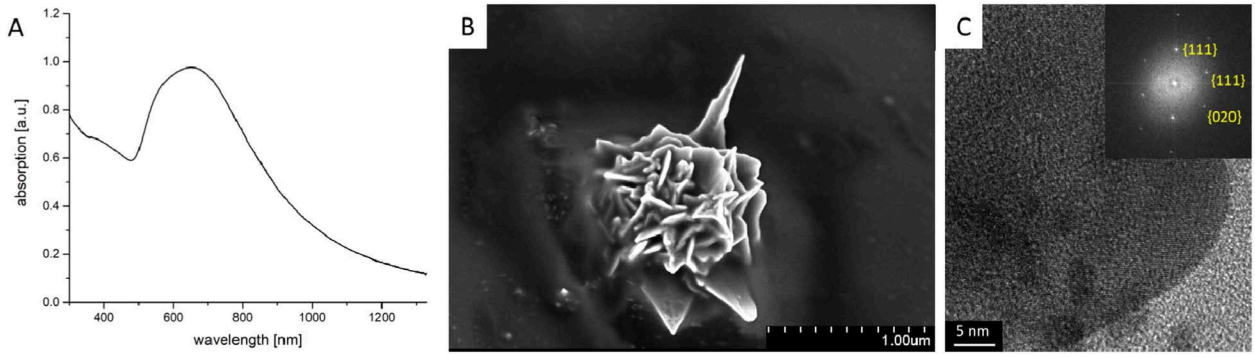

Figure 7. UV–vis spectra of the gold nanoflower dispersion with corresponding SEM micrograph and HRTEM micrograph (inset: fast Fourier transformation) of a spike of the sharp-edged nanoflowers formed at room temperature by slow addition of AA in the presence of Ag^{+} ions.

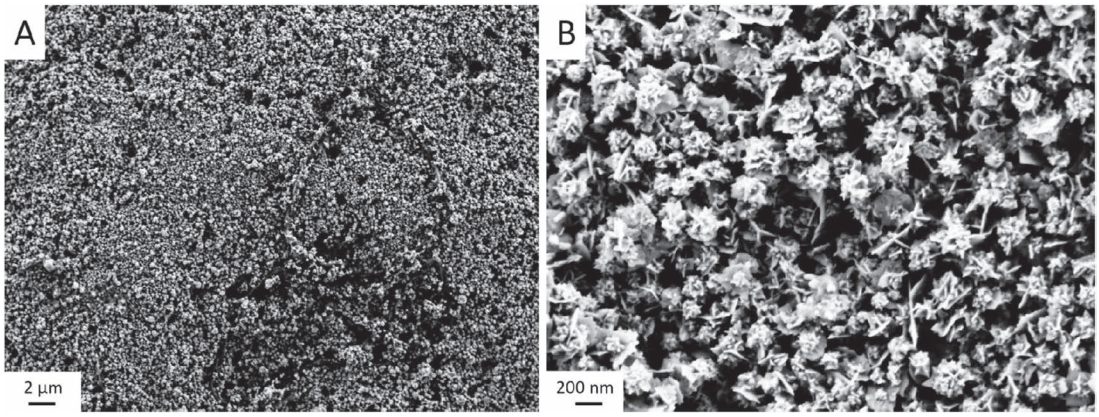

Figure 8. SEM micrograph of the gold nanoflower layer on Si substrate.

Symmetry-breaking properties of the Ag^{+} ions attached to the gold nanoparticles embedded in the fragments seem to be responsible for the non-regular crystallization process in different directions to form curved nanoplatelets, which self-assemble to supramolecular flower-like nanoparticles. SERS experiments were performed to check the catalytic properties of these supramolecular formed NFs.

To investigate the performance in SERS, a droplet of the gold NF dispersion was set on a Si substrate. To avoid the coffee-ring effect and to obtain a close-packed layer of the nanoparticles, an ethanol–toluene mixture in a ratio of 5:1 was added to the droplet, as already detailed described in [31]. Thus, the nanoparticles were transported to the interface and remain as a closely-packed layer after solvent evaporation (figure 8).

SERS has been used to provide 'fingerprint' information of the probed analyte, with higher sensitivity compared to conventional Raman scattering. Anisotropic nanoparticles such as gold nanotriangles and gold nanostars have been reported to show extraordinary SERS enhancement owing to their tips. These tips act as nanoantennas, at which the electromagnetic field and therefore Raman scattering is enhanced [55]. Herein, Rhodamine R6G was used to testify the SERS performance of the gold NFs. The gold NFs were deposited on silicon wafer and an uniform film was formed. Figure 9 shows the obtained SERS spectrum of R6G when

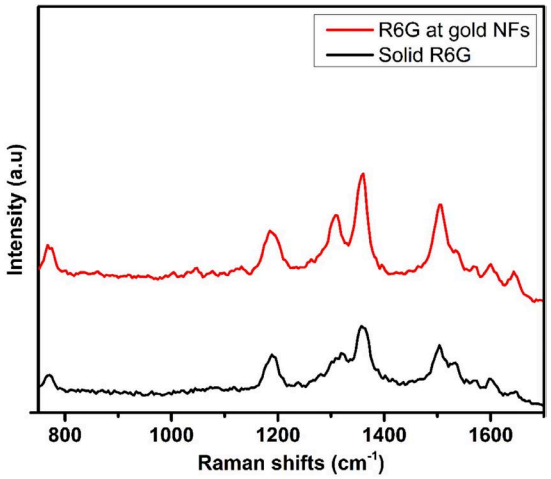

Figure 9. Surface-enhanced Raman scattering performance of the self-assembled gold nanoflowers and the bulk R6G molecules and the self-assembled gold nanoflowers.

the sample was immersed in a 1 mM aqueous solution of R6G. The SERS spectrum reproduced the characteristic Raman bands of the bulk R6G, where peaks at 1184 and 1307 cm^{-1} were assigned to the C-C and C-O-C stretching modes, respectively. The peaks at 1356 and 1504 cm^{-1} were

assigned to the aromatic ring C-C stretching modes of the R6G molecules [56].

The SERS enhancement factor (EF) of the NF film was estimated using the following equation:

$$EF = \frac{I_{SERS}}{I_{Raman}} \cdot \frac{N_{Raman}}{N_{SERS}}$$

where I_{SERS} and I_{Raman} are the intensities of a selected vibrational mode (vibrational mode at 1504 cm^{-1}) in the SERS and normal Raman spectra, respectively. N_{SERS} is the number of R6G adsorbed on the SERS substrate, while N_{Raman} is the number of the probed bulk R6G molecules. In this experiment, N_{SERS} and N_{Raman} were calculated to be $3.5 \cdot 10^5$ and $3 \cdot 10^{10}$, respectively. The SERS EF was estimated to be $1.7 \cdot 10^5$. Throughout the calculations, R6G molecules were assumed to form a monolayer on the gold NF substrate and each molecule was assumed to occupy 2.22 nm^2 of the illuminated area [57]. We attribute such high enhancement to the structure of the NFs, with many tips on their surfaces known as SERS hot spots, and to the nanogaps formed between these tips and their neighbors.

4. Conclusions

Catanionic vesicles are a new type of reducing agent for making gold clusters. The reduction process is terminated at the cluster level due to the templating effect of the catanionic vesicles. These gold clusters, with diameter $\leqslant$ 2 nm and well embedded into catanionic vesicles, can be used as a 'seed' solution to form anisotropic gold nanoparticles. By adding AA as a mild reducing agent, the clusters grow to colloidal dimensions of about 5 nm in size. This process is accompanied by a fragmentation of the initially formed super large vesicles and the formation of larger anisotropic gold nanoparticles. The growth mechanism of the anisotropic gold nanoparticles in the catanionic vesicle fragments at low temperatures can be described by a non-diffusion-limited Ostwald ripening process, in contrast to the diffusion-limited Ostwald ripening process in solution, recently shown by our small angle x-ray scattering experiments [21]. At low temperatures (0 °C) and with a slow addition rate of AA, round-edged nanoflowers can be formed. In the presence of Ag^+ ions the crystallization process in the fragments can be further influenced, and flat nanoplatelets are formed, which self-assemble to sharp-edged nanoflowers at room temperature. The sharp-edged nanoflower superstructures deposited on a Si wafer show an excellent enhancement factor in SERS experiments, one order of magnitude higher than individual gold nanotriangles well ordered in a large scale close-packed monolayer, as shown by us earlier [23].

Acknowledgments

The financial support from the German Research Foundation (KO 1387/14-1; INST 336/64-1) is gratefully acknowledged.

ORCID iDs

Joachim Koetz https://orcid.org/0000-0001-9113-1337

References

[1] Daniel M C and Astruc D 2004 *Chem. Rev.* **104** 293–346
[2] Millstone J E, Park S, Shuford K L, Qin L, Schatz G C and Mirkin C A 2005 *J. Am. Chem. Soc.* **127** 5312–3
[3] Frasca S, Rojas O, Salewski J, Neumann B, Stiba K, Weidinger I M, Tiersch B, Leimkühler S, Koetz J and Wollenberger U 2012 *Bioelectrochemistry* **87** 33–41
[4] Perrault S D, Walkey C, Jennings T, Fischer H C and Chan W C W 2009 *Nano Lett.* **9** 1909–15
[5] Duncan B, Kim C and Rotello V M 2010 *J. Control. Release* **148** 122–7
[6] Sau T K and Murphy C J 2004 *Langmuir* **20** 6414–20
[7] Skrabalak S E, Chen J, Sun Y, Lu X, Au L, Cobley C M and Xia Y 2008 *Acc. Chem. Res.* **41** 1587–95
[8] Lee J, Hasan W, Stender C L and Odom T W 2008 *Acc. Chem. Res.* **41** 1762–71
[9] Scarabelli L, Coronado-Puchau M, Giner-Casares J J, Langer J and Liz-Marzan L M 2014 *ACS Nano* **6** 5833–42
[10] Sun M, Ran G, Fu Q and Xu W 2015 *J. Exp. Nanosci.* **10** 1309–18
[11] Hirsch L R, Stafford R J, Bankson J A, Sershen S R, Rivera B, Price R E, Hazle J D, Halas N J and West J L 2003 *PNAS* **100** 13549–54
[12] Loo C, Lin A, Hirsch L R, Lee M H, Barton J, Halas N, West J and Drezek R 2004 *Technol. Cancer Res. Treat.* **3** 33–40
[13] Smith A M, Mancini M C and Nie S 2009 *Nat. Nanotechnol.* **4** 710–1
[14] Murphy C J and Jana N R 2002 *Adv. Mater.* **14** 80–2
[15] Jiang L, Tang Y, Liow C, Wu J, Sun Y, Jiang Y, Dong Z, Li S, Dravid V P and Chen X 2013 *Small* **9** 705–10
[16] Aldeanueva-Potel P, Carbo-Argibay E, Pazos-Perez N, Barbosa S, Pastoriza-Santos I, Alvarez-Puebla R A and Liz-Marzan L M 2012 *ChemPhysChem* **13** 2561–5
[17] Schlücker S 2014 *Angew. Chem., Int. Ed. Engl.* **53** 4756–95
[18] Zhang Q and Wang H 2014 *ACS Catal.* **4** 4027–33
[19] Burrows N D, Vartanian A M, Abadeer N S, Grzincic E M, Jacob L M, Lin W, Li J, Dennison J M, Hinman J G and Murphy C J 2016 *J. Phys. Chem. Lett.* **7** 632–41
[20] Barbosa S, Agrawal A, Rodriguez-Lorenzo L, Pastoriza-Santos I, Alvarez-Puebla R A, Kornowski A, Weller H and Liz-Marzan L M 2010 *Langmuir* **26** 14943–50
[21] Kumar P S, Pastoriza-Santos I, Rodriguez-Gonzales B, Javier Garcia de Abajo F and Liz-Marzan L M 2008 *Nanotechnology* **19** 015606
[22] Scott R W, Wilson O M and Crooks R M 2005 *J. Phys. Chem.* B **109** 692–704
[23] Ding W, Lin J, Yao K, Mays J M, Ramanathan M and Hong K 2013 *J. Mater. Chem.* B **1** 4212–6
[24] Lohse S E, Burrows N D, Scarabelli L, Liz-Marzán L M and Murphy C J 2014 *Chem. Mater.* **26** 34–43
[25] Smith D K and Korgel B A 2008 *Langmuir* **24** 644–9
[26] Yuan H, Khoury C G, Hwang H, Wilson C M, Grant G A and Vo-Dinh T 2012 *Nanotechnology* **23** 075102
[27] Schulze N, Prietzel and Koetz J 2016 *Colloid Polym. Sci.* **294** 1297–304
[28] Liebig F, Sarhan R M, Prietzel C, Reinecke A and Koetz J 2016 *RSC Adv.* **6** 33561–8
[29] Liebig F, Thünemann A F and Koetz J 2016 *Langmuir* **32** 10928–35

[30] von Reppert A, Sarhan R M, Stete F, Pudell J, Del Fatti N, Crut A, Koetz J, Liebig F, Prietzel C and Bargheer M 2016 *J. Phys. Chem.* C **120** 28894–9
[31] Liebig F, Sarhan R M, Sander M, Koopman W, Schuetz R, Bargheer M and Koetz J 2017 *ACS Appl. Mater. Interfaces* **9** 20247–53
[32] Jönsson B, Jokela P, Khan A, Lindman B and Sadaghiani A 1991 *Langmuir* **7** 889–95
[33] Villa C C, Mayano F, Ceolin M, Silber J J, Falcone R D and Correa N M 2012 *Chem. Eur. J.* **18** 15598–601
[34] Villa C C, Correa N M, Silber J J, Mayano F and Falcone R D 2015 *Phys. Chem. Chem. Phys.* **17** 17112–21
[35] Tah B, Pal P, Mahato M and Talapatra G B 2011 *J. Phys. Chem.* B **115** 8493–9
[36] Tan C Y, Khoo K S, Radiman S, Rahman I A and Amari N F 2014 *Sains Malaysiana* **43** 623–8
[37] Alkilany A M, Nagaria P K, Hexel C R, Shaw T J, Murphy C J and Wyatt M D 2009 *Small* **5** 701–8
[38] Orendorff C J and Murphy C J 2006 *J. Phys. Chem.* B **110** 3990–4
[39] Bullen C, Zijlstra P, Bakker E, Gu M and Raston C 2011 *Cryst. Growth Des.* **11** 3375–80
[40] Xiong Y, Cai H, Wiley B J, Wang J, Kim M J and Xia Y 2007 *J. Am. Chem. Soc.* **129** 3665–75
[41] Nikoobakht B and El-Sayed M A 2001 *Langmuir* **17** 6368–74
[42] Dar A A, Rather G M, Ghosh S and Das A R 2008 *J. Colloid Interface Sci.* **322** 572–81
[43] Lemke K, Prietzel C and Koetz J 2013 *J. Colloid Interface Sci.* **394** 141–6
[44] Jana N R, Gearhart L and Murphy C J 2001 *Langmuir* **17** 6782–6
[45] Burt J L, Elechiguerra J L, Reyes-Gasga J, Montejano-Carrizales J M and Jose-Yacaman M 2005 *J. Cryst. Growth* **285** 681–91
[46] Cabrera-Trujillo J, Montejano-Carrizales J, Rodriguez-Lopez J, Zhang W, Velazquez-Salazar J and Jose-Yacaman M 2010 *J. Phys. Chem.* C **114** 21051–60
[47] Liu M and Guyot-Sionnest P 2005 *J. Phys. Chem.* B **109** 22192–200
[48] Kharisov B I 2008 *Recent Patents on Nanotechnology* **2** 190–200
[49] Jena B K and Raj C R 2007 *Langmuir* **23** 4064–70
[50] Jena B K and Raj C R 2008 *Chem. Mater.* **20** 3546–8
[51] Yang D-P, Liu X, Teng C P, Owh C, Win K Y, Lin M, Loh X J, Wu Y-L, Li Z and Ye E 2017 *Nanoscale* **9** 15753–9
[52] Wang L, Wei G, Guo C, Sun L, Sun Y, Song Y, Yang T and Li Z 2008 *Colloids Surf.* A **312** 148–53
[53] Wang T, Hu X and Dong S 2006 *J. Chem.* B **110** 16930–6
[54] Winkler K, Kaminska A, Wojciechowski T, Holyst R and Fialkowski M 2011 *Plasmonics* **6** 697–704
[55] De Aberasturi D J, Serrano-Montes A B, Langer J, Henriksen-Lacey M, Parak W J and Liz-Marzán L M 2016 *Chem. Mater.* **28** 6779–90
[56] Zhai W-L, Li D-W, Qu L-L, Fossey J S and Long Y-T 2012 *Nanoscale* **4** 137–42
[57] Liu J, Yang T, Li C, Dai J and Han Y 2015 *Sci. Rep.* **5** 14942

ACS APPLIED MATERIALS & INTERFACES

Research Article

www.acsami.org

Deposition of Gold Nanotriangles in Large Scale Close-Packed Monolayers for X-ray-Based Temperature Calibration and SERS Monitoring of Plasmon-Driven Catalytic Reactions

Ferenc Liebig,[†] Radwan M. Sarhan,[‡,§,∥] Mathias Sander,[‡] Wouter Koopman,[‡] Roman Schuetz,[⊥] Matias Bargheer,[‡] and Joachim Koetz*[,†]

[†]Institute for Chemistry and [‡]Institute for Physics, University of Potsdam, 14476 Potsdam, Germany

[§]Chemistry Department, Faculty of Science, Cairo University, Cairo 12613, Egypt

[∥]School of Analytical Sciences Adlershof (SALSA), Humboldt-Universität zu Berlin, Albert-Einstein-Str. 5-9, 10099 Berlin, Germany

[⊥]Department of Biomaterials, Max Planck Institute of Colloids and Interfaces, Am Mühlenberg 1, 14476 Potsdam, Germany

Supporting Information

ABSTRACT: Anisotropic plasmonic particles such as gold nanotriangles have extraordinary structural, optical, and physicochemical properties. For many applications in different fields, it is essential to prepare them in a chemically and physically stable, structurally well-defined manner, e.g., as large and uniform coverage on a substrate. We present a direct method for the large scale close-packed monolayer formation of edge-to-edge ordered, ultrathin crystalline gold nanotriangles on Si wafers or quartz glass via the transfer of these asymmetric particles to the air−liquid interface after adding ethanol−toluene mixtures without any subsequent surface functionalization. X-ray diffraction monitoring of the close-packed, large area monolayer with a mosaicity of less than 0.1° allows for calibrating the temperature of the particles during continuous laser heating. This is important for characterizing the microscopic temperature of the metal particles in the plasmon-driven dimerization process of 4-nitrothiophenol (4-NTP) into 4,4′-dimercaptoazobenzene (DMAB), monitored in real time by surface-enhanced Raman scattering (SERS). The gold nanotriangles can act as a source of hot electrons and initiate the dimerization process.

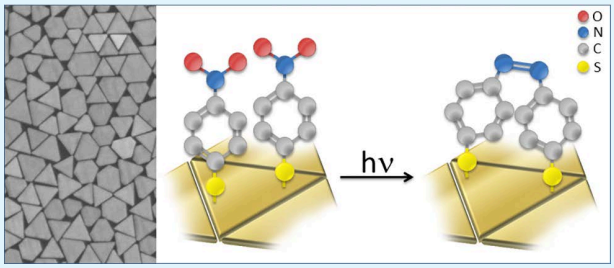

KEYWORDS: *gold nanotriangles, monolayer formation, SERS, dimerization, heat measurement*

1. INTRODUCTION

The unique size- and shape-dependent chemical and physical properties of anisotropic nanoparticles and their various applications lead to an increased interest in new strategies to create nanoparticles with well-defined topologies.[1−4]

In order to make them accessible in broader and more complex contexts in nanotechnology, we are challenged by the controlled self-assembly of robust and well-defined structures with tunable functionalities under specific conditions. The colloidal assembly of two-dimensional monolayers plays an important role as templates for colloid lithography[5] and is used for surface-enhanced Raman scattering (SERS),[6] plasmon enhanced fluorescence, biosensing, or photocatalysis.[7−10]

Recently, we described the growth mechanism of negatively charged gold nanotriangles with an edge length of about 175 nm and a thickness of 7.5 nm according to an Ostwald ripening process in vesicular template phases.[11] However, by varying the reaction conditions, it is not possible to synthesize monodisperse nanotriangles. Therefore, a separation of the triangle fraction from spherical nanoparticles is still required. The best way to do that is the so-called depletion flocculation in the presence of AOT-micelles and polyelectrolytes, recently shown by us.[12] However, the resulting negatively charged AOT-stabilized nanotriangles are stable up to a laser fluence of 2.9 mJ/cm^2 and offer special features in vibration and cooling behavior by ultrafast X-ray diffraction.[13] The adjustable UV−vis absorption in the near-infrared region by controlling size and thickness of anisotropic flat nanotriangles is of biological importance and enables tissue imaging[14] or hyperthermia of cancer cells.[15]

To unfold their full potential as SERS substrates, a close-packed gold nanotriangle monolayer is needed. At the junction between the sharp edges of the nanotriangles, the local electromagnetic field is strongly enhanced. The Raman signal enhancement used in SERS results mainly from these local electromagnetic "hot spots".[16,17] SERS has been shown to be sensitive to single molecules[18,19] and can thus be used for the detection of trace amounts[20] and for the real-time determi-

Received: May 22, 2017
Accepted: May 23, 2017
Published: May 23, 2017

DOI: 10.1021/acsami.7b07231
ACS Appl. Mater. Interfaces 2017, 9, 20247−20253

nation of catalytic reactions.[21] Close-packed gold nanotriangle monolayers offer a large amount of hot spots increasing the probability to observe the desired analyte or reaction. Moreover, flat monolayers of crystalline nanoparticles allow the use of X-ray diffraction as a probe to determine the nanoparticle temperature. Recent experiments have shown that temperature and laser intensity are important parameters in laser-assisted plasmon-driven reactions. However, there has been no reliable measurement of the nanoparticle temperature under the condition of intense laser irradiation.[22]

Colloidal self-assembly was studied in recent years to get highly ordered monolayers over a large area. Thereby the research is focused on simple and reproducible techniques.[23] On the one hand, drop-casting is the easiest way to produce monolayers, but with limitations in size[24] and the accumulation of particles at the drop's outer edge, a phenomenon called the "coffee ring" effect, which allows only a local order.[25] On the other hand, air−liquid interface self-assembly methods provide large monolayers with a high degree of order and can be transferred onto substrates.[26,27] However, such a procedure requires surface functionalization[28] or ligand exchange.[29] Lee et al. used the Langmuir−Schaefer technique to fabricate large-area (≈1 cm^2) dense monolayer films of CTAB-coated gold nanoprisms after PVP functionalization.[30] Without functionalization CTAB-capped gold nanotriangles form only self-assembled "suprastructures" within an area of hundreds of square micrometers under well-defined experimental conditions. Now, we present a facile method to produce self-assembled monolayers (up to 1.5 cm^2) directly on different substrates, e.g., silicon wafer or quartz glass, without a functionalization of the negatively charged AOT-stabilized gold nanotriangles, synthesized in a one-step preparation process (without a transfer step) in the presence of AOT/phospholipid multivesicular vesicles.[12]

In this work, we present a facile method to produce self-assembled monolayers directly on substrates without processing the gold nanotriangle dispersion, containing highly purified gold nanoplatelets (yield of nanoplatelets >99.7% with a polydispersity of 10%) after several purification steps by shape-controlled depletion flocculation in the presence of AOT micelles and polyelectrolytes.[12] In contrast to the drop-casting method, the nanoparticles were initially transferred to the air−liquid interface by the addition of an ethanol−toluene mixture. After solvent evaporation, a thin closely packed gold nanotriangle monolayer was formed, as evidenced by TEM and SEM. X-ray diffraction experiments confirm the flat structural ordering of the monolayer. The symmetric (111) Bragg peak of the gold nanotriangles is subsequently used to determine the laser-induced temperature increase in the particles for continuous irradiation of the Au/Si sample with moderate laser intensities up to 3.5 W/cm^2. To demonstrate the potential of this template for SERS spectroscopy and for the analysis of plasmon-driven chemistry, we added a monolayer of 4-nitrothiophenol (4-NTP). For an appropriate laser fluence, we simultaneously observed the production of 4,4′-dimercaptoazobenzene (DMAB) and the consumption of 4-NTP; i.e., we monitored the dimerization reaction by SERS.

2. EXPERIMENTAL SECTION

2.1. Chemicals. Ethanol (≥99.8%, p.a.) was purchased from Roth and toluene from VWR. 4-Nitrothiophenol was obtained from Sigma-Aldrich. All chemicals were used as received. Milli-Q Reference A+ water was used in all experiments.

2.2. Preparation of Gold Nanotriangles and Monolayer Formation. The gold nanotriangles were synthesized in a one-step process in a mixed AOT/phospholipon vesicle phase in the presence of a strongly alternating polyampholyte, i.e., poly(*N*,*N*′-diallyl-*N*,*N*′-dimethylammonium-*alt*-3,5-bis-carboxyphenylmaleamic carboxylate (PalPhBisCarb), working as a reducing and shape controlling component.[31]

0.5 wt % phospholipid (PL90G; purity >97%) and 0.5 wt % dioctyl sodium sulfosuccinate (AOT) were dispersed in water together with 0.01 wt % PalPhBisCarb and stirred for 24 h at room temperature. The resulting template vesicle phase was mixed with the 2 mM tetrachloroaurate precursor solution and heated up to 45 °C for 45 min. The resulting nanoplatelets were separated from spherical nanoparticles by a depletion flocculation after adding a 0.02 M AOT micelle solution. The nanotriangle fraction was washed and separated several times by centrifugation. The final yield of nanoplatelets was >99% with a polydispersity of 10%.

For the monolayer formation process a highly diluted aqueous gold nanotriangle solution (3.5×10^{-4} g/cm^3) was injected by ethanol−toluene (E−T) mixtures varying in the E−T ratio. Best results were observed with an E−T ratio of 5:1.

2.3. Methods. For investigations of monolayer structures in preliminary experiments, transmission electron microscopy (TEM) was used. The samples were taken out by gently touching the monolayer with a carbon-coated copper grid parallel to the air−liquid interface and dried rapidly by removing the excess liquid with filter paper. Subsequently, the samples were examined using the JEM-1011 (JEOL, Japan) at an acceleration voltage of 80 kV. The quality and size of the gold nanotriangle monolayers on Si-wafers and quartz glass were determined by using the scanning electron microscope (SEM) Supra 55PV (ZEISS, Germany) at an acceleration voltage of 6 kV. Raman spectra were recorded using a confocal Raman microscope alpha300 (WITec, Germany) equipped with laser excitation at wavelength of 785 nm. The laser beam was focused through a Nikon 10× microscope objective with a NA of 0.25. The spectra were acquired with a thermoelectrically cooled Andor CCD detector DU401A-BV placed behind the spectrometer UHTS 300 from WITec with a spectral resolution of 3 cm^{-1}. The Raman band of a silicon wafer at 520 cm^{-1} was used to calibrate the spectrometer. XRD experiments were performed with a focused X-ray beam emitted from a micro focus X-ray tube (IFG). The 8 keV Kα radiation from the copper anode is monochromatized by a single reflection of a HOPG (highly ordered pyrolytic graphite) crystal. The out-of-plane lattice constant of the gold nanotriangles is determined by Bragg diffraction from the (111) lattice planes of the gold particles. The output of an 800 nm CW laser diode is feed into a fiber and guided to the sample to heat the monolayer continuously with moderate laser intensities up to 3.5 W/cm^2 while the lattice constant is simultaneously measured.

2.4. Preparation of SERS Substrate. The silicon wafer was cleaned in a solution of 30 wt % H_2O_2 and 30 wt % H_2SO_4 for 1 h. It was rinsed in deionized water and treated by ultrasound in ethanol. For the immobilization of the triangles, the substrate was dried before being used. The gold nanotriangles assembled on the substrate were immersed in 5 mM ethanolic solution of 4-NTP for 6 h. The sample was washed with ethanol to remove the unattached molecules and dried.

3. RESULTS

3.1. Self-Assembled Monolayer Formation. In this part, we will discuss the self-assembled monolayer formation on silicon wafers and quartz glass, which is based on the particle transfer to the interface and the subsequent evaporation of dispersion medium.

The idea behind this approach is the strategy developed by Liu et al. for the transfer of spherical gold nanoparticles to the interface and their cold-welding, which joins Au nanoparticles together into two-dimensional continuous structures without local heating.[32] Therefore, injections of different ratios of

DOI: 10.1021/acsami.7b07231
ACS Appl. Mater. Interfaces 2017, 9, 20247−20253

ethanol−toluene mixtures from the bottom of the dispersion were used to bring gold nanoparticles to the air−liquid interface at a specific addition rate. Subsequently the layer can be transferred onto a TEM grid for a detailed analysis.

Scheme 1. Simplified Illustration of the Self-Assembly Process of Gold Nanotriangles at the Water−Toluene Interface after Adding the Ethanol−Toluene (E−T) Mixture

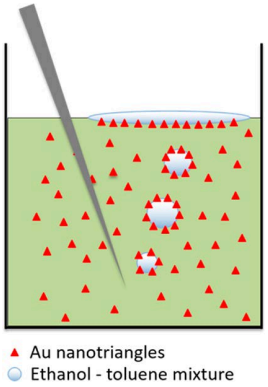

In our system, this method leads to a monolayer formation on the interface without cold-welding ambitions. The key parameter for the cold-welding of chemically produced nanoparticles is the removal of the capping molecules, i.e., in our system the negatively charged AOT surfactant molecules. That means in the absence of AOT molecules at the edges of the triangles an uncapped surface increases the nanotriangle surface energy and hence favors the NT coalescence. The cleaning of the surface is usually realized by heating or desorption of the capping molecules. This means the Au nanoplatelets in the monolayer are separated from each other without a particle−particle coalescence or fusion, when the edges of the NTs are still capped by AOT molecules. As recently described by Liu et al., the degree of welding depends on the size of spherical nanoparticles. For larger particles of 59 nm,[32] only a slightly fused network structure can be produced. Thus, it is not surprising that for the large triangles with an edge length of about 175 nm no welding takes place. Another reason for the disappearance of cold-welding effects is the strong Coulombic repulsion between AOT-capped gold NTs. The distance between the particles can be influenced by changing the volume ratio between ethanol and toluene. Ethanol reduces the surface charge of gold nanoparticles and changes the lateral capillary attraction between interfacial nanoparticles. If we increase the amount of toluene toward ethanol, a stacking of the particles can be found. In case of Figure 1, we used an ethanol−toluene volume ratio of 5:1. At the air−liquid interface a homogeneous monolayer film can be seen (Figure 1B). Figure 1A show this monolayer after the transfer onto a TEM grid. This transfer process destroys the close packing of the triangles at the surface of the solution, and a similar incomplete layer transfer is observed for Si wafers instead of a TEM grid (Figure S1, Supporting Information). In contrast, the successful deposition of the continuous layer at the liquid surface onto a Si substrate by solvent evaporation is shown in Figure 2.

Usually SERS experiments are conducted on Si substrates under a microscope. In the case of simple drop-casting, that means in the absence of the oil mixture, no monolayer formation occurs. After solvent evaporation of the aqueous dispersion without additives, the formation of islands was observed. The islands are caused by stacking of the anisotropic particles (Figure S2). Similar results were obtained by Fu et al.[33] With a complex experiment setup of a wide-mouth bottle containing water at the bottom, they influenced the evaporation rate by changing the temperature and the tilt angle of the silicon wafer and thus the quality of assembled gold nanotriangles formation. In our case, we remedy the problem by adding a mixture of ethanol and toluene to the droplet at room temperature (Scheme 2).

According to Scheme 2, a droplet of the dispersion was set on the substrate, and the ethanol−toluene mixture was added. Because of the change of the wetting properties, the droplet spread and wetted the substrate completely. Simultaneously, the formation of a shimmering layer on the film was observed.

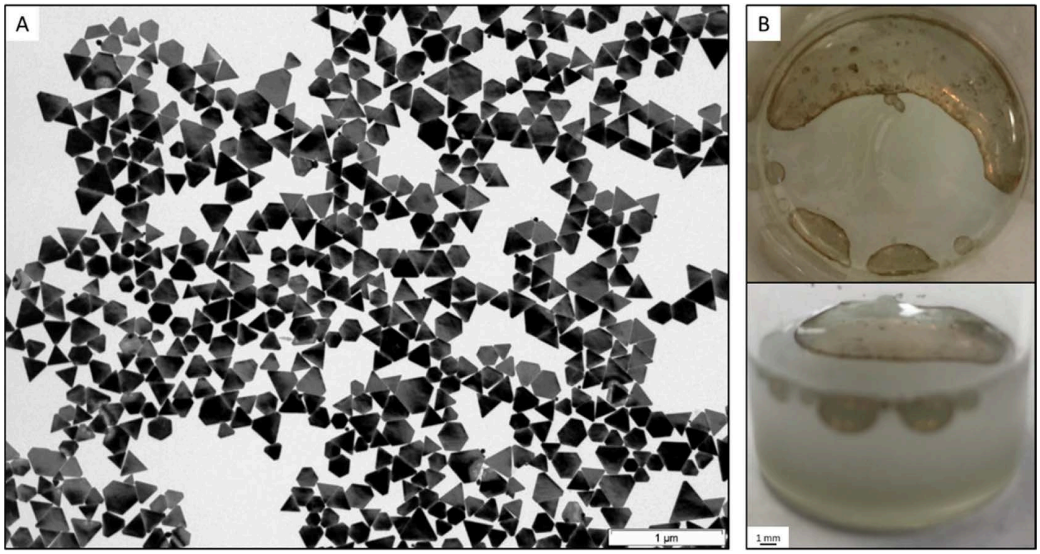

Figure 1. Self-assembled gold nanotriangles transferred onto a TEM grid (A); monolayer formation at the air−liquid interface in a glass vessel (B) after adding an ethanol−toluene (5:1) mixture.

DOI: 10.1021/acsami.7b07231
ACS Appl. Mater. Interfaces 2017, 9, 20247−20253

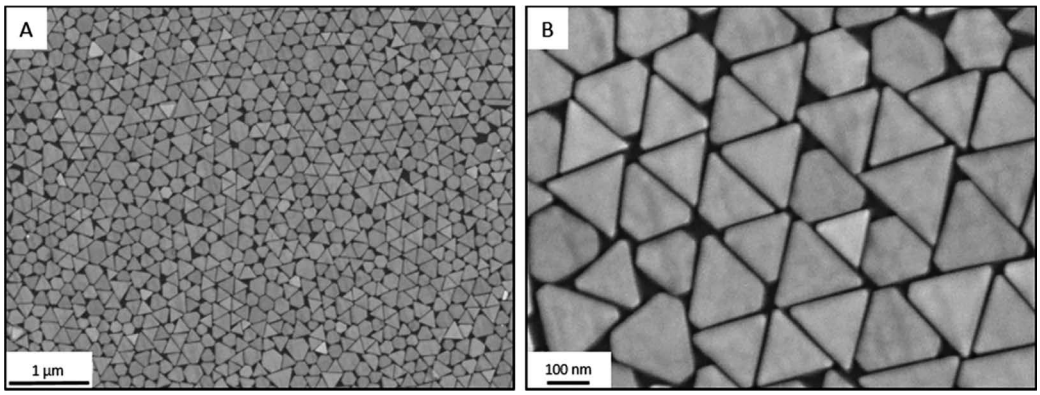

Figure 2. SEM micrographs of self-assembled gold nanotriangles closely packed in a monolayer on a Si substrate.

Scheme 2. Simplified Illustration of Film-Casting and Monolayer Formation after Adding the Ethanol−Toluene (E−T) Mixture

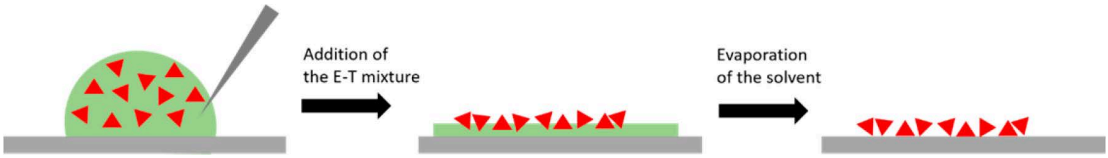

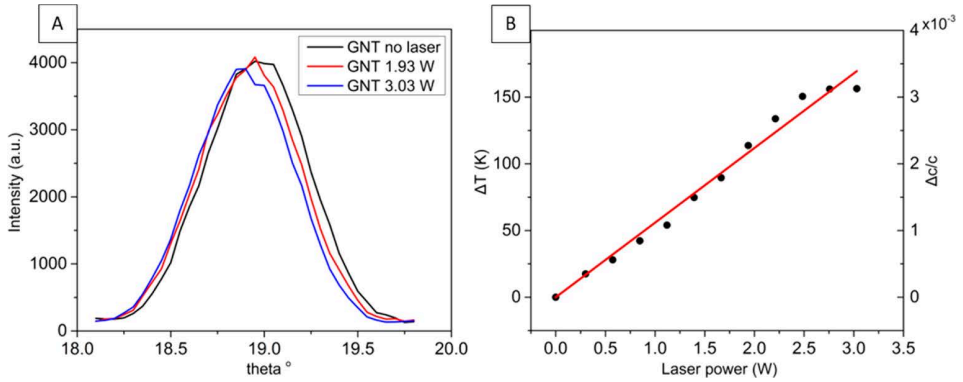

Figure 3. Θ−2Θ scans of the (111) Bragg reflection of a monolayer of Au triangles (GNT) deposited on quartz glass for three selected laser fluences (A) and temperature change ΔT of the Au particles determined from the peak shift ΔΘ as a function of the laser power (B) (error bars are smaller than the size of diagram spots).

After solvent evaporation, the assembly of the nanotriangles was examined by SEM and confirmed to be a close-packed edge-to-edge nanotriangle monolayer (Figure 2).

In similarity to the experiments in the glass vessel, size and quality of the monolayer are directly influenced by the volume ratio of the oil mixture. If the amount of toluene is increased, the size of the monolayer decreases and the triangles start to stack or to form large multilayer aggregates. Another key factor is the volume ratio between the droplet of the dispersion and the added oil mixture as well as the concentration of the dispersion. A lower oil mixture volume favors isolated and stacked particles, whereas a larger oil mixture volume leads to a fracture of the monolayer. Consequently, all these parameters act together and must receive attention to enable the correct setting for the monolayer formation. Note that self-assembly requires both ethanol and toluene for stable attachment to the surface.[34] Ethanol is decisive for the transport of gold nanotriangles from the aqueous dispersion to the water/oil interface.[34−36]

Best results of a close-packed monolayer without stacking were achieved by using a volume ratio of 1:0.4 between the droplet and the oil mixtures with ethanol−toluene volume ratio of 5:1. The concentration of gold nanotriangles was 3.5×10^{-4} g/cm^3 (Figure 2). In this case, we can easily prepare highly ordered monolayer films with a large area on silicon wafers as well as quartz glass (Figures S3 and S4) of about 1 cm^2. This corresponds to more than 3 billion gold nanotriangles. Keeping the ratios fixed, the method can be scaled.

The mechanism of the monolayer formation can be related to the self-assembly process rate (ν_{self}) in comparison to the solvent evaporation rate (ν_{solv}). Both processes strongly depend on the ethanol content in the system. When the evaporation of solvent is fast ($\nu_{solv} > \nu_{self}$), e.g., at a higher E−T ratio of 5:1, the AOT concentration is increased and the protection of the individual NTs is enhanced, too. This leads to self-assembled edge-to-edge ordered superstructures in the monolayer.

3.2. Temperature Calibration of Laser Heated Gold Nanotriangles. There is no established method to monitor the temperature of the metal nanoparticles themselves. Raman scattering permits an estimate of the temperature of the molecules attached to the particles. However, since SERS signals are dominated by molecules in hot spots, the

DOI: 10.1021/acsami.7b07231
ACS Appl. Mater. Interfaces 2017, 9, 20247−20253

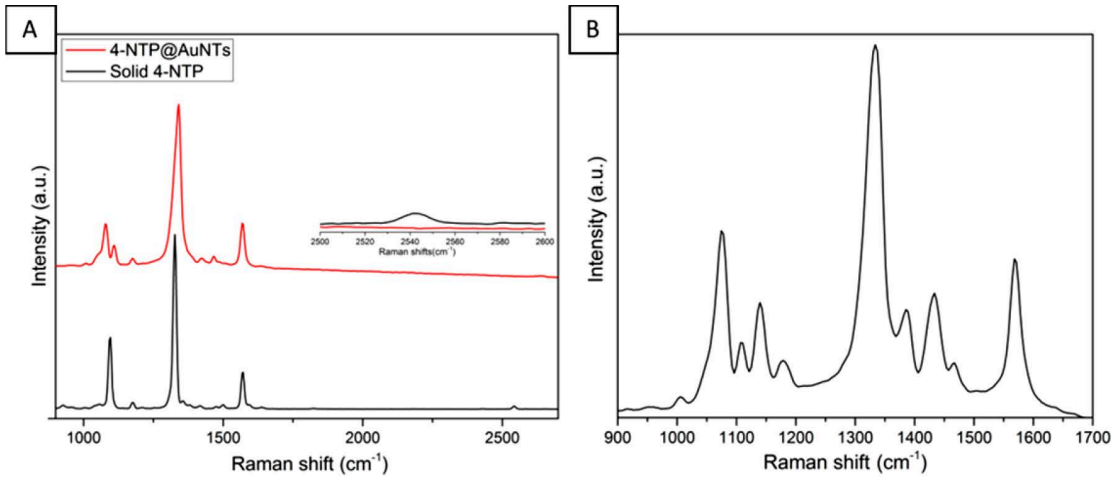

Figure 4. Raman spectrum of 4-NTP adsorbed on gold NTs (red) and solid 4-NTP (black) at low laser power of 0.5 mW (A); SERS spectrum of 4-NTP at high laser power of 5 mW (B).

interpretation is ambiguous. Measuring the optical response of plasmonic particles in principle allows for temperature assignments, but it is difficult to predict the spectral changes in the nonequilibrium situation. Note that the temperature of the particles may be much higher than the surrounding medium because the heat is deposited locally and the interface conductance is low.[13] The influences of temperature changes of the particles and their surroundings have a different influence on the particles' spectra. Therefore, stationary heating experiments do not result in the same spectral changes. X-ray diffraction, in contrast, selectively probes the lattice of the gold particles, and therefore an unambiguous temperature determination is possible. In order to demonstrate that monitoring the temperature of gold particles by X-ray diffraction is an easy task, we have used a very simple X-ray diffraction setup with a rather poor X-ray spot size of about 0.5 mm and a rather poor monochromator realized by a thin HOPG flake. The Bragg peak of the 7 nm thick particles is naturally broadened, showing a Bragg peak width of 0.6° from which we estimate a mosaicity of less than 0.1°. A simple diode laser is moderately collimated to homogeneously irradiate the X-ray spot on the sample. The Θ−2Θ scans of the (111) Bragg peak, shown in Figure 3A, shift to smaller diffraction angles when the laser intensity is increased from 0 to 3.5 W/cm^2. From the shift ΔΘ of the Bragg peak position we calculate a temperature change via $\cot\theta\Delta\theta = -\frac{\Delta c}{c} = -\alpha\Delta T$, where $\alpha = 1.4 \times 10^{-5}$ K^{-1} is the thermal expansion coefficient and $\frac{\Delta c}{c}$ is the relative change of the out-of plane lattice constant.[37] The shift depends linearly on the laser power (compare Figure 3B). It increases the particle temperature by 56 ± 1 K/(W/cm^2). With the highest available fluence we did not observe any dimerization of the attached 4-NTP. In the SERS microscope, we observe considerable dimerization with 5 mW focused on a spot with 1 μm radius corresponding to 5 orders of magnitude larger fluence.

Our current setup cannot provide such high laser fluences. It requires a more advanced but not extraordinary setup to obtain an X-ray microfocus that can be excited with the required fluence. Here we have demonstrated that already the very small shifts of the Bragg peak under low fluence conditions can resolve the temperature differences. We emphasize that the 5 orders of magnitude larger fluence in the SERS microscope does not imply 5 orders of magnitude larger temperature difference. The heat transport around the laser spot in the microscope is three-dimensional, whereas in our X-ray setup the large irradiated area makes it one-dimensional.

3.3. SERS Monitoring of Plasmon-Driven Catalytic Reaction. We used the dimerization of 4-NTP into DMAB as a model reaction to study the photocatalytic activity of the gold nanotriangles. A 4-NTP monolayer was assembled on the nanotriangles via the S−Au bond which has been confirmed by disappearance of S−H vibrational mode at 2443 cm^{-1} (inset in Figure 4A). The nanotriangles showed an excellent SERS enhancement factor of 2.76×10^4, somewhat larger than the best value (1.6×10^4) obtained by Lee et al. for the monolayer-over-mirror substrates of CTAB-based gold nanoprisms functionalized with PVP.[30] The distinct Raman peaks of 4-NTP are reproduced in the Raman microscope with 0.5 mW and 1 s integration time.[11] At low laser power, the SERS spectrum of 4-NTP remains similar to the Raman spectrum of the neat 4-NTP solid as it is shown in Figure 4A, where the spectra are dominated by three characteristic peaks at 1099, 1332, and 1573 cm^{-1}. These peaks were assigned to the C−H bending, NO_2 symmetric stretching, and C═C stretching modes of 4-NTP, respectively (compare Table 1). However, at higher laser power above 5 mW, three new peaks were observed at 1134, 1387, and 1434 cm^{-1} (Figure 4B). These peaks were assigned to the C−N symmetric stretching and N═N stretching vibrational modes of DMAB,[38] implying that a considerable fraction of the 4-NTP molecules have been dimerized on the surface of the gold nanotriangles.

Table 1. Raman Wavenumbers of 4-Nitrothiophenol (4-NTP) and 4,4′-Dimercaptobenzene (DMAB)

Raman wavenumber (cm^{-1})	SERS assignment of 4-NTP	SERS assignment of DMAB
854	C−N stretch	
1075	C−H bending	
1134		C−N stretch
1332	NO_2 stretch	
1387, 1434		N═N stretch
1568	C═C stretch	

DOI: 10.1021/acsami.7b07231
ACS Appl. Mater. Interfaces 2017, 9, 20247−20253

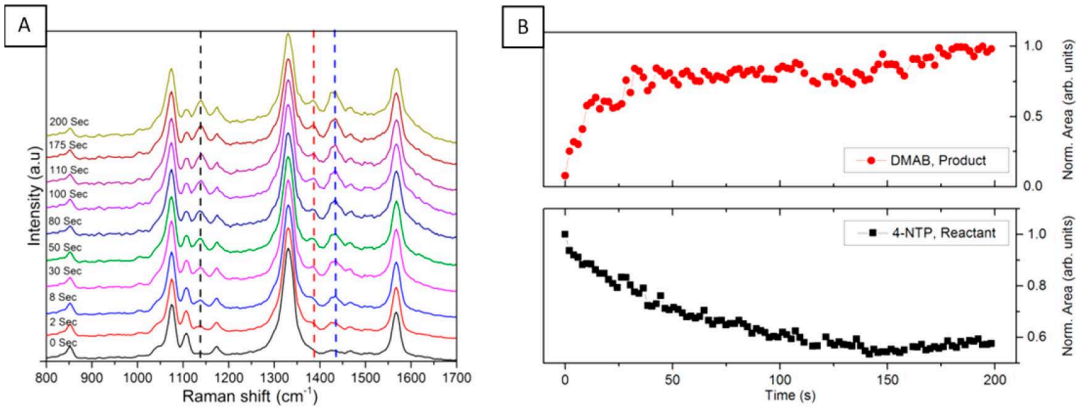

Figure 5. Time-dependent SERS spectra for a laser power of 5 mW at room temperature. Spectra taken at various time delays. At 0 s, only peaks assigned to the reactant 4-NTP are observed. The dashed lines indicate the main spectral signatures of the product, DMAB (A). Integrated areas of the peaks at 1332 cm^{-1} for the reactant and at 1134 cm^{-1} for the product as a function of time (B).

To further monitor the dimerization reaction dynamics, a time-dependent SERS study was carried out. Figure 5A shows SERS spectra of 4-NTP adsorbed on the gold nanotriangle. The immediately measured spectrum (t = 0) showed existence of only one species (4-NTP). DMAB peaks started to appear after 2 s and were increasing in intensity with increasing the laser exposure time. We integrated the area under the peak at 1134 cm^{-1} to present the concentration of DMAB, while the area under the peak at 1332 cm^{-1} measures the concentration of 4-NTP. Figure 5B shows the concentration over the reaction time, where the concentration of DMAB is increased with increasing irradiation time, while the concentration of 4-NTP is decreased. It was reported that the dimerization reaction of 4-NTP is driven by plasmonically generated hot electrons.[39] The gold nanotriangles are supposed to act as a source of hot electrons which populate unpopulated orbitals of the adsorbed 4-NTP and initiate the dimerization process. Therefore, increasing the laser power or the irradiation time would increase the generated hot electrons as well as the rate of the reaction. Our results show that the gold nanotriangles efficiently drive the photocatalytic reaction and that SERS allows for a real-time monitoring of the reaction dynamics.

4. CONCLUSION

In this article, we have presented a special method for the fabrication of large scale, self-assembled close-packed monolayers of gold nanotriangles with a high degree of ordering. The method is based on the simple procedure of adding a toluene–ethanol mixture to the aqueous gold nanotriangle dispersion and in particular does not need a functionalization of the particle surface in advance. The size of the monolayer can be easily controlled by either changing the concentration of the dispersion or varying the volume ratio of the droplet and the oil mixture. The exact ratio of the compounds is important to avoid stacking of the nanotriangles or the rupture of the monolayer.

We successfully demonstrated the applicability of the triangle monolayer as a substrate for monitoring photocatalytic reactions by SERS. Moreover, due to the flat structural ordering of the monolayer, X-ray measurements could be employed to observe small laser-induced temperature changes of particles under continuous laser heating. The combination of both experiments might become important for investigation of plasmon assisted reactions or photothermal applications. In essence, under the described preparation conditions, we show a facile and repeatable way for the fabrication of dense packed nanotriangle monolayers on different substrates, i.e., on silicon wafers or quartz glass, and demonstrated its potential as a platform for advanced nanochemical research.

■ ASSOCIATED CONTENT

Supporting Information

The Supporting Information is available free of charge on the ACS Publications website at DOI: 10.1021/acsami.7b07231.

Three SEM micrographs, one optical photograph (PDF)

■ AUTHOR INFORMATION

Corresponding Author

*(J.K.) E-mail koetz@uni-potsdam.de; Ph +49 331 977 5220.

ORCID

Wouter Koopman: 0000-0001-5402-345X

Matias Bargheer: 0000-0002-0952-6602

Joachim Koetz: 0000-0001-9113-1337

Notes

The authors declare no competing financial interest.

■ ACKNOWLEDGMENTS

The financial support from the German Research Foundation (KO 1387/14-1) is gratefully acknowledged. F.L. acknowledges financial support by the DFG and RMS by the graduate school SALSA.

■ REFERENCES

(1) Wiley, B.; Sun, Y.; Xia, Y. Synthesis of Silver Nanostructures with Controlled Shapes and Properties. *Acc. Chem. Res.* **2007**, *40*, 1067–1076.

(2) Knittel, P.; Bibikova, O.; Kranz, C. Challenges in Nano-electrochemical and Nanomechanical Studies of Individual Anisotropic Gold Nanoparticles. *Faraday Discuss.* **2016**, *193*, 353–369.

(3) Li, N.; Zhao, P.; Astruc, D. Anisotropic Gold Nanoparticles: Synthesis, Properties, Applications and Toxicity. *Angew. Chem., Int. Ed.* **2014**, *53*, 1756–1789.

(4) Bastús, N. G.; Comenge, J.; Puntes, V. Kinetically Controlled Seeded Growth Synthesis of Citrate-Stabilized Gold Nanoparticles of up to 200nm: Size Focusing *versus* Ostwald Ripening. *Langmuir* **2011**, *27*, 11098–11105.

(5) Burmeister, F.; Badowsky, W.; Braun, T.; Wieprich, S.; Boneberg, J.; Leiderer, P. Colloid Monolayer Lithography – A Flexible Approach

for Nanostructuring of Surfaces. *Appl. Surf. Sci.* **1999**, *144−145*, 461−466.
(6) Willets, K. A.; Van Duyne, R. P. Localized Surface Plasmon Resonance Spectroscopy and Sensing. *Annu. Rev. Phys. Chem.* **2007**, *58*, 267−297.
(7) Li, Y.; Duan, G.; Liu, G.; Cai, W. Physical Prosses-Aided Periodic Micro/Nanostructured Arrays by Colloidal Template Technique: Fabrication and Application. *Chem. Soc. Rev.* **2013**, *42*, 3614−3627.
(8) Ye, X.; Qi, L. Two-Dimensionally Patterned Nanostructures Based on Monolayer Colloidal Crystals: Controllable Fabrication, Assembly and Applications. *Nano Today* **2011**, *6*, 608−631.
(9) Hamon, C.; Novikov, S.; Scarabelli, L.; Basabe-Desmonts, L.; Liz-Marzán, L. M. Hierarchical Self-Assembly of Gold Nanoparticles into Patterned Plasmonic Nanostructures. *ACS Nano* **2014**, *8*, 10694−10703.
(10) Yahia-Ammar, A.; Sierra, D.; Mérola, F.; Hildebrandt, N.; Le Guével, X. Self-Assembled Gold Nanoclusters for Bright Fluorescence Imaging and Enhanced Drug Delivery. *ACS Nano* **2016**, *10*, 2591−2599.
(11) Liebig, F.; Thünemann, A. F.; Koetz, J. Ostwald Ripening Growth Mechanism of Gold Nanotriangles in Vesicular Template Phases. *Langmuir* **2016**, *32*, 10928−10935.
(12) Liebig, F.; Sarhan, R. M.; Prietzel, C.; Reinecke, A.; Koetz, J. Green" Gold Nanotriangles: Synthesis, Purification by Polyelectrolyte/Micelle Depletion Flocculation and Performance in Surface-Enhanced Raman Scattering. *RSC Adv.* **2016**, *6*, 33561−33568.
(13) von Reppert, A.; Sarhan, R. M.; Stete, F.; Pudell, J.; Del Fatti, N.; Crut, A.; Koetz, J.; Liebig, F.; Prietzel, C.; Bargheer, M. Watching the vibration and cooling of ultrathin gold nanotriangles by ultrafast X-ray diffraction. *J. Phys. Chem. C* **2016**, *120*, 28894−28899.
(14) Daniel, M. C.; Astruc, D. Gold Nanoparticles: Assembly, Supramolecular Chemistry, Quantum-Size-Related Properties, and Applications Toward Biology, Catalysis, and Nanotechnology. *Chem. Rev.* **2004**, *104*, 293−346.
(15) Loo, C.; Lin, A.; Hirsch, L.; Lee, M. H.; Barton, J.; Halas, N.; West, J.; Drezek, R. Nanoshell-Enabled Photonics-Based Imaging and Therapy of Cancer. *Technol. Cancer Res. Treat.* **2004**, *3*, 33−40.
(16) Jain, P. K.; Huang, W.; El-Sayed, M. A. On the Universal Scaling Behavior of the Distance Decay of Plasmon Coupling in Metal Nanoparticle Pairs: A Plasmon Ruler Equation. *Nano Lett.* **2007**, *7*, 2080−2088.
(17) Xue, B.; Wang, D.; Zuo, J.; Kong, X.; Zhang, Y.; Liu, X.; Tu, L.; Chang, Y.; Li, C.; Wu, F.; Zeng, Q.; Zhao, H.; Zhang, H. Towards High Quality Triangular Silver Prisms: Improved Synthesis, Six-Tips Based Hot Spots and Ultra-High Local Surface Plasmon Resonance Sensitivity. *Nanoscale* **2015**, *7*, 8048−8057.
(18) Kneipp, K.; Wang, Y.; Kneipp, H.; Perelman, L. T.; Itzkan, I.; Dasari, R.; Feld, M. S. Single Molecule Detection Using Surface-Enhanced Raman Scattering (SERS). *Phys. Rev. Lett.* **1997**, *78*, 1667−2670.
(19) Le Ru, E. C.; Etchegoin, P. G. Single-Molecule Surface-Enhanced Raman Spectroscopy. *Annu. Rev. Phys. Chem.* **2012**, *63*, 65−87.
(20) Cao, Y. W. C.; Jin, R. C.; Mirkin, C. A. Nanoparticles with Raman Spectroscopic Fingerprint for DNA and RNA Detection. *Science* **2002**, *297*, 1536−1540.
(21) Bao, Z. Y.; Lei, D. Y.; Jiang, R. B.; Liu, X.; Dai, J. Y.; Wang, J. F.; Chan, H. L. W.; Tsang, Y. H. Bifunctional Au@Pt Core-Shell Nanostructures for *In Situ* Monitoring of Catalytic Reactions by Surface-Enhanced Raman Scattering Spectroscopy. *Nanoscale* **2014**, *6*, 9063−9070.
(22) Xu, P.; Kang, L.; Mack, N. H.; Schanze, K. S.; Han, X.; Wang, H.-L. Mechanistic Understanding of Surface Plasmon Assisted Catalysis on a Single Particle: Cyclic Redox of 4-Aminothiophenol. *Sci. Rep.* **2013**, *3*, 2997.
(23) Lotito, V.; Zambelli, T. Self-Assembly of Single-Sized and Binary Colloidal Particles at Air/Water Interface by Surface Confinement and Water Discharge. *Langmuir* **2016**, *32*, 9582−9590.
(24) Walker, D. A.; Browne, K. P.; Kowalczyk, B.; Grzybowski, B. A. Self-Assembly of Nanotriangles Superlattices Facilitated by Repulsive Electrostatic Interaction. *Angew. Chem., Int. Ed.* **2010**, *49*, 6760−6763.
(25) Deegan, R. D. Pattern Formation in Drying Drops. *Phys. Rev. E: Stat. Phys., Plasmas, Fluids, Relat. Interdiscip. Top.* **2000**, *61*, 475−485.
(26) Retsch, M.; Zhou, Z.; Rivera, S.; Kappl, M.; Zhao, X. S.; Jonas, U.; Li, Q. Fabrication of Large-Area, Transferable Colloidal Monolayers Utilizing Self-Assembly at the Air/Water Interface. *Macromol. Chem. Phys.* **2009**, *210*, 230−241.
(27) Sánchez-Iglesias, A.; Grzelczak, M.; Pérez-Juste, J.; Liz-Marzán, L. M. Binary Self-Assembly of Gold Nanowires with Nanospheres and Nanorods. *Angew. Chem., Int. Ed.* **2010**, *49*, 9985−9989.
(28) Scarabelli, L.; Coronado-Puchau, M.; Giner-Casares, J. J.; Langer, J.; Liz-Marzán, L. M. Monodisperse Gold Nanotriangles: Size Control, Large-Scale Self-Assembly, and Performance in Surface-Enhanced Raman Scattering. *ACS Nano* **2014**, *8*, 5833−5842.
(29) Thierry, B.; Ng, J.; Krieg, T.; Griesser, H. J. A Robust Procedure for the Functionalization of Gold Nanorods and Noble Metal Nanoparticles. *Chem. Commun.* **2009**, 1724−1726.
(30) Lee, Y. H.; Lee, C. K.; Tan, B.; Tan, J. M. R.; Phang, I. Y.; Ling, X. Y. Using the Langmuir-Schaefer technique to fabricate large-area dense SERS-active Au nanoprism monolayer films. *Nanoscale* **2013**, *5*, 6404−6412.
(31) Schulze, N.; Prietzel, C.; Koetz, J. Polyampholyte mediated synthesis of anisotropic gold nanoplatelets. *Colloid Polym. Sci.* **2016**, *294*, 1297−1304.
(32) Liu, C.; Li, Y.-J.; Sun, S.-G.; Yeung, E. S. Room-Temperature Cold-Welding of Gold Nanoparticles for Enhancing the Electro-oxidation of Carbon Monoxide. *Chem. Commun.* **2011**, *47*, 4481−4483.
(33) Fu, Q.; Ran, G.; Xu, W. *Nano Res.* **2016**, *9*, 3247−3256.
(34) Li, Y. J.; Huang, W. I. J.; Sun, S. G. Direct Self-Assembly of CTAB-Capped Au Nanotriangles. *Angew. Chem., Int. Ed.* **2006**, *45*, 2537−2539.
(35) Reincke, F.; Hickey, S. G.; Kegel, W. K.; Vanmaekelbergh, D. Spontaneous Assembly of a Monolayer of Charged Gold Nanocrystals at the Water/Oil Interface. *Angew. Chem., Int. Ed.* **2004**, *43*, 458−462.
(36) Duan, H. W.; Wang, D. A.; Kurth, D. G.; Möhlwald, H. Directing Self-Assembly of Nanoparticles at Water/Oil Interfaces. *Angew. Chem., Int. Ed.* **2004**, *43*, 5639−5642.
(37) Shayduk, R.; Navirian, H.; Leitenberger, W.; Goldshteyn, J.; Vrejoiu, I.; Weinelt, M.; Gaal, P.; Herzog, M.; von Korff Schmising, C.; Bargheer, M. Nanoscale Heat Transport Studied by High-Resolution Time-Resolved X-Ray Diffraction. *New J. Phys.* **2011**, *13*, 093032.
(38) Zhang, J.; Winget, S. A.; Wu, Y.; Su, D.; Sun, X.; Xie, Z.-X.; Qin, D. Ag@Au Concave Cuboctahedra: A Unique Probe for MonitoringAu-Catalyzed Reduction and Oxidation Reactions by Surface-Enhanced Raman Spectroscopy. *ACS Nano* **2016**, *10*, 2607−2616.
(39) Yan, X.; Wang, L.; Tan, X.; Tian, B.; Zhang, J. Surface-Enhanced Raman Spectroscopy Assisted by Radical Capturer for Tracking of Plasmon-Driven Redox Reaction. *Sci. Rep.* **2016**, *6*, 30193−30199.

DOI: 10.1021/acsami.7b07231
ACS Appl. Mater. Interfaces 2017, 9, 20247−20253

Supporting Information

Deposition of gold nanotriangles in large scale close-packed monolayers for X-ray based temperature calibration and SERS monitoring of plasmon-driven catalytic reactions

Ferenc Liebig,[a] Radwan M. Sarhan,[b,c,d] Mathias Sander,[c] Wouter Koopman,[c] Roman Schuetz,[e] Matias Bargheer,[c] Joachim Koetz[a*]

[a] Institute for Chemistry, University of Potsdam, Karl-Liebknecht-Strasse 24-25, Haus 25, 14476 Potsdam, Germany

[b] Chemistry Department, Faculty of Science, Cairo University, Cairo 12613, Egypt

[c] Institute for Physics, University of Potsdam, Karl-Liebknecht-Strasse 24-25, Haus 27, 14476 Potsdam, Germany

[d] Humboldt-Universität zu Berlin, School of Analytical Sciences Adlershof (SALSA), Albert-Einstein-Str. 5-9, 10099 Berlin, Germany

[e] Department of Biomaterials, Max Planck Institute of Colloids and Interfaces, Am Mühlenberg 1, 14476 Potsdam, Germany

* Corresponding author: Joachim Koetz

E-mail: koetz@uni-potsdam.de

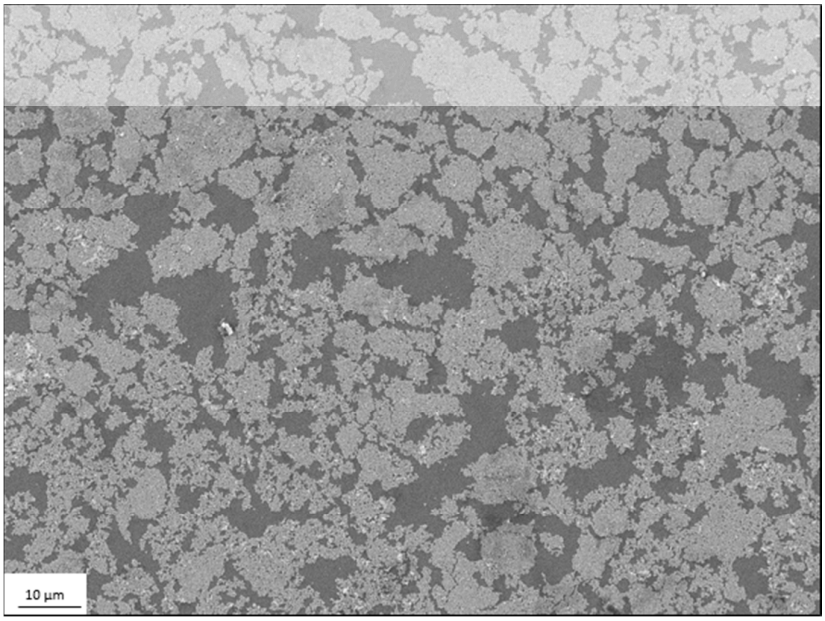

Figure S1. SEM micrographs of self-assembled gold nanotriangles transferred onto a Si-wafer

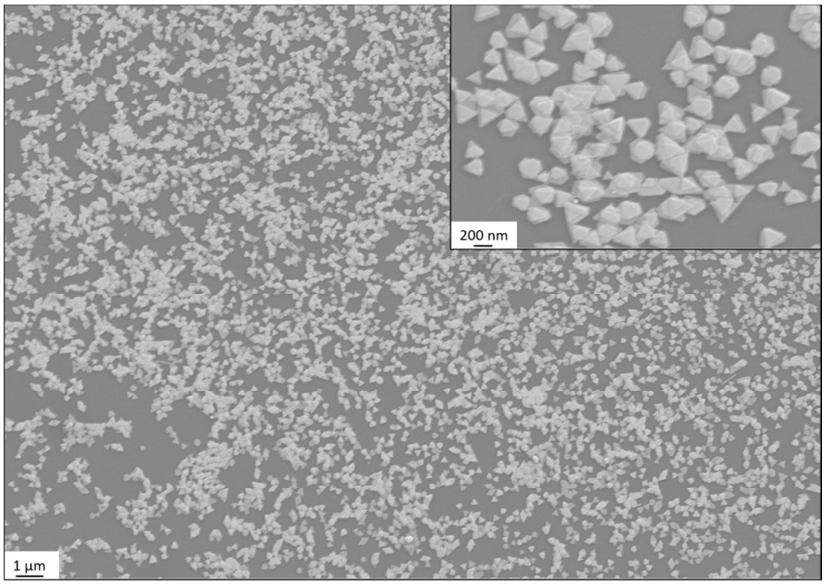

Figure S2. SEM micrographs of gold nanotriangles after drop casting and rapid evaporation of the droplet in absence of an oil component

Figure S3. Optical photograph of self-assembled monolayer formation on quartz glass substrate

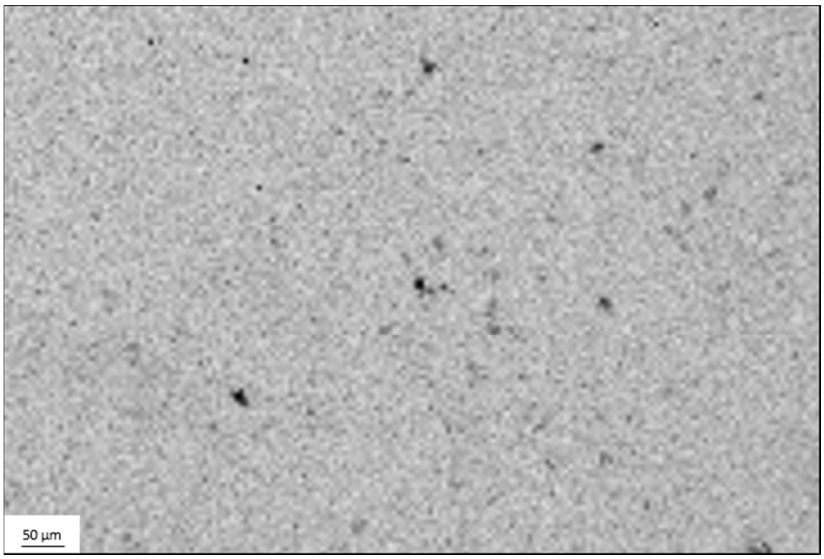

Figure S4. SEM micrograph of self-assembled monolayer formation on Si-wafer substrate

THE JOURNAL OF PHYSICAL CHEMISTRY C

Article

pubs.acs.org/JPCC

Watching the Vibration and Cooling of Ultrathin Gold Nanotriangles by Ultrafast X-ray Diffraction

A. von Reppert,[†] R. M. Sarhan,[†,∥] F. Stete,[†,∥] J. Pudell,[†] N. Del Fatti,[‡] A. Crut,[‡] J. Koetz,[§] F. Liebig,[§] C. Prietzel,[§] and M. Bargheer*[,†,⊥]

[†]Institut für Physik & Astronomie, Universität Potsdam, Karl-Liebknecht-Str. 24-25, 14476 Potsdam, Germany

[‡]FemtoNanoOptics Group, Institut Lumière Matière, Université de Lyon, CNRS-Université Lyon 1, 69622 Villeurbanne, France

[§]Institut für Chemie, Universität Potsdam, Karl-Liebknecht-Str. 24-25, 14476 Potsdam, Germany

[∥]Humboldt-Universität zu Berlin, School of Analytical Sciences Adlershof (SALSA), Albert-Einstein-Str. 5-9, 10099 Berlin, Germany

[⊥]Helmholtz Zentrum Berlin, Albert-Einstein-Str. 15, 12489 Berlin, Germany

ABSTRACT: We study the vibrations of ultrathin gold nanotriangles upon optical excitation of the electron gas by ultrafast X-ray diffraction. We quantitatively measure the strain evolution in these highly asymmetric nano-objects, providing a direct estimation of the amplitude and phase of the excited vibrational motion. The maximal strain value is well reproduced by calculations addressing pump absorption by the nanotriangles and their resulting thermal expansion. The amplitude and phase of the out-of-plane vibration mode with 3.6 ps period dominating the observed oscillations are related to two distinct excitation mechanisms. Electronic and phonon pressures impose stresses with different time dependences. The nanosecond relaxation of the expansion yields a direct temperature sensing of the nano-object. The presence of a thin organic molecular layer at the nanotriangle/substrate interfaces drastically reduces the thermal conductance to the substrate.

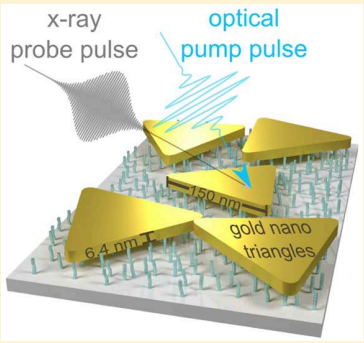

INTRODUCTION

Metallic nanoparticles have been in the focus of intensive research over decades,[1] in part because they may potentially help to realize large bandwidth optical nanoelectromechanical systems or similar small and fast devices.[2] From the perspective of physical chemistry, colloidal particles present versatile and accessible nano-objects, which can be grown as spheres, rods, cubes, pyramids, platelets, or prisms, just to name a few examples. Special shapes are useful for tailoring the plasmon-resonance and catalytic activity of the particles or to optimize them for surface-enhanced Raman scattering. Investigations of the ultrafast thermal and vibrational dynamics of such nanostructures[3−6] are often justified by applications like photothermal therapy or catalysis.[7] The strong interest in these phenomena also lies in the fundamental questions of how heat transport and vibrational response are altered on the nanoscale, when surface effects may start to play a role, making the validity of continuum descriptions questionable.[8−12] Recently the focus of ultrafast studies has shifted from spherical particles over nanorods toward truly asymmetric structures such as prisms.[4,13−15] These particles often exhibit special crystalline structures with well-defined orientation,[16] which influence not only the growth and stability but also the optical and acoustic properties.[17]

The vibrational dynamics of nano-objects have been studied by a myriad of ultrafast optical pump−probe experiments looking at absorption, reflection, or scattering of ensembles.[3,4,6] Because the polydispersity of the samples leads to a dephasing of the observed vibrations, more recently such experiments were carried out on individual nano-objects.[18,19] Although much has been learned by optical techniques and the simulations using continuum mechanics or molecular dynamics, a thorough discussion of purely optical measurements is required to obtain information about the amplitude and phase with which individual vibrational modes are excited.[4,5,20,21] Ultrafast structural tools such as ultrafast X-ray or electron diffraction are the most direct ways to study changes of the crystal lattice induced by laser excitation. Although diffraction on the femtosecond time scale started to become available 20 years ago, only very few studies of nanoparticle dynamics with dynamics faster than 100 ps have been reported.[22−24] An experiment at the free-electron laser has monitored the breathing[25] and melting[26] of a single few hundred nanometers large ellipsoidal nanocrystal. Studying asymmetric and much thinner objects has, however, remained a challenge, and, in general, ultrafast single-particle studies using X-rays can exclusively be performed at free-electron laser facilities.[10] Demonstrating the possibility to use a laser-based femtosecond X-ray source for ultrafast structural measurements on ensembles of nanoparticles is therefore a major breakthrough.

We present such ultrafast X-ray diffraction (UXRD) experiments that precisely determine the average out-of-plane

Received: November 18, 2016
Revised: November 25, 2016
Published: November 27, 2016

DOI: 10.1021/acs.jpcc.6b11651
J. Phys. Chem. C 2016, 120, 28894−28899

strain $\varepsilon(t)$ of an ensemble of <111> oriented gold nanotriangles (NTs) as a function of the time delay t after the excitation. On the basis of the sound velocity v_{111} = 3.528 nm/ps along the [111] direction,[27] the oscillation period of T = 3.6 ps corresponding to the fastest out-of-plane vibration mode yields a particle thickness $d_0 = v_{111} \cdot T/2$ = 6.4 nm, consistent with particle shape characterized by thorough TEM measurements. The amplitude of the first oscillation and the maximal expansion $\varepsilon_{max} = 3 \times 10^{-3}$ of the particle after ~20 ps are consistent with a 1D acoustic model, where the expansion mode of the film is excited by a time-dependent pressure $\sigma(t)$ imposed by hot electrons and phonons. The pump−pulse absorption is calculated by a complete 3D numerical optical model.[19,28,29] A careful analysis by electron microscopy is used to prove that the NTs shape is robust under the experimental conditions. From the measured lattice strain, ε, one can directly read the temperature change ΔT_0 via

$$\epsilon = \int_{T_0}^{T_0+\Delta T_0} \alpha_{Au}(T)\, dT \quad (1)$$

using the expansion coefficient $\alpha_{Au}(T)$ measured in thermal equilibrium. The cooling on the nanosecond time scale evidences the rather good thermal insulation given by the ~1 nm thick organic layer that was used for functionalizing the surface of the silicon substrate.

EXPERIMENTAL SECTION

Very thin gold NTs were prepared in a one-step synthesis in the presence of mixed AOT/phospholipid vesicles via a process that can be described by an Ostwald ripening growth mechanism.[31] To reduce the polydispersity of the product, the anisotropic nanoparticles were separated by using a combined polyelectrolyte/AOT micelle depletion flocculation.[31] The NTs were deposited on a silicon wafer functionalized by 3-mercaptopropyltrimethoxysilane (3-MPTMS).[32] The NTs were attached to the thiol group at a distance of ~1 nm above the Si surface. AFM investigations of >40 nanoplatelets reveal an average thickness of 8.5 ± 1.5 nm. Subtracting 1 nm of the 3-MPTMS layer, this is in full agreement with the 6.4 nm platelet thickness derived from the UXRD data. Figure 1 shows a thorough characterization of the sample by electron microscopy. The sideview (Figure 1a) of two individual NTs with 6.7 and 8.2 nm thickness illustrates the thickness of ~7.5 ± 1.5 nm. While the base length of the NTs is ~150 nm with a large size distribution (Figure 1d), the distribution of the platelet-thickness is rather sharp. The zoom into the NTs (Figure 1b)) can be Fourier-transformed to determine the periodicity of the lattice structure. Figure 1c proves the <111> orientation of the entire triangle.[30] Figure 1e confirms that the NTs are intact after UXRD experiments performed at a base temperature T_0 = 24 K with a pump wavelength of 400 nm and a fluence of F = 2.9 mJ/cm^2. Figure 1f,g shows the permanent deformation of the NTs under similar fluence conditions at room temperature. The UXRD experiments[33−35] subsequently discussed in this paper were conducted under the nondestructive conditions T_0 = 24 K and F = 2.9 mJ/cm^2. The pump pulses had a duration of ~80 fs, and the pulse length of the hard X-ray probe pulses at 8 keV derived from a laser-driven plasma source reduced the time resolution of the setup to ~200 fs.[34,35] Figure 2 illustrates the static XRD characterization of the sample in the geometry of the UXRD setup.[34] Figure 2b shows the reciprocal space map of the

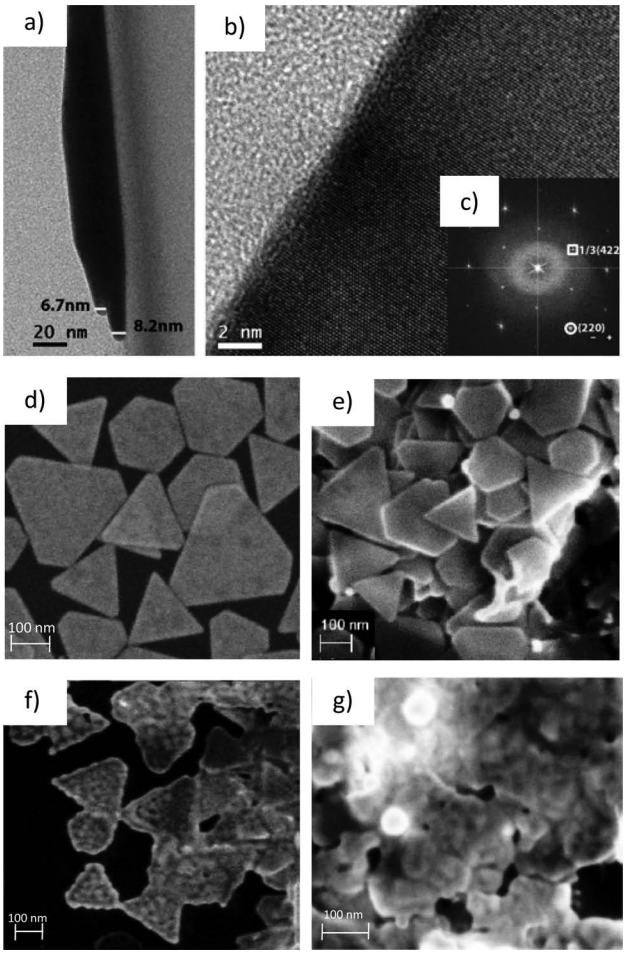

Figure 1. TEM and SEM pictures of the gold nanotriangle sample. (a) TEM sideview of gold-NTs. (b) High-resolution TEM and (c) its Fourier transform show 1/3{422} and {220} reflections characteristic of NTs with <111> orientation.[30] (d) SEM micrograph showing the polydisperse nature of the nanoplatelets. (e) SEM micrograph of the sample after the pump−probe experiment at T_0 = 24 K with F = 2.9 mJ/cm^2. (f) SEM micrograph of the sample after treatment with F = 3 mJ/cm^2 at room temperature. (g) Same for F = 5 mJ/cm^2. Triangles deform or melt together and reshape to spheres.

pristine sample, whereas the integrated X-ray diffraction intensity as a function of the Bragg angle θ in Figure 2a also reports a comparison to the diffraction from a sample after excessive irradiation with optical pump-pulses at 300 K. The reshaping of the Bragg peak indicating the permanent deformation of the gold particles at high fluence excitation at room temperature is clearly visible also in the reciprocal space map (not shown). The very weak and broad reflection from the gold (1 1 1) lattice planes (Figure 2b) renders the UXRD data acquisition extremely difficult, especially because the fluence must be reduced such that no sample damage occurs during several hours of optical pumping. Figure 2c compares the shifted Bragg peaks after 2.1 and 19 ps in the UXRD experiment with the Bragg peak at negative pump−probe delay. At low temperature and with the applied fluence the shape of these peaks is unchanged during the acquisition of the UXRD data.

DOI: 10.1021/acs.jpcc.6b11651
J. Phys. Chem. C 2016, 120, 28894−28899

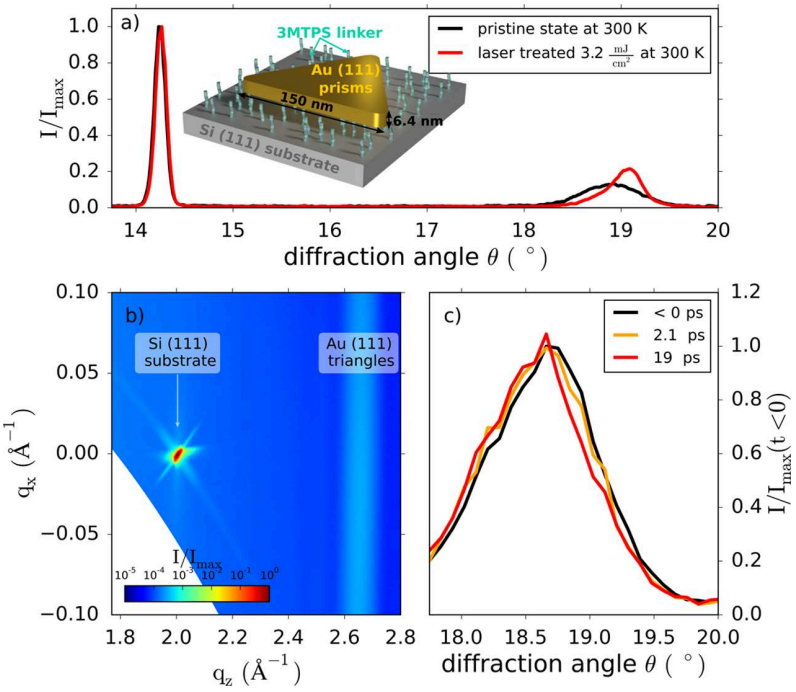

Figure 2. (a) Integrated X-ray intensity as a function of the Bragg angle θ for the pristine sample (black) and for a sample spot that was excessively irradiated at room temperature (red). Inset: Schematic of the ideal situation where all gold-NTs are attached to the surface with equally long organic spacer molecules. (b) Reciprocal space map showing the sharp Si substrate peak and the very weak and broad reflection of the gold NTs. The diffraction does not correspond to a Debye−Scherrer ring but to a single-crystal diffraction with a large mosaic spread of about ±5° originating from the nonperfect sample that also contains stacked NTs. (c) Integrated X-ray diffraction intensity for three different time delays at a fluence of 2.9 mJ/cm^2 that does not permanently modify the sample. We essentially observe a peak shift to smaller angles, indicating the ultrafast out-of-plane expansion.

RESULTS AND DISCUSSION

Figure 3 shows the lattice strain $\varepsilon(t)$ as a function of the time delay t after excitation of the gold NTs at T_0 = 24 K with 400 nm pulses. The fluence F = 2.9 mJ/cm^2 is given by the light intensity on the sample surface at the incidence angle of 40°. The femtosecond pulse excitation leads to an oscillation of the measured out-of-plane strain with a period of T = 3.6 ps, which is consistent with the fundamental breathing mode of a film with thickness 6.4 nm. The strain reaches a first maximum of $\varepsilon = 2.3 \pm 0.3 \times 10^{-3}$ after ∼2 ps. The signal oscillates and reaches a maximum of $\varepsilon_{max} = 3 \pm 0.3 \times 10^{-3}$ after ∼20 ps. The lattice slowly contracts on a nanosecond time scale as the heat flows out of the nanoparticle.

To interpret the observed maximum expansion ε_{max}, we calculated the temperature rise of a gold NT originating from the absorption of 400 nm pulses under 40° incidence. We computed the absorption cross-section using a finite-element approach accounting for the inhomogeneous nano-object environment induced by its deposition on a silicon substrate,[19,28,29] yielding σ_{abs} = 1200 nm^2 for NTs with 6.4 nm thickness and 150 nm side length. Neglecting heat transfer to the environment on short time scale, the temperature rise of a thermalized gold NT ΔT_0 = 285 K at T_0 = 24 K is calculated by numerical integration of

$$\sigma_{abs} F/(\rho_{Au} V) = \int_{T_0}^{T_0+\Delta T_0} c_{Au}(T)\, dT \qquad (2)$$

where ρ_{Au} = 19.3 g/cm^3 is the density, $c_{Au}(T)$ is the strongly temperature-dependent heat capacity of gold, and V is the volume of the particle. From eq 1 we calculate an expansion of $\varepsilon^{calc} = 3 \times 10^{-3}$, in excellent agreement with the data. For room temperature, the calculation yields the same result. This can be understood by invoking the Grüneisen parameter of gold, γ, which is a temperature-independent[36,37] measure of the thermal stress $\sigma = \gamma \cdot Q$ upon deposition of an energy density Q.[37] The heat expansion coefficient $\alpha(T)$ and heat capacity $c(T)$ share the same temperature dependence, both for the electronic contribution and for the phonon contribution, which are given by their quantum nature. Therefore, the electronic and phononic Grüneisen parameters of gold $\gamma_e \sim \alpha_e(T)/c_e(T)$ and $\gamma_p \sim \alpha_p(T)/c_p(T)$ are independent of temperature.

To quantitatively describe the oscillation of the signal at short times, we have to account for the fact that the optical excitation first heats up the electron gas, yielding a corresponding electron stress σ_e driving the out-of-plane expansion of the NT. We estimate an electronic temperature rise of T_e(100 fs) = 4000 K from the electronic specific heat of $c_e(T) = \gamma_s T$, where $\gamma_s = 3.7 \times 10^{-6}$J/(gK) is the Sommerfeld-coefficient of gold.[38] The electron pressure $\sigma_e(t) = \gamma_e Q_e(t) = \gamma_e Q^e_{max} e^{-t/\tau_e}$ relaxes with the characteristic electron−phonon coupling time τ_e. With the same time constant, the phonon pressure $\sigma_p(t) = \gamma_p Q^p_{eq}(1 - e^{-t/\tau_e})$ rises until the electron and phonon temperatures have equilibrated. The electron−phonon coupling time in gold in the low perturbation limit is 1 ps at room temperature and 0.6 ps at 24 K.[39,40] However, under strong excitation conditions, the electronic heat capacity c_e rises with temperature, and equilibration times can exceed 5 ps under our conditions.[38,41,42] At t = 20 ps, we can safely assume that the electron and phonon system have reached a mutual

DOI: 10.1021/acs.jpcc.6b11651
J. Phys. Chem. C 2016, 120, 28894−28899

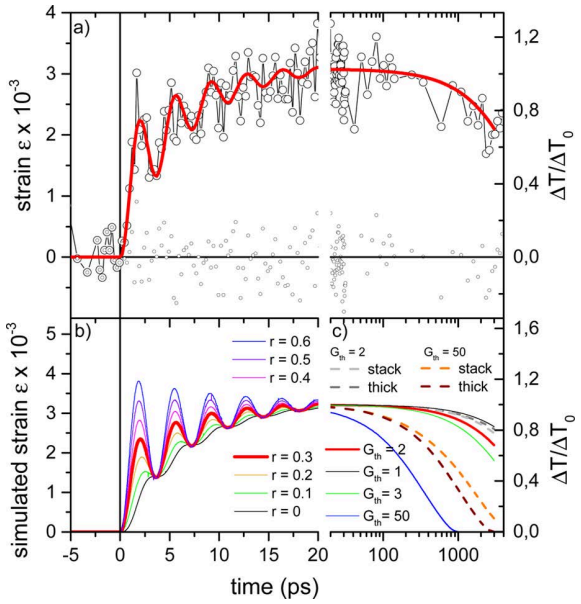

Figure 3. (a) Time-dependent strain measured by UXRD (open circles) together with the best fits from the models (red lines). The time axis is split according to the two models. The small dots represent the difference of the data and the simulation indicating only little contributions from additional vibrational modes. The relative error 3×10^{-4} of the strain measurement is estimated from the variation of data for $t < 0$ and around the maximum. (b) Model simulation according to eq 4 with a single oscillator driven by the phononic and electronic stresses according to eq 3. $r = \gamma_e/\gamma_p$ is ratio of the electronic and phononic Grüneisen parameters. (c) Results from the 3D heat-transport simulations. The thin lines are obtained for a single Au triangle separated from Si by a layer with a thermal interface conductance G_{th} in MW/(m^2 K). The fat red line indicates the best fit that is reproduced in panel a. The dashed lines are cross-checks for heat transport out of three stacked NTs (see the text).

thermal equilibrium so that a single temperature suffices to describe both systems.

The UXRD data provide a unique access to the phase and amplitude of the oscillations, which are both sensitive to the exact form of the total driving stress, which is given by the following functional form[42−44]

$$\sigma(t) = \sigma_e(t) + \sigma_p(t) = \sigma_\infty H(t)\left(1 + \left(\frac{\gamma_e}{\gamma_p} - 1\right)e^{-t/\tau_e}\right) \tag{3}$$

where $H(t)$ denotes the Heaviside function. The maximum stress $\sigma_\infty = C_{eff}\varepsilon(20\ \text{ps})$ can be deduced from the measured strain and the effective elastic modulus C_{eff} along the [111] direction. To model the early time vibrations (Figure 3a), we consider the homogeneous increase of the particle thickness $d(t)$ as the only relevant vibrational mode with frequency ω_0 and damping rate η. It is excited by the time-dependent stress $\sigma(t)$ stated in eq 3. The explicit differential equation used to describe the time-dependent out-of-plane strain $\varepsilon(t) = \frac{d(t) - d_0}{d_0}$ of the particles is then

$$\frac{d^2\varepsilon}{dt^2} + 2\eta\frac{d\varepsilon}{dt} + \omega_0^2\varepsilon = P\sigma(t) \tag{4}$$

The constant prefactor P on the right-hand side is due to dimensional reasons as it relates the driving stress $\sigma(t)$ to an acceleration of the strain. The equation of motion can be solved using the Green's function of the damped harmonic oscillator $G(t, t') = H(t - t')\frac{i}{\omega_- - \omega_+}(e^{i\omega_+(t-t')} - e^{i\omega_-(t-t')})$, where $\omega_\pm = i\eta \pm \sqrt{\omega_0^2 - \eta^2}$. The time-dependent strain can then simply be found via integration

$$\varepsilon(t) = P\int_{-\infty}^{t'} G(t, t')\sigma(t')\,dt' \propto \int_{-\infty}^{t'} G(t, t')\sigma(t')\,dt' \tag{5}$$

The magnitude of the prefactor P is dictated by the strain that is attained after the oscillations are damped out. We vary $P{\cdot}\sigma_\infty$ to match the signal at $t = 20$ ps and adjust the ratio r of the Grüneisen parameters to $r = \gamma_e/\gamma_p = 0.3$ and the damping constant $\eta = 0.15\ \text{ps}^{-1}$ to match the amplitude of the first oscillations. The time constant $\tau_e = 6.5$ ps is found to be close to those previously measured in similar strong perturbation conditions.[38] Figure 3a shows the measured data (open circles) together with the fit according to this model (red line) up to 20 ps. The black dots in Figure 3 represent the difference $\varepsilon_{exp}(t) - \varepsilon_{sim}(t)$ of the data and the simulation. They give an estimate of how much vibrational modes with lower frequency contribute to the out-of-plane expansion of the NTs. Because of the lateral size distribution, we expect that contributions by low-frequency modes rapidly dephase and thus are below the noise level. The left panel of Figure 3b shows simulations with a ratio $r = \gamma_e/\gamma_p$ varied from 0 to 0.6. The best fit is obtained for $r = 0.3$, a value that is smaller than the theoretical ratio expected for bulk gold $r = 0.5$[42] but consistent with other experiments performed on acoustic vibrations of small noble-metal nanoparticles.[43] We note that for $0 < r < 1$ the phase of the oscillation is delayed more and more as r approaches zero. For $r > 1$ the oscillations would start somewhat earlier. Therefore, both the amplitude and the phase of the observed UXRD signal allow us to assess the temporal form of the driving stress $\sigma(t)$.

For larger time delays (right panel), we plot the data on a logarithmic time axis and the red line represents the results of a 3D finite-element model of NT cooling, accounting for both 3D heat diffusion and thermal resistance at the triangle/substrate interface. We simulated a 6.4 nm thick gold triangle with initial temperature $T_i = T_0 + \Delta T$, which is attached to a Si substrate with a fixed temperature of $T_0 = 24$ K at the backside. Initial heating of the absorbing substrate was neglected as it weakly affects the cooling dynamics of the triangle due to the high thermal conductivity of silicon. We take the temperature-dependent bulk values[45−47] of the heat capacity $c_{Au/Si}$ and thermal conductivity $\kappa_{Au/Si}$ for Si and Au and account for the 1 nm thick organic layer by imposing a thermal interface conductance of $G_{th} = 2$ MW/(m^2 K) between Au and Si. This numerical value yields the best fit to the data in the model where a single gold particle is separated from the Si surface by an organic layer. For an epitaxial Au film on Si, one would expect an interface conductance of 50 to 150 MW/(m^2 K), which would lead to a much faster cooling.[48] For convenience, heat diffusion simulations with varying interface conductance are shown in Figure 3c for $t > 20$ ps as thin solid lines. The best fit $G_{th} = 2$ MW/(m^2 K) is shown as a thick line. To estimate the systematic error originating from the model, we also simulated the heat flow out of a "stack" of three gold NTs, which, in addition to the finite Au/Si thermal interface conductance G_{th}, have the same interface conductance between each gold

DOI: 10.1021/acs.jpcc.6b11651
J. Phys. Chem. C 2016, 120, 28894−28899

particle. As a further crosscheck, we have plotted results for "thick" NTs with a triple thickness and with only one interface with G_{th} from the gold to Si. All three models require the heat flow out of the particles to be strongly reduced by the 1 nm organic layer in comparison with a direct contact of Au on Si to achieve a good fit. The interface conductance is considerably lower than the values above 50 MW/(m^2 K) derived for Au–water interfaces with various surface functionalizations[49] and for the interface conductance of Au to Quartz across a self-assembled monolayer.[50,51] The attempt to rationalize the reduced heat flow by a low thermal conductivity of the 1 nm thick 3-MPTMS layer would require a value of 2×10^{-3}W/mK typical of dilute gases. We can therefore conclude that the slow cooling dynamics observed experimentally mostly originates from a low thermal conductance at the Au–Si interface.

CONCLUSIONS

Ultrafast X-ray diffraction measurements on an ensemble of 6.4 nm thick gold NTs directly and quantitatively measure the out-of plane expansion dynamics after optical excitation at 400 nm. The primary oscillatory motion can be explained by a single damped out-of-plane breathing mode with a period of T = 3.6 ps. The phase and amplitude of the UXRD signal are sensitive measures of the functional form $\sigma(t)$ of the time-dependent stress from hot electrons and phonons. The cooling time of several nanoseconds is dictated by the 1 nm thin organic layer that connects the gold-NTs to the silicon substrate. We can rationalize the observations by numerical models. In comparison with the situation expected for a thin gold layer on Si, our experiments demonstrate a slight modification of the relative ratio of the electronic and phononic Grüneisen parameters and a surprisingly strong reduction of heat conduction by a thin organic functional layer. Future UXRD studies on monodisperse asymmetric Au nanoparticles might also be able to quantify the contributions of other vibrational modes and can finally lead to a microscopic understanding of their reshaping under laser excitation. We believe that this pioneering experiment studying the dynamics of nanoparticles with a laser-based femtosecond X-ray source may trigger a broad range of novel experiments, for example, studying the nanoparticle temperature in photocatalytic experiments or during the magnetic heating of nanoparticles for catalysis. We emphasize that the heat-transport characteristics can be obtained by our method via synchrotron-based time-resolved X-ray diffraction, which is accessible for users from any field of natural sciences.

AUTHOR INFORMATION

Corresponding Author

*E-mail: bargheer@uni-potsdam.de. Tel: +49 (0)331 977 4272. Fax: +49 (0)331 977 5493.

ORCID

M. Bargheer: 0000-0002-0952-6602

Notes

The authors declare no competing financial interest.

ACKNOWLEDGMENTS

R.M.S. and F.S. acknowledge financial support by the DFG via the graduate school SALSA, J.P. is supported by the DFG via BA 2281/8-1, and F.L. is supported via KO 1387/14-1.

REFERENCES

(1) Tchebotareva, A.; Ruijgrok, P.; Zijlstra, P.; Orrit, M. Probing the Acoustic Vibrations of Single Metal Nanoparticles by Ultrashort Laser Pulses. *Laser Photonics Reviews* **2010**, *4*, 581–597.
(2) Chen, K.; Razinskas, G.; Feichtner, T.; Grossmann, S.; Christiansen, S.; Hecht, B. Electromechanically Tunable Suspended Optical Nanoantenna. *Nano Lett.* **2016**, *16*, 2680–2685.
(3) Crut, A.; Maioli, P.; Del Fatti, N.; Vallée, F. Time-Domain Investigation of the Acoustic Vibrations of Metal Nanoparticles: Size and Encapsulation Effects. *Ultrasonics* **2015**, *56*, 98–108.
(4) Crut, A.; Maioli, P.; Del Fatti, N.; Vallée, F. Acoustic Vibrations of Metal Nano-Objects: Time-Domain Investigations. *Phys. Rep.* **2015**, *549*, 1–43.
(5) Huang, W.; Qian, W.; El-Sayed, M. A. Coherent Vibrational Oscillation in Gold Prismatic Monolayer Periodic Nanoparticle Arrays. *Nano Lett.* **2004**, *4*, 1741–1747.
(6) Hartland, G. V. Coherent Excitation of Vibrational Modes in Metallic Nanoparticles. *Annu. Rev. Phys. Chem.* **2006**, *57*, 403–430.
(7) Blum, O.; Shaked, N. Prediction of Photothermal Phase Signatures from Arbitrary Plasmonic Nanoparticles and Experimental Verification. *Light: Sci. Appl.* **2015**, *4*, e322.
(8) Cahill, D. G.; Ford, W. K.; Goodson, K. E.; Mahan, G. D.; Majumdar, A.; Maris, H. J.; Merlin, R.; Phillpot, S. R. Nanoscale Thermal Transport. *J. Appl. Phys.* **2003**, *93*, 793–818.
(9) Cahill, D. G.; Braun, P. V.; Chen, G.; Clarke, D. R.; Fan, S.; Goodson, K. E.; Keblinski, P.; King, W. P.; Mahan, G. D.; Majumdar, A.; et al. Nanoscale Thermal Transport. II. 2003–2012. *Appl. Phys. Rev.* **2014**, *1*, 011305.
(10) Hartland, G. V.; Shang Lo, S. Spectroscopy Beyond the Single-Particle Limit. *Science* **2013**, *341*, 36–37.
(11) Sauceda, H. E.; Mongin, D.; Maioli, P.; Crut, A.; Pellarin, M.; Del Fatti, N.; Vallée, F.; Garzón, I. L. Vibrational Properties of Metal Nanoparticles: Atomistic Simulation and Comparison with Time-Resolved Investigation. *J. Phys. Chem. C* **2012**, *116*, 25147–25156.
(12) Juvé, V.; Crut, A.; Maioli, P.; Pellarin, M.; Broyer, M.; Del Fatti, N.; Vallée, F. Probing Elasticity at the Nanoscale: Terahertz Acoustic Vibration of Small Metal Nanoparticles. *Nano Lett.* **2010**, *10*, 1853–1858.
(13) Major, T. A.; Lo, S. S.; Yu, K.; Hartland, G. V. Time-Resolved Studies of the Acoustic Vibrational Modes of Metal and Semiconductor Nano-objects. *J. Phys. Chem. Lett.* **2014**, *5*, 866–874.
(14) Mahmoud, M. A.; O'Neil, D.; El-Sayed, M. A. Shape- and Symmetry-Dependent Mechanical Properties of Metallic Gold and Silver on the Nanoscale. *Nano Lett.* **2014**, *14*, 743–748.
(15) Fedou, J.; Viarbitskaya, S.; Marty, R.; Sharma, J.; Paillard, V.; Dujardin, E.; Arbouet, A. From Patterned Optical Near-Fields to High Symmetry Acoustic Vibrations in Gold Crystalline Platelets. *Phys. Chem. Chem. Phys.* **2013**, *15*, 4205–4213.
(16) Köth, A.; Appelhans, D.; Prietzel, C.; Koetz, J. Asymmetric Gold Nanoparticles Synthesized in the Presence of Maltose-Modified Poly(ethyleneimine). *Colloids Surf., A* **2012**, *414*, 50–56.
(17) Goubet, N.; Yan, C.; Polli, D.; Portalès, H.; Arfaoui, I.; Cerullo, G.; Pileni, M.-P. Modulating Physical Properties of Isolated and Self-Assembled Nanocrystals through Change in Nanocrystallinity. *Nano Lett.* **2013**, *13*, 504–508.
(18) Zijlstra, P.; Orrit, M. Single Metal Nanoparticles: Optical Detection, Spectroscopy and Applications. *Rep. Prog. Phys.* **2011**, *74*, 106401.
(19) Crut, A.; Maioli, P.; Del Fatti, N.; Vallée, F. Optical Absorption and Scattering Spectroscopies of Single Nano-Objects. *Chem. Soc. Rev.* **2014**, *43*, 3921–3956.
(20) Del Fatti, N.; Voisin, C.; Chevy, F.; Vallée, F.; Flytzanis, C. Coherent Acoustic Mode Oscillation and Damping in Silver Nanoparticles. *J. Chem. Phys.* **1999**, *110*, 11484–11487.
(21) Bonacina, L.; Callegari, A.; Bonati, C.; van Mourik, F.; Chergui, M. Time-Resolved Photodynamics of Triangular-Shaped Silver Nanoplates. *Nano Lett.* **2006**, *6*, 7–10.

DOI: 10.1021/acs.jpcc.6b11651
J. Phys. Chem. C 2016, 120, 28894–28899

(22) Ruan, C.-Y.; Murooka, Y.; Raman, R. K.; Murdick, R. A. Dynamics of Size-Selected Gold Nanoparticles Studied by Ultrafast Electron Nanocrystallography. *Nano Lett.* **2007**, *7*, 1290−1296.
(23) Plech, A.; Kürbitz, S.; Berg, K.-J.; Graener, H.; Berg, G.; Grésillon, S.; Kaempfe, M.; Feldmann, J.; Wulff, M.; von Plessen, G. Time-Resolved X-Ray Diffraction on Laser-Excited Metal Nanoparticles. *Europhys. Lett.* **2003**, *61*, 762−768.
(24) Plech, A.; Kotaidis, V.; Grésillon, S.; Dahmen, C.; von Plessen, G. Laser-Induced Heating and Melting of Gold Nanoparticles Studied by Time-Resolved X-Ray Scattering. *Phys. Rev. B: Condens. Matter Mater. Phys.* **2004**, *70*, 195423.
(25) Clark, J. N.; Beitra, L.; Xiong, G.; Higginbotham, A.; Fritz, D. M.; Lemke, H. T.; Zhu, D.; Chollet, M.; Williams, G. J.; Messerschmidt, M.; et al. Ultrafast Three-Dimensional Imaging of Lattice Dynamics in Individual Gold Nanocrystals. *Science* **2013**, *341*, 56−59.
(26) Clark, J. N.; Beitra, L.; Xiong, G.; Fritz, D. M.; Lemke, H. T.; Zhu, D.; Chollet, M.; Williams, G. J.; Messerschmidt, M. M.; Abbey, B.; et al. Imaging Transient Melting of a Nanocrystal using an X-Ray Laser. *Proc. Natl. Acad. Sci. U. S. A.* **2015**, *112*, 7444−7448.
(27) Neighbours, J. R.; Alers, G. A. Elastic Constants of Silver and Gold. *Phys. Rev.* **1958**, *111*, 707−712.
(28) Davletshin, Y. R.; Lombardi, A.; Cardinal, M. F.; Juvé, V.; Crut, A.; Maioli, P.; Liz-Marzán, L. M.; Vallée, F.; Del Fatti, N.; Kumaradas, J. C. A Quantitative Study of the Environmental Effects on the Optical Response of Gold Nanorods. *ACS Nano* **2012**, *6*, 8183−8193.
(29) Pertreux, E.; Lombardi, A.; Florea, I.; Spuch-Calvar, M.; Gómez-Graña, S.; Ihiawakrim, D.; Hirlimann, C.; Ersen, O.; Majimel, J.; Tréguer-Delapierre, M.; et al. Surface Plasmon Resonance of an Individual Nano-Object on an Absorbing Substrate: Quantitative Effects of Distance and 3D Orientation. *Adv. Opt. Mater.* **2016**, *4*, 567−577.
(30) Germain, V.; Li, J.; Ingert, D.; Wang, Z. L.; Pileni, M. P. Stacking Faults in Formation of Silver Nanodisks. *J. Phys. Chem. B* **2003**, *107*, 8717−8720.
(31) Liebig, F.; Thünemann, A.; Koetz, J. Ostwald Ripening Growth Mechanism of Gold Nanotriangles in Vesicular Template Phases. *Langmuir* **2016**, *32*, 10928−10935.
(32) Xie, W.; Walkenfort, B.; Schlücker, S. Label-Free SERS Monitoring of Chemical Reactions Catalyzed by Small Gold Nanoparticles Using 3D Plasmonic Superstructures. *J. Am. Chem. Soc.* **2013**, *135*, 1657−1660.
(33) Schick, D.; Shayduk, R.; Bojahr, A.; Herzog, M.; von Korff Schmising, C.; Gaal, P.; Bargheer, M. Ultrafast Reciprocal-Space Mapping with a Convergent Beam. *J. Appl. Crystallogr.* **2013**, *46*, 1372−1377.
(34) Schick, D.; Bojahr, A.; Herzog, M.; von Korff Schmising, C.; Shayduk, R.; Leitenberger, W.; Gaal, P.; Bargheer, M. Normalization Schemes for Ultrafast X-Ray Diffraction Using a Table-Top Laser-Driven Plasma Source. *Rev. Sci. Instrum.* **2012**, *83*, 025104.
(35) Schick, D.; Bojahr, A.; Herzog, M.; Gaal, P.; Vrejoiu, I.; Bargheer, M. Following Strain-Induced Mosaicity Changes of Ferroelectric Thin Films by Ultrafast Reciprocal Space Mapping. *Phys. Rev. Lett.* **2013**, *110*, 095502.
(36) Nix, F. C.; MacNair, D. The Thermal Expansion of Pure Metals: Copper, Gold, Aluminum, Nickel, and Iron. *Phys. Rev.* **1941**, *60*, 597−605.
(37) McLean, K. O.; Swenson, C. A.; Case, C. R. Thermal Expansion of Copper, Silver, and Gold Below 30 K. *J. Low Temp. Phys.* **1972**, *7*, 77−98.
(38) Del Fatti, N.; Arbouet, A.; Vallée, F. Femtosecond Optical Investigation of Electron-Lattice Interactions in an Ensemble and a Single Metal Nanoparticle. *Appl. Phys. B: Lasers Opt.* **2006**, *84*, 175−181.
(39) Groeneveld, R. H. M.; Sprik, R.; Lagendijk, A. Femtosecond Spectroscopy of Electron-Electron and Electron-Phonon Energy Relaxation in Ag and Au. *Phys. Rev. B: Condens. Matter Mater. Phys.* **1995**, *51*, 11433−11445.
(40) Arbouet, A.; Voisin, C.; Christofilos, D.; Langot, P.; Del Fatti, N.; Vallée, F.; Lermé, J.; Celep, G.; Cottancin, E.; Gaudry, M.; et al. Electron-Phonon Scattering in Metal Clusters. *Phys. Rev. Lett.* **2003**, *90*, 177401.
(41) Kiel, M.; Möhwald, H.; Bargheer, M. Broadband Measurements of the Transient Optical Complex Dielectric Function of a Nanoparticle/Polymer Composite upon Ultrafast Excitation. *Phys. Rev. B: Condens. Matter Mater. Phys.* **2011**, *84*, 165121.
(42) Nicoul, M.; Shymanovich, U.; Tarasevitch, A.; von der Linde, D.; Sokolowski-Tinten, K. Picosecond Acoustic Response of a Laser-Heated Gold-Film Studied with Time-Resolved X-Ray Diffraction. *Appl. Phys. Lett.* **2011**, *98*, 191902.
(43) Voisin, C.; Del Fatti, N.; Christofilos, D.; Vallée, F. Time-Resolved Investigation of the Vibrational Dynamics of Metal Nanoparticles. *Appl. Surf. Sci.* **2000**, *164*, 131−139.
(44) Wright, O. B. Ultrafast Nonequilibrium Stress Generation in Gold and Silver. *Phys. Rev. B: Condens. Matter Mater. Phys.* **1994**, *49*, 9985−9988.
(45) Ho, C. Y.; Powell, R. W.; Liley, P. E. Thermal Conductivity of the Elements. *J. Phys. Chem. Ref. Data* **1972**, *1*, 279−421.
(46) Flubacher, P.; Leadbetter, A.; Morrison, J. The Heat Capacity of Pure Silicon and Germanium and Properties of their Vibrational Frequency Spectra. *Philos. Mag.* **1959**, *4*, 273−294.
(47) Geballe, T. H.; Giauque, W. F. The Heat Capacity and Entropy of Gold from 15 to 300K. *J. Am. Chem. Soc.* **1952**, *74*, 2368−2369.
(48) Duda, J. C.; Yang, C.-Y. P.; Foley, B. M.; Cheaito, R.; Medlin, D. L.; Jones, R. E.; Hopkins, P. E. Influence of Interfacial Properties on Thermal Transport at Gold:Silicon Contacts. *Appl. Phys. Lett.* **2013**, *102*, 081902.
(49) Ge, Z.; Cahill, D. G.; Braun, P. V. Thermal Conductance of Hydrophilic and Hydrophobic Interfaces. *Phys. Rev. Lett.* **2006**, *96*, 186101.
(50) Losego, M.; Grady, M.; Sottos, N.; Cahill, D.; Braun, P. Effects of Chemical Bonding on Heat Transport Across Interfaces. *Nat. Mater.* **2012**, *11*, 502−506.
(51) O'Brien, P.; Shenogin, S.; Liu, J.; Chow, P.; Laurencin, D.; Mutin, P.; Yamaguchi, M.; Keblinski, P.; Ramanath, G. Bonding-Induced Thermal Conductance Enhancement at Inorganic Heterointerfaces Using Nanomolecular Monolayers. *Nat. Mater.* **2012**, *12*, 118−122.

DOI: 10.1021/acs.jpcc.6b11651
J. Phys. Chem. C 2016, 120, 28894−28899

SCIENTIFIC REPORTS

OPEN

The importance of plasmonic heating for the plasmon-driven photodimerization of 4-nitrothiophenol

Received: 12 November 2018
Accepted: 21 December 2018
Published online: 28 February 2019

Radwan M. Sarhan[1,3], Wouter Koopman[1], Roman Schuetz[4], Thomas Schmid[3,5], Ferenc Liebig[2], Joachim Koetz[2] & Matias Bargheer[1,6]

Metal nanoparticles form potent nanoreactors, driven by the optical generation of energetic electrons and nanoscale heat. The relative influence of these two factors on nanoscale chemistry is strongly debated. This article discusses the temperature dependence of the dimerization of 4-nitrothiophenol (4-NTP) into 4,4′-dimercaptoazobenzene (DMAB) adsorbed on gold nanoflowers by Surface-Enhanced Raman Scattering (SERS). Raman thermometry shows a significant optical heating of the particles. The ratio of the Stokes and the anti-Stokes Raman signal moreover demonstrates that the molecular temperature during the reaction rises beyond the average crystal lattice temperature of the plasmonic particles. The product bands have an even higher temperature than reactant bands, which suggests that the reaction proceeds preferentially at thermal hot spots. In addition, kinetic measurements of the reaction during external heating of the reaction environment yield a considerable rise of the reaction rate with temperature. Despite this significant heating effects, a comparison of SERS spectra recorded after heating the sample by an external heater to spectra recorded after prolonged illumination shows that the reaction is strictly photo-driven. While in both cases the temperature increase is comparable, the dimerization occurs only in the presence of light. Intensity dependent measurements at fixed temperatures confirm this finding.

The optical excitation of metal nanoparticles allows novel chemical transformation pathways, unknown in conventional chemical synthesis[1–3]. The mechanism driving these reactions is however still a source of a much controversy. In particular, the relative influences of plasmonic nanoscale heating[4–6] compared to the generation of energetic electrons has been debated[7–10].

Plasmons are coherent oscillations of the nanoparticle conduction-band electrons. Energetic electrons are formed as a consequence of the dephasing of this coherent electron motion – known as plasmon relaxation[11]. Electron-electron scattering subsequently leads to a thermalization of the electron gas, described by the Fermi-Dirac distribution with elevated temperatures[6]. Some of these "hot" energetic electrons might have sufficient energy to populate the orbitals of molecules residing on the particle surface and initiate chemical transformations. This mechanism has been known in the femto-chemistry community for a long time as desorption induced by electron transfer (DIET). It is often considered as primary source for plasmon driven chemistry as well. In femtosecond time-resolved experiments, cooling of the electrons by electron-phonon coupling is observed after few picoseconds, where the energy exchange between the electrons and the phonon mode of the nanoparticles results in an increase of the nanoparticle lattice temperature[12–14]. This heat is dissipated to the surrounding environment on a longer timescale[11]. An important question is whether this excess heat plays a significant role for plasmon driven reactions.

[1]University of Potsdam, Institute of Physics and Astronomy, Karl-Liebknecht-Str. 24-25, 14476, Potsdam, Germany. [2]University of Potsdam, Institute of Chemistry, Karl- Liebknecht- Straße 24-25, 14476, Potsdam, Germany. [3]School of Analytical Sciences Adlershof (SALSA), Humboldt-Universität zu Berlin, Albert-Einstein-Str. 5–9, 10099, Berlin, Germany. [4]Max Planck Institute of Colloids and Interfaces, Department of Biomaterials, Am Mühlenberg 1, 14476, Potsdam, Germany. [5]Federal Institute for Materials Research and Testing, Richard-Willstätter-Str. 11, 12489, Berlin, Germany. [6]Helmholtz Zentrum Berlin, Albert-Einstein-Str. 15, 12489, Berlin, Germany. Correspondence and requests for materials should be addressed to W.K. (email: koopman@uni-potsdam.de)

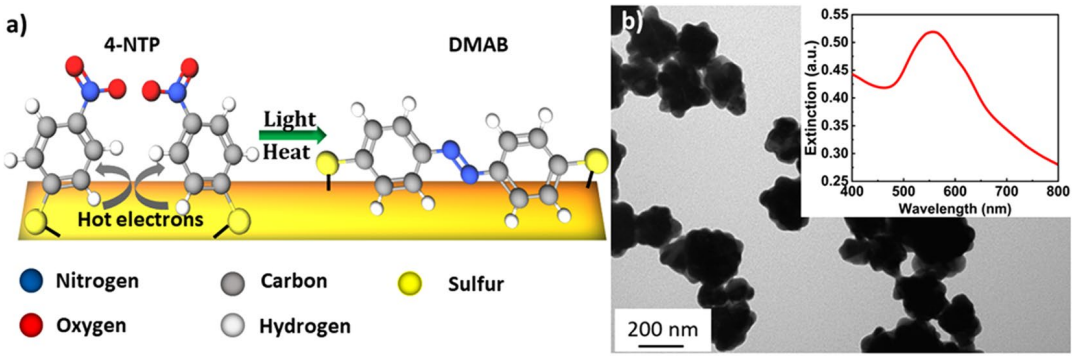

Figure 1. (**a**) Schematic of the chemical structures and the reaction. (**b**) TEM micrograph of gold nanoflowers (GNFs). The inset in (**b**) shows the extinction spectrum of the GNFs.

The dimerization of 4-nitrothiophenol (4-NTP) or 4-aminothiophenol (4-ATP) into 4,4′-dimercaptoazobenzene (DMAB) is considered a model example of plasmon driven reactions (Fig. 1a)[15–18]. Osawa *et al*. observed already in 1994 that SERS spectra of 4-NTP and 4-ATP molecules adsorbed on metal nanoparticles differed remarkably from Raman spectra in bulk powder[19]. It took about 15 years to realize that the molecules undergo a dimerization reaction and that the spectral changes are not the evidence of the chemical-enhancement mechanism of SERS[20]. The presence of DMAB was in the following time experimentally confirmed by surface mass spectrometry[21].

However, these reactions are still a point of debate, since the mechanism of the reaction, and in particular the relative influence of energetic electron generation and nanoscale heating, is unclear[22]. For instance, dimerization of 4-ATP was explained to be driven by the plasmonic-heating process with assistance of the oxygen as the oxidizing agent[23]. However, the reaction was completely inhibited when the ammonium oxalate was added to the reaction medium as a hole-capturer. This suggests that the reaction is driven by a charge-transfer mechanism injecting electrons form the particle to the reactant[24]. On the other hand, *Kwan Kim* and co-worker have measured SERS spectra of 4-NTP adsorbed on silver nanoparticle-substrate at liquid nitrogen temperature (77 K)[8]. The authors showed that hot electrons were efficiently generated at this temperature while they did not observe any reaction signatures, which raised the debate about the role of the operating temperature. It was claimed that either the hot electrons did not have enough energy to reach the molecular orbitals of the adsorbate or the adsorbed molecules might be trapped in the ice crystal which cannot form the dimer form[8]. We may agree with the first reason since the SERS spectra of the 4-ATP molecules showed the vibrational modes of DMAB under the same conditions.

Recently, *Golubev et al*. claimed that plasmonic heating is the key of the plasmonic reaction of 4-NTP[7], while around the same time *Keller and Frontiera* presented evidence produced by ultrafast Raman thermometry that heating is not a primary mechanism for plasmon-driven photocatalysis of 4-NTP[25]. Their experiments suggest that the temperature of the reactant rises only moderately by few ten Kelvin and the heat is dissipated within a few ps. However, no evidence of a substantial formation of products was given so it remains unclear if the reaction conditions were reached in these experiments.

On the other hand, we recently reported an increase of the nanoparticle lattice temperature of about 100 K during irradiation with a CW laser, which was detected by x-ray diffraction monitoring of the thermal expansion[26]. Other publications discuss that a temperature of 150–220 °C leads to bubble-formation in the solvent[27]. Such high temperatures caused by the plasmonic heating were not only reported to initiate chemical reactions of the adsorbed molecule[4], but also to enhance the rate of hot electron-driven reactions[10]. For instance, the visible light-driven degradation of the methylene blue dye was reported on Au-ZnO NRs system[28]. The authors found that under resonant excitation of the system, the local temperature reached to 300 °C, which significantly increased the quantum yield of the degradation. Static Raman thermometry of plasmon driven charge injection into methylene blue even suggest molecular vibrational temperatures of up to 1000 K[29].

In this contribution to the debate, we monitor the dimerization reaction of 4-NTP adsorbed on gold nanoflower-modified silicon substrates at different operating temperature. We show that the rate of the reaction depends on the operating temperature and on the intensity, which on the one hand increases the temperature, but on the other hand increases the number of hot carriers that initiate the reaction. From the Anti-Stokes-Stokes-ratio we measure the *in-situ* molecular and nanoparticle temperature induced by light and find a significant light induced heating of both. Moreover, the average DMAB product molecules are clearly much hotter than the average nanoparticle temperature. We conclude that DMAB forms preferentially at hot spots of the plasmonic excitation SERS sensing. Gradually increasing the operating temperature up to the damage threshold of the sample structure while measuring SERS spectra with very low laser power and very short integration time (resembling the dark environment) we do not observe the dimerization reaction. This is consistent with a plasmon-driven dimerization reaction of the 4-NTP which is mainly initiated by a hot-electron-transfer process, while the high temperature induced by the light only enhances the rate of the reaction. This finding is corroborated by changing the intensity by two orders of magnitude.

Material and Methods

Materials. Hydrogen tetrachloroaurate (III) trihydrate ($HAuCl_4.3H_2O$), 4-nitrothiophenol (4-NTP), and N-(2-Hydroxyethyl)piperazine-N′-(2-ethanesulfonic acid) (HEPES) were purchased from Sigma-Aldrich and used without further purification. Aqueous solutions of the chemicals were prepared using deionized water generated by a Millipore-Q system.

Synthesis of gold nanoflowers (AuNFs). Irregularly shaped gold nanoparticles, previously termed AuNFs in literature, were prepared according to the established procedure[30,31]. Briefly, 200 µl of 100 mM of HEPES buffer solution (pH 7.4 + 0.5) were thoroughly mixed with 1.8 mL water for 5 min. 40 µl of 25 mM aqueous solution of HAuCl4 was then quickly added. The final mixture was left undisturbed for 2 h, during which the color turned from pale yellow to colorless and finally to dark blue confirming the reduction process. The AuNFs were washed several times by centrifugation and finally dispersed in 500 µl water.

Fabrication of SERS-substrate. 1 cm^2 pieces of silicon wafers were cleaned by immersing them in a solution of 30 wt % H_2O_2 and 30 wt % H_2SO_4 for 1 hour. The wafers were then washed in ethanol and water several times before being used. 50 µl of the AuNFs solution was then deposited on the silicon wafer and left to dry for several hours. The 4-NTP molecules were self-assembled by immersion of the nanoflower-fabricated wafer in an ethanolic solution of 5 mM of 4-NTP for 6 h. The wafer was then washed with ethanol and water to remove the unattached molecules before being measured.

Characterization. AuNFs were placed on a carbon-coated copper grid and imaged by transmission electron microscope (JEM-1011, JEOL Japan) operated at an acceleration voltage of 80 kV. A typical TEM image of the particles is shown in Fig. 1b. The extinction spectrum of the AuNFs was measured using a standard UV-Vis spectrometer (VIRIAN CARY 5000) Fig. 1b, inset).

Raman spectra were measured using a confocal Raman microscope (alpha 300; WITec, Ulm, Germany) equipped with a laser excitation of a wavelength at 785 nm. The laser wavelength was chosen such that it lies well separated from any direct vibrionic excitation of the molecules, but still within the plasmon band of the particles. This way photoreactions by direct excitation of the reactant can be exclude. The laser beam was focused on the sample through 10 × (Nikon, NA = 0.25) microscope objective. The spectra were acquired with a thermoelectrically cooled CCD detector (DU401A-BV, Andor, UK) placed behind the spectrometer (UHTS 300; WITec, Ulm, Germany). A Raman band of a silicon wafer at 520 cm^{-1} was used to calibrate the spectrometer. For the temperature dependent Raman measurements, the sample was placed in a closed chamber of a Linkam heating stage where the laser was focused through a transparent window into the sample.

The Raman thermometry was performed by simultaneously recording the Stokes and anti-Stokes Raman spectra using a confocal Raman microscope (JASCO NRS-4100) coupled with a laser excitation of a wavelength of 785 nm at different excitation powers. An intensity calibration delivered by the manufacturer was used to correct the wavelength-dependent sensitivity of the silicon CCD. Different excitation powers were achieved using neutral density filters with a transmission of 0.01%, 0.1% and 1%. That corresponds to laser powers of 20 µW, 150 µW and 1 mW, respectively.

Results and Discussion

Gold nanoflowers (AuNFs) with a diameter of about 60 nm ± 10 nm shown in (Fig. 1b) were prepared using a facile method, where the HEPES buffer was used as the structural-directing and reducing agent. 4-NTP molecules were self-assembled on the surface of the deposited nanoflowers. Plasmonic nanostructures such as the nanoflowers were reported to exhibit a high SERS enhancement owing to their tips, at which the electric field and therefore Raman scattering is enhanced[32–36]. The high signal enhancement enables monitoring of the plasmon-driven dimerization of 4-NTP on both the Stokes and the anti-Stokes spectral range in real time as the reaction proceeds. (Fig. 2a) shows Stokes and anti-Stokes SERS spectra of 4-NTP recorded with low intensity (2.4 kW/cm^2), with no indication of the reaction product. The spectrum is dominated by the main Raman peaks of 4-NTP at 1082, 1332, and 1575 cm^{-1}, assigned to the C−H bending, NO_2 symmetric stretching, and C = C stretching modes of 4-NTP, respectively[37]. Increasing the laser intensity (127 kW/cm^2) induces the dimerization reaction as evidenced by the Raman peaks of DMAB. (Fig. 2b) displays SERS spectra of 4-NTP measured with an integration time of 1 second, showing the reaction product in both the Stokes and the anti-Stokes regions, where peaks at 1134, 1387, and 1434 cm^{-1} assigned to the C−N symmetric stretching and N=N stretching vibrational modes of DMAB (marked with black arrows)[38,39].

From the intensity ratio I_{AS}/I_S of the anti-Stokes and Stokes SERS spectra we determined the temperature $T_{vib} = \frac{-h\nu}{k_B \ln\left(\frac{I_{AS}}{C \cdot I_S}\right)}$ for the vibrational band at the frequency ν during the reaction[40]. Here, $C = \left(\frac{\nu_L + \nu}{\nu_L - \nu}\right)^4$ describes the dependence of the Raman scattering on the laser frequency ν_L . The temperature of the 4-NTP bands increases from room temperature for excitation with 2.4 kW/cm^2 and 127 kW/cm^2 by about $\Delta T_{vib,4NTP} = 60\ K$ and 200 K, respectively. As we will discuss later in Fig. 3b, 200 K temperature increase during the reaction by stationary heating strongly enhances the reaction rate.

In order to visualize the accuracy of the temperature assignment, we plot the Stokes Raman signal on top of an anti-Stokes Raman signal, which has been intensity-scaled according to $I_{AS} = C \cdot I_S e^{\frac{h\nu}{k_B T_{vib}}}$ after subtracting a constant background. Subtracting inelastic light scattering according to the Fermi-Dirac statistics does not considerably change our conclusion[29,41]. More important is the striking systematic intensity increase of the DMAB bands in the anti-Stokes spectra which in fact would be consistent with a considerably higher vibrational temperature rise of $\Delta T_{vib,DMAB} = 350K$. A possible explanation for this temperature difference between reactant and product is that the reaction preferentially proceeds at the hot spots.

To compare the vibrational temperatures of the molecule to the electron temperature of the nanoparticle, we made use of the observation by the Boerigter *et al.* that the anti-Stokes background intensity measures the rate anti-Stokes shifted photons scattered from the Fermi-Dirac distributed electrons in the nanoparticle[29]. Following their procedure, we fitted the anti-Stokes background by $I_{AS,bg} = I_0[e^{h\nu/k_B T} + 1]^{-1}$, were I_0 is the background at

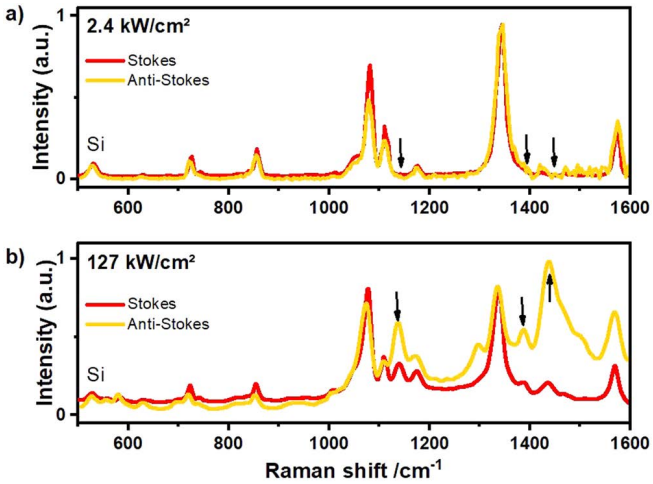

Figure 2. SERS spectra of 4-NTP recorded in both the Stokes and the anti-Stokes regions for an intensity of (**a**) 2.4 kW/cm^2 and (**b**) 127 kW/cm^2. The anti-Stokes region has been temperature adapted using the temperature of the 1332 cm^{-1} peak for comparison to the Stokes spectrum as discussed in the text.

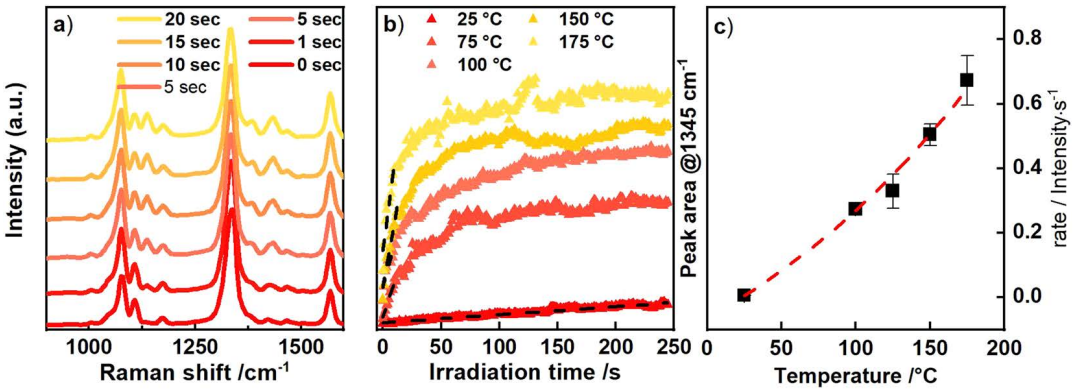

Figure 3. (**a**) SERS spectra of 4-NTP after different irradiation times with a laser intensity of 25.5 kW/cm^2 (**a**) at a bath temperature of T = 293 K. (**b**) Kinetics of the product extracted from the peak area at 1345 cm^{-1} in a) for different temperatures. The NT temperature is around 75 K higher than the external heating temperature indicated in the legend. (**c**) Rates extracted from kinetics in (**b**) (fitting indicated in (**b**) by dashed lines).

$\nu = 0$. At 2.4 kW/cm^2 excitation the temperature rise of the particle was with $\Delta T_{NP} \approx 60\ K$ approximately identical to the vibrational temperature of the molecules. For the higher excitation intensity of 127 kW/cm^2 , on the other hand, the electron temperature of the particle rises with $\Delta T_{NP} \approx 150\ K$, which is significantly less than the temperature of both 4NTP and DMAB, but in good agreement with recent measurements of the phonon temperature of the nanoparticles under laser irradiation by X-ray diffraction[26]. In both high and low intensity measurements, the particle temperature is roughly identical with the temperature of the silicon substrate, which could be determined from the prominent Si peak at $\nu_{Si} = 550 cm^{-1}$. Evidently, the molecular vibrational occupation is not in equilibrium with the particles, while the particles are in thermal equilibrium with the substrate phonons.

Since the particle temperature is approximately identical to the substrate temperature, we investigated the influence of the temperature on the product formation, by time-dependent SERS measurements recorded while heating the substrate with an external heater to 25, 75, 100, 150 and 175 °C, respectively. The sample was held in a closed chamber of the Linkam stage and the temperature was automatically controlled. The temperatures were chosen, such that the higher temperatures were similar to the particle temperatures obtained by pure laser heating. Despite the similar particle temperatures, the observed reactant temperatures could not be reproduced by external heating of the sample, since for $\Delta T_{heater} \geq 175\ K$ the particles started to melt. By using an intensity of 25.5 kW/cm^2, the lowest intensity for which we obtained a clearly visible DMAB signal, we kept laser heating to the minimum possible. From the values for laser heating discussed earlier, we estimate an additional laser heating at this intensity of roughly $\Delta T_{Laser} = 75\ K$.

We exemplify the evolution of the reaction product at room temperature by SERS spectra taken after different laser irradiation times (Fig. 3a). The increase of the peak area at 1134 cm^{-1}, i.e. the formation of the number of reaction products, is shown for all bath temperatures in Fig. 3b. We estimated the temperature dependence of the kinetic rate, by fitting the initial product increase with a linear function (Fig. 3c). The zero-order rate extracted

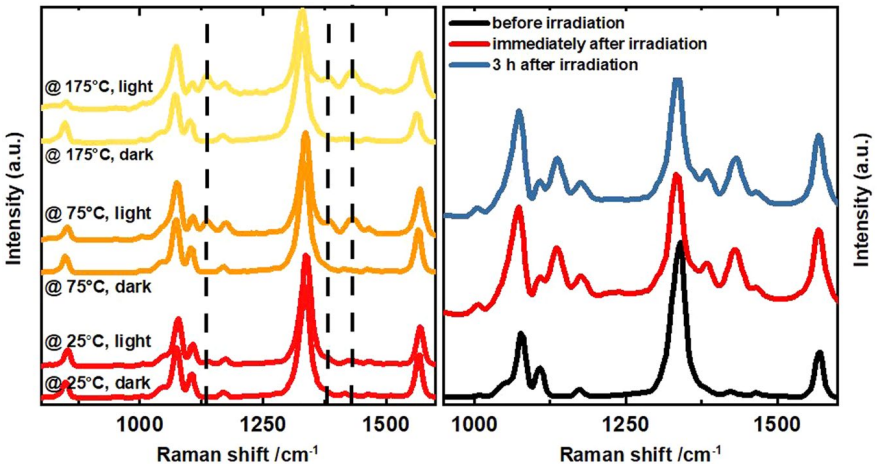

Figure 4. (**a**) Temperature dependent SERS of 4-NTP measured with 2.44 kW/cm² intensity Raman laser after keeping the sample spot under dark (no light) and bright (25.4 kW/cm² for 5 min) conditions. SERS spectra measured with an intensity of 2.4 kW/cm². (**b**) SERS spectra of 4-NTP confirming the stability of the DMAB product.

this way follows an exponential dependence of the temperature indicating that the reaction has an Arrhenius-type behavior. The activation energy however cannot be calculated without knowing the Raman cross-section of the reactant molecules. Qualitatively, the rate-temperature plot shows that heating the setup by $\Delta T_{heater} = 150$ K enhances the reaction rate by two orders of magnitude.

Simultaneous to DMAB peak increase, the NO_2 Raman peak of the 4-NTP at 1332 cm^{-1} gradually decreases, confirming the loss of reactants required for the dimerization reaction (Fig. 3a). However, when the intensity of the DMAB peak is saturated about 70% of the 4-NTP intensity remains. Thus the reaction can only proceed for a small fraction of the molecules on the AuNF surface, and probably the SERS enhancement even biases our observation towards those molecules which receive the highest light intensity. This observation further strengthens the argument that the reaction indeed takes place at hot spots only.

Since temperature turns out to be an important parameter for the reaction, we attempted to drive the reaction solely by supplying heat. The sample was heated by the external heater stage keeping the sample in the dark. (Fig. 4a) displays temperature-dependent SERS spectra captured with very low excitation intensity and integration time (2.4 kW/cm^2 and 0.5 s), after keeping the sample for 5 min at constant elevated temperature in the dark. These measurement conditions guarantee that the dimerization of 4-NTP can only be driven by heat, while the influence of the laser on the reaction process is kept to a minimum. None of these dark measurements in Fig. 4a show any signature of DMAB formation. Even considering the laser heating ($\Delta T_{laser} = 75\ K$), a clear reaction was observed in Fig. 3b at the same nanoparticle temperature.

A further control sequence of SERS spectra taken under the same conditions, except that during the 5 min the sample was continuously irradiated by 25.5 kW/cm², show pronounced peaks related to the reaction product (DMAB) at high temperatures (Fig. 4a). In a second control experiment we irradiated the solution of the 4-NTP molecules without the gold nanoflowers with high laser intensity for a long irradiation time. No reaction product bands were observed (NOT SHOWN).

Finally, we confirm that DMAB is a stable product in the dark and the reaction is not reversible when the light is switched off for several hours. The SERS spectrum is unmodified when switching the laser off for 3 hours as shown in (Fig. 4b).

Combining Figs 2 and 4 we see that a room temperature experiment, where light-driven heating leads to a nanoparticle heating of about 150 K, shows a large reaction yield within 1 second, whereas keeping the system at 175 K in the dark for 5 minutes does not produce the faintest signature of the product. These data confirm that the dimerization reaction is initiated by photons, probably by providing energetic electrons which are not thermalized to the Au lattice temperature[42,43]. The heating of the Au lattice and the molecular vibrations by a heating stage or by absorption of the photons by the particle only enhances the reaction rate.

To summarize, our experiments show that the dimerization reaction of 4-NTP on AuNFs cannot be triggered by normal heating. The AuNFs melt at temperatures above 473 K and the Raman signal breaks down (NOT shown). If the AuNFs are heated by laser irradiation, the reaction proceeds although the vibrational temperature of the Au lattice and of the molecules stays below 473 K. This suggests that the electron system in the AuNFs is not in a thermal equilibrium with the lattice, thus providing energetic electrons which can initiate the reaction. It is experimentally very difficult to precisely investigate this reaction in a systematic sequence of experiments, since it is irreversible and each new spot on the plasmonic template may have different hot spots, which will lead to a broad distribution of field enhancement. Therefore, we could not check the functional dependence of the reaction rate on the light intensity.

To give at least some quantification of the strongly nonlinear character of the reaction, we show in Fig. 5A series of experiments at room temperature, where spots with similar field enhancement have seen a similar total number of photons, however at drastically different intensities. Figure 5A confirms the absence of DMAB for an

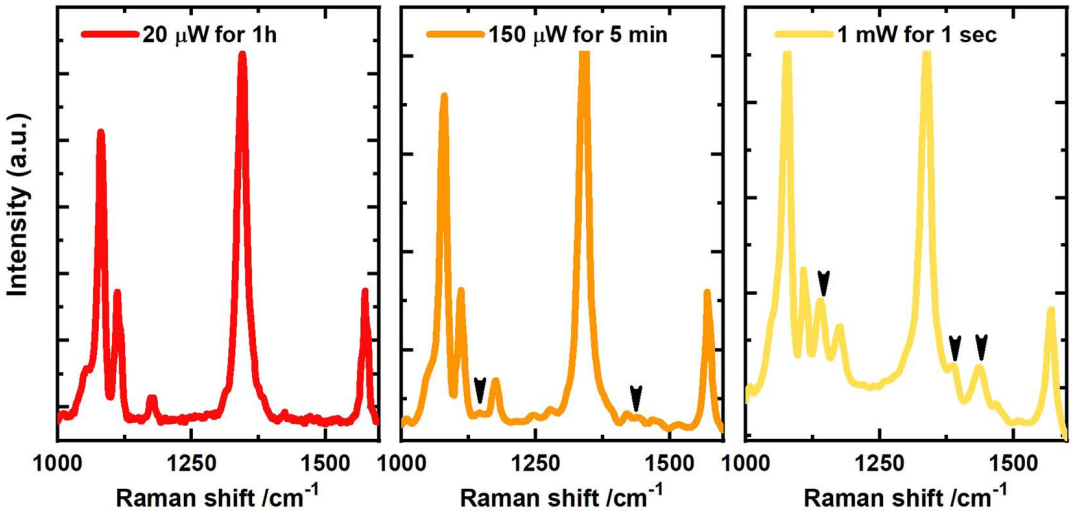

Figure 5. Comparing the product yield for the same number of photons and reactants. (**A**,**B**) show spectra recorded with the same integral photon number, however, at 10 times different power and integration time. (**C**) shows a spectrum after irradiation with 30 times less photons, however, at 10 times increased laser power.

intensity of 2.4 kW/cm^2 even after irradiation for 60 min. Increasing the laser intensity by a factor of 8 (19 kW/cm^2) and reducing the irradiation time by the same factor yields tiny DMAB peaks already. Increasing the intensity by another factor of 7 (127.4 kW/cm^2) yields a dramatic increase of the signal after 1 second, although the same integral photon number would be reached after 30 seconds.

In order to rationalize that there might be a non-thermalized electron distribution, which either does not have the same temperature as the lattice and the molecular vibrations, or may even not be described by a Fermi-Dirac distribution, we recall the electron-phonon coupling time of 1 ps typically observed in Au nanoparticles by femtosecond laser-spectroscopy[25] or ultrafast x-ray diffraction[44]. Next we calculate that under the relevant intensity of 240 kW/cm^2, each nanoparticle with a diameter of 70 nm is hit by a photon every 200 fs. Although not all photons impinging on the nanoparticle are absorbed, we believe that at least around hot spots of the plasmonic structure, the photons are absorbed faster than their energy is dissipated by *e-ph* interaction.

Conclusion

In summary, we have observed the temperature dependence of the dimerization reaction of 4-NTP to DMAB. Simultaneous measurement of the Stokes and the anti-Stokes regions of the SERS spectrum enabled the *in-situ* temperature measurements under the reaction conditions. The average temperature of the product is larger than that of the reactant because the reaction proceeds preferentially at hot spots. Both measured vibrational temperatures exceed the temperature of the nanoparticles crystal lattice, in good agreement with previous findings[29]. We think that the temperature of the electrons and lattice at the Au tips is reduced on the femtosecond timescale by heat transport within the metal, whereas the cooling of the molecules proceeds slower by vibrational interactions. This corroborates the hypothesis that hot electrons emitted from the tips trigger the dimerization reaction, since the temperature within Au is smaller than the molecular temperature and vibrational heat alone could be ruled out as the driving mechanism. Nonetheless, the reaction rate can be increased by an order of magnitude by stationary heating of 150 K, which implies that the effect of vibrational temperature cannot be neglected when analyzing this plasmon driven reaction. Clearly it is not the total number of absorbed photons which is relevant but rather the collective action of several photons is required for triggering the reaction.

Data Availability

The datasets generated and analyzed during the current study are available from the corresponding author on reasonable request.

References

1. Cortés, E. Activating plasmonic chemistry. *Science (New York, N.Y.)* **362**, 28–29, https://doi.org/10.1126/science.aav1133 (2018).
2. Zhang, X. *et al*. Product selectivity in plasmonic photocatalysis for carbon dioxide hydrogenation. *Nature communications* **8**; https://doi.org/10.1038/ncomms14542 (2017).
3. Kazuma, E., Jung, J., Ueba, H., Trenary, M. & Kim, Y. Real-space and real-time observation of a plasmon-induced chemical reaction of a single molecule. *Science (New York, N.Y.)* **360**, 521–526, https://doi.org/10.1126/science.aao0872 (2018).
4. Adleman, J. R., Boyd, D. A., Goodwin, D. G. & Psaltis, D. Heterogenous catalysis mediated by plasmon heating. *Nano letters* **9**, 4417–4423, https://doi.org/10.1021/nl902711n (2009).
5. Kale, M. J., Avanesian, T. & Christopher, P. Direct Photocatalysis by Plasmonic Nanostructures. *ACS Catal.* **4**, 116–128, https://doi.org/10.1021/cs400993w (2013).
6. Linic, S., Aslam, U., Boerigter, C. & Morabito, M. Photochemical transformations on plasmonic metal nanoparticles. *Nature materials* **14**, 567–576, https://doi.org/10.1038/nmat4281 (2015).
7. Golubev, A. A., Khlebtsov, B. N., Rodriguez, R. D., Chen, Y. & Zahn, D. R. T. Plasmonic Heating Plays a Dominant Role in the Plasmon-Induced Photocatalytic Reduction of 4-Nitrobenzenethiol. *J. Phys. Chem. C* **122**, 5657–5663, https://doi.org/10.1021/acs.jpcc.7b12101 (2018).

8. Kim, K., Choi, J.-Y. & Shin, K. S. Surface-Enhanced Raman Scattering of 4-Nitrobenzenethiol and 4-Aminobenzenethiol on Silver in Icy Environments at Liquid Nitrogen Temperature. *J. Phys. Chem. C* **118**, 11397–11403, https://doi.org/10.1021/jp5015115 (2014).
9. Miao, P. *et al*. Photothermally Enhanced Plasmon-Driven Catalysis on Fe 5 C 2 @Au Core-Shell Nanostructures. *ChemCatChem* **10**, 1084–1088, https://doi.org/10.1002/cctc.201701901 (2018).
10. Zhang, X. *et al*. Plasmon-Enhanced Catalysis. Distinguishing Thermal and Nonthermal Effects. *Nano letters* **18**, 1714–1723, https://doi.org/10.1021/acs.nanolett.7b04776 (2018).
11. Keller, E. L., Brandt, N. C., Cassabaum, A. A. & Frontiera, R. R. Ultrafast surface-enhanced Raman spectroscopy. *The Analyst* **140**, 4922–4931, https://doi.org/10.1039/c5an00869g (2015).
12. Fedoruk, M., Meixner, M., Carretero-Palacios, S., Lohmüller, T. & Feldmann, J. Nanolithography by plasmonic heating and optical manipulation of gold nanoparticles. *ACS nano* **7**, 7648–7653, https://doi.org/10.1021/nn402124p (2013).
13. Jonsson, G. E., Miljkovic, V. & Dmitriev, A. Nanoplasmon-enabled macroscopic thermal management. *Scientific reports* **4**, 5111, https://doi.org/10.1038/srep05111 (2014).
14. Neumann, O. *et al*. Solar vapor generation enabled by nanoparticles. *ACS nano* **7**, 42–49, https://doi.org/10.1021/nn304948h (2013).
15. Chu, J. *et al*. Ultrafast Surface-Plasmon-Induced Photodimerization of p -Aminothiophenol on Ag/TiO 2 Nanoarrays. *Chem Cat Chem* **8**, 1819–1824, https://doi.org/10.1002/cctc.201600172 (2016).
16. Li, P., Ma, B., Yang, L. & Liu, J. Hybrid single nanoreactor for *in situ* SERS monitoring of plasmon-driven and small Au nanoparticles catalyzed reactions. *Chemical communications (Cambridge, England)* **51**, 11394–11397, https://doi.org/10.1039/c5cc03792a (2015).
17. Xie, W. & Schlücker, S. Hot electron-induced reduction of small molecules on photorecycling metal surfaces. *Nature communications* **6**, 7570, https://doi.org/10.1038/ncomms8570 (2015).
18. Xie, W. & Schlücker, S. Surface-enhanced Raman spectroscopic detection of molecular chemo- and plasmo-catalysis on noble metal nanoparticles. *Chemical communications (Cambridge, England)* **54**, 2326–2336, https://doi.org/10.1039/c7cc07951f (2018).
19. Osawa, M., Matsuda, N., Yoshii, K. & Uchida, I. Charge transfer resonance Raman process in surface-enhanced Raman scattering from p-aminothiophenol adsorbed on silver: Herzberg-Teller contribution. *J. Phys. Chem.* **98**, 12702–12707, https://doi.org/10.1021/j100099a038 (1994).
20. Wu, D.-Y. *et al*. Surface Catalytic Coupling Reaction of p -Mercaptoaniline Linking to Silver Nanostructures Responsible for Abnormal SERS Enhancement: A DFT Study. *J. Phys. Chem. C* **113**, 18212–18222, https://doi.org/10.1021/jp9050929 (2009).
21. Huang, Y.-F. *et al*. When the signal is not from the original molecule to be detected. Chemical transformation of para-aminothiophenol on Ag during the SERS measurement. *Journal of the American Chemical Society* **132**, 9244–9246, https://doi.org/10.1021/ja101107z (2010).
22. Kang, L. *et al*. Laser wavelength- and power-dependent plasmon-driven chemical reactions monitored using single particle surface enhanced Raman spectroscopy. *Chemical communications (Cambridge, England)* **49**, 3389–3391, https://doi.org/10.1039/c3cc40732b (2013).
23. Xu, P. *et al*. Mechanistic understanding of surface plasmon assisted catalysis on a single particle. Cyclic redox of 4-aminothiophenol. *Scientific reports* **3**, 2997, https://doi.org/10.1038/srep02997 (2013).
24. Yan, X., Wang, L., Tan, X., Tian, B. & Zhang, J. Surface-Enhanced Raman Spectroscopy Assisted by Radical Capturer for Tracking of Plasmon-Driven Redox Reaction. *Scientific reports* **6**, 30193, https://doi.org/10.1038/srep30193 (2016).
25. Keller, E. L. & Frontiera, R. R. Ultrafast Nanoscale Raman Thermometry Proves Heating Is Not a Primary Mechanism for Plasmon-Driven Photocatalysis. *ACS nano*. https://doi.org/10.1021/acsnano.8b01809 (2018).
26. Liebig, F. *et al*. Deposition of Gold Nanotriangles in Large Scale Close-Packed Monolayers for X-ray-Based Temperature Calibration and SERS Monitoring of Plasmon-Driven Catalytic Reactions. *ACS applied materials & interfaces* **9**, 20247–20253, https://doi.org/10.1021/acsami.7b07231 (2017).
27. Baffou, G., Polleux, J., Rigneault, H. & Monneret, S. Super-Heating and Micro-Bubble Generation around Plasmonic Nanoparticles under cw Illumination. *J. Phys. Chem. C* **118**, 4890–4898, https://doi.org/10.1021/jp411519k (2014).
28. Bora, T., Zoepfl, D. & Dutta, J. Importance of Plasmonic Heating on Visible Light Driven Photocatalysis of Gold Nanoparticle Decorated Zinc Oxide Nanorods. *Scientific reports* **6**, 26913, https://doi.org/10.1038/srep26913 (2016).
29. Boerigter, C., Aslam, U. & Linic, S. Mechanism of Charge Transfer from Plasmonic Nanostructures to Chemically Attached Materials. *ACS nano* **10**, 6108–6115, https://doi.org/10.1021/acsnano.6b01846 (2016).
30. Cui, Q. *et al*. Fabrication of bifunctional gold/gelatin hybrid nanocomposites and their application. *ACS applied materials & interfaces* **6**, 1999–2002, https://doi.org/10.1021/am5000068 (2014).
31. Xie, J., Zhang, Q., Lee, J. Y. & Wang, D. I. C. The synthesis of SERS-active gold nanoflower tags for *in vivo* applications. *ACS nano* **2**, 2473–2480, https://doi.org/10.1021/nn800442q (2008).
32. Yang, W. *et al*. Self-Assembled Plasmonic Pyramids from Anisotropic Nanoparticles for High-Efficient SERS. *J. Anal. Test.* **1**, 335–343, https://doi.org/10.1007/s41664-017-0033-5 (2017).
33. Reguera, J., Langer, J., Jiménez de Aberasturi, D. & Liz-Marzán, L. M. Anisotropic metal nanoparticles for surface enhanced Raman scattering. *Chemical Society reviews* **46**, 3866–3885, https://doi.org/10.1039/c7cs00158d (2017).
34. Li, Q. *et al*. High surface-enhanced Raman scattering performance of individual gold nanoflowers and their application in live cell imaging. *Small (Weinheim an der Bergstrasse, Germany)* **9**, 927–932, https://doi.org/10.1002/smll.201201065 (2013).
35. Liu, D. *et al*. Rapid synthesis of monodisperse Au nanospheres through a laser irradiation-induced shape conversion, self-assembly and their electromagnetic coupling SERS enhancement. *Scientific reports* **5**, 7686, https://doi.org/10.1038/srep07686 (2015).
36. Liu, D. *et al*. Black Gold: Plasmonic Colloidosomes with Broadband Absorption Self-Assembled from Monodispersed Gold Nanospheres by Using a Reverse Emulsion System. *Angewandte Chemie (International ed. in English)* **54**, 9596–9600, https://doi.org/10.1002/anie.201503384 (2015).
37. Liebig, F. *et al*. Undulated Gold Nanoplatelet Superstructures. *In Situ* Growth of Hemispherical Gold Nanoparticles onto the Surface of Gold Nanotriangles. *Langmuir: the ACS journal of surfaces and colloids* **34**, 4584–4594, https://doi.org/10.1021/acs.langmuir.7b02898 (2018).
38. Dong, B., Fang, Y., Chen, X., Xu, H. & Sun, M. Substrate-, wavelength-, and time-dependent plasmon-assisted surface catalysis reaction of 4-nitrobenzenethiol dimerizing to p,p'-dimercaptoazobenzene on Au, Ag, and Cu films. *Langmuir: the ACS journal of surfaces and colloids* **27**, 10677–10682, https://doi.org/10.1021/la2018538 (2011).
39. Kang, L. *et al*. *In Situ* Surface-Enhanced Raman Spectroscopy Study of Plasmon-Driven Catalytic Reactions of 4-Nitrothiophenol under a Controlled Atmosphere. *Chem Cat Chem* **7**, 1004–1010, https://doi.org/10.1002/cctc.201403032 (2015).
40. Sun, M., Zhang, Z., Zheng, H. & Xu, H. *In-situ* plasmon-driven chemical reactions revealed by high vacuum tip-enhanced Raman spectroscopy. *Scientific reports* **2**, 647, https://doi.org/10.1038/srep00647 (2012).
41. Hugall, J. T. & Baumberg, J. J. Demonstrating photoluminescence from Au is electronic inelastic light scattering of a plasmonic metal. The origin of SERS backgrounds. *Nano letters* **15**, 2600–2604, https://doi.org/10.1021/acs.nanolett.5b00146 (2015).
42. Cortés, E. *et al*. Plasmonic hot electron transport drives nano-localized chemistry. *Nature communications* **8**, 14880, https://doi.org/10.1038/ncomms14880 (2017).
43. Kim, M., Lin, M., Son, J., Xu, H. & Nam, J.-M. Hot-Electron-Mediated Photochemical Reactions: Principles, Recent Advances, and Challenges. *Advanced Optical Materials* **5**, 1700004, https://doi.org/10.1002/adom.201700004 (2017).
44. Reppert, Avon *et al*. Watching the Vibration and Cooling of Ultrathin Gold Nanotriangles by Ultrafast X-ray Diffraction. *J. Phys. Chem. C* **120**, 28894–28899, https://doi.org/10.1021/acs.jpcc.6b11651 (2016).

Acknowledgements
We acknowledge the support of the Deutsche Forschungsgemeinschaft and Open Access Publishing Fund of University of Potsdam. Radwan M. Sarhan gratefully acknowledges the financial support from the School of Analytical Science Adlershof (SALSA).

Author Contributions
Radwan M. Sarhan, Wouter Koopman and Matias Bargheer wrote the main manuscript text. Radwan M. Sarhan, Wouter Koopman contributed to the preparation of all figures. Radwan M. Sarhan, Wouter Koopman, Roman Schuetz and Thomas Schmid contributed to the Raman data acquisition and the preparation of Figs 2–5. Ferenc Liebig has prepared Fig. 1b and contributed to section 2. Joachim Koetz and Matias Bargheer supervised the work.

Additional Information
Competing Interests: The authors declare no competing interests.

Publisher's note: Springer Nature remains neutral with regard to jurisdictional claims in published maps and institutional affiliations.

THE JOURNAL OF PHYSICAL CHEMISTRY C

Article

Cite This: J. Phys. Chem. C 2019, 123, 9352−9357

pubs.acs.org/JPCC

Scaling Up Nanoplasmon Catalysis: The Role of Heat Dissipation

Radwan M. Sarhan,[†,§] Wouter Koopman,[*,†] Jan Pudell,[†] Felix Stete,[†,§] Matthias Rössle,[∥] Marc Herzog,[†] Clemens N. Z. Schmitt,[⊥] Ferenc Liebig,[‡] Joachim Koetz,[‡] and Matias Bargheer[†,∥]

[†]Institute of Physics and Astronomy and [‡]Institute of Chemistry, University of Potsdam, 14476 Potsdam, Germany

[§]School of Analytical Sciences Adlershof (SALSA), Humboldt-Universita¨t zu Berlin, Albert-Einstein-Str. 5-9, 10099 Berlin, Germany

[∥]Helmholtz Zentrum Berlin, Albert-Einstein-Straße 15, 12489 Berlin, Germany

[⊥]Max Planck Institute of Colloids and Interfaces, 14476 Potsdam, Germany

Supporting Information

ABSTRACT: Nanoscale heating by optical excitation of plasmonic nanoparticles offers a new perspective of controlling chemical reactions, where heat is not spatially uniform as in conventional macroscopic heating but strong temperature gradients exist around microscopic hot spots. In nanoplasmonics, metal particles act as a nanosource of light, heat, and energetic electrons driven by resonant excitation of their localized surface plasmon resonance. As an example of the coupling reaction of 4-nitrothiophenol into 4,4′-dimercaptoazobenzene, we show that besides the nanoscopic heat distribution at hot spots, the microscopic distribution of heat dictated by the spot size of the light focus also plays a crucial role in the design of plasmonic nanoreactors. Small sizes of laser spots enable high intensities to drive plasmon-assisted catalysis. This facilitates the observation of such reactions by surface-enhanced Raman scattering, but it challenges attempts to scale nanoplasmonic chemistry up to large areas, where the excess heat must be dissipated by one-dimensional heat transport.

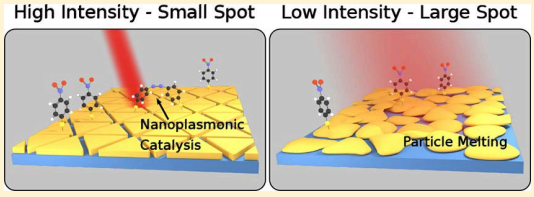

INTRODUCTION

Thermoplasmonics is a recently developed field of research, which started in 2002 for medical purposes.[1] Metal nanoparticles (NPs) have been used as a nanosource of heat for several applications such as photothermal cancer therapy,[2−5] bioimaging,[6] and nanosurgery.[7] Likewise, chemistry can benefit from nanoplasmonics, since many chemical reactions are heavily influenced by heat.[8−11]

Plasmonic metal nanostructures can be tuned to efficiently interact with light, converting the photons' energy into energetic charge carriers and heat. This allows noble metal nanoparticles to act as nanoreactors.[12] Chemical transformations of molecules attached to the particles' surfaces are fostered by the enhanced electromagnetic field at the particle surface along with generated energetic charge carriers and heat. As a result, plasmonic NPs present a unique playground for steering chemical transformation by light at the nanoscale.[13]

The first indications of nanoplasmonic chemistry were discovered in investigations using a micro-Raman apparatus to study surface enhanced Raman scattering (SERS) activity on nanoparticle templates.[14−16] In several microscope-based SERS experiments, the photons used for the Raman spectroscopy happen to also drive a catalytic reaction.[17−19] Recently, several important reaction types have been reported to be driven or catalyzed by plasmonic NPs such as the decomposition of organic molecules,[20,21] dissociation of hydrogen,[22,23] and oxidation−reduction reactions.[24,25]

In the current understanding, these chemical transformations are initialized by photogenerated energetic electrons. In addition, several studies have shown that the heat deposited in the particles by optical excitation enhances the reactions.[26−29] Heating by optical excitation of NPs is different from the conventional macroscopic heating because the heated volume is confined to certain hot spots or to the nanoparticle size. This may be exploited for controlling reactions at the nanometer scale and at specific locations. Around hot spots the cooling is generally three-dimensional (3D) and hence for low NP concentrations the heat can be quickly dissipated. Studying this nanoparticle heating is however rather difficult, as nanoscale thermometers are required.

In this article, we provide experimental evidence that removal of excess heat from the nanoscopic reaction site is a crucial factor for successful plasmonic chemistry, more importantly, for scaling up the plasmonic catalysis. In particular, the cooling geometry and the heat conductivity of the structure limits the maximum area of the plasmon-driven reaction, given by the spot size of the optical excitation. On the one hand, the light intensity (power per unit area) must have a minimum value to trigger plasmon-assisted catalytic reaction, but at the same time, the maximum power (not intensity) is limited by NP melting and/or destruction of the reactant or product molecules by excessive laser-driven static heating.

Received: December 31, 2018
Revised: March 7, 2019
Published: March 11, 2019

DOI: 10.1021/acs.jpcc.8b12574
J. Phys. Chem. C 2019, 123, 9352−9357

We investigated the static heating imposed on gold nanotriangles (NTs) by optical excitation by monitoring the shift of the nanoparticles' Bragg reflection via synchrotron-based X-ray diffraction (XRD). Subsequently, we verified, by SERS microscopy at very low light intensity, whether the plasmon-assisted reaction took place. Our measurements show that for small laser excitation spot sizes, the product formation could proceed, whereas for large spot sizes for the same light intensities, the SERS spectrum completely vanished. We reason that for microscopic excitation spot sizes, the deposited heat can be dissipated into a half sphere of the substrate in all three dimensions. In contrast, for very large excitation areas, the heat transport into the substrate is only in one dimension and therefore less effective. Therefore, the heat is trapped in the substrate for a much longer time, which enables melting of the plasmonic particles (the reaction platform). XRD measurements of the nanotriangles' lattice constant confirm that small laser excitation spot sizes lead to a lower temperature increase compared to the large spots for the same incident intensity. The faster rate of the 3D heat dissipation in a small excitation spot allows the excitation of the system with high light intensities necessary for the formation of the reaction product. In contrast, slower one-dimensional (1D) heat dissipation perpendicular to the substrate plane occurs for large spots sizes. The less efficient heat removal leads to higher temperatures and melting of the nanotriangles, as confirmed by scanning electron microscopy (SEM).

This phenomenon does not only explain the great success of observing plasmon-driven chemical reaction in SERS microscopes but also simultaneous absence of experiments evidencing plasmon-driven reactions over large surface areas. It also hints at the main advantage of nanoplasmonics for controlling chemical reactions, since unprecedented large heat dissipation rates can be found in a narrow spatial region of the hot spots.

MATERIALS AND EXPERIMENTAL METHODS

We used the plasmon-driven dimerization of 4-nitrothiophenol (4-NTP) into 4,4′-dimercaptoazobenzene (DMAB) as a model reaction.[30−32] This reaction is known to occur only in the presence of a plasmonic platform such as gold, silver, and copper nanoparticles.[33,34] The reaction is reasoned to occur as a result of the hot electrons generated upon the plasmon excitation,[35−37] whereas the influence of the plasmon-generated heat is a point of debate.[29,38] Here, we used a homogeneous large-scale monolayer of approximately 7 nm thick gold nanotriangles (NTs) deposited on substrates as the plasmonic platform.[39] The gold NTs were prepared using a one-step method in a mixed dioctyl sodium sulfo-succinate (AOT)/phospholipon vesicle phase in the presence of poly(*N*,*N*′-diallyl-*N*,*N*′-dimethylammonium-*alt*-3,5-bis-carboxyphenylmaleamic carboxylate (PalPhBisCarb) as a structure-directing agent and separated from spherical gold nanoparticles by depletion flocculation in the presence of AOT micelles.[40] The monolayer was formed at the liquid/air interface using a mixture of ethanol and toluene,[39] and it was then deposited on glass and silicon substrates after controlled evaporation of the solvents (compare Figure 1a). The extinction spectrum of the monolayer displayed a broad plasmon band located in the range of 500−2000 nm (inset in Figure 1), where it is in a good resonance with the excitation wavelengths. 4-NTP molecules were self-assembled on the gold NTs monolayer.

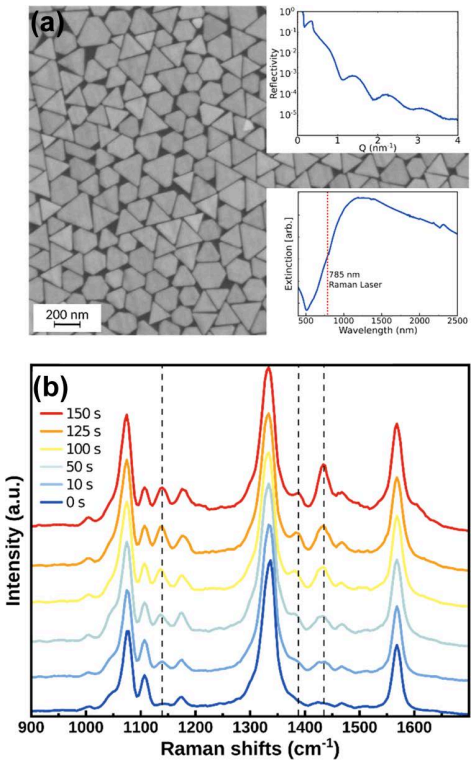

Figure 1. (a) SEM images of the gold NTs monolayer. The upper inset shows the X-ray reflectometry (XRR) data confirming a large-scale monolayer of approximately 7 nm thickness. The lower inset shows the optical extinction of a NT monolayer. (b) Time-dependent SERS spectra of 4-NTP assembled on the monolayer. Dashed lines indicate the three main product vibrational bands of DMAB.

The reaction was studied by SERS microscopy. Pronounced differences in the Raman spectra of the reactant (NTP) and product (DMAB) allowed us to assess the formation of DMAB. The heat expansion of the nanotriangles induced by continuous laser irradiation was measured by static X-ray diffraction at the KMC3-XPP end station of the Berlin synchrotron radiation facility BESSY II. A flat monolayer ordering of the nanotriangle SERS platform guaranteed that the lattice constant perpendicular to the triangles was oriented out of the substrate plane for all particles, which allows for low-intensity X-ray diffraction measurements in the symmetric Bragg configuration in any conventional XRD device.[39,41] The out-of-plane lattice expansion of the gold nanotriangles was calibrated by a careful measurement of the particles' lattice temperature. We conducted all experiments on different irradiated spots with varying sizes using different focusing conditions.

RESULTS AND DISCUSSION

We start our explanation by showing spectra of the 4-NTP molecules chemisorbed on our gold nanotriangle template in a typical SERS microscope with a 5 μm spot size (full width at half maximum, FWHM) using a continuous wave laser of 785 nm wavelength with a power of 30 mW. Figure 1a shows the transmission electron microscopy images of the well-ordered template and the X-ray reflectometry (XRR) results (inset) confirming that the platform indeed consists of a large area monolayer of gold nanotriangles with a thickness of 7 $\pm$ 2 nm on silicon. In this experiment, the laser light is simultaneously

DOI: 10.1021/acs.jpcc.8b12574
J. Phys. Chem. C 2019, 123, 9352−9357

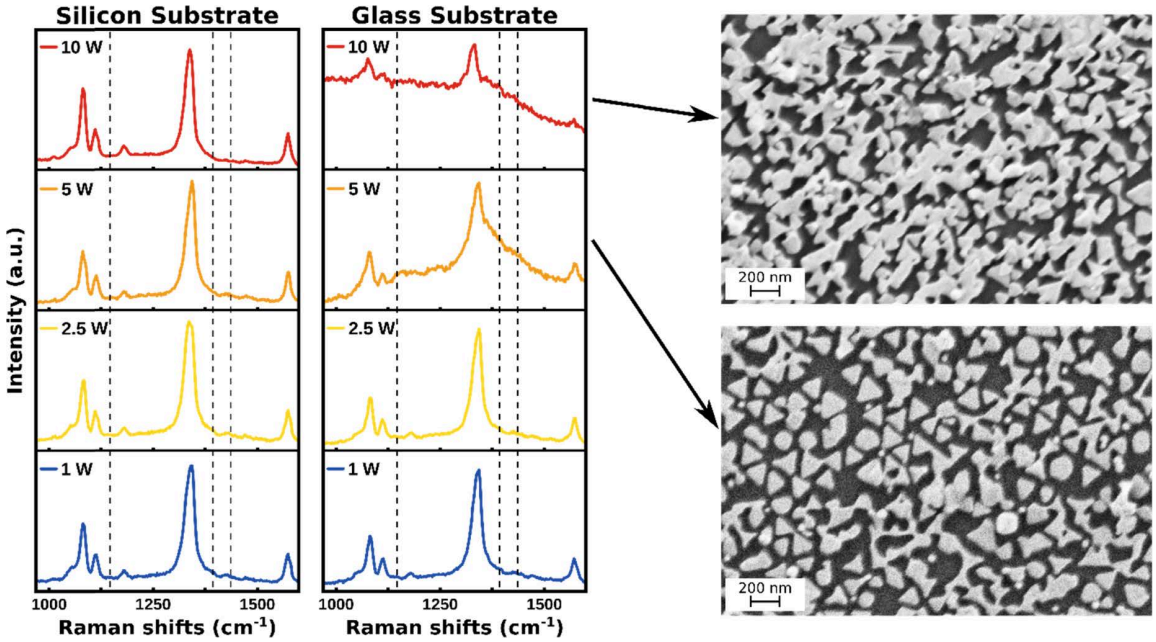

Figure 2. Low-intensity SERS spectra of 4-NTP assembled on gold NTs deposited on silicon and glass substrate probed after the sample was irradiated with different laser powers with 5 mm spot size for 5 min. Dashed lines show the frequencies, where the DMAB product would be expected. SEM images show the melting of the gold NTs on glass substrate for 5 W (lower image) and for 10 W (upper image).

responsible for SERS detection and for triggering the plasmon-assisted reaction. The time-dependent SERS spectra in Figure 1b confirm the transformation of 4-NTP to DMAB. The 4-NTP spectrum at 0 s displays main vibrational modes at 1082, 1332, and 1575 cm^{-1}, assigned to the C−H bending, NO_2 symmetric stretching, and C═C stretching modes of the 4-NTP,[42,43] respectively. After few seconds, new Raman peaks appear at 1134, 1387, and 1434 cm^{-1}, which are assigned to the C−N symmetric stretching and the N═N stretching vibrational modes of the DMAB confirming the coexistence of both molecules.[44,45] The light intensity in these experiments attains a very high value of 10 kW/cm^2. In the rest of the paper, we use far less intensity for SERS sensing to avoid driving the chemical reaction with the SERS laser.

In a first naïve attempt to drive the same reaction across an area that was larger than typically investigated in a microscope, we used a high-power diode laser module operating at 920 nm with a power up to 25 W. We increased the irradiated area by a factor of 10^6 to 5 mm spot diameter (FWHM), varying the irradiation power from 1 to 10 W, i.e., a 30- to 300-fold increase of the laser power. After irradiation for 5 min, the irradiated spots were investigated using the Raman microscope with very low laser power and short integration time (0.5 mW and 1 s). The SERS spectra of such spots are displayed in Figure 2 for the NTs deposited on silicon and glass substrates. The reaction clearly did not occur (no bands at the dashed lines, which indicate where product bands are expected). No signature of DMAB molecules was observed because we in fact decreased the intensity $I = P/A$ by a factor of 3000 to 30 000 compared to the microscopic irradiation. The Raman spectrum of the sample on glass changes at 5 W, acquiring a large background contribution, and the Raman peaks become hardly visible for 10 W irradiation. Melting of the NTs was found to be the reason as confirmed by SEM images (Figure 2), despite the very low laser intensity. Similar damage and no DMAB was observed for the silicon substrate after irradiating the sample with 15 W. The melting at higher laser power is related to the thermal conductivity of the glass, which is 2 orders of magnitude smaller than that for the silicon substrate. Therefore, the heating of the gold induced by light is dissipated more quickly by the substrate to avoid melting of the NPs.

The fact that the particles already melt at the intensity of 400 mW/cm^2 under the large spot really makes it surprising that in a microscope focus the intensity can be easily increased by 3 orders of magnitude above this intensity without any signs of melting. It illustrates at the same time the great opportunities of nanoscale heating.

To check the role of the focusing conditions, the laser driving the reaction was focused through different plano-convex lenses onto the sample irradiating spots of different sizes. The laser power was tuned to obtain approximately the same final laser intensity.

Figure 3 shows the Raman spectra taken from spots irradiated with an intensity of about 50 kW/cm^2. The SERS spectra recorded on the spots with 70 and 115 μm diameter generated by 30 and 50 mm focusing lenses show the characteristic DMAB Raman peaks, which indicate the plasmon-driven coupling reaction. The intensity of the DMAB peak decreases relative to the 4-NTP peak with increasing spot size. For the 175 μm spots (75 mm lens), the peaks are hardly discernible and for the 230 μm spots (100 mm lens), the Raman spectrum only consists of a noisy electronic background from the hot and molten NPs, which is confirmed by SEM images similar to the ones shown in Figure 2. The hot spots of the plasmonic platform, which provide the largest SERS enhancement and the largest reaction yield, melts first and therefore the excessive heating deteriorates the reaction rate.

The heat dissipation, excluding light absorption, was numerically calculated solving the 3D heat equation by means of a numerical finite elements (FEM) solver (COMSOL

DOI: 10.1021/acs.jpcc.8b12574
J. Phys. Chem. C 2019, 123, 9352−9357

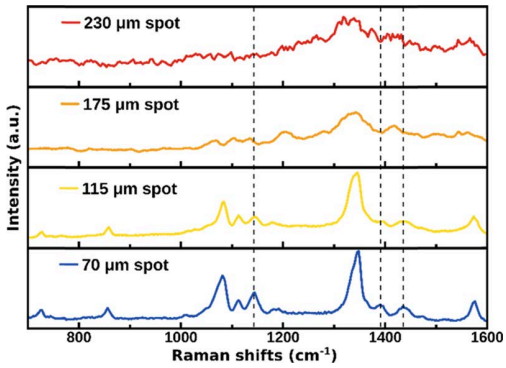

Figure 3. SERS spectra of 4-NTP assembled on gold NTs and probed with different laser spot sizes of 70, 115, 175, and 230 μm diameter. The intensity of the exciting laser beam in all four measurements is identical.

Multiphysics) using the temperature-dependent heat capacity and heat conductivity for gold,[46,47] silicon,[46−48] and glass.[49,50] In our model, the laser heating was simulated using a homogeneous heating of an area of the size of the laser spot (von Neumann boundary condition), whereas the lower substrate interface was kept at a constant temperature of T = 288.15 K. Indeed, the irradiated spot size strongly influences the rate of heat dissipation. Small spots demonstrate a three-dimensional temperature gradient (Figure 4a), indicative of a three-dimensional heat flow. On the other hand, in the center portions of the larger spots with the same excitation intensity, the heat mainly dissipates along the temperature gradient perpendicular to the substrate (Figure 4b), resulting in less efficient one-dimensional heat transport for a large fraction of the spot. Therefore, small spots cool faster and can absorb and dissipate much larger intensities without NP melting. Such high level of absorbed and dissipated energy enables the formation of DMAB molecules. Attempts to flow the same amount of energy per unit area through a large spot inevitably leads to melting of the NPs.

Irradiating the NP continuously with different laser intensities on different spot sizes (100, 250, and 500 μm), we measured their temperatures by XRD via lattice heat expansion. The analysis is based on the detection of the shifts in the (222) Bragg reflection of the gold NTs in Θ−2Θ scans. This shift was then transformed to the temperature change of the NTs based on Bragg's law and the linear thermal expansion

$$\cot\theta\Delta\theta = \frac{\Delta c}{c} = -\alpha\Delta T$$

Here, $\Delta\theta$ is the shift of the Bragg peak, $\Delta c/c$ is the relative change of the out-of-plane lattice constant, and $\alpha = 1.49 \times 10^{-5}\ 1/K$ is the thermal expansion coefficient of the gold nanotriangles previously measured by X-ray diffraction using conventional heating, which is slightly increased compared to bulk gold.[51] To perform the Bragg-angle-based temperature measurement during laser irradiation, the sample was glued with silver paste onto a Peltier cooled sample holder with an active feedback loop stabilized to 288.15 K.

Figure 4c shows the temperature of the gold NTs measured for different spot sizes on a 0.5 mm thick Si substrate, which increases linearly with the laser intensity. For a large spot of 500 μm, a laser intensity of approximately 10 kW/cm^2 is sufficient to increase the particle temperature to 96 K. For a small spot of 100 μm, a 10 times larger intensity leads to less heating of only 70 K. For glass substrates, the heating is even more dominant, and Figure 4c compares the 500 μm spot on Si to a glass substrate. The silicon substrate has considerably higher thermal conductivity. For high laser intensities, a Bragg peak sharpening is observed that is related to an increase of the gold NTs thickness due a particle coalescence (for more information, see the Supporting Information).

FEM simulations of the temperature increases using the model described earlier confirm that the temperature changes can be fully explained by the different spot sizes (solid lines in Figure 4c,d). The simulated temperature increases indeed match the measured temperature increases very well. It should be noted that a phenomenological absorption factor was used to adapt the simulation to the measurements. It reduced the total power entering the simulation to take into account both the optical absorption coefficient of the sample and the possible heat resistances at the gold−substrate interface. The same absorption factor was used for each substrate material.

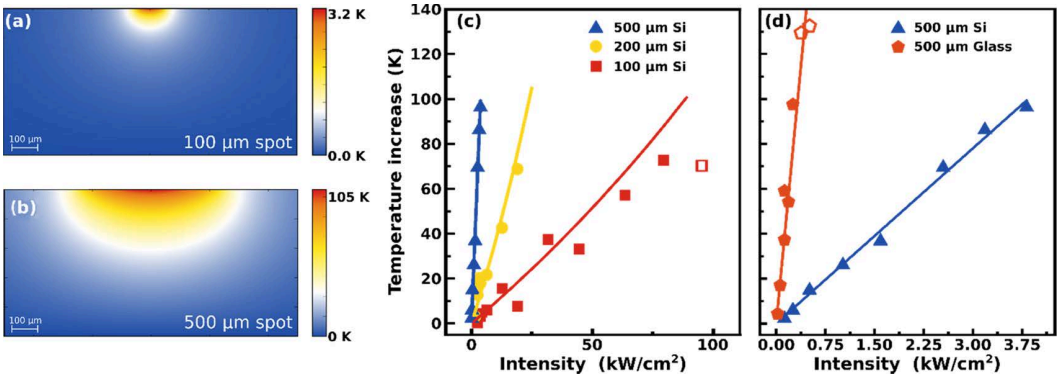

Figure 4. (a, b) FEM simulation of the temperature gradient in the substrate for an excitation intensity of 100 kW/cm^2 with two different spot sizes. The temperature change of the gold NTs as determined from the Bragg-reflection shift (c) as a function of the laser intensity due to irradiation with different laser spot sizes on silicon and (d) on different substrates for the same spot size of 500 μm. The solid lines represent the result of a FEM simulation of the temperature increase. The unfilled symbols in (c) and (d) represent intensities at which a Bragg peak sharpening was observed. The model does not consider the light absorption.

DOI: 10.1021/acs.jpcc.8b12574
J. Phys. Chem. C 2019, 123, 9352−9357

CONCLUSIONS

In conclusion, we have shown that driving a plasmonic chemical reaction on a SERS template structure with a fixed light intensity is only possible up to a certain maximum area of the laser focus because the heat transport turns from 3D to 1D and the excessive heating destroys the sample structure. The silicon substrate turns out to be more suited for plasmonic chemistry than conventional glass substrates, since its high thermal conductivity improves the dissipation of heat and therefore a higher light intensity can be used with more photons triggering the reaction and without melting the plasmonic template structure. This is true, although additional photons are absorbed in the substrate. With laser wavelength above the silicon band gap and by appropriate thermal engineering, the substrate heating could be further reduced.

These microscopic findings underline the importance of heat transport at the nanoscale for a profound understanding of nanoplasmonic chemistry. Although time-resolved measurements of the gold NT's lattice temperature rise with subpicosecond time resolution has been recently reported, there is so far no report on driving plasmon-assisted chemistry with femtosecond laser pulses.

ASSOCIATED CONTENT

Supporting Information

The Supporting Information is available free of charge on the ACS Publications website at DOI: 10.1021/acs.jpcc.8b12574.

Damage caused by irradiation; X-ray reflectivity of gold nanotriangles; X-ray diffraction (XRD); determination of the linear expansion coefficient; temperature-dependent lattice constant (PDF)

AUTHOR INFORMATION

Corresponding Author

*E-mail: koopman@uni-potsdam.de.

ORCID

Wouter Koopman: 0000-0001-5402-345X

Joachim Koetz: 0000-0001-9113-1337

Matias Bargheer: 0000-0002-0952-6602

Notes

The authors declare no competing financial interest.

ACKNOWLEDGMENTS

R.M.S. and F.S. gratefully acknowledge the financial support by the DFG via the School of Analytical Science Adlershof (SALSA).

REFERENCES

(1) Boyer, D.; Tamarat, P.; Maali, A.; Lounis, B.; Orrit, M. Photothermal imaging of nanometer-sized metal particles among scatterers. *Science* **2002**, *297*, 1160−1163.

(2) Cognet, L.; Berciaud, S.; Lasne, D.; Lounis, B. Photothermal methods for single nonluminescent nano-objects. *Anal. Chem.* **2008**, *80*, 2288−2294.

(3) Huang, X.; Jain, P. K.; El-Sayed, I. H.; El-Sayed, M. A. Plasmonic photothermal therapy (PPTT) using old nanoparticles. *Lasers Med. Sci.* **2008**, *23*, 217−228.

(4) Hirsch, L. R.; Stafford, R. J.; Bankson, J. A.; Sershen, S. R.; Rivera, B.; Price, R. E.; Hazle, J. D.; Halas, N. J.; West, J. L. Nanoshell-mediated near-infrared thermal therapy of tumors under magnetic resonance guidance. *Proc. Natl. Acad. Sci. U.S.A.* **2003**, *100*, 13549−13554.

(5) Govorov, A. O.; Richardson, H. H. Generating heat with metal nanoparticles. *Nano Today* **2007**, *2*, 30−38.

(6) Timko, B. P.; Dvir, T.; Kohane, D. S. Remotely triggerable drug delivery systems. *Adv. Mater.* **2010**, *22*, 4925−4943.

(7) Pelton, M.; Aizpurua, J.; Bryant, G. Metal-nanoparticle plasmonics. *Laser Photonics Rev.* **2008**, *2*, 136−159.

(8) Baffou, G.; Quidant, R. Thermo-plasmonics: using metallic nanostructures as nano-sources of heat. *Laser Photonics Rev.* **2013**, *7*, 171−187.

(9) Zhang, Y.; Nelson, T.; Tretiak, S.; Guo, H.; Schatz, G. C. Plasmonic hot-carrier-mediated tunable photochemical reactions. *ACS Nano* **2018**, *12*, 8415−8422.

(10) Hattori, Y.; Abdellah, M.; Rocha, I.; Pavliuk, M. V.; Fernandes, D. L. A.; Sá, J. Light-induced ultrafast proton-coupled electron transfer responsible for H2 evolution on silver plasmonics. *Mater. Today* **2018**, *21*, 590−593.

(11) Cao, L.; Barsic, D. N.; Guichard, A. R.; Brongersma, M. L. Plasmon-assisted local temperature control to pattern individual semiconductor nanowires and carbon nanotubes. *Nano Lett.* **2007**, *7*, 3523−3527.

(12) Long, R.; Li, Y.; Song, L.; Xiong, Y. Coupling solar energy into reactions: Materials design for surface plasmon-mediated catalysis. *Small* **2015**, *11*, 3873−3889.

(13) Link, S.; Masiello, D. J. Introduction: Plasmonics in chemistry. *Chem. Rev.* **2018**, *118*, 2863−2864.

(14) Cui, L.; Wang, P.; Fang, Y.; Li, Y.; Sun, M. A plasmon-driven selective surface catalytic reaction revealed by surface-enhanced Raman scattering in an electrochemical environment. *Sci. Rep.* **2015**, *5*, No. 11920.

(15) Fang, Y.; Li, Y.; Xu, H.; Sun, M. Ascertaining p,p'-dimercaptoazobenzene produced from p-aminothiophenol by selective catalytic coupling reaction on silver nanoparticles. *Langmuir* **2010**, *26*, 7737−7746.

(16) Huang, Y.-F.; Zhu, H.-P.; Liu, G.-K.; Wu, D.-Y.; Ren, B.; Tian, Z.-Q. When the signal is not from the original molecule to be detected: chemical transformation of para-aminothiophenol on Ag during the SERS measurement. *J. Am. Chem. Soc.* **2010**, *132*, 9244−9246.

(17) van Schrojenstein Lantman, E. M.; Deckert-Gaudig, T.; Mank, A. J. G.; Deckert, V.; Weckhuysen, B. M. Catalytic processes monitored at the nanoscale with tip-enhanced Raman spectroscopy. *Nat. Nanotechnol.* **2012**, *7*, 583−586.

(18) Sun, M.; Xu, H. A novel application of plasmonics: plasmon-driven surface-catalyzed reactions. *Small* **2012**, *8*, 2777−2786.

(19) Chen, X.-J.; Cabello, G.; Wu, D.-Y.; Tian, Z.-Q. Surface-enhanced Raman spectroscopy toward application in plasmonic photocatalysis on metal nanostructures. *J. Photochem. Photobiol., C* **2014**, *21*, 54−80.

(20) Chen, H. L.; Li, C.-J.; Peng, C.-J.; Leu, H.-J.; Hung, W.-H. Plasmon-induced hot electrons on mesoporous carbon for decomposition of organic pollutants under outdoor sunlight irradiation. *ACS Appl. Mater. Interfaces* **2017**, *9*, 327−334.

(21) Kowalska, E.; Yoshiiri, K.; Wei, Z.; Zheng, S.; Kastl, E.; Remita, H.; Ohtani, B.; Rau, S. Hybrid photocatalysts composed of titania modified with plasmonic nanoparticles and ruthenium complexes for decomposition of organic compounds. *Appl. Catal., B* **2015**, *178*, 133−143.

(22) Mukherjee, S.; Libisch, F.; Large, N.; Neumann, O.; Brown, L. V.; Cheng, J.; Lassiter, J. B.; Carter, E. A.; Nordlander, P.; Halas, N. J. Hot electrons do the impossible: Plasmon-induced dissociation of H2 on Au. *Nano Lett.* **2013**, *13*, 240−247.

(23) Zhou, L.; Zhang, C.; McClain, M. J.; Manjavacas, A.; Krauter, C. M.; Tian, S.; Berg, F.; Everitt, H. O.; Carter, E. A.; Nordlander, P.; et al. Aluminum nanocrystals as a plasmonic photocatalyst for hydrogen dissociation. *Nano Lett.* **2016**, *16*, 1478−1484.

(24) Yasuda, S.; Yoshii, T.; Chiashi, S.; Maruyama, S.; Murakoshi, K. Plasmon-induced selective oxidation reaction at single-walled carbon nanotubes. *ACS Appl. Mater. Interfaces* **2017**, *9*, 38992−38998.

(25) de Nijs, B.; Benz, F.; Barrow, S. J.; Sigle, D. O.; Chikkaraddy, R.; Palma, A.; Carnegie, C.; Kamp, M.; Sundararaman, R.; Narang, P.; et al. Plasmonic tunnel junctions for single-molecule redox chemistry. *Nat. Commun.* **2017**, *8*, No. 994.
(26) Adleman, J. R.; Boyd, D. A.; Goodwin, D. G.; Psaltis, D. Heterogenous catalysis mediated by plasmon heating. *Nano Lett.* **2009**, *9*, 4417−4423.
(27) Xu, P.; Kang, L.; Mack, N. H.; Schanze, K. S.; Han, X.; Wang, H.-L. Mechanistic understanding of surface plasmon assisted catalysis on a single particle: cyclic redox of 4-aminothiophenol. *Sci. Rep.* **2013**, *3*, No. 2997.
(28) Bora, T.; Zoepfl, D.; Dutta, J. Importance of plasmonic heating on visible light driven photocatalysis of gold nanoparticle decorated Zinc oxide nanorods. *Sci. Rep.* **2016**, *6*, No. 26913.
(29) Golubev, A. A.; Khlebtsov, B. N.; Rodriguez, R. D.; Chen, Y.; Zahn, D. R. T. Plasmonic heating plays a dominant role in the plasmon-induced photocatalytic reduction of 4-nitrobenzenethiol. *J. Phys. Chem. C* **2018**, *122*, 5657−5663.
(30) Kang, L.; Han, X.; Chu, J.; Xiong, J.; He, X.; Wang, H.-L.; Xu, P. In situ surface-enhanced Raman spectroscopy study of plasmon-driven catalytic reactions of 4-nitrothiophenol under a controlled atmosphere. *ChemCatChem* **2015**, *7*, 1004−1010.
(31) Xie, W.; Walkenfort, B.; Schlücker, S. Label-free SERS monitoring of chemical reactions catalyzed by small gold nanoparticles using 3D plasmonic superstructures. *J. Am. Chem. Soc.* **2013**, *135*, 1657−1660.
(32) Yan, X.; Wang, L.; Tan, X.; Tian, B.; Zhang, J. Surface-enhanced Raman spectroscopy assisted by radical capturer for tracking of plasmon-driven redox reaction. *Sci. Rep.* **2016**, *6*, No. 30193.
(33) Dong, B.; Fang, Y.; Chen, X.; Xu, H.; Sun, M. Substrate-, wavelength-, and time-dependent plasmon-assisted surface catalysis reaction of 4-nitrobenzenethiol dimerizing to p,p'-dimercaptoazobenzene on Au, Ag, and Cu films. *Langmuir* **2011**, *27*, 10677−10682.
(34) Cho, F.-H.; Kuo, S.-C.; Lai, Y.-H. Surface-plasmon-induced azo coupling reaction between nitro compounds on dendritic silver monitored by surface-enhanced Raman spectroscopy. *RSC Adv.* **2017**, *7*, 10259−10265.
(35) Ding, Q.; Chen, M.; Fang, Y.; Zhang, Z.; Sun, M. Plasmon-driven diazo coupling reactions of p -nitroaniline via −NH 2 or −NO 2 in atmosphere environment. *J. Phys. Chem. C* **2017**, *121*, 5225−5231.
(36) Zhang, Z.; Chen, L.; Sun, M.; Ruan, P.; Zheng, H.; Xu, H. Insights into the nature of plasmon-driven catalytic reactions revealed by HV-TERS. *Nanoscale* **2013**, *5*, 3249−3252.
(37) Zhang, Z.; Kinzel, D.; Deckert, V. Photo-Induced or plasmon-induced reaction: Investigation of the light-induced azo-coupling of amino groups. *J. Phys. Chem. C* **2016**, *120*, 20978−20983.
(38) Kim, K.; Choi, J.-Y.; Shin, K. S. Surface-enhanced Raman scattering of 4-nitrobenzenethiol and 4-aminobenzenethiol on silver in icy environments at liquid nitrogen temperature. *J. Phys. Chem. C* **2014**, *118*, 11397−11403.
(39) Liebig, F.; Sarhan, R. M.; Sander, M.; Koopman, W.; Schuetz, R.; Bargheer, M.; Koetz, J. Deposition of gold nanotriangles in large scale close-packed monolayers for X-ray-based temperature calibration and SERS monitoring of plasmon-driven catalytic reactions. *ACS Appl. Mater. Interfaces* **2017**, *9*, 20247−20253.
(40) Liebig, F.; Sarhan, R. M.; Prietzel, C.; Reinecke, A.; Koetz, J. "Green" gold nanotriangles: synthesis, purification by polyelectrolyte/micelle depletion flocculation and performance in surface-enhanced Raman scattering. *RSC Adv.* **2016**, *6*, 33561−33568.
(41) von Reppert, A.; Sarhan, R. M.; Stete, F.; Pudell, J.; Del Fatti, N.; Crut, A.; Koetz, J.; Liebig, F.; Prietzel, C.; Bargheer, M. Watching the vibration and cooling of ultrathin gold nanotriangles by ultrafast X-ray diffraction. *J. Phys. Chem. C* **2016**, *120*, 28894−28899.
(42) Ling, Y.; Xie, W. C.; Liu, G. K.; Yan, R. W.; Wu, D. Y.; Tang, J. The discovery of the hydrogen bond from p-nitrothiophenol by Raman spectroscopy: guideline for the thioalcohol molecule recognition tool. *Sci. Rep.* **2016**, *6*, No. 31981.
(43) Kuo, S.-C.; Tasi, J.-J.; Li, J.-S.; Hou, Z.-H.; Li, C.-H.; Jeng, U.-S.; Lai, Y.-H. Enhancement of surface enhanced Raman scattering activity of Au nanoparticles through the mesostructured metallic nanoparticle arrays. *APL Mater.* **2014**, *2*, No. 113310.
(44) Shin, D. Two different behaviors in 4-ABT and 4,4′-DMAB surface enhanced Raman spectroscopy. *J. Raman Spectrosc.* **2017**, *48*, 343−347.
(45) Kim, K.; Shin, D.; Kim, K. L.; Shin, K. S. Surface-enhanced Raman scattering of 4,4′-dimercaptoazobenzene trapped in Au nanogaps. *Phys. Chem. Chem. Phys.* **2012**, *14*, 4095−4100.
(46) Ho, C. Y.; Powell, R. W.; Liley, P. E. Thermal conductivity of the elements. *J. Phys. Chem. Ref. Data* **1972**, *1*, 279−421.
(47) Pankratz, L. B.; Mrazek, R. V. *Thermodynamic Properties of Elements and Oxides*; U.S. Department of the Interior, Bureau of Mines, 1982.
(48) Desai, P. D. Thermodynamic properties of iron and silicon. *J. Phys. Chem. Ref. Data* **1986**, *15*, 967−983.
(49) Kingery, W. D. Heat-conductivity processes in glass. *J. Am. Ceram. Soc.* **1961**, *44*, 302−304.
(50) Lucks, C. F.; Deem, H. W.; Wood, W. D. *Thermal Properties of Six Glasses and Two Graphites*; Battelle Memorial Institute: Columbus, OH, 1960; Vol. *39*.
(51) Nix, F. C.; MacNair, D. The thermal expansion of pure metals: copper, gold, aluminum, nickel, and iron. *Phys. Rev.* **1941**, *60*, 597−605.

DOI: 10.1021/acs.jpcc.8b12574
J. Phys. Chem. C 2019, 123, 9352−9357

Scaling-Up Nano-Plasmon Catalysis: The Role of Heat Dissipation

Radwan M. Sarhan,[1,2] Wouter Koopman,[1] Jan Pudell,[1] Felix Stete,[1,2] Matthias Rössle,[3] Marc Herzog,[1] Clemens N. Z. Schmitt,[4] Ferenc Liebig,[5] Joachim Koetz,[5] and Matias Bargheer[1,3]

[1] *Institute of Physics and Astronomy, University of Potsdam, 14476 Potsdam, Germany*
[2] *School of Analytical Sciences Adlershof (SALSA), Humboldt-Universität zu Berlin, Albert-Einstein-Str. 5-9, 10099 Berlin, Germany*
[3] *Helmholtz-Zentrum Berlin, Albert-Einstein-Str. 15, 12489 Berlin, Germany*
[4] *Max Planck Institute of Colloids and Interfaces, 14476 Potsdam, Germany*
[5] *Institute of Chemistry, University of Potsdam, 14476 Potsdam, Germany*

DAMAGE CAUSED BY IRRADIATION

We confirmed by SEM (Figure S1) that the degradation of the Raman spectra presented in Figure 3 of the manuscript were caused by damages to the nanoparticle substrate. As the high total power of the excitation laser beam could not dissipate quickly enough, a partial melting of the particles occurred.

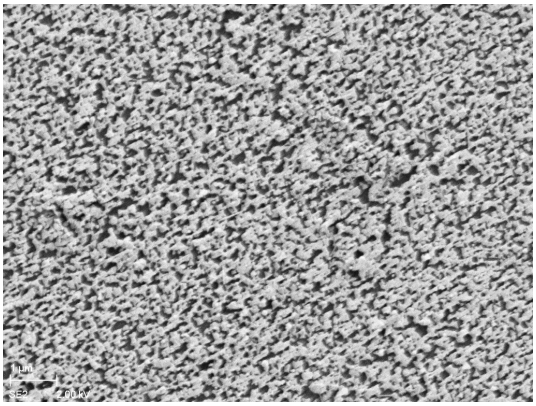

FIG. S1. **SEM 175 µm spot:** 8 µm × 5.5 µm SEM image of from the center of the irradiated spot with a diameter of 175 µm. The damage due to the melting of the nanotriangles is clearly visible.

X-RAY REFLECTIVITY OF GOLD NANO TRIANGLES

X-ray reflectivity (XRR) is a technique that allows the surface-sensitive characterization of thin layers by interference of specular reflections of the bottom and top interfaces of the layer that give rise to characteristic minima and maxima as function of the energy transfer, $Q = 4/\lambda \sin\vartheta$, with ϑ being the incidence angle of the X-rays with wavelength λ onto the sample. We measured a monolayer of gold nano triangles (NTs) on a Silicon substrate at the XPP-KMC-3 endstation at the synchrotron BESSY II. The incidence angle of the X-rays on the sample was scanned between 0 and 3° incidence angle, which corresponds to $Q = 0$ to $4\,\mathrm{nm}^{-1}$ in reciprocal space. The corresponding dataset shown in the inset of Fig. 1a) contains a dominant oscillation frequency that corresponds to a wavelength of $\lambda = 0.9\,\mathrm{nm}^{-1}$ determined by a Fourier-transformation. This wavelength corresponds to a layer-thickness of $7 \pm 2\,\mathrm{nm}$. The absence of higher frequencies in the signal proofs that our sample contains a negligible part of stacked gold-nano-triangles over the X-ray spot size of approximately $0.5 \times 10\,\mathrm{mm}^2$.

X-RAY DIFFRACTION (XRD)

We measured at the XPP-KMC-3 endstation at the synchrotron source BESSY II the 222 Bragg reflection of the [111] oriented gold NTs at the X-ray energy of 8 keV. We selected the 2nd order Bragg reflection to minimize the X-ray footprint. The sample was mounted on Peltier-cooled sample mount, which results in a stable substrate

temperature of 15°C that was attached with silver paint to the Peltier cooler. In Figure S2a) and b) we show the Bragg peaks of the gold NTs on Si and glass substrates for different Laser intensities, respectively. For every measured laser intensity, a new spot on the sample was selected and measured before illumination (black thick curves) and during illumination. For every measurement we waited 60 s for thermal equilibration between gold NTs.

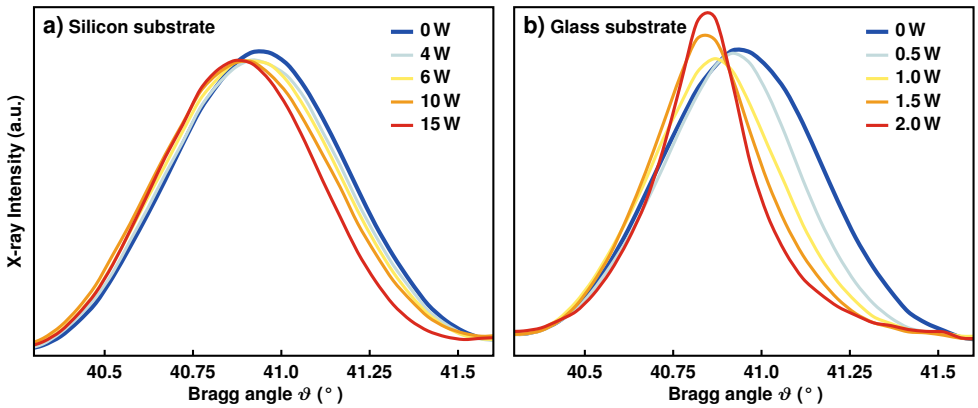

FIG. S2. **XRD results:** Bragg peak shift of gold NTs on a) a silicon substrate and b) glass substrate for different intensities. The Bragg peak shift to smaller angles due to heating of the gold NTs. On the glass substrate a sharpened peak is observed for high intensities.

We note a peak sharpening at high intensities. For very thin layer we can neglect typical Bragg broadening effects and the width of the Bragg peak is approximately given by the thickness. In our case the peak width is slightly smaller as theoretical values for 7 nm layers, which indicates a small amount of stacked gold NTs (5-10%). After illumination of the sample with glass substrate with high intensities we observe a sharpened Bragg peak that is related to thicker nano particles. This indicates a particle coalescence of the gold NTs.

DETERMINATION OF THE LINEAR EXPANSION COEFFICIENT

The temperature-dependent shift of the Bragg peak allows us to calculate the linear expansion coefficient for gold NTs along the [111] direction. It is measured with a closed-cycle cryostat setup available at the XPP-KMC-3 endstation at the synchrotron source BESSY II that allows the variation of the sample temperature from 20 to 350 K. From the Bragg Peak position the out-of-plane lattice constant in [111] direction is extracted and shown in Figure S3. A linear fit yields the linear expansion coefficient of $\alpha = 1.49 \cdot 10^{-5}\,1/\mathrm{K}$.

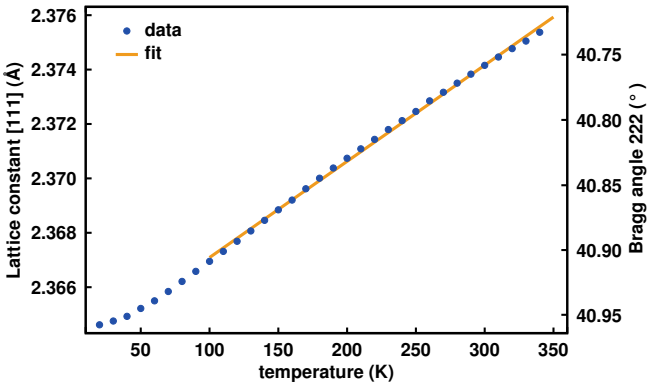

FIG. S3. **The Temperature-dependent lattice constant** is measured from 20 to 350 K and fitted to extract the linear expansion coefficient α.

Declaration

I hereby declare that this doctoral thesis entitle “Plasmon-driven photocatalytic reactions monitored by surface-enhanced Raman spectroscopy” was carried out by me and I did not use any unnamed source or aid. I assure that the present thesis for the acquisition of the doctoral degree was not submitted either in this or in any other University.

Signed:_____ Date:_____